

**An *in vivo* investigation of dynamic  
contrast - enhanced ultrasound  
(DCE-US) imaging for the  
assessment of tumour response to  
radiotherapy**

A thesis submitted for the degree of Doctor of Philosophy  
of the  
University of London

Dana Naser Tahboub

April 2022

Division of Radiotherapy & Imaging

Institute of Cancer Research

University of London

# Declaration

I hereby declare that this thesis reports on my own original work. Contributions made to this research by others are explicitly acknowledged within the thesis.

Dana Naser Tahboub

# Abstract

Imaging biomarkers of early response to cancer therapy can facilitate more effective treatment adaptation and improve cancer management. These biomarkers can detect functional, structural or molecular tumour changes that occur shortly after treatment and inform on response. For radiation therapy, such indicators of response could be obtained from the tumour vasculature; hypofractionated radiation has been shown to lead to tumour vascular damage, which is suggested to be an important determinant of overall tumour response. This thesis investigated the potential of dynamic contrast enhanced ultrasound (DCE-US) imaging to detect vascular changes associated with tumour response to radiotherapy in preclinical models of cervical and head and neck cancer.

Longitudinal two-dimensional (2D) DCE-US was used to image xenograft tumours prior to, and shortly following, single-fraction radiation. A decrease in the DCE-US metrics modified transit time (MTT), washout time (WOUT), and area under the curve (AUC) was observed following treatment, indicating radiation-induced vascular disruption. A greater decrease in these 2D DCE-US metrics was observed in tumours with a complete response, compared to tumours with a partial response, supporting the potential of DCE-US imaging as a biomarker of response. The use of three-dimensional (3D) DCE-US imaging revealed a decrease in wash-in time (WIT) is associated with response, which was not detected with 2D imaging. However, 3D imaging did not detect changes in any other metrics.

The repeatability of 2D and 3D DCE-US was examined through imaging of the mouse kidney, and it was revealed that the measurement variation associated with both 3D and 2D DCE-US is of the same order of magnitude as the measured significant changes. Hence improving repeatability will be important in the development of DCE-US for longitudinal monitoring of the tumour vasculature.

In summary, DCE-US can detect vascular changes associated with response to radiotherapy, and further technical validation could improve its accuracy as a biomarker of response to radiotherapy.

## **Statement of Covid Impact**

Lockdowns introduced by the COVID pandemic led to a disruption of studies from March 2020 to July 2020. After this interruption, the main aim was to begin imaging experiments with the 3D imaging system. The setup for the system was further delayed due to the furlough (July 2020 to December 2021) of other team members who were responsible for developing the system. An extension to this PhD was granted to cover the period of lockdown, however, it is hard to estimate the full impact of delays to the system. One task that could not be fully completed in time for inclusion in this thesis, was that of histopathological validation of DCE-US imaging and the results reported here are restricted to a visual comparison of DCE-US metrics and histopathological markers of vasculature.

# Acknowledgments

I would first like to thank my incredible team of supervisors Dr Emma Harris, Dr Carol Box, Professor Jeff Bamber, and Dr Simon Robinson. I am forever grateful for your mentorship, advice, and unwavering patience. Your constant enthusiasm for science and research is inspiring to witness and contagious.

Next, I would like to thank the Ultrasound team members, who provided invaluable support and help over the course of my PhD and made this experience incredibly enjoyable. I am grateful for Dr Elahe Moghimirad and Dr John Civale for help with setup of the Verasonics scanner, Dr Vaideesh Parasaram for carrying out the histopathology staining, and especially Nigel Bush for his tremendous help with animal imaging. I would also like to thank Dr Yann Jamin and Dr Jessica Boulton for helping with animal procedure.

I would also like to thank the BSU team for their continuous support, and advice during animal experiments. And Louise Howell from the microscope facility for trying relentlessly to teach how to use the microscope.

I would like to thank my fellow PhD student cohort, and all my friends in London for making my PhD years fun and memorable. Finally, my family who are too many to name, but are each an endless source of joy and love. My siblings, grandparents, aunt, uncles, and cousins. Most importantly, I will forever be in debt to my parents for their unconditional support and love, and for instilling in me and my siblings a sense of duty towards our society that is to be fulfilled through knowledge and learning. This PhD would not be possible without them, without my mom always putting us first. This PhD is dedicated to my dad, who passed away before seeing me achieve this milestone, but his pride was always on display. He adamantly insisted that I can finish a PhD in 18 months. And while that's certainly not true, his (inflated) confidence and belief in me is the encouragement I needed to complete this journey.

# Table of Contents

<b>DECLARATION</b>	<b>2</b>
<b>ABSTRACT</b>	<b>3</b>
<b>STATEMENT OF COVID IMPACT</b>	<b>4</b>
<b>ACKNOWLEDGMENTS</b>	<b>5</b>
<b>TABLE OF CONTENTS</b>	<b>6</b>
<b>LIST OF FIGURES</b>	<b>14</b>
<b>LIST OF TABLES</b>	<b>17</b>
<b>LIST OF ACRONYMS</b>	<b>18</b>
<b>1 CHAPTER INTRODUCTION</b>	<b>21</b>
<b>1.1 RADIOTHERAPY: POTENTIAL FOR PERSONALISATION</b>	<b>21</b>
1.1.1 <i>Radiotherapy in head and neck cancer</i>	21
1.1.2 <i>Radiotherapy for cervical cancer</i>	23
<b>1.2 BIOMARKERS FOR PREDICTION AND ASSESSMENT OF RESPONSE TO RADIOTHERAPY</b>	<b>23</b>
1.2.1 <i>Predictive biomarkers</i>	24
1.2.2 <i>Biomarkers for response assessment</i>	24
1.2.3 <i>Imaging biomarkers</i>	26
1.2.3.1 <i>Positron emission tomography (PET)</i>	27
1.2.3.2 <i>Magnetic resonance imaging (MRI)</i>	27
1.2.3.3 <i>Computed tomography (CT)</i>	28
1.2.3.4 <i>Ultrasound imaging</i>	28
<b>1.3 THE ROLE OF FUNCTIONAL VASCULATURE IN TUMOUR RESPONSE TO RADIOTHERAPY</b>	<b>30</b>
1.3.1 <i>Prediction of response based on pretreatment vasculature</i>	30
1.3.2 <i>Radiation-induced vascular changes and association with response</i>	32
<b>1.4 DYNAMIC CONTRAST-ENHANCED ULTRASOUND IMAGING</b>	<b>34</b>

1.4.1	<i>Clinical use of DCE-US imaging</i>	35
1.4.2	<i>Basis of DCE-US imaging</i>	35
1.4.2.1	Ultrasound Contrast Agents	35
1.4.2.2	Detection of UCA signal	36
1.4.3	<i>Quantification of DCE-US imaging</i>	37
1.4.3.1	Bolus contrast injection	37
1.4.3.2	Disruption replenishment imaging	38
1.4.4	<i>Validation of DCE-US for imaging vasculature</i>	38
1.4.5	<i>Current challenges to the use of DCE-US for the prediction and assessment of response to radiotherapy</i>	41
1.4.5.1	Lack of evidence in radiotherapy	41
1.4.5.2	Limits of 2D DCE-US imaging	41
1.4.5.3	Repeatability of DCE-US	42
<b>2</b>	<b>CHAPTER THESIS AIM AND ORGANISATION</b>	<b>43</b>
2.1	<b>AIMS</b>	<b>43</b>
2.2	<b>ORGANISATION OF THESIS</b>	<b>44</b>
<b>3</b>	<b>CHAPTER MATERIALS &amp; METHODS</b>	<b>45</b>
3.1	<b>TUMOUR MODELS</b>	<b>45</b>
3.1.1	<i>Cell preparation</i>	45
3.1.2	<i>Cell injection</i>	45
3.1.3	<i>Tumour growth monitoring</i>	46
3.1.4	<i>Radiation response</i>	47
3.2	<b>DCE-US IMAGING</b>	<b>48</b>
3.2.1	<i>Imaging schedule</i>	48
3.2.2	<i>Animal anaesthesia and cannulation for imaging</i>	48
3.2.3	<i>Contrast agent</i>	49
3.2.4	<i>Two-dimensional (2D) DCE-US imaging</i>	50
3.2.5	<i>Three-dimensional (3D) DCE-US imaging</i>	52
3.3	<b>DCE -US DATA ANALYSIS</b>	<b>54</b>
3.3.1	<i>2D DCE-US data</i>	55
3.3.1.1	Whole-ROI analysis	55
3.3.1.2	TAC metric maps	56
3.3.1.3	Subregion analysis	57
3.3.1.4	Histogram analysis	59
3.3.2	<i>3D DCE-US data</i>	60

3.3.2.1	Frame selection	60
3.3.2.2	Motion correction	63
3.3.2.3	Whole-tumour ROI analysis	63
3.3.2.4	3D TAC metric maps	65
3.3.2.5	Subregion analysis	65
3.3.2.6	Histogram analysis	65
<b>3.4</b>	<b>RADIATION TREATMENT</b>	<b>66</b>
<b>3.5</b>	<b>HISTOPATHOLOGY</b>	<b>69</b>
3.5.1	<i>Frozen tissue processing</i>	69
3.5.2	<i>Hoechst staining</i>	70
3.5.3	<i>Pimonidazole</i>	70
3.5.4	<i>Frozen section CD31 staining</i>	70
3.5.5	<i>Formalin-fixed tissue processing</i>	71
3.5.6	<i>CD31 staining of formalin-fixed samples</i>	71
3.5.7	<i>Fixed section H&amp;E staining</i>	72

## **4 CHAPTER IN VIVO CHARACTERISATION OF THE RADIORESPONSE AND VASCULATURE OF TUMOUR MODELS 73**

<b>4.1</b>	<b>INTRODUCTION</b>	<b>73</b>
4.1.1	<i>Aims</i>	76
<b>4.2</b>	<b>MATERIALS AND METHODS</b>	<b>76</b>
4.2.1	<i>Tumourigenicity studies</i>	77
4.2.2	<i>In vivo radioresponse</i>	78
4.2.3	<i>Characterisation of tumour vasculature using DCE-US imaging</i>	79
4.2.3.1	Correlation of whole-ROI and pixel-wise TAC metrics	79
4.2.3.2	Comparison of C33A and HN5 tumours	80
4.2.3.3	Validation of DCE-US imaging with histopathology	80
<b>4.3</b>	<b>RESULTS</b>	<b>81</b>
4.3.1	<i>Tumourigenicity of cervical cancer cell lines</i>	81
4.3.1.1	ME-180 tumour model	81
4.3.1.2	C33A tumour model	83
4.3.2	<i>Radioresponse of in vivo tumour models</i>	84
4.3.2.1	C33A tumour model	84
4.3.2.2	HN5 tumour model	87
4.3.3	<i>Characterisation of tumour vasculature</i>	89
4.3.3.1	Whole-ROI analysis	89
4.3.3.2	Intratour heterogeneity	93

4.3.3.3	Correlation of metrics _____	97
4.3.3.4	Correspondence of DCE-US imaging with CD31 staining _____	102
<b>4.4</b>	<b>DISCUSSION _____</b>	<b>104</b>
4.4.1	<i>Establishing in vivo tumour models of head &amp; neck and cervical cancer</i> _____	105
4.4.1.1	ME-180 tumour model _____	105
4.4.1.2	C33A tumour model _____	106
4.4.1.3	HN5 tumour model _____	107
4.4.2	<i>Characterisation of tumour vasculature</i> _____	108
4.4.2.1	C33A tumour model _____	109
4.4.2.2	HN5 tumour model _____	110
4.4.2.3	Correlation of DCE-US metrics _____	111
4.4.2.4	Biological validation of DCE-US imaging _____	113
<b>4.5</b>	<b>LIMITATIONS _____</b>	<b>113</b>
<b>4.6</b>	<b>CONCLUSION _____</b>	<b>115</b>
<b>5</b>	<b>CHAPTER PRELIMINARY INVESTIGATION OF DCE-US FOR ASSESSMENT OF RESPONSE TO RADIOTHERAPY _____</b>	<b>116</b>
<b>5.1</b>	<b>INTRODUCTION _____</b>	<b>116</b>
<b>5.2</b>	<b>STUDY AIM &amp; DESIGN _____</b>	<b>116</b>
<b>5.3</b>	<b>METHODS _____</b>	<b>117</b>
5.3.1	<i>Experimental setup</i> _____	118
5.3.1.1	2D DCE-US imaging _____	118
5.3.1.2	Repeat 2D DCE-US _____	118
5.3.1.3	Irradiation of mouse xenograft tumours _____	118
5.3.2	<i>DCE-US analysis for assessment of radioresponse</i> _____	118
5.3.3	<i>Repeatability of DCE-US imaging analysis</i> _____	119
5.3.3.1	Variation of whole-ROI metrics _____	119
5.3.3.2	Variation of whole-ROI metrics due to noise _____	119
5.3.3.3	Variation of whole-ROI metrics TACs due to ROI delineation _____	120
5.3.3.4	Variation of histogram analysis _____	120
5.3.3.5	Spatial repeatability of DCE-US _____	121
<b>5.4</b>	<b>RESULTS _____</b>	<b>121</b>
5.4.1	<i>Characterisation of radiation response</i> _____	121
5.4.1.1	HN5 tumour model _____	121
5.4.1.2	C33A tumour model _____	122

5.4.2	<i>Association of radioresponse with pretreatment DCE-US metrics</i>	123
5.4.3	<i>Association of radioresponse with changes in DCE-US metrics</i>	125
5.4.3.1	HN5 tumour model _____	125
5.4.3.2	C33A tumour model _____	128
5.4.4	<i>Tumour volume changes following treatment</i> _____	133
5.4.5	<i>Repeatability of 2D DCE-US</i> _____	134
5.4.5.1	Variation of whole-ROI DCE-US metrics _____	134
5.4.5.2	Variation improvement using model fitting and TAC filtering	136
5.4.5.3	Variation of whole-ROI DCE-US metrics due to ROI delineation	140
5.4.5.4	Variation of intratumour heterogeneity _____	142
5.4.5.5	Spatial repeatability of DCE-US metric maps _____	145
<b>5.5</b>	<b>DISCUSSION</b> _____	<b>147</b>
5.5.1	<i>Radioresponse of cervical and head and neck tumour models</i>	147
5.5.2	<i>Association of radioresponse with pretreatment DCE-US metrics</i>	147
5.5.3	<i>Association of radioresponse with changes in DCE-US metrics</i>	148
5.5.4	<i>Repeatability of 2D DCE-US imaging</i> _____	151
<b>5.6</b>	<b>LIMITATIONS</b> _____	<b>156</b>
<b>5.7</b>	<b>CONCLUSION</b> _____	<b>158</b>

## **6 CHAPTER REPEATABILITY OF THE 2D AND 3D DCE-US TIME-AMPLITUDE CURVE METRICS OF THE RENAL VASCULATURE \_\_\_\_\_ 159**

<b>6.1</b>	<b>INTRODUCTION</b> _____	<b>159</b>
6.1.1	<i>Aims</i> _____	161
<b>6.2</b>	<b>MATERIALS &amp; METHODS</b> _____	<b>162</b>
6.2.1	<i>Study design</i> _____	162
6.2.2	<i>Animal setup</i> _____	162
6.2.3	<i>DCE-US imaging</i> _____	163
6.2.4	<i>DCE-US analysis</i> _____	165
6.2.5	<i>Intraday variation</i> _____	165
6.2.6	<i>Interday variation</i> _____	165
6.2.7	<i>Variation of TAC</i> _____	166
6.2.8	<i>Statistical testing</i> _____	166

<b>6.3</b>	<b>RESULTS</b>	<b>167</b>
6.3.1	<i>DCE-US metrics from repeat injections</i>	167
6.3.2	<i>Comparison of intraday and interday absolute variation</i>	169
6.3.3	<i>Comparison of 2D and 3D DCE-US absolute variation</i>	169
6.3.4	<i>Correlation between TACs</i>	172
<b>6.4</b>	<b>DISCUSSION</b>	<b>172</b>
<b>6.5</b>	<b>LIMITATIONS</b>	<b>175</b>
<b>6.6</b>	<b>CONCLUSIONS</b>	<b>177</b>
<b>7</b>	<b>CHAPTER 3D DCE-US FOR ASSESSMENT OF RESPONSE TO RADIATION</b>	<b>178</b>
<b>7.1</b>	<b>INTRODUCTION</b>	<b>178</b>
7.1.1	<i>Aims</i>	179
<b>7.2</b>	<b>MATERIALS &amp; METHODS</b>	<b>179</b>
7.2.1	<i>Study design</i>	179
7.2.2	<i>3D DCE-US imaging</i>	180
7.2.3	<i>DCE-US image analysis</i>	180
7.2.3.1	<i>Centre tumour-ROI and whole-VOI analysis</i>	181
7.2.3.2	<i>Metric maps and histogram analysis</i>	181
7.2.4	<i>Comparison of DCE-US quantification between studies</i>	181
7.2.5	<i>Agreement of whole-VOI and centre tumour-ROI TAC metrics</i>	182
7.2.6	<i>3D DCE-US repeatability</i>	182
7.2.7	<i>Validation of 3D DCE-US imaging with histopathology</i>	183
<b>7.3</b>	<b>RESULTS</b>	<b>183</b>
7.3.1	<i>Characterisation of radiation response</i>	183
7.3.1.1	<i>HN5 tumour model</i>	183
7.3.1.2	<i>C33A tumour model</i>	184
7.3.2	<i>Agreement of whole-VOI and centre tumour-ROI TAC metrics</i>	184
7.3.3	<i>Association of radioresponse with pretreatment DCE-US metrics</i>	187
7.3.4	<i>Association of radioresponse with changes in whole-VOI TAC metrics</i>	187
7.3.5	<i>Association of radioresponse with changes in centre tumour-ROI TAC metrics</i>	190
7.3.6	<i>Comparison of pretreatment DCE-US metrics with preliminary studies</i>	191

7.3.7	<i>Association of radioresponse with changes in DCE-US metrics histogram distribution</i>	193
7.3.8	<i>Combining tumour models</i>	196
7.3.9	<i>Tumour volume changes following radiation</i>	196
7.3.10	<i>Repeatability of 3D DCE-US imaging</i>	197
7.3.10.1	Repeatability of centre tumour-ROI & whole-VOI TAC metrics	197
7.3.10.2	Repeatability of histogram analysis	198
7.3.10.3	Repeatability of the spatial distribution of metrics	199
7.3.11	<i>Correspondence of DCE-US imaging with CD31 staining</i>	201
<b>7.4</b>	<b>DISCUSSION</b>	<b>202</b>
7.4.1	<i>Comparison of DCE-US quantification between studies</i>	202
7.4.2	<i>Association of radioresponse with 3D DCE-US imaging</i>	204
7.4.3	<i>Repeatability of 3D DCE-US imaging</i>	206
<b>7.5</b>	<b>LIMITATIONS</b>	<b>207</b>
<b>8</b>	<b>CHAPTER CONCLUSION</b>	<b>209</b>
<b>8.1</b>	<b>CONCLUSIONS</b>	<b>209</b>
8.1.1	<i>Characterisation of in vivo models of H&amp;N and cervical cancer</i>	209
8.1.2	<i>Assessment of 2D DCE-US metrics for use as imaging biomarkers of radiotherapy response</i>	210
8.1.3	<i>Assessment of 3D DCE-US metrics for use as imaging biomarkers of radiotherapy response</i>	213
<b>8.2</b>	<b>SUMMARY</b>	<b>216</b>
<b>8.3</b>	<b>FUTURE WORK</b>	<b>216</b>
8.3.1	<i>Biological validation of DCE-US imaging</i>	216
8.3.2	<i>Technical validation of DCE-US</i>	217
8.3.3	<i>DCE-US data analysis</i>	218
8.3.4	<i>Radiotherapy fractionation</i>	218
<b>BIBLIOGRAPHY</b>		<b>219</b>
<b>APPENDIX 239</b>		
<b>A1.</b>	<b>INTRATUMOUR HETEROGENEITY</b>	<b>240</b>
<b>A2.</b>	<b>PIXEL – WISE TAC METRIC CORRELATIONS</b>	<b>242</b>
<b>A3.</b>	<b>HISTOGRAM ANALYSIS OF HN5 TUMOURS</b>	<b>246</b>
<b>A4.</b>	<b>VARIATION IN SKEWNESS</b>	<b>249</b>

**A5. COMBINING HN5 AND C33A TUMOURS FOR ANALYSIS OF 3D  
DCE-US** \_\_\_\_\_ **250**

# List of Figures

Figure 1-1: TACs of bolus injection and disruption replenishment imaging .....	38
Figure 3-1: Uncertainty of tumour volume measurement using callipers.....	47
Figure 3-2: Set-up for 2D DCE-US imaging.....	50
Figure 3-3: DCE-US imaging of tumour.....	51
Figure 3-4: Set-up for 3D DCE-US imaging.....	53
Figure 3-5 : TAC metrics calculation.....	55
Figure 3-6: TACs of non-perfused tumour pixels,.....	57
Figure 3-7 : Spatial subregion analysis.....	59
Figure 3-8: Frame selection workflow for 3D DCE-US imaging.....	62
Figure 3-9: Estimation of AT for 3D DCE-US imaging.....	64
Figure 3-10: Radiation delivery workflow with the SARRP. ....	68
Figure 4-1: ME-180 tumour growth – pilot study.....	82
Figure 4-2: Ulceration of ME-180 tumours.....	82
Figure 4-3: ME-180 tumour growth – second study.....	83
Figure 4-4 C33A tumour growth .....	84
Figure 4-5: C33A tumour growth following radiation.....	86
Figure 4-6: C33A & HN5 tumour growth to treatment volume .....	87
Figure 4-7 : HN5 tumour growth following radiation .....	88
Figure 4-8 : TACs of C33A and HN5 tumours obtained using 2D DCE-US .....	90
Figure 4-9: 2D DCE-US images of a C33A tumour .....	91
Figure 4-10 : 2D DCE-US images of a HN5 tumour .....	92
Figure 4-11: Whole-ROI DCE-US metrics of C33A and HN5 tumours.....	93
Figure 4-12 : Spatial metric maps for a C33A and HN5 tumour .....	95
Figure 4-13: Intratumour heterogeneity of AUC for C33A and HN5 tumours. ..	96
Figure 4-14 :Intratumour heterogeneity of AT for C33A and HN5 tumours .....	97
Figure 4-15: Correlation matrices between whole-ROI DCE-US metrics .....	99
Figure 4-16: Correlation matrices of pixel-wise DCE-US metrics. ....	100
Figure 4-17: Plot of pixel-wise PE vs AUC for a C33A and HN5 tumour.....	101
Figure 4-18 : Spatial correspondence of DCE-US imaging and CD31 staining. .....	103
Figure 5-1 : Timeline of 2D DCE-US study.....	117

Figure 5-2: Software used for Savitzky-Golay filtering.....	120
Figure 5-3: HN5 tumour growth following radiation .....	122
Figure 5-4: C33A tumour growth following radiation.....	123
Figure 5-5: WIT before treatment for the HN5 cancer model. ....	125
Figure 5-6: Change in DCE-US metrics from pre- to post- radiation in the HN5 tumour model using whole-ROI analysis. ....	126
Figure 5-7: Subregion analysis of HN5 tumours. ....	127
Figure 5-8: Change in DCE-US metrics from pre- to post- radiation in the C33A tumour model using whole-ROI analysis .....	129
Figure 5-9: Subregion analysis of C33A tumours.....	131
Figure 5-10: Representative WOUT metric maps in C33A tumours pre- and post-treatment.....	132
Figure 5-11: Change in WOUT histogram parameters in C33A tumours .....	133
Figure 5-12: Tumour volume changes shortly following irradiation in HN5 and C33A tumours.....	134
Figure 5-13: Variation for DCE-US metrics from repeat imaging calculated using whole-ROI analysis.....	135
Figure 5-14: Absolute variation of DCE-US metrics derived from the raw data TAC and the Arditi model.....	137
Figure 5-15: Bland Altman plots of metrics calculated from the raw data TAC or fitted to the Arditi model.. ....	138
Figure 5-16: Example of poor Arditi model fit . ....	139
Figure 5-17: Variation of whole-ROI metrics from video TACs and Savitzky-Golay filtered TACs .....	139
Figure 5-18: Bland Altman plots of metrics derived using the Savitzky-Golay (S-G) filter and video data TACs. ....	140
Figure 5-19: Absolute variation of TAC metrics of the same injection analysed with different ROIs. ....	141
Figure 5-20: WOUT maps analysed with two independent ROIs. ....	141
Figure 5-21: Variation of whole-ROI metrics from 2 repeat injections analysed using the same ROI .....	142
Figure 5-22 : Absolute and signed variation in histogram parameters of DCE - US metrics obtained of repeat DCE-US imaging.....	144

Figure 5-23: Histogram distributions of AT, WIT and MTT for two repeat DCE-US acquisitions. ....	145
Figure 5-24: Correlation coefficient of metric maps obtained from two DCE-US acquisitions. ....	146
Figure 5-25: Spatial correlation of metric maps of repeat injections. ....	146
Figure 6-1: Anatomical structure of the kidney .....	161
Figure 6-2: 2D DCE-US imaging of the left and right kidney .....	165
Figure 6-3: DCE-US metrics of kidney for three consecutive injections. ....	168
Figure 6-4 : TACs of 2D and 3D repeat DCE-US imaging of the kidney .....	169
Figure 6-5: Intraday and interday absolute variation of DCE-US metrics of the kidney using 2D and 3D imaging .....	171
Figure 6-6: Correlation of TACs compared intra- and interday for 2D and 3D imaging. ....	172
Figure 6-7: Subregion analysis of kidney centre slice. ....	177
Figure 7-1: HN5 tumour growth following radiation .....	183
Figure 7-2: C33A tumour growth following radiation.....	184
Figure 7-3: The difference in DCE-US metrics calculated using centre tumour-ROI and whole-VOI TACs. ....	186
Figure 7-4: Change in DCE-US metrics of HN5 tumours following radiation obtained from the tumour centre and the whole tumour volume .....	188
Figure 7-5: Change in DCE-US metrics of C33A tumours following radiation obtained from the tumour centre and the whole tumour volume.....	189
Figure 7-6: Comparison of DCE-US metrics obtained from the tumour centre using 2D imaging with the Aplio scanner and 3D imaging with the Verasonics .....	192
Figure 7-7: TACs of HN5 tumours imaged with the Aplio and Verasonics scanners .....	193
Figure 7-8: Change in the histogram distribution of DCE-US metrics in HN5 tumours following radiation .....	194
Figure 7-9: Changes in the histogram distribution of MTT for the tumour centre and whole tumour volume in C33A tumour model.....	195
Figure 7-10: Tumour volume changes in HN5 tumours and C33A tumours following radiation. ....	197

Figure 7-11: Variation of DCE-US metrics obtained from the tumour centre and tumour volume between repeat imaging.....	198
Figure 7-12: Absolute variation of histogram parameters of DCE-US metrics from two acquisitions for the tumour centre and tumour volume .....	2000
Figure 7-13: Correlation coefficient of metric maps of the centre tumour-ROI obtained from two DCE-US acquisitions.....	201
Figure 7-14: Spatial correspondence of DCE-US imaging and CD31 staining. ....	202

## List of Tables

Table 3-1 : Definition of DCE-US metrics derived from the TAC.....	55
Table 4-1 Summary of studies discussed in the thesis .....	78
Table 4-2 : Summary of whole-ROI metrics for C33A and HN5 tumours.....	90
Table 4-3 : Correlation matrix of whole-ROI TAC metrics in C33A tumours.....	98
Table 4-4 : Correlation of whole - ROI TAC metrics in HN5 tumours.....	99
Table 5-1: Classification of HN5 tumours as complete and partial responders. ....	122
Table 5-2: Classification of C33A tumours as complete and partial responders.....	123
Table 5-3 : Absolute and signed variation of DCE-US metrics of repeat DCE-US imaging. ....	136
Table 5-4: Quality of fit of raw TACs to Arditi and Gamma perfusion models.....	136
Table 5-5: Variation of histogram parameters for DCE-US metrics of repeat imaging .....	143
Table 6-1 : Summary of study timepoints .....	162
Table 7-1: Ratio of the value and change in DCE-US metrics obtained from centre tumour-ROI and whole tumour volume. ....	185
Table 7-2 : Absolute and signed variation of DCE-US metrics obtained from centre tumour-ROI whole tumour volume obtained from repeat DCE-US imaging. ....	199

# List of Acronyms

2D/3D	Two dimension/Three dimensional
[ <sup>18</sup> F] FMISO	[ <sup>18</sup> F] fluoromisonidazole
[ <sup>18</sup> F] FETNIM	[ <sup>18</sup> F] fluoroerythronitroimidazole
ASMase	Acid sphingomyelinase enzyme
AT	Arrival time
AUC	Area under the curve
BOLD-MRI	Blood oxygen level dependent MRI
BSA	Bovine serum albumin
BSU	Biological Services Unit
CEA	Carcinoembryonic antigen
CBCT	Cone-beam computed tomography
CoV	Coefficient of variation
CT	Computed tomography
CTCs	Circulating tumour cells
ctDNA	Circulating tumour DNA
DVH	Dose volume histogram
DCE-US	Dynamic contrast-enhanced ultrasound
DCE-MRI	Dynamic contrast enhanced MRI
DMEM	Dulbecco's Modified Eagle's Medium
DWI- MRI	Diffusion weighted imaging MRI
FBS	Foetal bovine serum
FDG-PET	2-[ <sup>18</sup> F]-fluoro-2- deoxy-D-glucose PET
FFPE	Formalin-fixed paraffin-embedded
H&N	Head and neck
H&E	Haematoxylin and eosin
HbT	Total haemoglobin
HBSS	Hanks' Balanced Salt Solution
HCC	Hepatocellular carcinoma
HEPS	Hydrogenated egg yolk phosphatidyl serine
HIF-1	Hypoxia inducible factor-1
HPV	Human papillomavirus

IQR	Interquartile range
Kur	Kurtosis
KXA	Ketamine xylazine acepromazine
LION-HN5	HN5
MVD	Mean vessel density
mFWHM	Modified full width half maximum
MI	Mechanical index
MRI	Magnetic resonance imaging
MTT	Modified transit time
NO	Nitric oxide
PCR	Polymerase chain reaction
PE	Peak enhancement
PET	Positron emission tomography
PDX	Patient derived xenografts
PFB	Perfluorobutane
PI	Perfusion index
PSA	Prostate-specific antigen
PS	Permeability–surface product
RECIST	Response evaluation criteria in solid tumours
ROI	Region of interest
RSI	Relative signal intensity
RT	Radiotherapy
SARRP	Small animal radiation research platform
SaO <sub>2</sub>	Oxygen saturation
SD	Standard deviation
SF2	Surviving fraction at 2 Gy
S-G	Savitzky-Golay filter
STR	Short tandem repeat
TAC	Time amplitude curve
US	Ultrasound
UCA	Ultrasound contrast agent
VEGF	Vascular endothelial growth factor
VOI	Volume of interest
WHO	World health organisation

WIT Wash-in time  
WOUT Washout time

# 1 CHAPTER Introduction

## 1.1 Radiotherapy: potential for personalisation

Radiotherapy is one of the main treatments currently used for cancer along with chemotherapy and surgery. Approximately 50% of cancer patients receive radiotherapy for curative or palliative purposes [1]. Radiotherapy is key to accomplishing local tumour control in both resectable and unresectable tumours. Clinical external beam radiotherapy most commonly uses megavoltage energy X-ray beams that are directed at the tumour, or tumour bed post-surgery. Megavoltage X-rays can transfer their energy to tissue, primarily via inelastic scattering, which generates high energy electrons. Electrons are ionising particles which can directly interact with the cellular DNA creating structural damage, such as DNA strand breaks, which potentially lead to cell death. More frequently, electrons interact with cellular water creating free radicals in tumour cells that are highly reactive and react with DNA creating DNA free radicals that can also lead to structural damage [1]. When DNA double strand breaks occurs, some can be repaired but due to imperfect repair mechanisms that are more prevalent in cancer cells, some double strand breaks remain unrepaired and the tumour cells undergo programmed cell death, potentially leading to tumour control.

### *1.1.1 Radiotherapy in head and neck cancer*

Head and neck (H&N) cancer is the 6<sup>th</sup> most common cancer worldwide with a reported incidence of 890,000 cases in 2018 [2]. H&N cancers are mostly squamous cell carcinomas and originate in the different parts of the head and neck region including the oral cavity, pharynx nasopharynx, oropharynx, hypopharynx and larynx [2]. There are several factors associated with the risk of developing head and neck cancer including tobacco and alcohol consumption, environmental pollution, and human papillomavirus (HPV) infection. Head and neck cancer often presents at the locally advanced stage and requires multimodality treatment including concurrent chemoradiation and surgery.

Radiotherapy is involved in the treatment in most cases of H&N cancer, except for early-stage oral cavity cancers that are treated solely with surgery [2]. An estimated 43% to 85% of patients receive primary or adjuvant radiotherapy depending on the cancer site [3-5], with a standard curative total dose of approximately 70 Gy delivered as 2 Gy per daily fraction (typically 5 fractions are delivered per week) [6]. The outcomes of radiotherapy for H&N cancer have been aided by technological advances in treatment delivery such as intensity modulated and image-guided radiotherapy that more precisely deliver high doses to the tumour while sparing nearby organs at risk [3, 7, 8].

Despite this, local treatment failure, and thus poor survival, is still probable and has been reported to occur in 50 % of cases [9]. Locoregional recurrence rates have been estimated at 27 % [10], 30 % [11], and 35 % [12]. The persistence or recurrence of a tumour within the irradiation field indicates that treatment failure is caused by tumour radioresistance. Radioresistance in H&N cancer has been attributed to intrinsic tumour radiosensitivity [7, 13], tumour cell proliferation [14], and hypoxia [15]. All of these factors have been shown to correlate with worse treatment outcome [13]. Radioresistant tumours can benefit from treatment modification, including dose escalation [16], altered fractionation regimes [17] or the addition of radiosensitising agents such as nimorazole [18]. Modifications can improve tumour control and overall survival [16], leading to the suggestion that radiotherapy dose and/or dose distribution may be adjusted in patients (personalised) according to phenotypical or genotypical differences in their tumours that are related to their radioresponse [7].

Equally, more radiosensitive H&N cancers might be exposed to a larger than necessary dose and increased toxicity as a result. The toxicity level associated with radiotherapy in H&N is considered at the tolerance limit and can have a substantial impact on quality of life. As, such dose de-escalation strategies are attractive [19]. This approach was investigated in HPV associated oropharyngeal cancer, as this subset of H&N cancers are now understood to be more radiosensitive than HPV-negative cancers [15]. A reduced dose of 60 Gy [20, 21], and even as low as 54 Gy in patients responding to induction chemotherapy

showed similar overall survival outcomes and a reduction in toxicity events [22, 23]. This is considered encouraging evidence to support radiotherapy personalisation by the oncology community but still better understanding of precise stratification of tumours is required as distant metastasis of HPV-positive tumours remains a concern and dose de-intensification could lead to undertreatment resulting in treatment failure [24-26].

### *1.1.2 Radiotherapy for cervical cancer*

Cervical cancer is the fourth most common cancer worldwide in females, with an incidence of 570,000 new cases in 2018 [27]. Almost all cases of cervical cancer are associated with persistent HPV infection [28]. Radiotherapy is administered as external beam radiation of 40 to 50 Gy in standard fraction size (2 Gy) and additional brachytherapy in the case of advanced disease, accounting for 40 % of patients [29]. Locoregional occurrences occurs in 10 % of treated cases while distant relapse is at a higher risk of 30 %, especially for advanced stage disease [30]. Radioresistance of cervical cancer is primarily attributed to tumour hypoxia, and hypoxia has been linked to poor treatment and outcome [30, 31]. Additional radioresistance factors predicting poor outcome include the tumour's ability to evade apoptosis, angiogenesis, and high proliferation rate [32]. Thus, the primary goal of personalised radiotherapy in the context of cervical cancer would be improving the radioresponse in radioresistant tumours through strategies including dose escalation using dose painting [31, 33] or radiosensitisation of tumours via hyperbaric oxygen or nitroimidazole agents [31]. Clinical trials could not demonstrate an improvement in survival by using radiosensitising agents and revealed large variation in outcome [34, 35]. This supports the urgent need for a personalised treatment approach.

## **1.2 Biomarkers for prediction and assessment of response to radiotherapy**

The required information about the tumour to achieve personalised radiotherapy can be attained using biomarkers. A biomarker is defined as 'defined characteristic that is measured as an indicator of normal biological processes,

pathogenic processes or responses to an exposure or intervention, including therapeutic interventions' [36]. Predictive biomarkers can predict response prior to initiation of treatment based on the tumour radiosensitivity, while response biomarkers examine response during the course of treatment.

### *1.2.1 Predictive biomarkers*

As discussed above, there are several well recognized causes of radioresistance for both head and neck and cervical cancer. Predictive biomarkers can thus be developed based on these factors, but so far none have been widely adopted clinically. The main challenge in personalising therapy is that the assessment of the relevant factors is currently primarily achieved using histopathological analysis of tumour biopsies. This is an invasive procedure and can only examine a small sample tumour volume, which is known to be spatially heterogenous. Furthermore, radiosensitivity is dependent on multiple factors and the complexity of the tumour response to treatment is still not fully uncovered [37], and it is difficult to examine all of these factors using biopsy. Additionally, the dynamic nature of microenvironmental factors such as hypoxia [30, 38], combined with the fractionated nature of treatment suggests that their examination during treatment is also of importance for response. Consequently, alternative biomarkers of response, that are not reliant on multiple repeat biopsies, are needed to inform radiotherapy personalisation.

### *1.2.2 Biomarkers for response assessment*

Biomarkers of response provide information about the tumour's response to standard treatment which can then inform necessary treatment modification. Effective personalised radiotherapy requires biomarkers that can assess response early during treatment, early enough that changes in treatment may be effective or that unnecessary normal tissue toxicity can be avoided. Current response criteria standards are inadequate for this purpose; widely adopted guidelines, like response evaluation criteria in solid tumours (RECIST) [39] or the World Health Organization (WHO) criteria [40] define response based on anatomical tumour changes, typically assessed using computed tomography

(CT) [39], which are present at later stages of the radiotherapy. Recent incorporation of response definitions based on the tumour metabolic rate using positron emission tomography (PET) imaging (discussed in more detail in section 1.2.3.1) can allow earlier assessment of response [41]. Novel response biomarkers that detect early biological changes in the tumour that are associated with eventual response as defined clinically are required. These early changes may include apoptosis and tumour cell loss, reoxygenation and decreased hypoxia, changes in perfusion, and changes in tumour metabolism [42]. This project focuses on the identification of biomarkers of vascular changes in response to radiotherapy, which may also influence the oxygenation of the tumour.

By nature, assessing response involves tumour inspection at multiple timepoints before and during treatment. Thus, response biomarkers must be developed from techniques with minimal invasiveness and ease of use. This requirement means that histopathological tumour biomarkers are unsuitable. Instead, development of early response biomarkers has focused on less invasive methods, including blood-based tumour biomarkers, or liquid tumour biomarkers. Liquid tumour biomarkers are derived from tumour-related material that can be detected in the patient's blood, which includes circulating tumour cells (CTCs), circulating tumour proteins, circulating tumour nucleic acids (RNA and DNA), and extracellular vesicles [43]. Tumour protein-based biomarkers are used clinically for diagnosis, such as the prostate-specific antigen (PSA) in prostate cancer [43], and early detection of recurrence in colorectal cancer using carcinoembryonic antigen (CEA) and in breast cancer using CA 15-3 [44]. Research into developing blood-based early response biomarkers has primarily focused on circulating tumour DNA (ctDNA). This is based on the documented correlation of ctDNA concentration with tumour volume [45]. A decrease in ctDNA concentration 20 days after chemoradiotherapy was seen in patients with successful treatment in a small study of H&N cancer [45]. Yet, ctDNA may suffer from low sensitivity [37], is expensive [44], and offers no spatial information that can be used to accordingly modify treatment to tumour sub-volumes. Moreover, the decrease in ctDNA associated with response can be confounded by a transient increase in ctDNA following treatment-induced tumour cell death [44].

### *1.2.3 Imaging biomarkers*

The discussed requirements of predictive biomarkers and biomarkers of response and the highlighted challenges in the available biomarkers suggests the suitability of functional imaging biomarkers. Functional imaging refers to imaging techniques that can map physiological and/or biological properties of the tumour. Precise measurement of functional imaging signals presents the opportunity to derive biomarkers that might inform on tumour physiology or biology, which can be indicative of response. The main advantages of imaging biomarkers are their relative non-invasiveness (compared to biopsy), the opportunity for repeated monitoring, and examining intratumour spatial heterogeneity. Moreover, the already widespread use of imaging modalities for response assessment, diagnosis, and staging [46] facilitates the incorporation of new functional techniques into the treatment pathway.

Validation of clinically useful imaging biomarkers involves three components [47]; technical, biological and clinical. Technical validation assesses the precision of the technique, defined as its repeatability and reproducibility. The repeatability of an imaging method determines its ability to resolve biological changes, while reproducibility dictates its suitability for widespread multicentre use. Biological validation refers to correlation of imaging metrics with the proposed underlying biological features, typically done using gold standard histopathological metrics which are biological correlates themselves. Finally, clinical validation of the role of the biomarker examines the benefit of adopting the established biomarker in clinical practice. Currently, no imaging metric of early response has completed all stages of validation, but research has showed potential in several techniques, which are described below. These imaging modalities have been used to both assess predictive markers of radioresponse and for identifying early response changes.

### 1.2.3.1 Positron emission tomography (PET)

PET imaging uses radioisotope tracers that can target metabolic and molecular components of the tumour. 2-[<sup>18</sup>F]-fluoro-2- deoxy-D-glucose PET (FDG-PET) is used to examine tumour metabolism and has been routinely adopted for response evaluation in head and neck cancer at least 3 to 4 months after chemoradiation [48, 49]. The recommended timing for FDG-PET (/CT) imaging is 8 – 12 weeks after the end of radiotherapy treatment [41], with response assessment at earlier timepoints yielding lower accuracy [49, 50]. This makes the primary aim of FDG-PET in H&N cancer the detection of residual or recurrent disease, rather than early response assessment. In cervical cancer, response evaluation has been proposed earlier at 4 weeks after chemoradiation, with low FDG uptake shown to correlate to response indicated at later timepoints [48]. The use of other PET tracers has been examined for tumour response prediction or assessment based on detection of tumour apoptosis [51], changes in tumour perfusion using <sup>15</sup>O-H<sub>2</sub>O PET [51, 52] , and hypoxia using [<sup>18</sup>F]fluoromisonidazole ([<sup>18</sup>F]FMISO) and [<sup>18</sup>F] fluoroerythronitroimidazole ([<sup>18</sup>F]FETNIM) [52]. Except for FDG PET, these tracers are still experimental in nature and their clinical utility has yet to be established. Whilst PET shows promise in terms of its broad range of functional and molecular targets there are several disadvantages to PET imaging. These include the cost associated with the production and handling of radiopharmaceuticals, the time required for patient scanning when patients can often be very frail and the capital cost of equipment. It also imparts an ionizing radiation dose to the patient, which should be considered when patients require longitudinal monitoring, especially in the case of younger patients. PET imaging also has inferior spatial resolution of a few millimetres compared to sub-millimetre spatial resolution obtained with other imaging modalities.

### 1.2.3.2 Magnetic resonance imaging (MRI)

Several magnetic resonance imaging (MRI) techniques have been utilized for prediction and response assessment. Perfusion imaging using dynamic contrast enhanced MRI (DCE-MRI) was shown to be predictive of local tumour control based on pretreatment perfusion and was also able to assess response based

on perfusion changes within 2 weeks after treatment initiation in H&N cancer [53, 54]. In cervical cancer, DCE-MRI metrics before treatment and changes within 3 days of chemoradiotherapy were correlated with tumour recurrence [55] .

Diffusion weighted imaging (DWI-) MRI provides information about the tumour structure and has been used to quantify tumour cellularity, an indicator of cell death. In H&N cancer, a decrease in tumour cellularity 1 week after radiotherapy indicated response [51]. Several, novel MRI techniques that may be useful for tumour response prediction and assessment are under investigation. For example, oxygen enhanced MRI and blood oxygen level dependent (BOLD) MRI [56] for the measurement of tumour hypoxia and intravoxel incoherent motion MRI for the characterisation of the vasculature without the need for contrast agents [57]. Like PET, MRI is a costly imaging modality with long acquisition times and has several contraindications including claustrophobia and risk of toxicity associated with gadolinium-based contrast agents used for DCE-MRI [58, 59]. Access to MRI is also an issue, the UK has one of the lowest numbers of MRI machines per million of population in Europe, 6 compared to 16 in Italy or 22 in Finland [60].

#### 1.2.3.3 Computed tomography (CT)

CT is commonly used with the RECIST criteria to assess response to treatment [34]. In terms of functional imaging, perfusion imaging can be used to image functional vasculature using iodine-based contrast agents. Changes in tumour perfusion within 3 weeks of chemoradiotherapy using perfusion CT imaging correlated to response assessed at 3 months in both H&N [61] and cervical cancer [62]. The main limitation for longitudinal CT imaging is its use of ionising radiation [46].

#### 1.2.3.4 Ultrasound imaging

Although one of the most widely used imaging modalities, in the context of H&N and cervical cancer prediction and response assessment ultrasound (US) remains less popular than CT, PET or MRI. Ultrasound has many advantages to

offer including wider availability, lower cost relative to MRI, PET and CT and safer use with no ionizing radiation or has little risk associated with ultrasound contrast agents. This allows more frequent imaging with ultrasound, enabling more frequent longitudinal monitoring of cancer both during and after therapy.

Imaging of functional vasculature can be done using several ultrasound techniques. Doppler imaging can detect the direction and velocity of blood flow based on changes in the ultrasound wave frequency reflected from a moving object, in this case blood cells[63]. Dependence on blood flow to identify the vasculature limits the ability of Doppler imaging to visualise microvasculature with slow blood flow. Dynamic contrast-enhanced ultrasound imaging (DCE-US), on the other hand, uses intravenously injected contrast agents that can travel throughout the microvasculature and capillaries, and thus offers more sensitive imaging of functional vasculature. In addition to the practical advantages of US imaging, DCE-US offers higher temporal resolution than DCE-MRI or perfusion CT, allowing more precise estimation of blood velocity properties, and uses purely intravascular contrast agents and thus can quantify tumour perfusion without the confounding effect of contrast agent extravasation, i.e, ultrasound contrast signals typically map the vasculature and not tissue. Moreover, ultrasound contrast agents can be functionally modified to bind to receptors on endothelial cells [64], thereby establishing molecularly targeted imaging of targets such VEGF (vascular endothelial growth factor) as a surrogate for tumour angiogenesis [64]. Furthermore, DCE-US is an established diagnostic imaging technique, with US available on most clinical ultrasound scanners, and has been adopted for the diagnosis of liver lesions. Overall, these factors make it an attractive candidate for integration into clinical treatment pathways and the monitoring of treatment response. However, there is still significant work required to understand if DCE-US can be used to measure biomarkers of response to radiotherapy, which will rely on the correlation of DCE-US signals to underlying properties of the tumour vasculature, and that early changes in vasculature occur in response to radiotherapy and that these changes are detectable using DCE-US.

## **1.3 The role of functional vasculature in tumour response to radiotherapy**

The tumour functional vasculature is hypothesised to be an important determinant of response, both prior to treatment and through changes arising from treatment. The rationale behind this is the association of the vascular status with hypoxia, a well-recognized cause of radioresistance, and the impact of radiotherapy on the vasculature, which is essential to tumour survival. The following is a review of the evidence supporting the potential role of tumour vasculature in the prediction and assessment of response to radiotherapy.

### *1.3.1 Prediction of response based on pretreatment vasculature*

Prediction of the tumour's response to radiation based on its vascular supply has been studied extensively and two conclusions, that may appear contradictory, arguing for both good and poor tumour perfusion as a predictor of tumour control, have been put forward and will be discussed here. The literature reviewed here draws from fractionated and single fraction radiation studies.

The first collection of studies suggests a positive correlation of tumour perfusion with tumour response. This supports the idea that the tumour's functional vasculature determines its oxygen supply, and thus oxygenation level. Oxygen is a known radiosensitiser, where evidence suggests that following radiation and the generation of DNA free radicals, oxygen acts to 'fix' DNA damage [65, 66]. Further, good perfusion reduces tumour hypoxia, inhibiting the upregulation of hypoxia inducible factor-1 (HIF-1) [67] which promotes radioresistance[68]. This theory was supported by a clinical study in radiotherapy for cervical cancer. Using DCE-MRI and a semi-quantitative analysis, high signal enhancement compared to the precontrast injection baseline signal and a non-enhancing region of normal tissue (termed relative signal intensity or RSI) in the tumour region of interest (ROI) [69] and at the 10<sup>th</sup> percentile of enhanced pixels within the tumour ROI predicted local tumour control and survival with fractionated radiotherapy [70, 71] and chemoradiation treatment [71]. These metrics were important both before treatment [70] and within the first 2 weeks of treatment [69, 71]. The significance

of poor perfusion, examined using percentile analysis, was explained as indicating the presence of hypoxic tumour subregions which confer radioresistance [70, 71]. Similarly, homogeneously enhanced tumours had better response than tumours with no enhancement, or peripheral enhancement only [72]. Pharmacokinetic DCE-MRI metrics were associated with better tumour response, namely greater maximum amplitude obtained from the Brix model [73] and higher vascular permeability calculated using the Tofts model [72]. Both semi-quantitative (RSI) and pharmacokinetic metrics (amplitude) were shown to correlate to polarographic measurements of tumour pO<sub>2</sub> [73], thereby confirming the relationship between vascular status and tumour oxygenation.

Conversely, several studies have reported an opposite effect, with high blood volume or flow predicting treatment failure. This was reported in rectal cancer, where a greater perfusion index (defined as relative blood flow compared to arterial flow) and a large percentage of pixels with a high perfusion index enhancement on DCE-MRI were associated with no response to radiotherapy or chemoradiation [74, 75]. The association of high perfusion index (PI) with worse treatment outcome was explained by the authors as high PI indicating high blood flow through arteriovenous shunts, which do not facilitate nutrient or oxygen supply, or indicating a high permeability–surface product (PS) caused by increased angiogenic activity which suggests an aggressive tumour phenotype. In H&N cancer, multiple conflicting results have been reported. For example, enhancement with DCE-MRI could not predict response to accelerated radiotherapy, but was lower in controlled tumours after completion of radiotherapy [76]. Meanwhile, [<sup>15</sup>O]H<sub>2</sub>O PET imaging revealed higher blood flow before treatment in patients with poor response [52], evaluated using tumour control and patient survival, following radiotherapy and chemoradiation. Regions of high blood flow were associated with hypoxic regions, imaged using hypoxia [<sup>18</sup>F] FETNIM PET, with the theory that hypoxia induces angiogenesis, leading to high blood flow but not necessarily better oxygen delivery due to the abnormal tumour vasculature. Nevertheless, a review of studies using CT perfusion imaging for the prediction of treatment outcome in head and neck cancer showed a consensus of the correlation of high blood flow, high blood volume and high capillary permeability with favourable tumour response in both radiotherapy,

chemotherapy and combined treatment [77]. A similar review of DCE-MRI imaging for head and neck suggests that a higher  $K_{trans}$  metric, which measures the flow of contrast agent transferred between the blood plasma and extravascular space and depends on vascular permeability and blood flow, either prior to treatment or early during chemoradiation predicted tumour control [78], while lower  $K_{trans}$  values were found in hypoxic volumes [78]. Finally, great vascular heterogeneity measured through the skewness of  $K_{trans}$  distribution before treatment was predictive of chemoradiation treatment failure [79]. The difference between these results may be attributed to the different imaging modalities, different or insufficient follow up periods, and the intrinsic differences between cancer types.

### *1.3.2 Radiation-induced vascular changes and association with response*

Vascular changes following radiotherapy are well established, with studies showing evidence of both increased and decreased vascular function post radiation. Contradictory results may be due to the multiple factors affecting tumour vasculature and thus, perfusion. First, high dose single-fraction radiation was shown to cause endothelial cell apoptosis mainly through ceramide generation from sphingomyelin by the acid sphingomyelinase enzyme (ASMase) [80]. ASMase-mediated endothelial cell apoptosis increased 1 hour after radiation with 15 Gy, with maximum apoptosis at 6 hours *in vivo* in cancer models of fibrosarcoma and melanoma [81, 82]. Additionally, in the same cancer models, ASMase-mediated nitric oxide (NO) vasoconstriction has also been observed as early as 30 minutes after radiation [83]. This has the effect of causing macroscopic vascular damage, or a decrease in perfusion, which was evident as early as 24 hours after radiation and up to 11 days [84-90]. Thrombosis, oedema and endothelial cell swelling have also been suggested as a mechanism for the early decrease in perfusion within 24 hours [91, 92].

Conversely, an increase in tumour perfusion has been observed within the same timescale as the reported vascular damage. Using a single-fraction dose of  $> 8$  Gy, improved tumour perfusion within 6-24 hours was seen in murine models of squamous cell carcinoma [91, 93], mammary carcinoma [85], and fibrosarcoma

[84]. This early increase has been suggested to be due to a reduction in the tumour interstitial pressure induced by tumour cell kill which relieves compression of blood vessels [93-95], or an acute inflammation response causing vasorelaxation [95, 96].

Despite the clear evidence of vascular changes early within treatment evidence, it remains to be confirmed whether these changes have an impact on overall tumour cell death and treatment outcome [97]. The literature provides various conclusions, which are likely to be dependent on the cancer type, its microenvironment and dose-fractionation. Studies supporting improved radioresponse due to vascular response argue that macroscopic vascular damage deprives tumours cells of nutrients and oxygen supply, causing a second indirect wave of tumour cell kill following radiation. Supporting this hypothesis is the finding of greater tumour growth delay in tumour models grown in mice with intact ASMase activity compared to ASMase deficient mice lacking an endothelial cell apoptosis response [81, 98]. Endothelial cell apoptosis led to ineffective neovascularisation and was suggested to prevent tumour growth following irradiation and tumour cell recovery in a melanoma murine model [99]. Further, ischemic injury can impair repair of DNA double strand breaks [83]. On the other hand, other studies suggest that tumour cell radiosensitivity is the only significant determinant of response, which is supported by the good fit of the linear quadratic model, which only accounts for cell kill due to DNA damage, to single fraction large dose regimes [100]. The lack of a clear conclusion of the influence of vascular response on tumour control may be attributed to evidence that endothelial cell apoptosis is not present in all tumours [97], and that vascular damage can induce hypoxia which may promote an aggressive tumour phenotype [101].

In addition to the heterogeneity of vascular response across cancer types, intra-tumour heterogeneity of vascular response is also well established [102, 103]. The radiosensitivity of tumour vessels has been found to be dependent on their local microenvironment. For example, [104] reported increased vessel disruption within hypoxic regions of murine prostate tumours, suggesting increased radiosensitivity of vasculature in hypoxic regions. Greater vascular damage was

observed in the core of pancreatic xenograft tumour compared to the rim [92], supporting the proposition that vessels near the tumour boundaries that develop from surrounding normal tissue are more radioresistant than abnormal tumour vessels. In contrast, in glioma and squamous cell carcinoma xenografts, the vessel damage was localised to areas of viable normoxic cells with decreased signalling of proangiogenic factors [87]. Furthermore, the vessel morphology also affects its radiosensitivity, with vessels of smaller diameters thought to be more radiosensitive [105] and undergoing larger damage following radiation [106].

Imaging modalities used to examine the distribution of imaging metrics of tumour vasculature have been able to capture the heterogeneous nature of vascular changes, and its importance in assessing response. The change in the spatial distribution of the contrast wash-in rate in DCE-MR images had higher accuracy for the prediction of brain tumour response after radiotherapy compared to  $K_{trans}$  metric averaged over the whole tumour ROI, making it potentially a more powerful indicator of response [107]. A positive change in skewness and kurtosis of normalised cerebral blood volume histogram obtained from dynamic susceptibility contrast MRI was associated with pseudo-progression in glioblastomas after chemoradiotherapy compared to real tumour progression [108]. The differentiation of treatment outcome was more significant using a combination of histogram features. These studies suggest that analysis of subregions and metric maps, might provide more accurate assessment of dominant vascular changes that drive tumour response, instead of using whole tumour metrics to represent the tumour region of interest [103, 109].

## **1.4 Dynamic contrast-enhanced ultrasound imaging**

Ultrasound imaging is considered to have a number of practical advantages for the use in tumour response assessment to treatment which were discussed in section 1.2.3.4. DCE-US can be used to image the tumour vasculature and may be useful to detect the vascular changes in response to radiotherapy described above and establish DCE-US based biomarkers of response to radiotherapy.

### *1.4.1 Clinical use of DCE-US imaging*

Currently DCE-US, or contrast enhanced US (CEUS), has two main uses in routine clinical practice: cardiac imaging, and focal liver lesion imaging. Myocardial contrast echocardiography (MCE) allows delineation of the endocardial border, which is necessary for evaluating the left ventricular volume and function. MCE has also shown potential for use in the emergency department setting for the diagnosis of acute coronary syndromes[110].

CEUS is used in focal liver lesion imaging for both detection and differential diagnosis (benign vs malignant, or type of malignancy). Benign lesions, hepatocellular carcinomas (HCCs), and metastatic lesions, show different enhancement patterns, specifically during the early arterial phase (rim or nonrim enhancement) and the onset of washout, thus allowing their differentiation. CEUS has greater diagnostic confidence and accuracy than conventional Bmode ultrasonography, mainly through improved specificity [111]. CEUS has also been demonstrated to have greater accuracy of diagnosing malignant lesions than contrast enhanced CT [112, 113], and is equivalent to MR imaging [113], thus reducing the need for these more costly imaging techniques [111]. As outlined by the CEUS Liver Imaging Reporting and Data System (CEUS LI-RADS) guideline, a definite diagnosis of hepatocellular carcinomas (HCCs) using CEUS eliminates the need for confirmatory CT/MR imaging or biopsy [114, 115].

### *1.4.2 Basis of DCE-US imaging*

#### 1.4.2.1 Ultrasound Contrast Agents

DCE-US uses ultrasound contrast agents (UCA) to image the functional vasculature. UCAs are microbubbles, with a diameter typically of 1 to 6  $\mu\text{m}$  and are made of a gas-filled core surrounded by a shell. The UCA's structure generates a non-linear response to ultrasound waves unlike the approximately linear response of tissue, thereby allowing visualisation and observation of the vasculature. Due to their size, microbubbles are unable to extravasate to the interstitial space and remain intravascular once injected.

Over the years many UCAs have been investigated, with currently four clinically approved UCAs in different countries: SonoVue™, Optison™, Definity®, Sonazoid™ [116]. Sonazoid, which was used in this thesis, is composed of perfluorobutane (PFB) gas core enclosed with a hydrogenated egg yolk phosphatidyl serine (HEPS) lipid shell, with a mean diameter of 2.1 µm. In the liver, Sonazoid is taken up by Kupffer cells, around 10 – 15 minutes post injection, resulting in late phase enhancement of the liver parenchyma, which is also known as post-vascular phase [116]. This phase allows prolonged scanning of the liver and facilitates identification of metastatic lesions, that lack Kupffer cells and thus would appear hypo-enhanced. Compared to SonoVue, a more widely available contrast agent which does not produce late-phase enhancement, Sonazoid was able to detect a larger number of lesions in a clinical study of 65 patients [117]. Another study of 338 patients assessed Sonazoid and SonoVue CEUS to assess liver lesions as benign or malignant, and showed greater specificity and area under the curve value with Sonazoid but without reaching statistical significance [111]. In addition to the advantage introduced by the post-vascular phase, Sonazoid is more stable than SonoVue and suffers less bubble destruction during imaging. This feature has been suggested to allow reliable observation of washout in the lesions, resulting in higher sensitivity and accuracy of diagnosing HCCs [118]. Beyond this, clinical studies are investigating the use Sonazoid in breast cancer [119] in diagnosis, sentinel lymph node detection, and response evaluation to neoadjuvant chemotherapy, diagnosis of endometrial cancer and renal tumours, and guidance of tumour ablation [120].

#### 1.4.2.2 Detection of UCA signal

Detection of the contrast specific signal can be performed using several different approaches. Two common approaches include harmonic imaging and pulse modulation. The change in pressure caused by a low-pressure ultrasound wave causes a change in the microbubbles volume, leading to a nonlinear oscillatory refraction and expansion. The frequency of the signal produced by this phenomenon differs from the frequency of the transmitted ultrasound, referred to as the fundamental frequency. Harmonic imaging makes use of this difference, and detects the microbubbles signal by imaging at frequencies different to the

fundamental frequency [64]. Pulse modulation techniques use the nonlinearity of microbubbles response. Modulation based on the phase of the pulses can be achieved through pulse inversion. The nonlinear response of microbubbles to positive and negative pressure waves is not equivalent and opposite, unlike the linear signals produced by the tissue. Hence, pulse inversion methods sum consecutive negative and positive pulses, which cancels out the linear tissue signal and leaves microbubbles specific signal [121].

### *1.4.3 Quantification of DCE-US imaging*

The microbubbles specific signal can be quantified to devise metrics relating to the perfusion in a region of interest. Since microbubbles are intravascular agents and have similar hemodynamics to red blood cells [122], dynamic imaging of contrast microbubbles can provide information about blood volume and blood flow. Signal quantification is most often done using a time amplitude curve (TAC) of the average contrast signal in a region interest against time from contrast administration. Two methods of contrast administration are in routine use and produce TACs of different shapes and different perfusion metrics: bolus contrast and disruption replenishment imaging.

#### 1.4.3.1 Bolus contrast injection

In this method, the complete contrast dose is injected over a small period to mimic an instant injection. Imaging is done using low power mechanical index (MI) to avoid microbubbles disruption [123]. Dynamic imaging refers to continuous image acquisition typically over the period the wash-in of the contrast, and wash-out as it is being eliminated from the body. Commonly calculated metrics from a bolus TAC are the maximum signal enhancement following contrast injection, and the area under the TAC, which are related to blood volume within the region of interest [123]. Blood flow is inferred from time-based TAC metrics, including the wash-in time (or rate) to maximum enhancement, the mean transit time of microbubbles through the region of interest, and the wash out time (or rate) [123]. These metrics are often described as being semi-quantitative metrics since they do not provide absolute values of blood volume or flow.

### 1.4.3.2 Disruption replenishment imaging

Using this method, the contrast agent is injected using a slow constant infusion to achieve a steady state concentration of microbubbles in the region of interest. Once this is achieved, a high MI pulse is applied to destroy microbubbles in the field of view. The imaging then returns to low MI scanning to image the re-entrance of microbubbles into the tissue encompassed by the imaging field of view. Blood flow speed is then estimated from the rate of microbubbles wash-in after disruption, and the steady state signal enhancement correlates with blood volume [124]. The benefit of this method is that it is possible to image at several imaging positions using the same injection dose, but it is generally a more complicated protocol than the bolus methods and requires longer acquisition. A schematic representation of time amplitude curves produced with a bolus contrast injection and disruption replenishment imaging is shown in Figure 1-1.

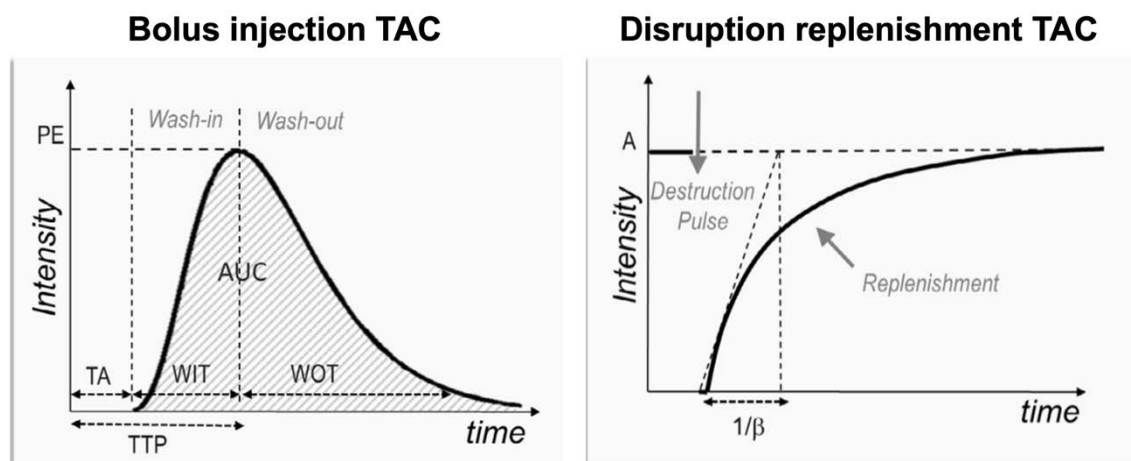


Figure 1-1 : TACs and their respective metrics obtained with a contrast bolus injection imaged with a low MI (left) and using disruption replenishment imaging (right). Adapted from [125]

### 1.4.4 Validation of DCE-US for imaging vasculature

DCE-US metrics obtained from TACs are expected to be able to characterise important vascular features based on studies that have validated DCE-US metrics against histopathological markers of vascular volume. PE and AUC were consistently shown to be related to the vascular volume, typically reported as the

mean vessel density (MVD) estimated via immunohistochemistry. MVD is typically estimated as the mean vessel count in regions of high vessel density and is considered a marker of angiogenesis [126]. PE and AUC were positively correlated with (MVD). Clinical studies showed that peak intensity calculated from tumour hotspots (regions with the highest enhancement) was moderately correlated ( $r = 0.43$ ) to MVD in breast cancer [127], as was AUC ( $r = 0.69$ ) in colorectal cancer [128]. Preclinical studies also revealed a correlation between PE and AUC and MVD in murine melanoma xenografts ( $r = 0.7$  and  $0.52$ , respectively) [129], between PE and MVD in Lewis lung carcinoma ( $r = 0.43$ ) [130] and in breast xenografts (linear regression coefficient =  $0.54$  and  $0.38$  respectively) [131]. The maximum intensity in the tumour relative to the intensity in a normal liver tissue in a syngeneic colon cancer model was correlated to the number of cells stained by Hoechst, reflecting perfused vessels ( $r = 0.82$  and  $0.63$ , in the centre and periphery of the tumour respectively) and MVD ( $r = 0.72$  and  $0.38$ , in the centre and periphery of the tumour respectively) [132]. These moderate correlations of MVD with PE and AUC may be explained by noting that MVD is usually calculated as the number of vessels counted within densely vascularized tissue regions and is thus not a true measure of vascular volume, which is expected to be more relevant to PE and AUC. Furthermore, MVD is often estimated from sections that have been stained with monoclonal antibodies such as CD31 that does not differentiate perfused and non-perfused vessels. The correlation of these metrics with MVD can be improved when accounting for different vessel diameters. This is shown in [129], where the correlation of PE and AUC with MVD was calculated separately for subregions containing microvessels between  $0\text{--}10\ \mu\text{m}$ ,  $10\ \mu\text{m} - 40\ \mu\text{m}$ , or larger than  $40\ \mu\text{m}$ . The correlation obtained through this analysis method was as high as  $0.92$  and  $0.98$  for PE and AUC, respectively, greater than correlations obtained without considering vessel diameter ( $r = 0.7$  and  $0.52$  respectively). In murine pancreatic tumour models, wash-in time and arrival time were negatively correlated ( $r = -0.24$  and  $-0.47$  respectively) to the total haemoglobin (HbT) measured using photoacoustic imaging, which is a surrogate of blood volume, while PE and AUC were positively correlated ( $r = 0.49$  and  $0.40$ , respectively) [133]. A similar positive correlation between AUC and haemoglobin concentration was seen in a prostate xenograft tumour model but not in a breast tumour model, which was

hypothesised to be due to the presence of blood lakes in that model, resulting in non-perfused regions with low AUC and high haemoglobin concentration [134].

Furthermore, DCE-US metrics may differentiate vascular morphology, specifically vessel diameter. TACs generated from ROIs in ovine ovaries containing predominately small microvessels ( $< 30 \mu\text{m}$ ) had smaller PE and longer time to peak compared to TACs of ROIs that encompassed both small microvessels and larger feeding vessels ( $> 200 \mu\text{m}$ ) [135]. In carcinogen-induced mammary tumours, the proportion of the tumour area with low contrast intensity corresponded to the proportion of small vessels ( $< 80 \mu\text{m}^2$ ) identified via immunohistochemistry, while regions of high contrast intensity also showed power Doppler signal, reflecting the presence of macrovessels [136]. In another study, murine sarcoma tumours with dense vascular networks of small and collapsed vessels had slower wash-in and lower contrast enhancement compared to a mammary tumour model with larger vessels [137]. The lower intensity observed in regions with small vessels and *vice versa* is reflection of the vascular volume occupied by vessels of different sizes.

Moreover, DCE-US metrics have been correlated with angiogenesis assessed via the expression of VEGF. In gliomas, the AUC during wash-in (referred to as time integrated intensity) was negatively correlated to VEGF expression ( $r = -0.54$ ) [138], but was not correlated to the vascular density as assessed by CD31 staining. This disagrees with [128] that shows a positive correlation of AUC with CD31 staining but not VEGF expression. The discrepancy was attributed to the higher biological variability in the clinical study [49].

Finally, DCE-US metrics have also been correlated with the oxygenation levels. Blood oxygen saturation ( $\text{SaO}_2$ ) measured using photoacoustic imaging in murine pancreatic tumour models was negatively correlated to the wash-in and arrival time ( $r = -0.50$  and  $-0.56$ , respectively) and positively correlated to PE and AUC ( $r = 0.31$  and  $0.34$ , respectively) [133]. A positive correlation between AUC and oxygen saturation was also reported in prostate and breast xenograft tumour models ( $r = 0.49$  and  $0.63$ , respectively) [134].

### *1.4.5 Current challenges to the use of DCE-US for the prediction and assessment of response to radiotherapy*

#### 1.4.5.1 Lack of evidence in radiotherapy

Current investigations of DCE-US have generally focused on detection and differential diagnosis of tumour lesions in the bladder, kidney, and liver [139]. While clinical studies of DCE-US response assessment have confirmed its potential use as a response biomarker for anti-angiogenic treatment [140-143], there has not been any studies examining DCE-US for radiotherapy response. Preclinically, one study investigated vascular changes in a xenograft prostate tumour model following single fraction radiotherapy of 7.5 or 10 Gy and showed an increase in vascular filling in treated tumours after 3 days but did not report a correlation of the vascular changes with response [144]. Similarly, a study of DCE-US in a rat fibrosarcoma model showed an initial increase in vascular volume following radiation doses of 15 to 25 Gy followed by vascular volume regression 5 days after treatment, but failed to differentiate between tumour control and failure based on the magnitude or onset of vascular changes [84].

#### 1.4.5.2 Limits of 2D DCE-US imaging

Imaging modalities undoubtedly provide more spatial information than other biomarker types but are usually limited to a single or few cross sections of the tumour, leaving the heterogeneity of the entire volume unexplored and providing only partial insight of the biological changes inside the tumour. Two-dimensional (2D) imaging may also obfuscate the detection of changes longitudinally when the initial imaging position cannot be easily reproduced.

Recent technological advances have enabled volumetric or 3D DCE-US imaging, which has shown potential in clinical applications. Studies primarily used a volumetric ultrasound transducer to image the volume of interest and relied on categorical and qualitative assessment of perfusion. Perfusion metrics measured by 2D and 3D DCE-US showed significant differences, which was attributed to the large intratumour vascular heterogeneity [145]. Compared to 2D imaging, 3D

DCE-US was considered to provide clearer visualization of the vascularisation of focal liver lesions, thereby improving the accuracy of diagnosis [146], and more accurate assessment of invasiveness in bladder cancer [137]. Moreover, 3D DCE-US imaging revealed significant differences in the vascular heterogeneity of benign and malignant breast lesions, increasing the diagnostic confidence [147]. A decrease in blood volume assessed qualitatively with 3D DCE-US of hepatocellular carcinoma after 1 week of angiogenic treatment was correlated to a decrease in mean vessel density [148]. Comparison of 3D DCE-US with other imaging modalities revealed comparable accuracy to that of contrast enhanced-CT imaging for the diagnosis of focal liver lesions [149] and to DCE-MRI for the assessment of response to chemotherapy in breast cancer [150].

#### 1.4.5.3 Repeatability of DCE-US

Reliable biological and clinical validation of DCE-US imaging relies on good precision of the modality. Repeatability and reproducibility studies examine the variation expected due to the imaging modality and define the level of biological changes it can detect. For DCE-US imaging, variability can arise from several sources. First, the contrast preparation and injection can influence the concentration and the size distribution of the injected microbubbles, leading to changes in the signal amplitude [151-153]. Secondly, the subject physiology including heart rate and blood pressure can affect the non-linear response of the microbubbles and their disruption rate, leading to changes in both signal amplitude and time-based metrics. Additionally, imaging scanner settings including MI, the dynamic range, imaging depth and data compression also affect both amplitude- and time-based metrics of DCE-US [153, 154]. Finally, the DCE-US data analysis workflow, including model fitting and region of interest placement, similarly affects the quantification of DCE-US metrics [124, 155, 156]. Still, data on the repeatability of DCE-US is scarce and heterogenous, and there is no consensus reached on the accepted level of variation since this depends on the intended use and the expected measured change. Hence, the variation in DCE-US imaging needs to be compared against the detected changes following radiotherapy, to judge its potential as an imaging biomarker of response.

# 2 CHAPTER Thesis Aim and Organisation

## 2.1 Aims

The overall aim of the work described in this thesis was to investigate the potential of imaging metrics measured using dynamic contrast enhanced ultrasound (DCE-US) imaging as early imaging biomarkers of tumour response to radiotherapy in head and neck and cervical cancer. The overall hypothesis was that metrics derived from time-amplitude curves acquired using DCE-US could be used to indicate radiotherapy response prior to treatment and to measure changes in tumour vasculature prior to changes in tumour volume that differed with radiotherapy response.

There were also several specific aims:

1. Establishment of preclinical models of H&N and cervical cancer, which are practical to use for ultrasound imaging studies of radioresponse. **(Chapter 4)**
2. Identification of suitable doses of radiation that result in both partial and complete tumour response to radiotherapy in preclinical models H&N and cervical cancer. **(Chapter 4)**
3. Evaluation of differences in pretreatment and the change in 2D DCE-US metrics and the distribution of pretreatment 2D DCE-US metrics (heterogeneity) between tumours with partial and complete response. **(Chapter 5)**
4. Evaluation of differences in pretreatment and the change in 3D DCE-US metrics and the distribution of 3D DCE-US metrics in response to radiotherapy between tumours with partial and complete response. **(Chapter 7)**
5. Assessment of the repeatability of 2D and 3D DCE-US in tumour and normal tissue. **(Chapter 5,6,7)**

6. Comparison of the use of 2D and 3D imaging for the measurement of changes in DCE-US metrics and the distribution of DCE-US metrics pre- and post-radiotherapy. (**Chapter 7**)

## **2.2 Organisation of thesis**

A description of materials and experimental methods common to multiple chapters in the thesis is presented in **Chapter 3**. **Chapter 4** describes the characterization of *in vivo* models to attain suitable models H&N and cervical cancer. This involved evaluation of the model's tumorigenicity, radioresponse and vascularity. The chapter also investigates the correlation of DCE-US metrics to establish how one metric may influence another. **Chapter 5** describes a preliminary study of the established H&N and cervical models, examining the ability of 2D DCE-US imaging to assess radioresponse based on vascular changes 48 hours after radiation, and investigates the repeatability of 2D DCE-US within a single imaging session. The work in **Chapter 6** examined the repeatability of a 3D DCE-US imaging system developed in-house using the kidney as a model of normal vasculature. Repeatability of same day and different day imaging was examined. Finally, the assessment of radioresponse using 3D DCE-US imaging was assessed in H&N and cervical cancer models and the repeatability of tumour imaging in a single session was examined in **Chapter 7**. **Chapter 8** provides a summary of the main findings and discusses the limitations of this work.

# 3 CHAPTER Materials & Methods

## 3.1 Tumour Models

### 3.1.1 Cell preparation

In *vivo* experiments were conducted under the UK Home Office project licence PCC916B22(SR)/01 with the experimental protocols reviewed and approved by the ICR Biological Services Unit in line with ARRIVE guidelines and the ICR Animal Welfare and Ethical Review Body. Two cervical cancer cell lines, C33A and ME-180, and LICR-LON-HN5 (HN5), a head and neck cancer cell line, were provided by Dr. Simon Robinson and Dr. Carol Box, Centre for Cancer Imaging, ICR, and their identity authenticated through short tandem repeat (STR) analysis using a GenePrint® 10 kit (Promega, UK), and analysed (by Daniela Novo, ICR) on a 3730xl DNA analyser (Applied Biosystems, Warrington, UK). The cells were tested for mycoplasma by an external provider (Surrey Diagnostics Ltd, UK) using a polymerase chain reaction (PCR) method.

All cells were grown in Dulbecco's Modified Eagle's Medium (DMEM) (Gibco™, ThermoFisher, UK) supplemented with 10% foetal bovine serum (FBS) (PAN Biotech, UK). While in a stage of exponential growth, at a confluence of 60 to 80%, cells were harvested and resuspended in Hanks' Balanced Salt Solution (HBSS) (Gibco™, ThermoFisher, UK) at a concentration of  $5 \times 10^7$  cells/mL for injection. Cells were placed on ice until they were injected.

### 3.1.2 Cell injection

Female Nude-Foxn1<sup>nu</sup> athymic nude mice bred in-house at the ICR Biological Services Unit were used for experiments described in Chapters 4 and 5. Due to discontinuation of this supply, NCr-Fox 1<sup>nu</sup> athymic nude mice supplied by Charles River Laboratories Ltd (Harlow, UK) were used for the experiments described in Chapter 7. The mouse target age at inoculation was 6 to 7 weeks, with a weight of 18 to 25 g.

Mice were injected with  $5 \times 10^6$  cells, in a volume of 100  $\mu\text{L}$ , subcutaneously in the flank under isoflurane anaesthesia. The injected cell number was increased to  $6 \times 10^6$  in one experiment with C33A cells, described in Chapter 4, to increase the growth rate of the tumours.

### 3.1.3 Tumour growth monitoring

Following tumour cell injection, tumour growth was monitored using calliper measurements of three orthogonal dimensions. The volume was calculated according to the ellipsoid volume equation [157] as follows:

$$V = \frac{\pi}{6} w \cdot l \cdot d \quad \text{Equation 3-1}$$

Where  $w$ ,  $l$ , and  $d$ , represent the width, length and depth of the tumour. The uncertainty of volume calculation was estimated as the average (over 69 mice and a range of tumour volumes) of the absolute difference between two measurements repeated on the same day, which gave an uncertainty of 27.2  $\text{mm}^3$ . The distribution of the volume measurement differences is shown in Figure 3-1.

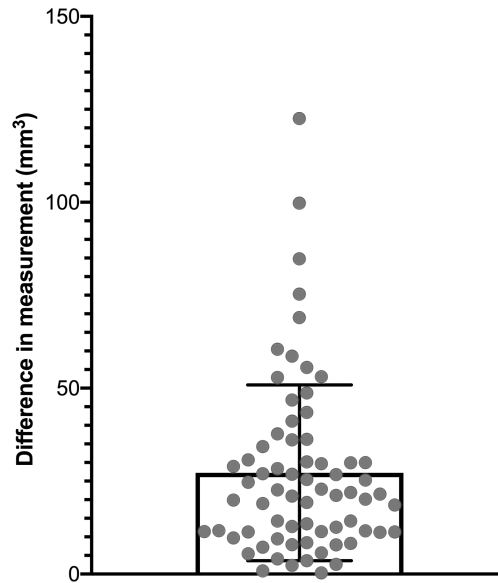


*Figure 3-1: Uncertainty was quantified using the absolute difference in repeat tumour volume measurement. Each point represents the absolute difference of two repeat measurements ( $n=69$ ). The bar represents the mean difference, and the error bar represents the standard deviation.*

#### 3.1.4 Radiation response

The first radiation experiment (described in section 4.3.2.1) was performed using a target treatment tumour volume of  $200 \text{ mm}^3$ , in line with reported treatment volumes in preclinical experiments [85, 158, 159], and based upon previous radiation-response studies carried out at the ICR [160]. The target volume was subsequently reduced to  $150 \text{ mm}^3$ , to ensure the tumour dimensions were small enough to yield adequate radiation coverage without the need for prolonged treatment times, as well as to allow more time for the tumour to respond to treatment before it reached licence limits.

Tumour volume following treatment was used to assess radioresponse. Tumours were allowed to almost grow up to the size limit of the project licence; the largest tumour dimension not exceeding 15 mm or an average of the two largest dimensions not exceeding 12 mm. In some cases, animals had to be culled earlier than this endpoint due to welfare concerns, which were mainly weight loss following imaging, severe tumour ulceration, or tumour growth impeding the animal's movement.

## 3.2 DCE-US Imaging

### 3.2.1 *Imaging schedule*

Tumours were longitudinally imaged typically ~24 hours before irradiation or sham treatment to obtain a pretreatment measure of vasculature, and then at multiple timepoints post treatment (from 24 hours to 1 week) to assess vascular changes using DCE-US metrics. More details are provided for each study in the relevant chapter.

In the first study of HN5 tumours, described in chapters 4 and 5, pretreatment imaging was performed on the same day as tumour irradiation. The adjustment was made to minimize the difference in tumour volume between pretreatment imaging and irradiation after observing a measurable increase in volume over 24 hours in an earlier C33A study (discussed in Chapter 5). However, subsequent studies readopted the original schedule as this was more practical and HN5 tumours did not show a substantial increase in tumour volume in the 24 h period between imaging and irradiation.

The imaging schedules for the kidney repeatability studies described in Chapter 6 were similar to those used in the tumour studies, with three imaging timepoints within 1 week, or imaging separated by 1 week, to investigate the effect of the repeated injections of contrast microbubbles and allow tail vein recovery from cannulation. The variation in the intervening time between injections was due to a restriction in the times at which the animals could be imaged.

### 3.2.2 *Animal anaesthesia and cannulation for imaging*

Animals were anaesthetised using an intraperitoneal injection of either:

- a 8 - 10  $\mu\text{L/g}$  mouse body weight combination of Hypnorm™ (fentanyl citrate and fluanisone) and Hypnovel™ (midazolam) diluted in sterile water in a ratio of 1:1:2, previously shown to have minimal effect on blood flow [161], or

- a 4  $\mu\text{L/g}$  mouse body weight combination of ketamine (100 mg/kg), xylazine (10 mg/kg) and acepromazine (3 mg/kg) diluted in sterile water.

The animal's body temperature was maintained using a heated imaging bed (Vevo Imaging Station, FUJIFILM VisualSonics Inc., Toronto, Canada). Animals were positioned on their side so that the tumour was uppermost and were secured with tape to minimise motion. A holder prevented the US transducer from moving during imaging. For the kidney studies described in Chapter 6, the animal was set up in the prone position to allow imaging of both kidneys.

Contrast microbubbles were injected through a 27 G Terumo Surflo<sup>®</sup> winged infusion catheter (Medisave UK Ltd, Weymouth, UK) inserted in a lateral tail vein. To reduce the catheter's dead space volume, the original 20 cm tubing was replaced with 7 cm PolyE<sup>®</sup> polyethylene tubing (Harvard Apparatus Ltd, Cambridge, UK) with an internal diameter of 0.4 mm, giving a dead space volume of 9  $\mu\text{L}$  in the tubing. The contrast mixture was loaded in a 1 mL Terumo syringe (Medisave UK Ltd) and connected to the catheter using a 27 G BD Microlance needle (Medisave UK Ltd). The patency of the cannulation was confirmed by injecting a small volume of saline before contrast injection. The tumour imaging setup is shown in Figure 3-2.

### 3.2.3 Contrast agent

Sonazoid<sup>™</sup> (GE Healthcare AB, Oslo, Norway) microbubble contrast agent was used in all experiments described in this thesis. It was supplied as dry powder and the bubbles were reconstituted as follows, within two hours of an experiment. Two mL of sterile water for injection was added to the powder, resulting in a concentration of  $2.1 \times 10^9$  microbubbles/mL [162]. The contrast mixture was loaded into the injection syringe using a 19 G BD Microlance needle (Medisave UK Ltd) to minimise bubble disruption. A bolus of 50  $\mu\text{L}$  was injected intravenously for each imaging acquisition. 2D DCE-US studies were performed with a manual injection, while for the 3D DCE-US studies, contrast was injected using an NE-1010 injection pump (New Era Pump Systems Inc., Farmingdale,

NY, USA) using a flow rate of 2.18 mL/min, chosen to mimic the duration of a manual injection (approximately 1.5 s).

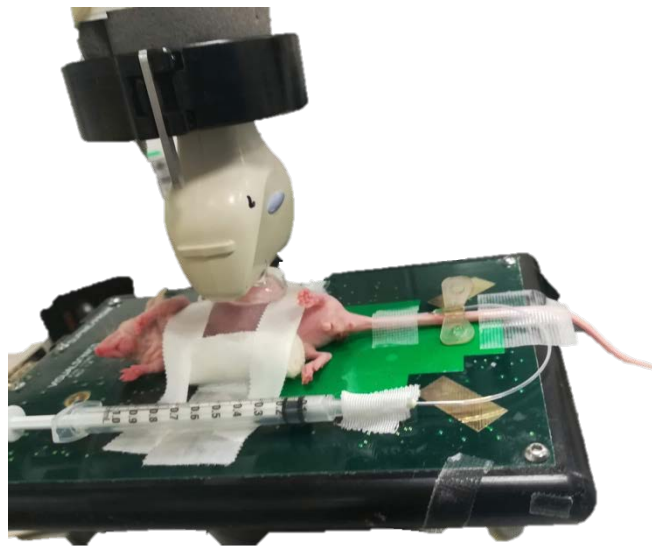


*Figure 3-2: Set-up for 2D DCE-US imaging. The animal was taped to a heated platform and positioned on its side so that the tumour was on top and accessible for imaging. The transducer was mounted using a holder clamped to a rigid support. The modified cannula with shorter tubing is also shown here, with the contrast syringe connected.*

### 3.2.4 Two-dimensional (2D) DCE-US imaging

2D DCE-US imaging was carried out using an Aplio XG™ system with a PLT-1204BT linear array transducer (Canon Medical Systems, Tokyo, Japan). The system's contrast harmonic imaging (CHI) mode enabled dual viewing of B-mode and contrast enhanced images through alternating acquisition. The B-mode images were used to locate the tumour and to reproduce the image plane between serial imaging timepoints. The scanner settings were central frequency = 8 MHz, mechanical index (MI) = 0.3, dynamic range = 55 dB, and a frame rate = 10 Hz. The settings were chosen based on a colleague's expertise (Nigel Bush) of using the scanner for preclinical contrast imaging. The transducer was positioned and the transmit focus was adjusted between 5 to 8 mm so that it was at approximately the same depth as the centre of the tumour, for differing skin-to-tumour-centre depths. The MI (as displayed by the scanner) was kept constant. In addition to the data produced for visualisation in real-time (video

data), the scanner provided a 'raw' data format of the contrast mode. For data analysis, raw data was considered superior to the displayed video data which is log compressed for visualisation and needs to be linearised using dedicated software for accurate quantification of signal [163].

Data acquisition was started 20 to 30 seconds prior to contrast injection to measure the baseline CHI signal amplitude and lasted 6 minutes overall. A timer was started at the time of injection which could be seen on the video data. The time of injection was then retrieved from the time stamp by identifying the frame at which the timer appears and could thus be automatically retrieved during data analysis. The acquisition time was long enough to image the contrast agent's arrival, its uptake and its wash out, thereby allowing estimation of the relevant flow metrics. Raw DCE-US images at different phases of contrast enhancement are shown in Figure 3-3. The imaging data was stored as DICOM files and read in MATLAB™ (2019b, MathWorks™, Natick, MA) using code developed by Nigel Bush.

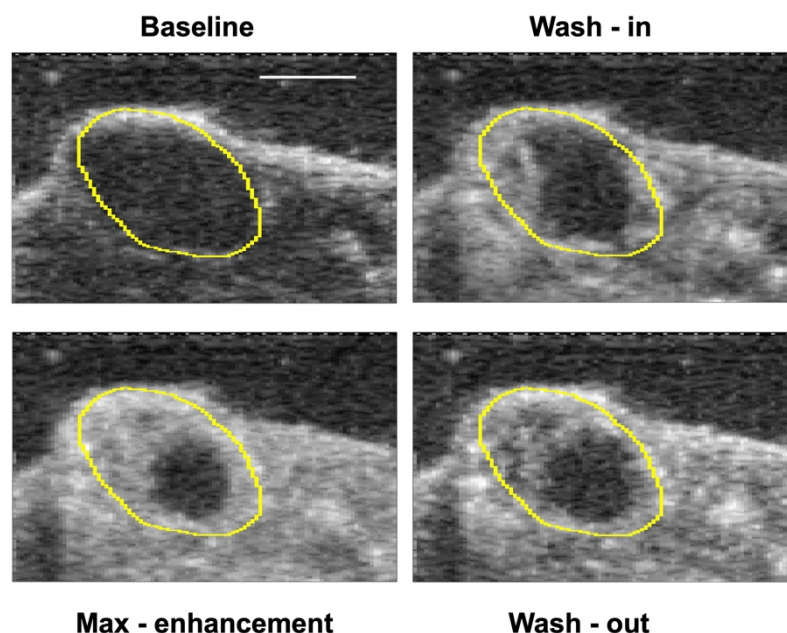


*Figure 3-3: Representative examples of raw contrast-mode images at several stages of contrast enhancement in a C33A tumour. The tumour is delineated in yellow. The scale bar shown in the top left image represents a length of 4 mm.*

### 3.2.5 *Three-dimensional (3D) DCE-US imaging*

3D DCE-US imaging was used to assess the perfusion of the whole tumour volume as an alternative to relying on a single central tumour cross section. This technique was developed by Dr. Elahe Moghimirad at the ICR. DCE-US imaging was performed using the Verasonics Vantage™ scanner (Verasonics Inc., USA) and the Philips ATL L7-4 transducer (Philips Co., The Netherlands). Contrast-mode imaging utilised pulse inversion (see 1.4.2), where the echoes received from a first pulse and those received from a second pulse that is the inverted replica of the first, are summed. This allows the detection of the nonlinear microbubble signal [121]. B-mode images were acquired simultaneously, using a single pulse from the pulse-inversion sequence. The imaging parameters, chosen by experiments in a flow phantom to maximise contrast signal and minimize bubble disruption [164], were: central frequency = 4.08 MHz, frame rate = 10 Hz, pulse interval of 150  $\mu$ s, F-number = 4.

3D imaging at baseline and throughout contrast wash-in and wash-out was achieved by continuously acquiring 2D image data during a reciprocating elevational motion of the transducer. Using a Direct Drive Translation Stage (DDSM50, Thorlabs Ltd., UK) and K-Cube motion controller (KBD101, Thorlabs Inc., UK), the transducer was moved 20 mm, reaching a speed of 20 mm/s after accelerating at 40 mm/s<sup>2</sup> for the first 5 mm and decelerating at the same rate for the final 5 mm, before turning around to repeat the sequence. Again, these parameters were chosen based on the work described in [165]. On average, tumours, which typically had dimension of  $\sim$ 10 mm in the direction of the transducer motion, could be imaged using 5 frames in each reciprocation half-cycle. Each full cycle, returning the transducer to its original position, took 3 seconds, i.e., 30 frames. The scan range of 20 mm ensured coverage of the tumour elevationally at any volume, up to the size limit, whilst ensuring that the tumour was not at the scan edges where the speed was not constant. Of the 30 frames per scan cycle, 10 were spent in the acceleration and deceleration regions, with 20 in the central 10 mm with an elevational sampling interval of 1 mm. The transducer was coupled to the tumour using a waterbag with a layer of ultrasound gel between the waterbag and the animal. This allowed smooth

motion of the transducer without loss of contact. The setup is shown in Figure 3-4.

The start of the transducer motion was synchronized with the beginning of image acquisition through a trigger signal from the Verasonics to the K-Cube motion controller. Once started in this way, the image acquisition and reciprocating motion of the transducer continued with no further synchronization signals. The animal was set up so that the tumour was approximately positioned at the centre of the scan range at 10 mm. 3D imaging was carried out for 50 seconds before contrast agent injection, encompassing 15 motion cycles. Contrast agent was then injected, and 3D imaging data were acquired for 5 minutes corresponding to 100 motion cycles. The start of contrast agent injection coincided with the beginning of 3D imaging (baseline imaging saved separately). B-mode and contrast mode imaging data were stored as MATLAB MAT files.

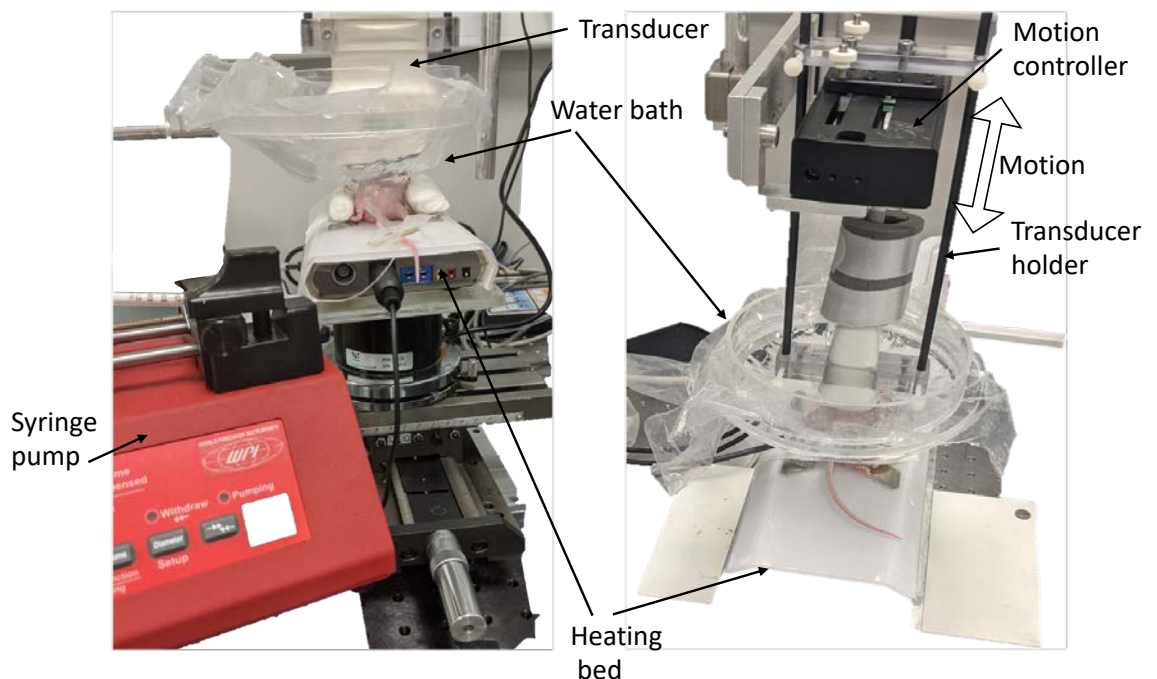


*Figure 3-4: 3D DCE-US setup. On the left is the animal setup with the injection pump and water bath to allow smooth motion of the Philips ATL transducer. The right picture shows the transducer holder and transducer mounted on the translation stage (a different transducer is shown here). The direction of motion of the transducer is indicated by the white arrow.*

### 3.3 DCE -US Data Analysis

As outlined in section 1.4.3.1, DCE-US data were used to generate time–amplitude curves (TACs) to derive semi-quantitative metrics of perfusion. The analyses reported in this thesis used the TAC metrics commonly found in the literature, outlined in . Two metrics were modified from common definition; the amplitude decrease for the modified transit time was set at 65% instead of the typically used 50 % in the mean transit time metric. This definition was adopted from the *in vitro* experiments for consistency. Similarly, the washout time was defined at 30 % amplitude decrease instead of zero because the imaging time *in vivo* often was not long enough to observe return to baseline signal. First, TAC metrics were estimated using whole-ROI analysis to assess overall blood flow changes following treatment, throughout the tumour being imaged (2D or 3D). Next, subregion (sub-ROI) analysis was employed to examine whether changes in the tumour vasculature occurred predominantly within specific subregions, e.g., the rim of the tumour, and could therefore be more accurately detected using sub-ROI TACs. Further, spatial metric maps were generated, and histogram analysis was used, to investigate intratumour vascular heterogeneity. Additionally, these analysis methods were used to explore whether the tumour’s initial perfusion at the pretreatment imaging timepoint was predictive of post-treatment trends. Programs in MATLAB were written for all the analyses described below.

<b>Metric</b>	<b>Abbreviation</b>	<b>Definition</b>
Peak enhancement (a.u.)	PE	Maximum minus baseline amplitude
Arrival time (seconds)	AT	Time to reach 5 % of PE from the injection time
Wash in time (seconds)	WIT	Time between AT and time of PE
Modified Transit time (seconds)	MTT	Time to amplitude decay to 65% of PE from AT
Wash out time (seconds)	WOUT	Time to amplitude decay to 30% of PE from WIT
Area under the curve (a.u.)	AUC	Sum of area between one signal sample and next over a period of 200 seconds from AT

*Table 3-1 : DCE-US metrics derived from the TAC and their definitions.*

### 3.3.1 2D DCE-US data

#### 3.3.1.1 Whole-ROI analysis

Whole-ROI analysis quantified the perfusion metrics of the imaged tumour central slice to represent tumour perfusion as in previous DCE-US research which tends to be in 2D. A region of interest (ROI) was delineated to include tumour tissue only, *i.e.*, excluding skin and normal tissues. The mean contrast-signal amplitude (across all pixels) in the ROI was calculated, the result for each frame providing a sample amplitude value in a TAC that was thus generated from the sequence of frames. The TAC was filtered with a temporal median filter with a length of 11 samples (frames), corresponding to a time interval of 1 second, to reduce respiratory and electronic noise modulations and their effect on TAC metric calculation. An example TAC is shown in Figure 3-5.

The relative change in a TAC metric was calculated as the difference in the metric value ( $M$ ) between two imaging timepoints ( $t_1$  and  $t_2$ ) divided by the metric value at the first timepoint as presented in Equation 3-2.

$$\Delta M = (M_{t_2} - M_{t_1}) / M_{t_1} \quad \text{Equation 3-2}$$

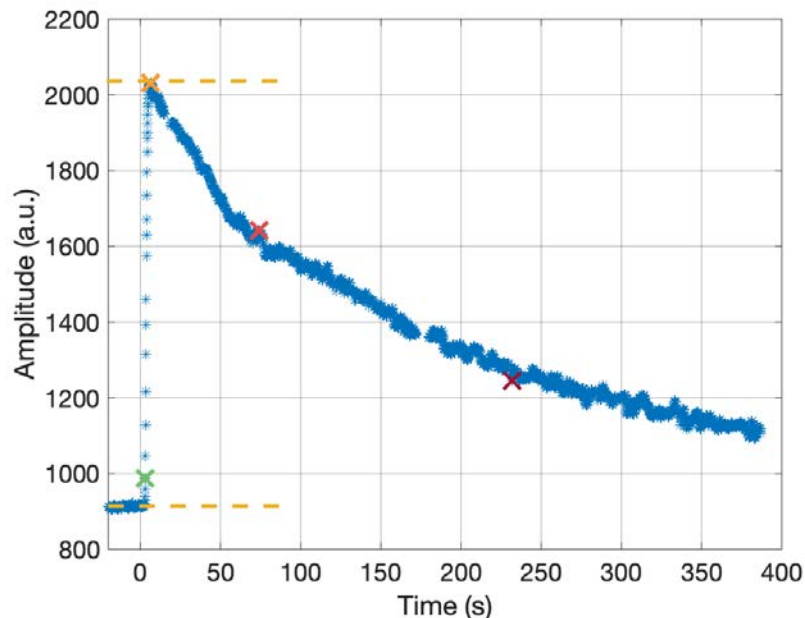
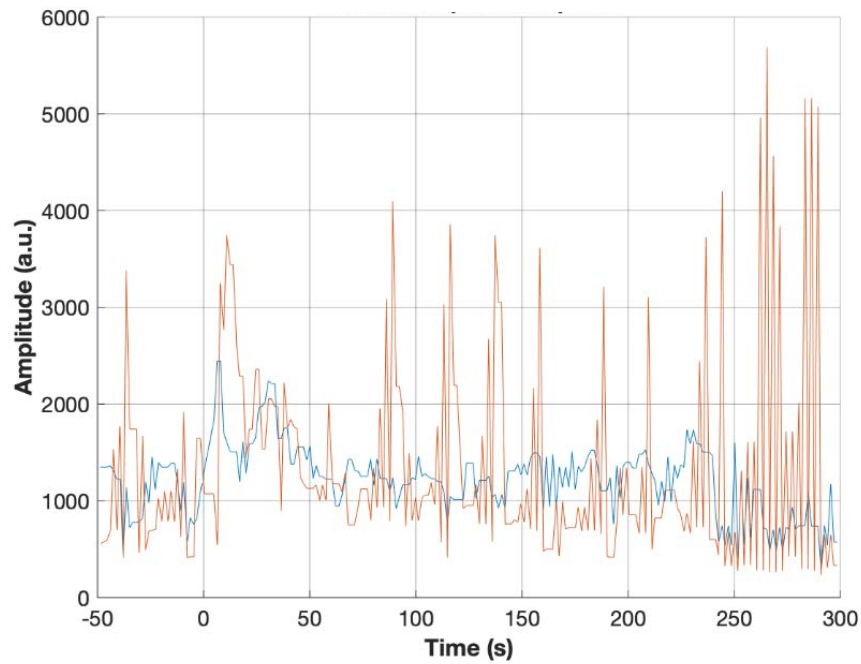


Figure 3-5 : A representative example of a whole-ROI 2D TAC, showing calculated TAC metrics: baseline (yellow dashed line), arrival time (green cross), peak enhancement (yellow cross), the MTT (red range-arrow) and the wash-out time (dark red cross). Not shown is the AUC. Injection was at time = 0 s.

### 3.3.1.2 TAC metric maps

TAC metric maps were generated to investigate the intra-tumour perfusion heterogeneity through subregion and histogram analysis. TAC metrics were calculated for each pixel within the tumour ROI. This involved median spatial filtering with a 5 x 5-pixel window of each frame of the contrast-signal data to improve the signal to noise ratio of the pixel-wise TAC, corresponding to spatial filtering of  $5 \times 171 \mu\text{m} = 855 \mu\text{m}$  laterally and  $5 \times 55 \mu\text{m} = 275 \mu\text{m}$  axially. A 3 x 3-pixel window was tried but was insufficient in reducing noise, especially in the presence of motion. Moreover, the following criteria were employed to improve the estimation of pixel-wise TAC metrics:

- Pixels with no detectable enhancement, defined as a peak enhancement 5 times larger than the standard deviation of the baseline amplitude, were excluded from time-based metric maps, but were assigned a value of zero in PE and AUC maps to indicate non-perfused pixels. Example TACs of such pixels are shown in Figure 3-6.
- Pixels that did not reach wash-out (30%) by the end of the acquisition, were assigned the maximum WOUT of the total acquisition. This was done to avoid excluding pixels with slow wash-out from the spatial map.
- AT was defined as the time to reach 15% of peak enhancement (vs 5% in whole-ROI TAC) to minimise inaccurate AT estimation due to the small noisy amplitude changes often seen at the individual contrast-signal pixel level (see examples in Figure 3-6).
- Pixels with a calculated arrival time of 1 second or less were excluded, as this was considered physiologically not possible and was an inaccurate estimation due to noise.



*Figure 3-6: Example single-pixel TACs of two non-perfused pixels, where PE was lower than the noise level, defined as 5 times the standard deviation of baseline.*

### 3.3.1.3 Subregion analysis

Regions of the tumour that are initially poorly perfused or non-perfused may undergo little detectable change in response to treatment whilst regions that are well perfused are more likely to undergo greater changes. Consequently, whole-ROI analyses may be less sensitive to vascular changes because they will average out response in all regions. Possible approaches to overcome this problem using subregion analysis were discussed in detail in the introduction to this thesis. (see 1.3.2). In this thesis, subregion analysis examined pretreatment perfusion and perfusion changes in response to treatment in subregions (sub-ROIs) defined using the pixels with the greatest metric values. These sub-ROIs were produced in the pretreatment images independently for each TAC metric. The metric-map pixels comprising the highest 10%, 20%, 40% and 50% of pixels, each produced their own sub-ROI. A sub-ROI TAC was then generated using only these pixels and sub-ROI TAC metrics calculated. This approach enabled examination of sub-ROIs that mainly comprise the rim of the tumour, where the tumours have a rim/core pattern of perfusion.

Two approaches were used to generate sub-ROIs in post-treatment images. The first approach, referred to as *spatial subregion analysis*, attempted to allow pre- and post-treatment TAC metric comparisons in spatially matched subregions while compensating for changes in the size and shape of the tumour between baseline and post-treatment imaging. This approach generated post-treatment sub-ROIs from pixels spatially corresponding to the pixels included in the pre-treatment sub-ROI. This was carried out by mapping the distance and angle between each sub-ROI pixel and its nearest boundary vertex. Boundary vertices were the (central) pixels at the minimum and maximum x and y coordinates within the whole tumour ROI. Using this information, a spatially correspondent pixel in a post-treatment image would be found at the same distance and angle from the same boundary vertex, while allowing for scaling due to tumour ROI changes. This method is shown in Figure 3-7.

The second approach, referred to as *functional subregion analysis*, defined the sub-ROIs in post-treatment images based on the highest percentiles of pixel-wise TAC metrics, as is done in the pre-treatment images. Spatial correspondence of sub-ROIs obtained using both spatial and functional analyses was assessed using the dice similarity coefficient. This can be useful in understanding the reproducibility of the imaging plane.

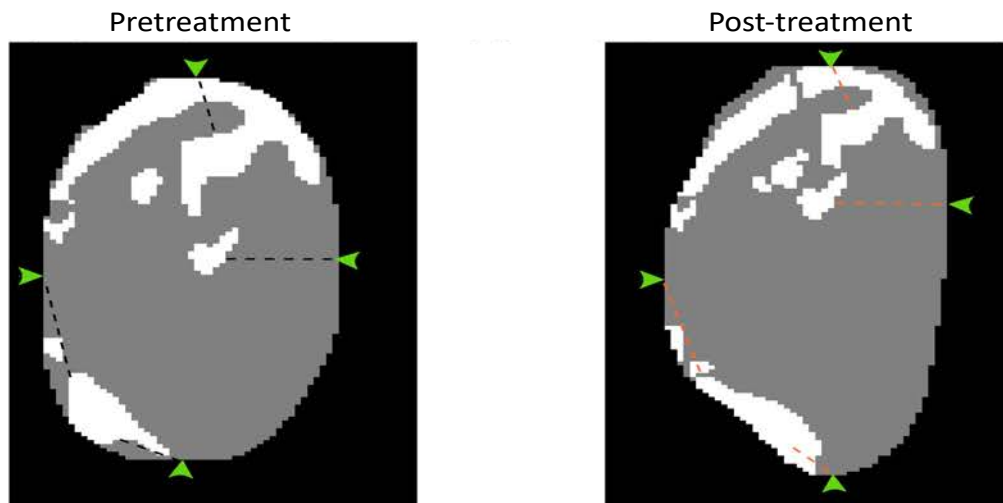


*Figure 3-7 : Spatial subregion analysis. For each TAC metric, a non-contiguous sub-ROI was created from pixels of the highest valued 20% of pixels in the pre-treatment images (left). The angle and distance between each pixel and its nearest tumour-boundary pixel (green arrows show these for example pixels) was calculated (black dashed lines show these, for the same example pixels) and used to transform the sub-ROI for overlay onto the post-treatment images (right) (orange dashed lines, show the new position of the pixels with respect to the tumour-boundary pixel).*

#### 3.3.1.4 Histogram analysis

To investigate if the distribution of DCE-US metrics could be used to detect changes in the pattern of perfusion in response to treatment, descriptive metrics of the histograms were used to quantify the heterogeneity of pixel-wise DCE-US metrics. A histogram of each metric map was generated using 400 bins. The histogram distribution was characterised using standard deviation (SD), coefficient of variation (CoV), modified full-width half maximum (mFWHM), skewness, and kurtosis. mFWHM calculation was replicated from [107]. It is the range between values covering 38% of the area on either side of the median of the distribution. The change in each histogram parameter from baseline following treatment was calculated using Equation 3-2. In addition, percentile analysis investigated the mean value of each metric at the 5%, 10%, 15% and 20% percentiles pretreatment and their change following treatment, similar to the analysis in studies discussed in section 1.3.1.

### 3.3.2 3D DCE-US data

3D DCE-US data analysis allowed 3D TAC-metric mapping for quantification of the intra-tumour perfusion heterogeneity, simulation of 2D DCE-US whole cross-section analysis of perfusion for individual tumour slices (whole-ROI TAC), and analysis of perfusion for the entire tumour volume of interest (whole-VOI TAC). To do so, the analysis required identification of the imaging frames containing the tumour (frame selection).

#### 3.3.2.1 Frame selection

Using the 3D DCE-US imaging settings described earlier in 3.2.5, each imaged tumour slice had 30 and 200 acquired frames in the baseline and injection acquisitions, respectively, with each cycle imaging the tumour twice. Although the mechanical motion and the imaging acquisition were initiated at the same time, there may have been a small lag between their starts. Indeed, for some acquisitions the start of the motion was delayed briefly (~ 1 second) due to a mechanical fault. Further, the motion of the platform was not expected to be perfect and therefore, even if synchronised at the start of the acquisition, the frame rate and motion cycles may have become unsynchronised during the scanning. This meant that it was not possible to determine which frame imaged which slice of tissue by simply counting the number of frames.

Frames corresponding to a sufficiently similar anatomical location in elevation were identified from the 3D imaging data using a frame-selection workflow. This involved first identifying a reference frame for each cross section from the B-mode images before contrast injection. The similarity between the reference and all other B-mode frames within the acquisition was evaluated using the built-in MATLAB correlation function (`corr2`) which yielded a correlation coefficient. A frame was selected as a corresponding frame (containing similar anatomy) if its correlation coefficient was higher than 0.65 and was the local maximum within 5 frames. Next, the time between consecutive selected frames was checked for any missing frames due to low correlation (time higher than 2.5 s). The correlation coefficient criterion was lowered to 0.58 and was confined to frames between the

nearest selected frames, while excluding the adjacent 5 frames that would have high correlation coefficient ( $> 0.5$ ). If no frames were selected still, a frame would be selected manually, by visual comparison of the reference frame and the frames within one sweep. The correlation coefficients chosen were based on the typical correlation coefficients seen between tumour frames. A schematic of the workflow is shown in Figure 3-8. Frames selected for two or more tumor slices would only be kept for the slice with the highest correlation and would be replaced in the remaining slices by their adjacent frame with the next highest correlation.

To validate the workflow, selected frames were compared to manually selected frames. for two tumour slices based on a visual assessment of similarity. Approximately 85 % of frames identified by the workflow were also manually selected, and the remaining 15% of frames were adjacent to the manually selected frame (1 frame apart).

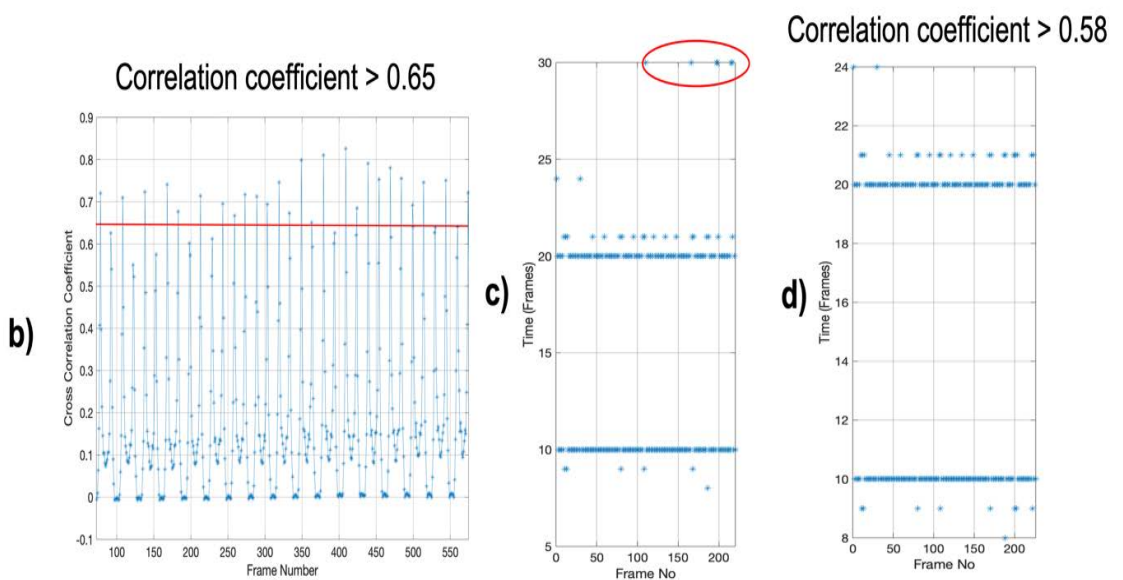
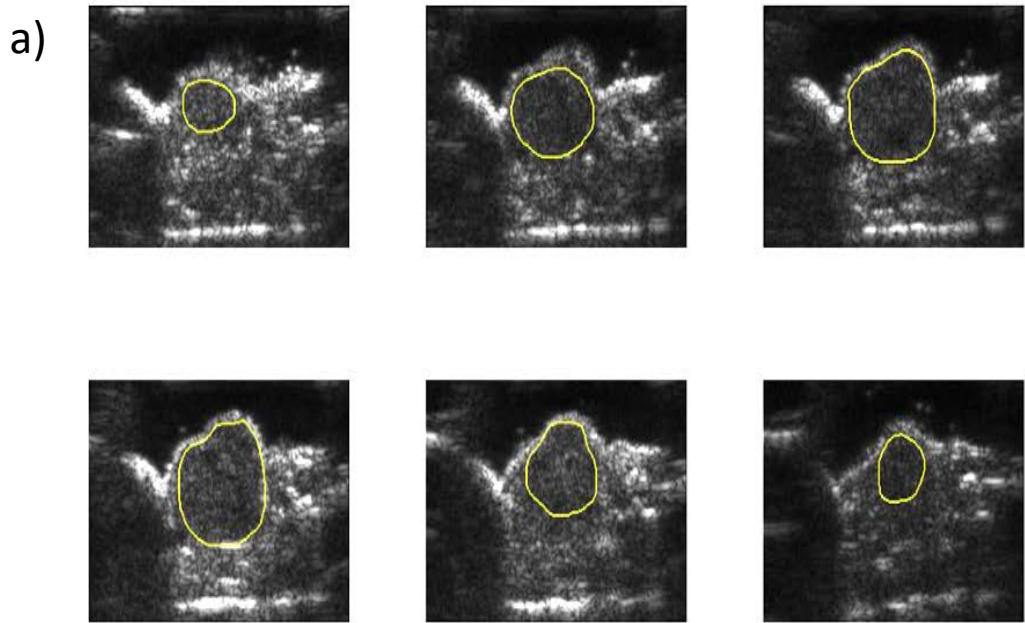


*Figure 3-8: Frame selection workflow for 3D DCE-US imaging. a) shows the reference frame of each identified slice of a tumour (delineated in yellow). The cross-correlation coefficient, computed between each frame and a reference frame of B-mode data is shown in b), with the correlation threshold of 0.65 plotted in red. In this example, which is for an off-centre slice of the tumour, anatomically similar frames are expected to be 10 frames and 20 frames apart, alternating between sweeps. Selected frames are identified using the correlation coefficient and the time between frames is plotted in c), showing several missed frames, where only one frame is identified per cycle (consecutive selected frames are 30 frames apart). With the lower correlation coefficient in d) the missing frames are selected.*

### 3.3.2.2 Motion correction

Selected frames were corrected for in-plane motion, i.e., in the axial and lateral directions. The optimal transformation between a B-mode frame and the reference frame was deduced using a normalised cross correlation method [166] using the built-in MATLAB function (xcorr2). The function calculated the correlation of the two images at progressively increasing axial and lateral integer relative displacements until the images no longer overlapped [167]. The correlation was performed using a search region encompassing the skin boundary to provide distinct features for the correlation and to minimise incorrect transformations based on regions with no features. As much as possible, the displacement yielding the highest correlation between the images would be accepted. However, a transformation with a sum exceeding 15 pixels was considered unrealistic and was replaced with an average of the transformation used for the two adjoining frames. The transformation was then applied to the corresponding contrast mode images. The result of the motion correction was assessed visually by checking the transformation between frames.

### 3.3.2.3 Whole-tumour ROI analysis

2D tumour ROIs were delineated using the reference frame (used for frame selection). Time-amplitude curves were derived for each tumour slice from the selected motion-corrected frames. The mean contrast signal amplitude over the tumour ROI was calculated for each frame, and the TAC was median filtered with a time window of 3 seconds (i.e., 3 frames at the same location).

With the exception of arrival time, the same TAC metric definitions used for 2D DCE-US were applied to the individual slices acquired during 3D imaging and the data generated from the whole tumour volume. For individual slices, the continuous translation of the transducer to generate 3D DCE-US images reduced the temporal resolution (1.5 Hz) relative to that for 2D imaging (10 Hz). This meant that the arrival of the contrast agent within the tumour ROI could not always be defined precisely, with the TAC reliably showing only data points with much greater contrast signal amplitude than the 5% of peak enhancement used to define AT in 2D DCE-US. Therefore, an approximate AT was estimated

through linear extrapolation of two data points within the quick rise period of the wash-in phase (Figure 3-9 left). The estimated AT was used in data analysis if it was greater than 1.5 seconds, (this threshold was based on the range of ATs observed using 2D DCE-US), and if it was earlier than the earliest data point on the TAC above 5%. Otherwise, it was not used and recorded as a “failed estimate”.

Using the TACs from each tumour slice, a single TAC could be generated to represent the perfusion metrics of the whole tumour volume, referred to as whole-VOI TAC. The time resolution of the 3D TAC was the same as a tumour slice whole-ROI TAC, in that the tumour volume would be captured in full, twice in each cycle, i.e., in each sweep of the transducer. The amplitude of the 3D TAC was thus calculated as the mean contrast signal of tumour slices acquired in each half cycle, plotted against the time at the central frame. The 3D TAC was also median filtered with a time window of 3 seconds to keep this filtering the same as in the 2D case.

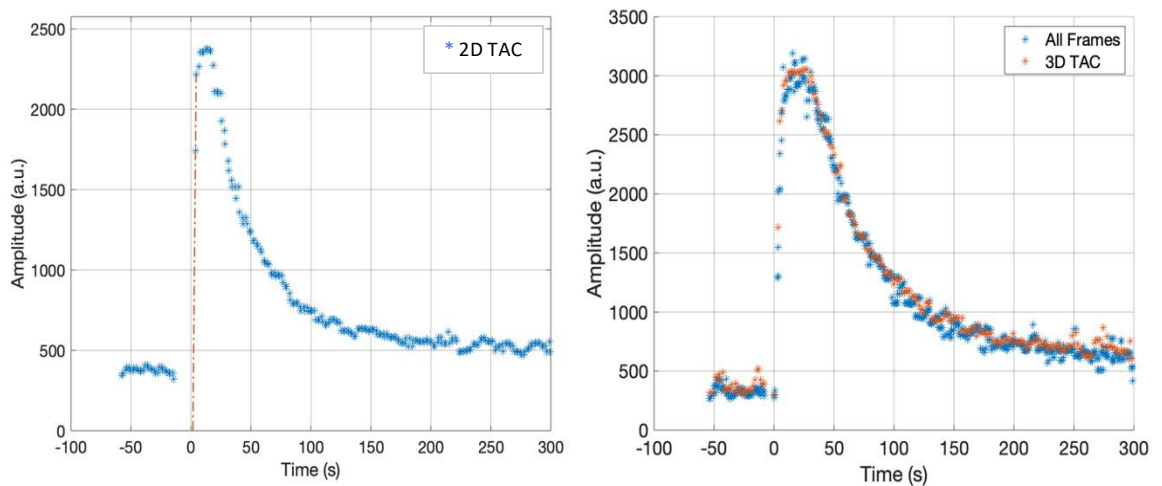


*Figure 3-9: Estimation of AT by linear extrapolation for a tumour cross section TAC acquired during a 3D acquisition (left) and for a 3D TAC that was generated either by plotting all individual 2D TACs (all frames - right) or by combining, by averaging, all the 2D TACs from individual frames (3D TAC - right).*

As with TACs of the individual tumour slices, the arrival time for the 3D whole-VOI TAC could not always be captured and had to be approximated using a linear fit. Here, however, there was an opportunity to effectively improve the temporal

resolution of the 3D TAC by plotting the 2D whole-ROI TACs for all selected frames of the tumour slices, each at their own known time point, rather than averaging their mean signal. An example of this type of 3D whole-ROI TAC is shown in (Figure 3-9 right). It was hypothesised that AT could be more precisely estimated with the greater temporal resolution, assuming that contrast arrival was uniform within the tumour and occurred simultaneously across the tumour slices. To avoid making these assumptions for all TAC metrics, this type of 3D whole-ROI TAC (i.e., using all frames individually) was used to calculate AT only and all other metrics were derived from 3D whole-ROI-averaged TACs.

#### 3.3.2.4 3D TAC metric maps

Metrics maps were generated on a frame-by-frame basis by median spatial filtering of the contrast image data with a 5 x 5-pixel window using motion corrected frames, corresponding to spatial filtering of  $5 \times \sim 148 \mu\text{m} = 740 \mu\text{m}$  axially and laterally. The metrics were calculated using the same definitions as whole-ROI metrics. The exclusion criteria for 2D DCE-US described in section 3.3.1.2 was also implemented. Pixels were considered perfused if the PE was larger than 5 times the standard deviation of the baseline (i.e., well above noise level). Arrival-time pixels where the AT could not be calculated were instead replaced with the AT of the whole ROI. It was decided not to generate metric maps in planes orthogonal to the elevational slices due to the large elevational width of the images.

#### 3.3.2.5 Subregion analysis

Subregion analysis was not applied to 3D TAC metric maps. Reasons for this are discussed in chapter 5.

#### 3.3.2.6 Histogram analysis

A 3D histogram was derived from the pixels of all tumour slices to represent the heterogeneity in the entire tumour volume. The same histogram parameters as those used for 2D analysis were calculated: standard deviation, coefficient of variation, skewness, kurtosis and modified mean width half maximum.

### 3.4 Radiation Treatment

All experiments used single-fraction radiation, with radiation doses of 10, 15, 20, or 25 Gy. Radiotherapy was delivered using the Small Animal Radiation Research Platform (SARRP, XStrahl Ltd, Camberley, UK) which allows localised treatment delivery to the tumour while reducing normal tissue irradiation through the use of treatment planning and collimated X-ray beams. Animals were anaesthetised with isoflurane delivered through oxygen (2 mL/min, 1-2% concentration) and placed on the treatment bed in the prone position. The animal was secured to the treatment bed and positioned such that the tumour protruded as much as possible to separate it from the animal's body, therefore minimising the likelihood of radiation damage to healthy tissue.

Treatment planning workflow started with acquiring a whole-body cone-beam computed tomography (CBCT) image. The image was acquired with voltage = 60 kV, current = 0.8 mA, a 1 mm aluminium filter, a pixel size of 0.25 x 0.25 x 0.25 mm, and 360 frames acquired within 67 seconds, resulting in an approximate imaging x-ray dose of 1.2 cGy. The CBCT image was then reconstructed in the treatment planning software, Muriplan<sup>®</sup> (XStrahl Ltd, Camberley, UK), where the imaging volume was segmented into tissue, lung, air, fat, and bone. This was necessary for accurate calculation of radiation doses delivered with kilovoltage X-rays where the photoelectric effect is dominant [168]. Fat was excluded from the segmentation since athymic nude mice do not have a significant portion of fat. The tumour was segmented as tissue. At this stage, the tumour volume was also contoured at every 5<sup>th</sup> axial slice to generate a dose volume histogram (DVH) later during dose verification.

Next the isocentre of a 10 mm x 10 mm radiation beam was positioned within the tumour, in such a way as to ensure coverage of all the tumour volume and minimise normal tissue inclusion within the beam. To minimise the entry dose at the skin, the radiation dose was delivered with two opposite beams (at 180°). The radiation beams were angled between 1° to 40° (the opposite beam being -179°

to  $-140^\circ$ ), if needed, to avoid surrounding organs at risk. If the tumour length exceeded 10 mm, two additional opposite beams of 5 x 5 mm collimator size were incorporated in the treatment.

The planned treatment was assessed through the isodose distributions and a dose volume histogram for the tumour. Isodoses were used to assess both tumour coverage and any significant irradiation of normal tissue. Using the DVH, a plan was accepted if at least 85% of the contoured tumour volume received at least 80% of the prescribed radiation dose. Radiation was then delivered using voltage = 220 kV, current = 13.0 mA and a 0.15 mm copper filter. The radiation workflow is shown in Figure 3-10 . The overall time for the procedure ranged between 25 and 40 minutes depending on the radiation dose and number of beams needed to provide full tumour coverage.

Animals in the control group were anaesthetised and set-up in the SARRP as described above. A CBCT was acquired, and the animals were kept under anaesthesia for a similar amount of time as treated animals. All animals were allowed to recover on a heated platform.

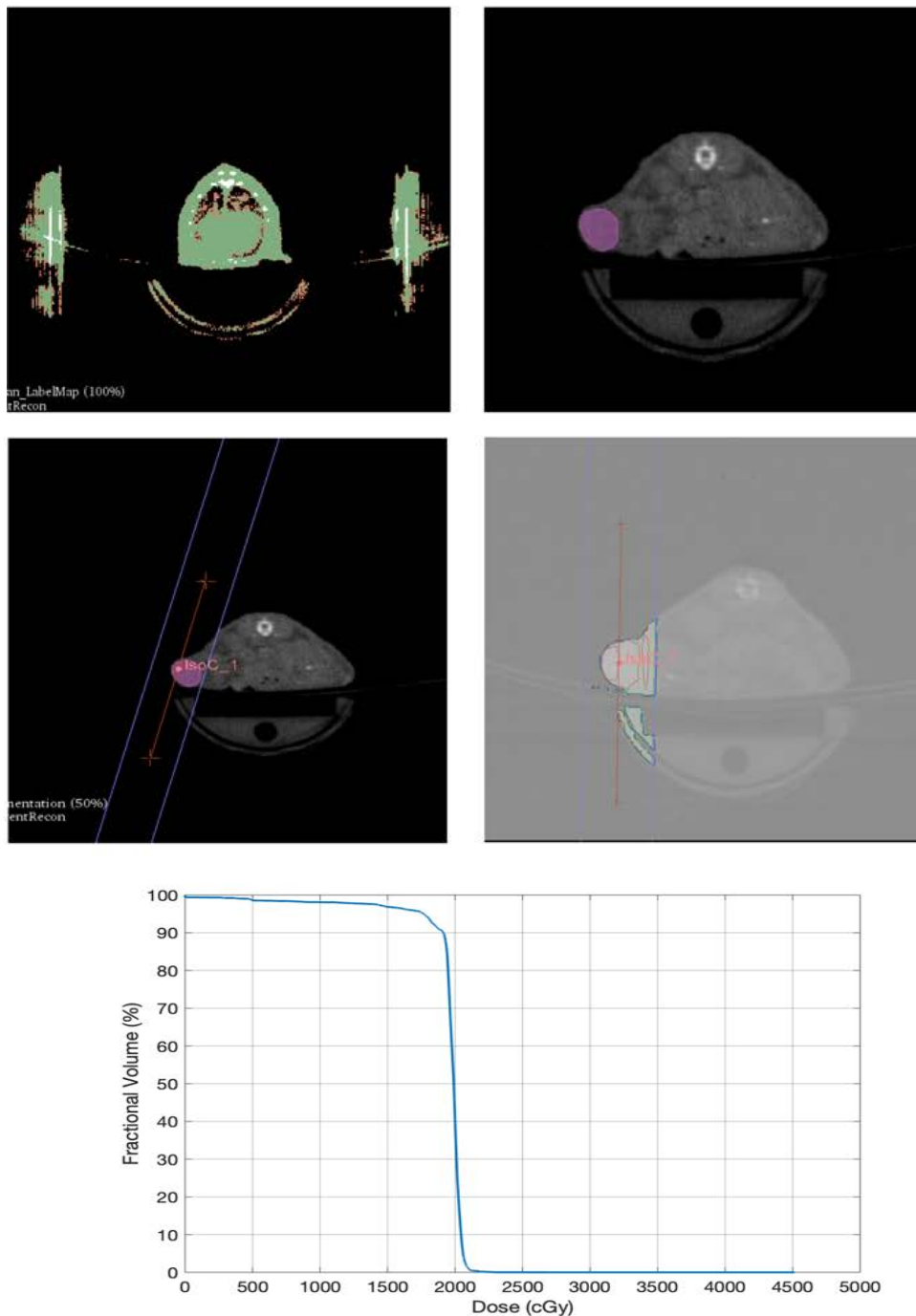


*Figure 3-10: Radiation delivery workflow with the SARRP. Top and middle row images present the axial view and show : (top left) tissue segmentation with air shown in black, lung in red, tissue in green and bone in white, (top right) tumour contouring is carried out for each 5<sup>th</sup> slice, (middle left) 10 x 10 mm radiation beams are added to the treatment and angled away from the tumour body and (middle right) isodoses for a planned treatment. On the bottom row is a typical tumour DVH.*

## 3.5 Histopathology

The use of histopathological analysis enables established markers of tumour pathology to be compared with the spatial distribution of DCE-US TAC metrics. Histopathological markers of potential relevance to DCE-US metrics, and often reported in the literature (see section 1.4.4.) , include CD31 for vascular staining, Hoechst dye for visualization of perfused vessels and pimonidazole staining of hypoxic tissues. In addition, assessing tumour viability using haematoxylin and eosin (H&E) staining can be helpful for interpreting results for other markers, e.g., identifying necrotic regions. All these markers were thus examined and compared to endpoint DCE-US images.

Following imaging and Hoechst and pimonidazole injection (described below), animals were sacrificed via cervical dislocation and the tumours excised. Tumours were cut in half at the imaging plane, with one half fixed in formalin and the other snap frozen in liquid nitrogen. Frozen tumour samples were used for fluorescent imaging of Hoechst uptake, CD31 and pimonidazole staining, while formalin fixed samples, in which tissue integrity was best preserved, were used for CD31 and H&E staining. Kidneys were also excised in the studies described in Chapter 6, with the whole organ frozen for Hoechst imaging and CD31 immunofluorescent staining. Stained sections were imaged using an Axioscan Z1 (Carl Zeiss Ltd, UK) and the Nano Zoomer XR (Hamamatsu, Japan) digital scanners at x 20 magnification.

### 3.5.1 Frozen tissue processing

Tumour and kidney frozen samples were stored at -80°C until sectioned. Ten-micron thick frozen tissue sections were cut using a Bright Cryostat (OTF6000, Bright Instruments, UK) at a temperature of -15 °C and mounted on SuperFrost® slides (VWR, UK). Tissue sections were stored in the dark at -20 °C until they were used for staining.

### *3.5.2 Hoechst staining*

Hoechst 33342 is a fluorescent dye that binds to DNA. While it is not specific to endothelial cells, it has been validated as a marker of the perfused vasculature when injected intravenously as it is rapidly taken up by endothelial cells lining functional vessels and remains stably bound. [169]. Hoechst 33342 (bisBenzimide H33342 trihydrochloride, Sigma-Aldrich, UK) was injected intravenously (dose of 15 mg/kg, concentration of 6 mg/mL in water). An additional 10  $\mu$ L was injected to account for the dead space of the cannula. It was allowed to circulate for 1 min before the animal was sacrificed.

The Hoechst signal was visualized using 4',6-diamidino-2-phenylindole (DAPI) fluorescent imaging, which visualizes nuclear DNA, with an excitation filter with a wavelength range of 330 – 375 nm and an emission filter with range of 430 – 470 nm. The exposure time was adjusted according to the intensity of the stained sample, with kidney sections requiring shorter exposure times of around 5 – 30 milliseconds compared to tumour sections with exposures of 50 – 200 milliseconds.

### *3.5.3 Pimonidazole*

Pimonidazole is an established hypoxia marker that binds to proteins in hypoxic tissues with an oxygen partial pressure below 10 mmHg. Pimonidazole hydrochloride (Hypoxyprobe™ Plus Kit, Hydroxprobe, USA) was injected intraperitoneally at least 45 minutes before animal sacrifice to allow sufficient time for protein adduct formation (dose of 60mg/kg, concentration of 20 mg/mL in PBS). Hypoxia staining could not be completed within the time limit of this project but nonetheless pimonidazole was injected in all studies and the sections are available to complete the staining at a later date.

### *3.5.4 Frozen section CD31 staining*

CD31 (Cluster of Differentiation 31) is receptor expressed in the membranes of endothelial cells and is a well-established marker of vasculature. By combining

CD31 staining with Hoechst dye uptake, it is possible to distinguish perfused from non-perfused vessels.

Following fixation in ice-cold acetone for 10 minutes, frozen sections were outlined with a hydrophobic barrier pen (ImmEdge® Pen, H-4000, Vector Laboratories, UK) then incubated with blocking solution containing goat serum and bovine serum albumin (BSA) for 30 minutes at room temperature. They were then incubated with 100 µL of rat anti-mouse CD31 antibody (5 µg/ml, Catalog #557355, BD Biosciences, UK) overnight at 4 °C. Sections were washed with PBS–0.1% (v/v) and Tween® detergent, and incubated with 100 µL of goat anti-rat secondary antibody conjugated to AlexaFluor® 546 (1:500 dilution, Catalog #A-11081, ThermoFisher, UK) in the dark (to prevent photobleaching) at 37 °C for 2 - 3 hours. Slides were washed again with PBS-Tween and a coverslip added with Vectashield Antifade Mounting Medium (Vector Laboratories, UK) before microscope scanning.

AlexaFluor™ 546 fluorescence was detected using an excitation filter with a wavelength range of 540 – 557 nm and an emission filter of 578 – 640 nm. The exposure time was adjusted according to the intensity of the stained sample, with a range of 30 – 80 milliseconds for kidney and tumour sections.

### *3.5.5 Formalin-fixed tissue processing*

Formalin-fixed paraffin-embedded tumour sections were processed and stained for histopathology by Dr Vaideesh Parasaram, ICR. After formalin fixation for 24 hours, tumours were stored in 70 % ethanol until processing then washed in PBS and embedded in paraffin. Sections for staining were cut at a thickness of 5 µm using a Leica manual microtome (Leica Biosystems, UK).

### *3.5.6 CD31 staining of formalin-fixed samples*

For CD31 staining of formalin-fixed paraffin-embedded (FFPE) tissues, sections were first de-paraffinised in xylene and hydrated in a series of decreasing ethanol

concentrations (100% to 70%). Antigen retrieval was carried out using citrate buffer (H3300, Vector Laboratories, UK) and a pressure cooker. The sections were incubated with Peroxidase Blocking Solution (S200380, Dako) to prevent staining of endogenous peroxidase. The sections were then incubated with 100  $\mu$ L rat anti-mouse CD31 (DIA-310, Dianova, 1: 30 in diluent) primary antibody for 1 hour at room temperature. Following that, sections were washed in TBS–0.025 % (v/v) Tween 20 3 times for 3 minutes then incubated with 2 drops of Rat Histofine<sup>®</sup> Max PO (414311F, Nichirei Bioscience) for 30 minutes at room temperature. Histofine<sup>®</sup> is a polymer comprised of an anti-rat antibody fragment and peroxidase. After washing 3 times in TBS-TWEEN, 100  $\mu$ L of DAB chromogen (3,3'-diaminobenzidine) (K3467, Dako) was added to the sections for 6 minutes. DAB is oxidized by the peroxidase in Histofine<sup>®</sup>, resulting in a dark brown color that can then be visualised by brightfield microscopy.

Haematoxylin counterstaining was carried out as outlined in H & E staining below. Sections were dehydrated in ethanol and xylene before mounting with coverslip, using DPX mountant, for microscopy imaging.

### *3.5.7 Fixed section H&E staining*

Haematoxylin and eosin (H &E) staining was used to characterize the tumours' structure and identify areas of necrosis. Haematoxylin stains nuclei purple/blue, while eosin stains cytoplasmic proteins pink. Regions with high intensity pink staining can indicate necrosis. Tumour sections were de-paraffinised and rehydrated as described for CD31 staining. They were they then washed in running tap water for 2 minutes and stained with Gill's haematoxylin for 1.5 minutes. After washing in running tap water for 5 minutes, sections were incubated in acid alcohol for 3 seconds to remove excess non-nuclear staining. Sections were rinsed again in running tap water for 4 minutes and immersed in eosin for 2 minutes then rinsed once again in tap water for 20 seconds. Sections were dehydrated and mounted with a coverslip using DPX mountant.

# 4 CHAPTER In vivo characterisation of the radioresponse and vasculature of tumour models

## 4.1 Introduction

Preclinical tumour models play an indispensable role in cancer research, and thus in developing imaging biomarkers of cancer [47]. Models of varying complexity have been developed; ectopic, typically subcutaneous, tumour models are easy to establish, and show good reproducibility, making them a practical model. Orthotopic models, where tumour cells are implanted into the equivalent tissue or organ from which the cancer originated may better mimic microenvironmental features, whilst genetically engineered models and patient derived xenografts (PDX) models can more accurately mimic molecular characteristics of human cancer. The model chosen should achieve a balance between practicality, the necessary biological features to test the imaging biomarker, and the burden on the animal health.

For the aims of the thesis, a subcutaneous xenograft model was considered suitable to investigate models of head and neck (H&N) and cervical cancer, based on the mentioned considerations. Xenograft models use human cancer cell lines implanted in immunocompromised mice, allowing the study of human cancer and are the most widely used preclinical model of H&N cancer [170] and cervical cancer[171]. Subcutaneous tumours typically have minimal effects on the animal's welfare and are practical for monitoring tumour growth and for imaging due to their superficial location. Specifically, the NCr-Foxn1<sup>nu</sup> nude mice strain is ideal because it lacks hair, making it practical for ultrasound imaging. Athymic mice such as these are immunocompromised because they lack T-cell function but do retain some immune function through natural killer and B cells [172].

H&N and cervical cancer mostly present as squamous cell carcinomas and comprise a diverse set of tumour subtypes, with heterogeneous radiosensitivity

observed in the clinic [9, 13-15, 32]. As such, the available head and neck and cervical cancer cell lines replicate this heterogeneity and differ in characteristics that may underlie response or resistance to radiotherapy [170, 172, 173]. The choice of cell line firstly relies on achieving good tumourigenicity and growth behaviour in athymic mice. An engraftment success rate of 100% and reproducible tumour growth minimises the number of mice needed and allows more precise experimental planning. Further, tumour growth within a practical time period (i.e., weeks, rather than months) keeps experiment durations manageable. Secondly, for the purpose of assessing radiotherapy response with DCE-US imaging, tumour models need to mimic the heterogeneous overall response seen clinically in both cancer types. Radiation doses that yield a range of responses and allow distinct classification of response facilitate the investigation of the relationship between DCE-US metrics and radioresponse. Hence, for the chosen cancer cell line the optimal radiation dose to produce this response should be identified.

It was reasonable to start with cell lines previously used at the ICR and for which there was local expertise with *in vivo* studies. For head and neck cancer, LICR-LON-HN5 head and neck squamous cell carcinoma (HN5) has been established as a reliable xenograft model when propagated in athymic mice and used for radiotherapy studies [174-176]. The HN5 cell line was derived from a squamous carcinoma of the tongue, and was shown to be transplantable in nude mice, producing xenografts with similar histological appearance to the patient specimen.

Similarly, two cervical cancer cell lines were available and had been grown previously as xenografts in athymic nude mice at the ICR. C33A and ME-180 cell lines were derived from squamous cell carcinoma, the most common type of cervical cancer [177]. ME-180 is HPV-positive, as are almost all cases of cervical squamous cell carcinoma [178], while C33A is HPV-negative. Both cell lines were shown to be radio responsive *in vitro* [179-183]. Although there are no reports of *in vivo* radioresponse of tumours grown from these cell lines, these studies demonstrate the intrinsic variation in their radiosensitivity, which suggests their

potential to produce tumours that would exhibit the desired heterogeneous radioresponse *in vivo*.

As this thesis focuses on assessing tumour response via imaging of its functional vasculature, it is also necessary to confirm that the selected tumours models have an initial level of perfusion that can be monitored reliably. Further, understanding the vascular properties of the tumour model can inform on its growth characteristics and radioresponse. Therefore, the vascular phenotype of the tumour models was assessed using DCE-US imaging at a nominal radiation treatment volume, through analysis of the overall perfusion of the tumour and intratumoural vascular heterogeneity

Additionally, the correlation across tumours between DCE-US metrics was assessed in each tumour model. Understanding these correlations aids in identifying the properties of blood flow and volume affecting each metric and the underlying vascular morphology of the tumour model. It can also discern which measured radiation-induced changes in the metrics are dependent. For example, since PE and AUC are both surrogates of blood volume, they are expected to be correlated, and to show coincident changes following radiotherapy. The correlation of whole-ROI DCE-US metrics across tumours from each model, was used to inspect model-specific correlations and give insight on the perfusion pattern of the model. The correlation of pixel-wise DCE-US metrics was also assessed in each tumour. Pixel-wise metrics expand the dataset available for correlation and examine the correlation between metrics in each tumour individually. A pixel-wise analysis is also expected to reveal correlations that cannot be detected with whole-ROI metrics as a whole-ROI TAC is an average of the heterogeneity of perfusion within the imaging slice.

Finally, to support any inferred conclusions of the tumour vasculature based on DCE-US imaging, DCE-US imaging at the endpoint was compared with histopathological markers of vascular density and cell viability.

### 4.1.1 Aims

This chapter discusses the work carried out to characterise preclinical models of cervical cancer (ME-180 and C33A) and head and neck cancer (HN5) *in vivo* using DCE-US. Specifically, the aims were:

- Establish suitable tumour models of head and neck and cervical cancer based on the tumourigenicity of candidate cell lines and tumour growth characteristics.
- Determine suitable radiation doses for each tumour model to achieve the desired variable radioresponse within a model.
- Assess the vascularisation of the tumour models using DCE-US, including overall perfusion and spatial heterogeneity.
- Compare DCE-US metrics of overall perfusion and heterogeneity between tumour models.
- Assess the correlation between DCE-US metrics.
- Examine the spatial correspondence of perfusion assessed using DCE-US with histopathological staining of vasculature.

## 4.2 Materials and Methods

To address the aims stated above, results from several studies were collated for each tumour model. The studies discussed here are summarised in Table 4-1 and are given abbreviations with a letter referencing the cell line name and a number corresponding to the study number. The tumorigenicity and growth characteristics of ME-180 and C33A cell lines were assessed in studies M1, M2, and C1. The radioresponse data for C33A tumour model is collated from studies C3, C5, C6 and C7. The radioresponse data for HN5 tumours is collated from studies H1, H2, and H3. Studies C5 and H1 inspected the DCE-US characteristics of the tumour. These studies are discussed in later chapters and are referred to using the same abbreviations. Study C4 was excluded as the injected cells were subsequently found to be infected with mycoplasma. This had

no apparent adverse effects on the mouse health status but may have had an effect on tumour growth.

#### 4.2.1 *Tumourigenicity studies*

The tumourigenicity of the ME-180 and C33A cell lines was assessed in two pilot studies (n = 6 mice per cell line), referred to as M1 and C1, respectively. Approximately,  $5 \times 10^6$  cells were injected in these initial studies. All six ME-180 tumours in the M1 study became ulcerated, therefore an additional study (M2) was carried out with the aim of reducing the number of tumours that ulcerated. It was hypothesised that this could be achieved by reducing the number of cells injected, and thereby slowing tumour growth rate. Mice were injected with either  $1$  or  $2 \times 10^6$  cells (n = 3 each), in line with the number of cells used previously at the ICR for this model. In this study, tumour measurements were carried out by staff of the ICR's Biological Services Unit (BSU) and only 2 tumour dimensions (width and length) were recorded. The tumour volume for the M2 study was calculated as:

$$V = 0.5 \times \max(w, l) \times \min(w, l)^2 \quad \text{Equation 4-1}$$

For the C33A cell line, the tumourigenicity was also assessed from a subsequent preliminary study of DCE-US imaging (C2, n = 5). The age of the mice for this study was higher than target age of 6 to 7 weeks, with mice at an age of 10 weeks.

Table 4-1 Studies discussed in chapter (and whole thesis)

STUDY	Number of mice	TUMOURIGENICITY	IMAGING	RADIATION DOSE
Cell line: ME-180				
M1	6	✓		
M2	6	✓		
Cell line: C33A				
C1	6	✓		
C2	5		✓	
C3	7		✓	10 Gy
C5	18		✓	15 & 20 Gy
C6	14		✓ (3D)	25 Gy
C7	14		✓ (3D)	25 Gy
Cell line: HN5				
H1	18		✓	20 & 25 Gy
H2	14		✓	20 & 25 Gy
H3	14		✓(3D)	20 & 25 Gy

#### 4.2.2 *In vivo* radioresponse

The *in vivo* radioresponse of C33A and HN5 tumour models was assessed from C3, C5, C5, C7, H1, H2, and H3 studies. Radiation was delivered as a single fraction using the SARRP as described in section 3.4 and response was characterised through monitoring changes in tumour progression. The target treatment volume was 200 mm<sup>3</sup> in the C3 study and was subsequently changed to 150 mm<sup>3</sup> due to the reasons described in 3.1.4 for all other studies.

For the C33A model, several radiation doses were tested due to the limited available information about the model's *in vivo* radiosensitivity. Tumours were first irradiated with 10 Gy in the C3 study (n = 7), then with 15 and 20 Gy in the C5 study (n = 18, 6 treated tumours for each dose), and was further increased to 25 Gy for C6 (n = 14, with 10 treated tumours) and C7 (n = 14, with 8 treated tumours).

The HN5 model was irradiated with 20 and 25 Gy. Radiation with 20 Gy was based on work carried out at the ICR by Dr Marcia Costa and Dr Sarah Brüningk [174]. The 25 Gy radiation dose was added to increase the number of tumours with complete regression following radiotherapy. All three studies of HN5 tumours used both doses; 10 tumors were treated in the H1 study (n =18) and 7 in each of the H2 and H3 studies (n =14).

#### 4.2.3 *Characterisation of tumour vasculature using DCE-US imaging*

The tumour vasculature of C33A and HN5 models was characterised at the treatment volume using DCE-US imaging at the pretreatment imaging timepoint from studies C5 and H1. Two dimensional DCE-US imaging was carried out as described in section 3.2.4. Animal setup and contrast agent are detailed in 3.2.1 and 3.2.2.

DCE-US metrics describing the tumour vasculature were generated from whole-ROI TAC analysis as described in section 3.3.1.2, metric maps detailed in section 3.3.1.23.3.1.4, and histogram analysis detailed in 3.4.1.4. Whole-ROI TAC metrics of the imaged tumour central slice are assumed to represent the overall tumour perfusion status, while metric maps and histogram analysis describe the intratumour vascular heterogeneity.

##### 4.2.3.1 Correlation of whole-ROI and pixel-wise TAC metrics

The correlation of whole-ROI DCE-US metrics was calculated using metrics obtained from all tumours at the pretreatment imaging timepoint for each tumour model (n = 17 for C33A tumours and n = 16 for HN5 tumours). The Pearson correlation coefficient ( $r$ ) was calculated and 95% confidence intervals (95% CI) of the correlation coefficient were calculated using the bootstrap method, which is a non-parametric method for calculating CIs through resampling of the data [184]. The 95% CI were calculated using 1000 resampling replications. A correlation was considered statistically significant if its 95% CI did not include zero. Significant differences in the correlations obtained from C33A tumours and

HN5 tumours were indicated if their 95% CIs did not overlap. This approach for identifying significant correlations was preferred as 95% CIs provide a precise estimate about the correlation strength, compared to p-values, which only test the correlation coefficient against a null hypothesis of no correlation.

The correlations of pixel-wise DCE-US metrics were calculated for a tumour also using the Pearson correlation coefficient. All tumour slices used for this analysis consisted of at least 1900 pixels, i.e., 1900 datapoints. The 95% CIs were estimated using the bootstrap method with 400 resampled datasets instead of 1000 to minimise the computation time. A correlation within a tumour was deemed significant if its 95% CI did not include zero. The signed Wilcoxon test was used to test if a correlation was significant for the tumour type (median correlation from all tumours significantly different than zero,  $p < 0.05$ ).

#### 4.2.3.2 Comparison of C33A and HN5 tumours

The perfusion status of the two tumour models pretreatment was compared using whole-ROI DCE-US metrics, intratumoural heterogeneity of metrics and the correlations between DCE-US metrics. This analysis was done to provide insight into the reasons for any observed differences in the models' radioresponse as well as the change in DCE-US metrics seen post treatment. Significant differences in correlations of pixel-wise DCE-US metrics were used to explore important differences in the vascular morphology. Statistically significant differences in all the above-mentioned metrics were examined using the Mann-Whitney U test.

#### 4.2.3.3 Validation of DCE-US imaging with histopathology

Biological validation of DCE-US imaging was carried out at endpoint imaging. Excised tumours were cut at the imaging slice, fixed in formalin, and stained with CD31 and haematoxylin counterstain as described in section 3.5.6. The agreement of CD31 staining and the DCE-US metric maps was assessed visually. The results shown here were obtained from the C33A C5 study.

Formalin fixed HN5 tumours from the H1 study were difficult to cut and did not produce complete sections.

## 4.3 Results

### 4.3.1 *Tumourigenicity of cervical cancer cell lines*

#### 4.3.1.1 ME-180 tumour model

Growth curves obtained from ME-180 tumours following subcutaneous injection of  $5 \times 10^6$  cells are shown in Figure 4-1. All tumours ( $n = 6$ ) developed ulcerations, that necessitated the animals being killed before the tumour reached the project licence limits. Ulcerations appeared at different stages of tumour growth. In two animals, the tumour grew up to and beyond the proposed treatment volume ( $150$  to  $200 \text{ mm}^3$ ) before they formed visibly haemorrhagic regions, which subsequently led to necrosis, visible as black regions, and tumour collapse. Ulceration appeared earlier in the remainder of the cohort, negating growth beyond a volume of  $100 \text{ mm}^3$ . An example of a tumour with haemorrhagic regions and a collapsed tumour are shown in

Figure 4-2. Growth curves obtained from ME-180 tumours propagated following subcutaneous injection of either  $1 \times 10^6$  or  $2 \times 10^6$  cells ( $n=3$  per cell number) are shown in Figure 4-3. A reduction in the injected cell number did not improve the tumourigenicity of the model. While the onset of ulceration was delayed, with all tumours growing up to the treatment volume, its development could not be eliminated and resulted in tumour collapse in three out of the six tumours. Three tumours grew to the licence size limits, but only one of these grew within a practical timescale, whilst the other two tumours only began to grow at around 60 days after cell injection.

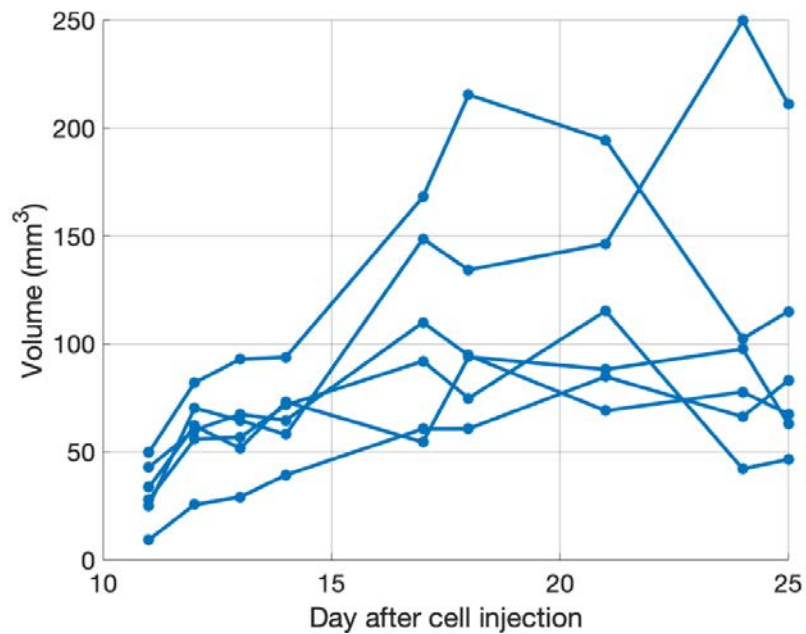


Figure 4-1: Growth curves obtained from ME-180 tumours propagated following subcutaneous injection of  $5 \times 10^6$  cells ( $n=6$ ). Each line represents the progression of a tumour, measured using callipers. Tumours initially grew and subsequently regressed in volume as ulceration developed.



Figure 4-2: Characteristic ulceration seen in ME-180 tumours. A large tumour (volume =  $215 \text{ mm}^3$ , lateral width =  $8.9 \text{ mm}$ ) is shown on the left with the beginning of a haemorrhage. On the right is a smaller tumour (volume =  $63 \text{ mm}^3$ , lateral width =  $7.2 \text{ mm}$ ) with ulceration and associated tissue collapse evident.

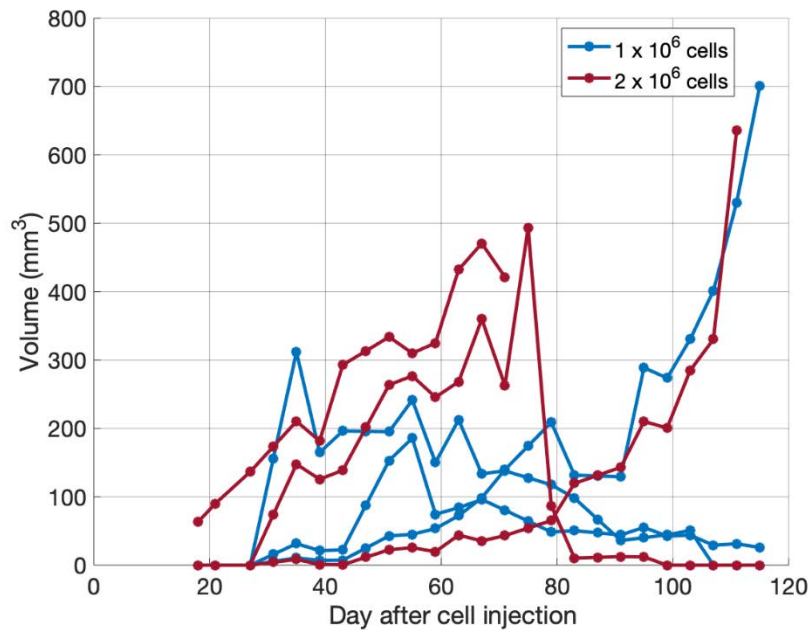


Figure 4-3: Growth curves obtained from ME-180 tumours propagated following subcutaneous injection of 1 or 2 x 10<sup>6</sup> cells (n=3 each). Each line represents the progression of a tumour, measured using callipers. Ulceration and subsequent tumour collapse were observed in 3 tumours. The other 3 tumours progressed with no ulceration, but the growth rate was slow, with two tumours beginning to grow 60 days after cell injection.

#### 4.3.1.2 C33A tumour model

Growth curves for C33A tumours propagated as a pilot study following subcutaneous injection of 5 x 10<sup>6</sup> cells are shown in Figure 4-4. Initial tumour growth from injection was slow but followed the expected exponential growth behaviour once tumours reached ~ 50 mm<sup>3</sup>, typically around 30 days after cell injection. Intertumour variation of growth within this model was minimal, with one animal having discernably slower tumour growth.

In a subsequent DCE-US imaging study, C33A tumour growth was considerably slower than that observed in the initial (pilot) study, as shown in Figure 4-4. In this cohort, only one tumour exhibited a similar growth pattern to those in the pilot study, with no tumour development in 2 of 5 mice and slower growth seen in the remaining two tumours.

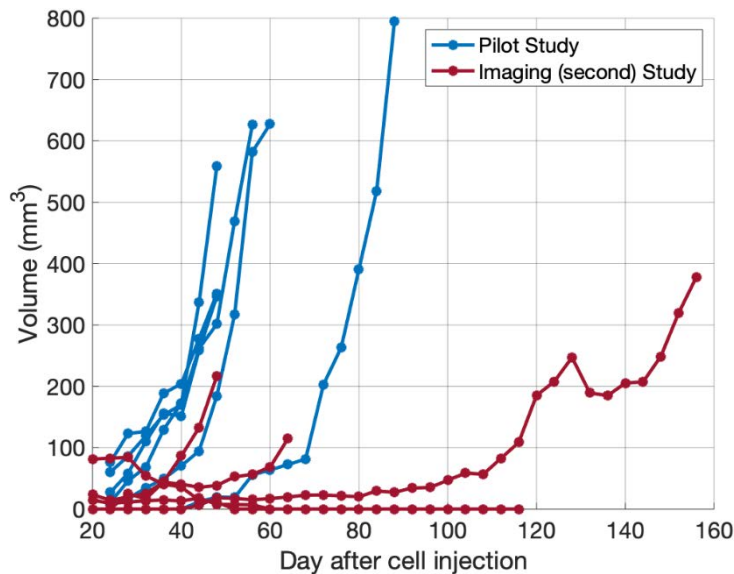


Figure 4-4 : Growth curves of C33A tumours propagated following subcutaneous injection  $5 \times 10^6$  cells from the pilot study (blue,  $n = 6$ ) and a following imaging study (red,  $n=5$ ). Each line represents the progression of a tumour, measured using callipers. Tumours in the pilot study showed exponential growth within 30 days of injection with minimal variation between animals. The imaging study had a lower tumour uptake rate and slower growth.

#### 4.3.2 Radioresponse of *in vivo* tumour models

##### 4.3.2.1 C33A tumour model

C33A tumours reached the target treatment volume of  $150 \text{ mm}^3$  within a median of 30 days, with an interquartile range (IQR) of 7 days. The number of days to reach the target treatment volume for all irradiated C33A tumours is shown in Figure 4-6 . Untreated C33A tumours typically approached the Home Office licence size limits 8 to 18 days after reaching the target treatment volume.

Growth curves of C33A tumours obtained following treatment with either 0, 10, 15, 20 or 25 Gy from radioresponse studies C3, C5, C6, and C7 are shown in Figure 4-5. Out of 7 tumours treated with 10 Gy, only 3 exhibited growth inhibition and slowed tumour following irradiation. The other 4 tumours continued to grow at a rate similar to pretreatment growth and control tumours. Using higher doses of 15 or 20 Gy in study C5 elicited a wider range of response; two tumours treated with 15 Gy and one treated with 20 Gy exhibited tumour regression within 5 days

of radiation. The remaining tumours (9 out of 12 total) demonstrated tumour growth delay of varying degrees. Subsequent regrowth was similar to pretreatment growth rates in 3 of the tumours and was considerably slower in the rest. Regrowth occurred as early as day 7 and was inhibited as late as day 20. As no tumour exhibited complete regression following irradiation with either dose, it was decided to increase the radiation dose to 25 Gy in subsequent experiments.

Eighteen C33A tumours were treated with 25 Gy in C6 and C7 studies. Two animals were culled due to weight loss before day 10, and hence tumour response could not be assessed. All treated tumours exhibited response by day 5, with tumour regression persisting up until day 13. Following this timepoint, two tumours continued to regress until complete regression (no visible tumour volume), with another regressing and stabilising at a volume lower than the pretreatment volume. All other tumours regrew after an initial growth delay, with two tumours growing at rates comparable to pretreatment growth. One animal had to be culled due to weight loss at day 35 before reaching the size limit. Radiation with 25 Gy led to skin erythema near the tumour in small proportion of animals, but all cases healed and required no intervention.

In three mice with irradiated tumours, a separate growth was observed beneath the forelimb of the mouse during the regrowth stage of the treated tumour. This was histologically confirmed as a secondary tumour mass. No effects on the animals' health were apparent.

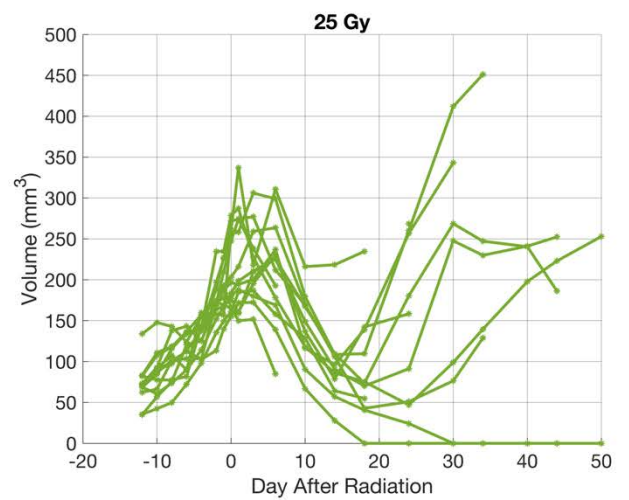
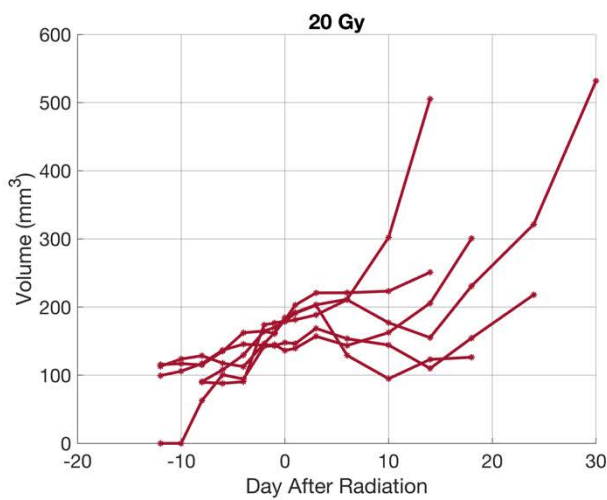
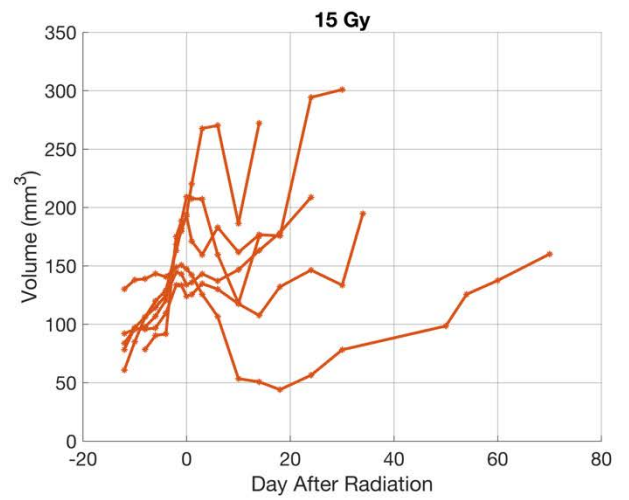
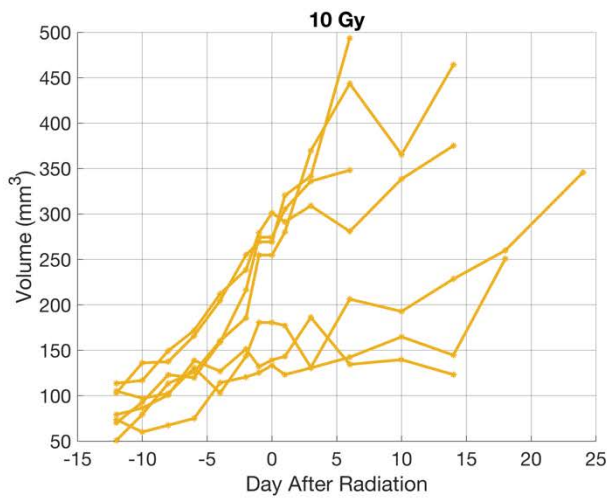
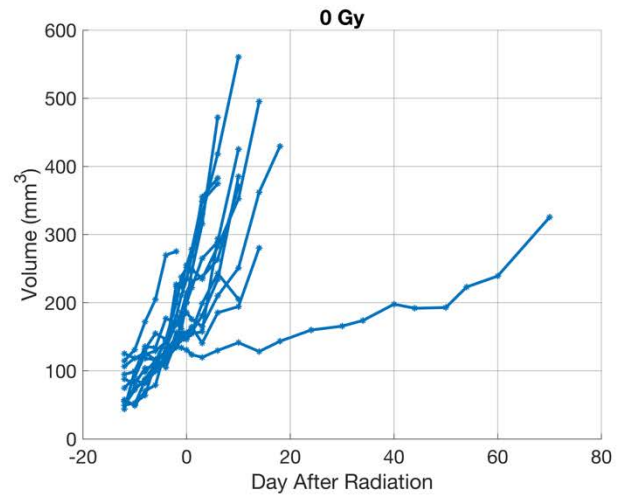
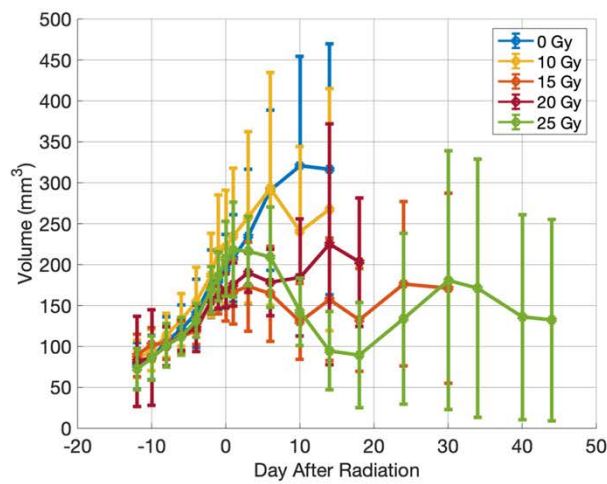
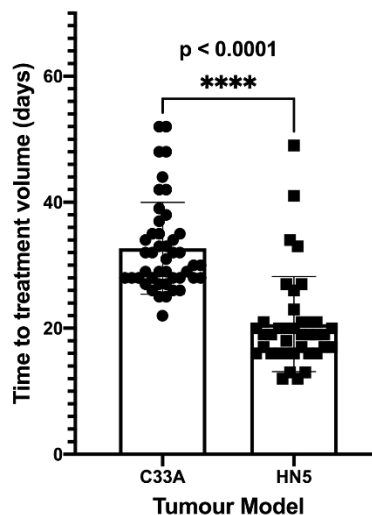


Figure 4-5: C33A tumour growth following treatment with either 0,10,15,20 or 25 Gy irradiation. The figure shows the average tumour volume  $\pm$  standard deviation for each radiation dose (top left), and the individual tumour growth curves obtained for each dose. A dose of 10 Gy caused tumour growth delay but not regression, while a dose of 15 or 20 Gy led to tumour regression and later regrowth in some tumours. A dose of 25 Gy led to variable response, with complete tumour regression in some tumours as is desired.

#### 4.3.2.2 HN5 tumour model

HN5 tumours reached the target treatment volume in a median time of 12 days and IQR of 5 days, as shown in Figure 4-6. As expected from previous local experience with this model, tumours were prone to ulceration. Ulceration manifested as necrosis at the surface of the tumour, near the skin boundary, resulting in skin rupture and tumour collapse in severe cases. Complete tumour collapse before reaching the target treatment volume occurred in 3 tumours across all studies (3 of 46). Untreated tumours grew up to the licence size limits typically between 7 to 17 days after reaching the target treatment volume as shown in Figure 4-7. Two untreated tumours had ulcerations which caused regression followed by regrowth, and one suffered severe ulceration after reaching the target treatment volume, leading to tumour collapse.



*Figure 4-6: The number of days to reach the treatment volume of 150 mm<sup>3</sup> for C33A and HN5 tumours from cell inoculation. Each datapoint represents one tumour. C33A tumours had slower growth to the treatment volume, demonstrated by significantly greater number of days compared to HN5 tumours.*

HN5 tumours treated with either 20 or 25 Gy exhibited similar radioresponsiveness and therefore the doses are discussed jointly. One of the 24 treated tumours did not respond and continued to grow at the same rate as before radiation. All other tumours exhibited response defined as growth inhibition or regression by day eight, typically arising by day 5. One animal was killed due to weight loss and ulceration at day 7, and another did not recover from

anaesthesia during imaging, and therefore their radioresponse could not be assessed. Two treated tumours had severe ulceration with tumour collapse and the animals were culled. Nine tumours with regression showed no regrowth for at least 40 days after treatment, with complete or near complete regression seen in 5 tumours, and regrowth after 70 days in the other two. The other 10 treated tumours regrew towards the Home Office licence limits. Ulcerations were observed in six of these tumours.

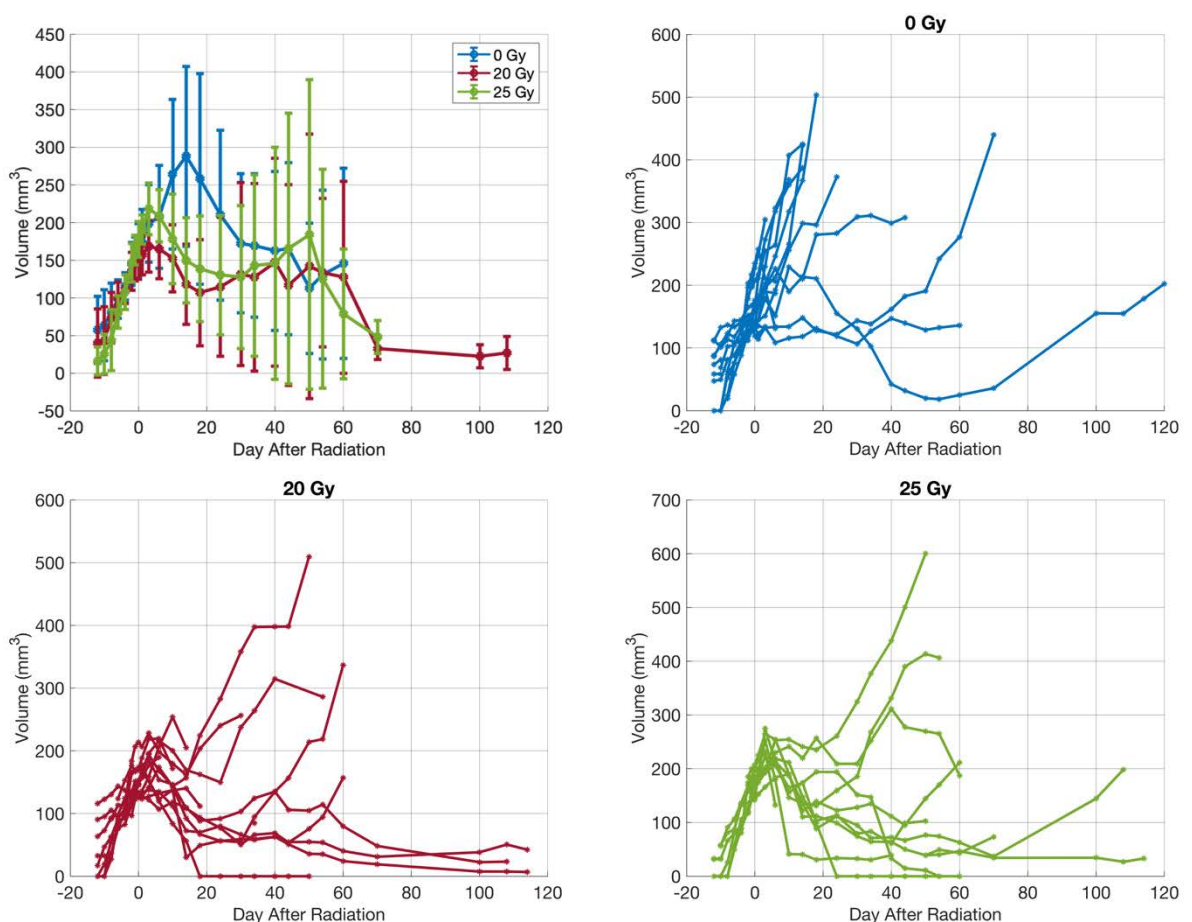


Figure 4-7 : HN5 tumour growth following treatment with either 0 ,20 or 25 Gy irradiation. The figure shows the average tumour volume  $\pm$  standard deviation for each radiation dose (top left), and the individual tumour growth curves obtained for each dose. Doses of 20 and 25 Gy caused tumour growth delay or regression in most treated tumours, with complete regression observed in some tumours, providing the desired heterogenous radioresponse.

### 4.3.3 Characterisation of tumour vasculature

#### 4.3.3.1 Whole-ROI analysis

The whole-ROI DCE-US metrics for C33A and HN5 tumours are presented in Table 4-2, and the TACs are shown in Figure 4-8. Contrast enhancement in C33A tumours typically occurred over two phases: an initial phase of quick rise following contrast arrival, and a slower increase up to peak enhancement (PE). This pattern is evident in Figure 4-9, where it can be seen that the early rise in contrast-specific image signal amplitude is driven by enhancement in the tumour periphery (Figure 4-9, image acquired at  $t = 5.0$  s), while enhancement of the tumour core is slower (Figure 4-9, images at  $t = 10.0$  s and  $16.8$  s) and results in a delayed whole-ROI wash-in time (WIT). On the other hand, HN5 tumours exhibited quicker wash-in with a near constant rate of contrast-signal increase without the deceleration as the peak enhancement was approached (Figure 1-8, right), which was associated with a more spatially homogenous enhancement in the tumour slice at times before the PE, followed by a quick wash-out. This pattern is shown in Figure 4-10.

Comparison of the whole-ROI DCE-US metrics revealed several significant differences between the two models, as shown in Figure 4-11. C33A tumours had significantly lower PE ( $p = 0.031$ ) and AUC ( $p = 0.001$ ), longer WIT ( $p < 0.001$ ) and MTT ( $p = 0.021$ ), compared to HN5 tumours. At the same time, the actual volume at treatment was higher for C33A tumours ( $p = 0.033$ )

Table 4-2 : Whole-ROI DCE-US metrics obtained from C33A (n=17) and HN5 (n=16) tumours at the target treatment volume, also presented. Data is shown as mean  $\pm$  standard deviation.

Metric	C33A	HN5
<b>Peak enhancement</b>	999 $\pm$ 192	1140 $\pm$ 172
<b>PE (a.u.)</b>		
<b>Area under the curve</b>	2.31 $\pm$ 0.27 x 10 <sup>6</sup>	2.66 $\pm$ 0.32 x 10 <sup>6</sup>
<b>AUC (a.u.)</b>	10 <sup>6</sup>	
<b>Arrival time</b>	3.32 $\pm$ 0.55	3.68 $\pm$ 1.52
<b>AT (s)</b>		
<b>Wash-in time</b>	11.1 $\pm$ 9.11	3.05 $\pm$ 1.43
<b>WIT (s)</b>		
<b>Modified transit time</b>	95.6 $\pm$ 37.7	72.7 $\pm$ 39.5
<b>MTT (s)</b>		
<b>Wash-out time</b>	265 $\pm$ 51.3	254 $\pm$ 71.8
<b>WOUT (s)</b>		
<b>Volume at radiation</b>	169 $\pm$ 32	148 $\pm$ 24
<b>(mm<sup>3</sup>)</b>		

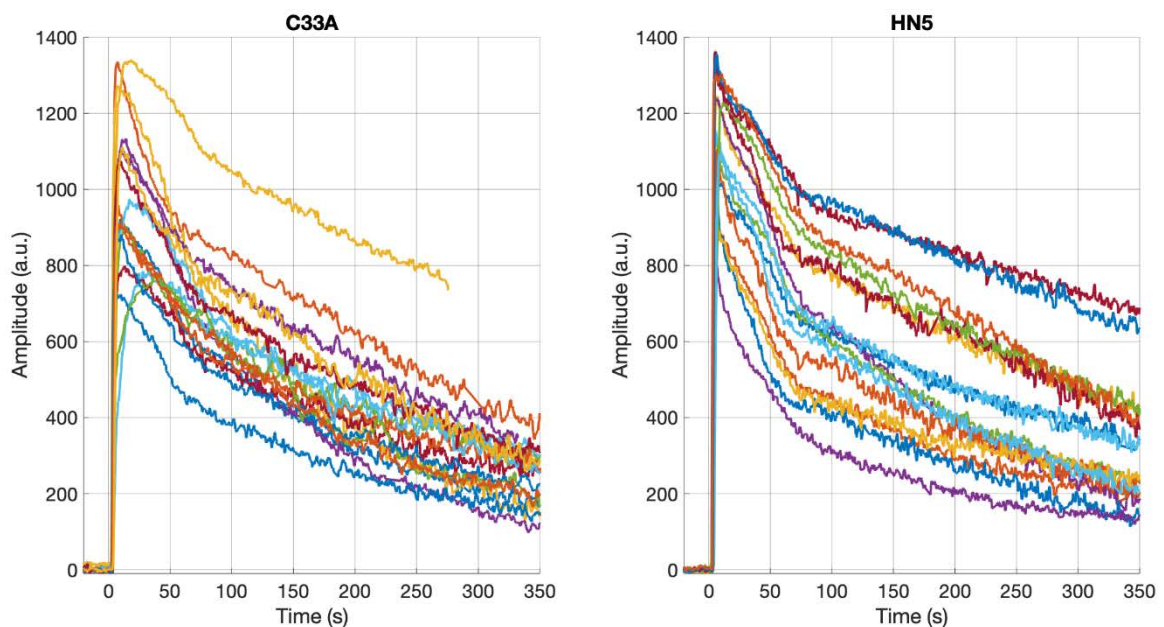


Figure 4-8 : Time amplitude curves obtained at 10 sample points per second (joined in a line for visualisation) from C33A tumours (n=17) (left) and HN5 tumours (n=16) (right) at the target treatment volume. Each line represents one animal. The signal amplitude is shown relative to baseline amplitude before injection. Time = 0 s corresponds to the time of injection.

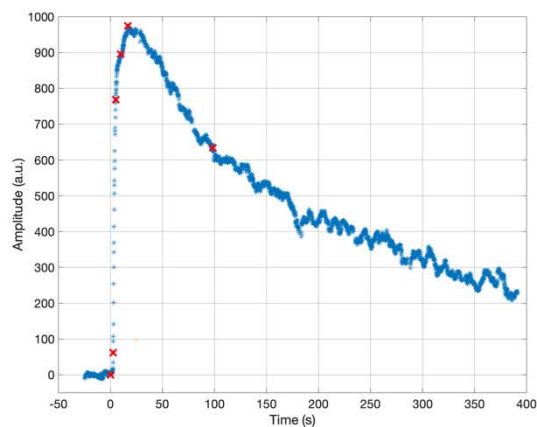
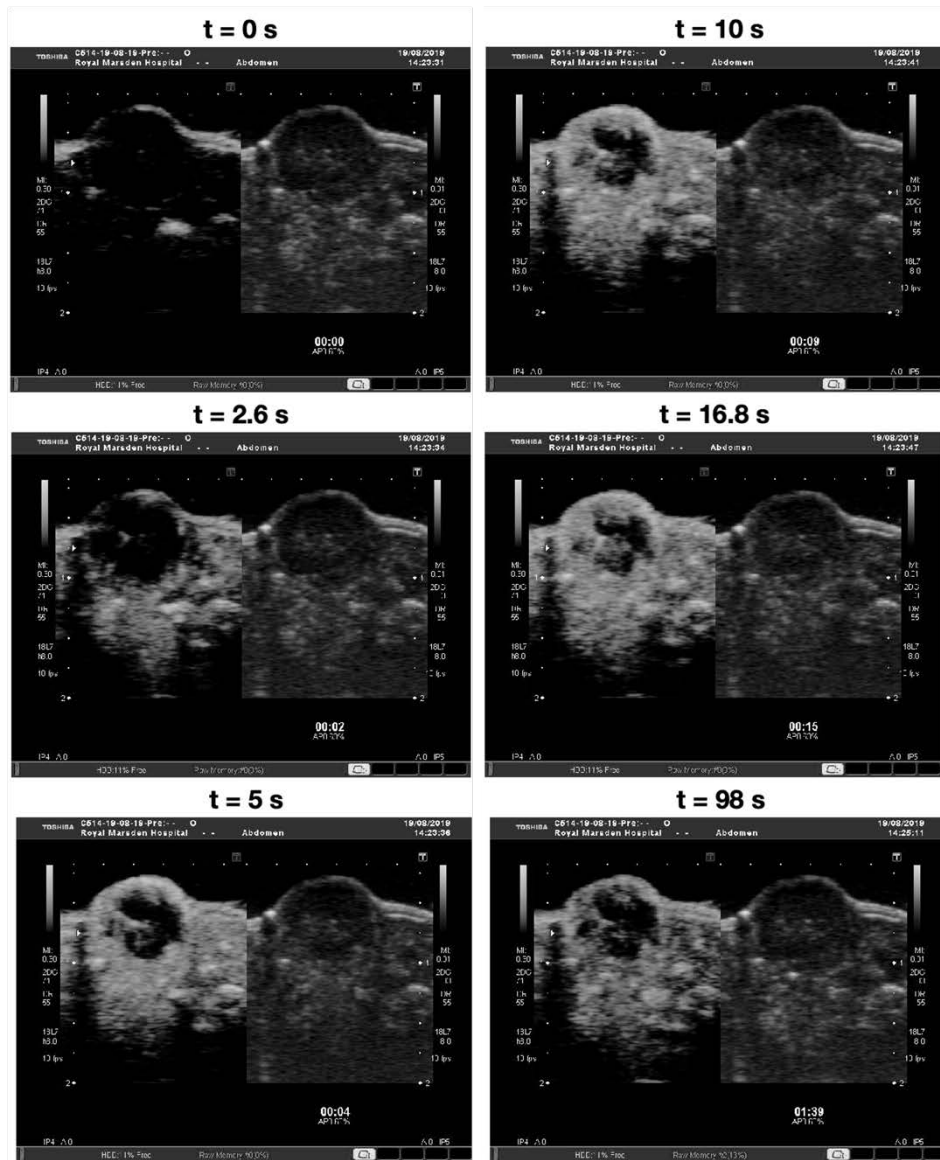


Figure 4-9: DCE-US images (contrast mode left and B-mode right) of the central slice in a C33A tumour at several time points:  $t = 0$  s corresponds to time of contrast injection,  $t = 2.6$  s is contrast arrival (AT),  $t = 5$  s corresponds to the end of the early quick wash-in,  $t = 10$  s lies within the slower wash-in phase. Peak enhancement is observed at  $t = 16.8$  s, and  $t = 98$  s is the time of modified transit time. The display video data is shown here for better visualisation. The corresponding whole-ROI time amplitude curve is shown at the bottom with the data points corresponding to the

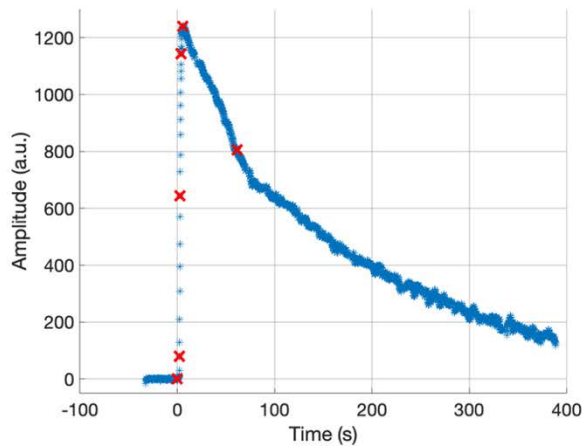
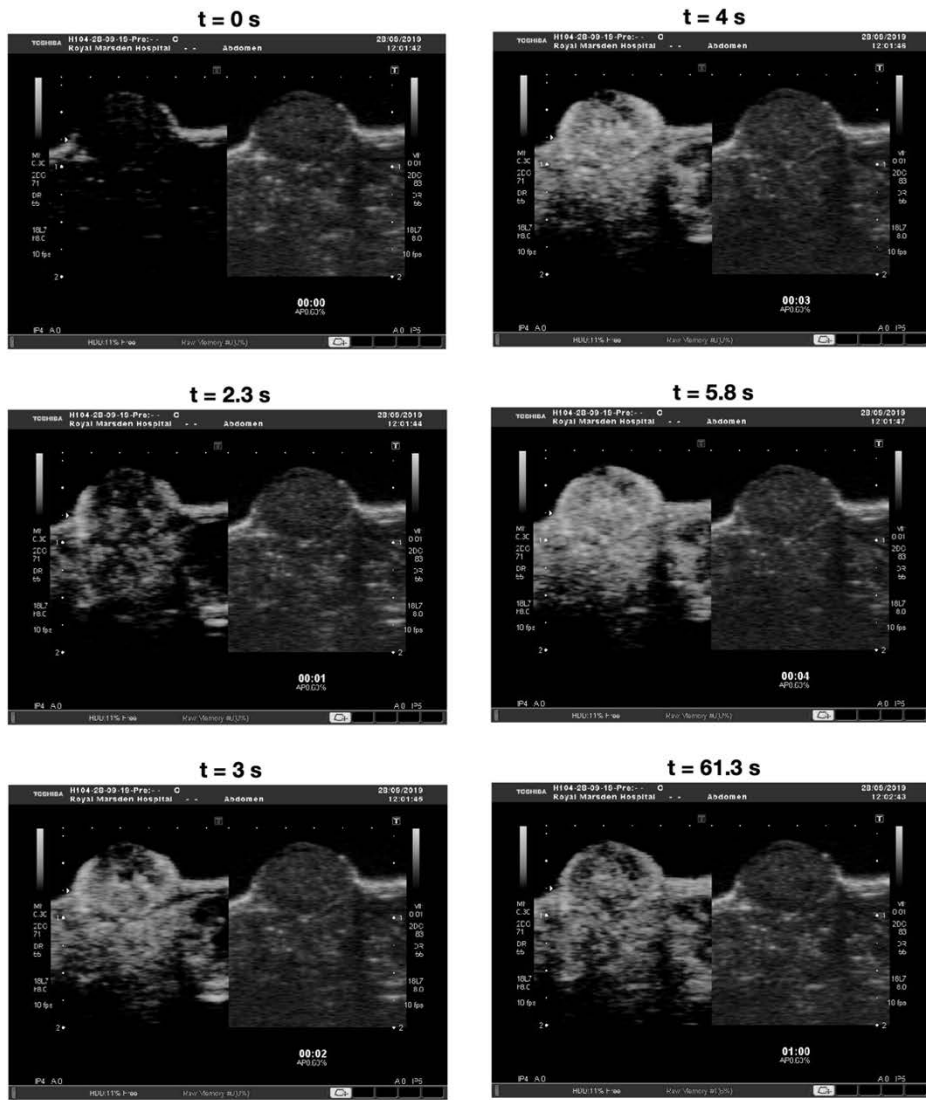


Figure 4-10 : DCE-US images (contrast mode left and B-mode right) of the central slice in an HN5 tumour at several time points:  $t = 0$  s corresponds to injection,  $t = 2.3$  s is contrast arrival (AT),  $t = 3$  s and  $t = 4$  s are during the early quick wash-in. Peak enhancement is observed at  $t = 5.8$  s, and  $t = 61.3$  s is the time of modified transit time. The display video data is shown here for better visualisation. The corresponding whole-ROI time amplitude curve is shown at the bottom with the data points corresponding to the images marked (red cross)

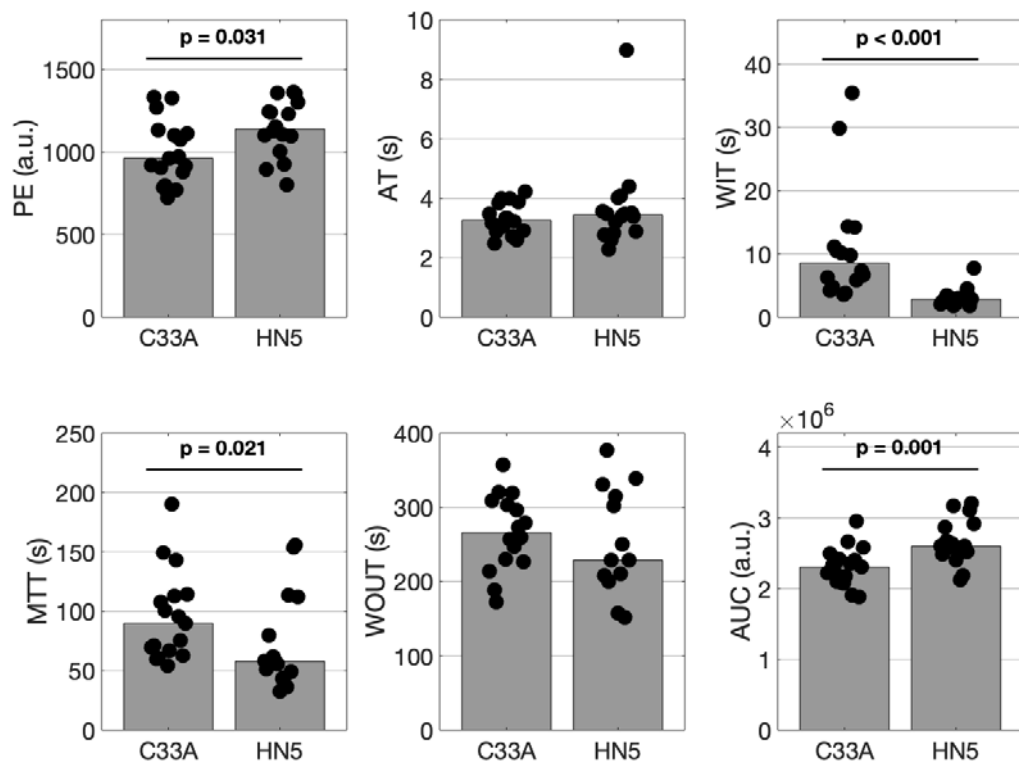


Figure 4-11: Comparison of the DCE-US metrics obtained from C33A (n=17) and HN5 (n=16) tumours using whole-ROI analysis. Each data point represents an individual tumour, whilst the top of the bar is the median value for each model.

#### 4.3.3.2 Intratumour heterogeneity

Intratumour vascular heterogeneity was examined through metric maps and metric histogram parameters. Metric maps of the C33A model exhibited a rim/core perfusion pattern with higher PE and AUC in the rim compared to the less enhanced core, as shown in Figure 4-12 and displayed slower contrast agent AT in the tumour core compared to the rim. This agreed with the enhancement pattern seen in the DCE-US images (Figure 4-9). In contrast, metric maps of HN5 tumours showed no distinct rim/core pattern and displayed more spatial homogeneity of metrics, compared to C33A.

The difference in the spatiotemporal enhancement patterns of the two tumour models was quantified by the histogram parameters, which point to higher

intratumoural vascular heterogeneity in the C33A model. The SD ( $p = 0.006$  and  $p < 0.001$ ), CoV ( $p = 0.023$  and  $p < 0.001$ ) and mFWHM ( $p = 0.009$  and  $p < 0.001$ ) of PE and AUC respectively were significantly higher for C33A tumours. Moreover, significantly higher SD ( $p = 0.002$ ), CoV ( $p < 0.001$ ) and mFWHM ( $p < 0.001$ ) of the AT suggest more heterogeneous blood velocities in C33A tumours. Significantly higher SD and mFWHM were also detected in WIT and MTT in C33A tumours, but not CoV. Since the whole-ROI metric WIT and MTT were also significantly higher in the C33A model, the higher SD and mFWHM are likely because of the larger value of the metric rather than its distribution. Histogram parameters for AUC and AT in both tumour models are shown in Figure 4-13 and Figure 4-14 . Summary data for all other DCE-US metrics can be found in the Appendix A1.

### C33A Tumour

### HN5 Tumour

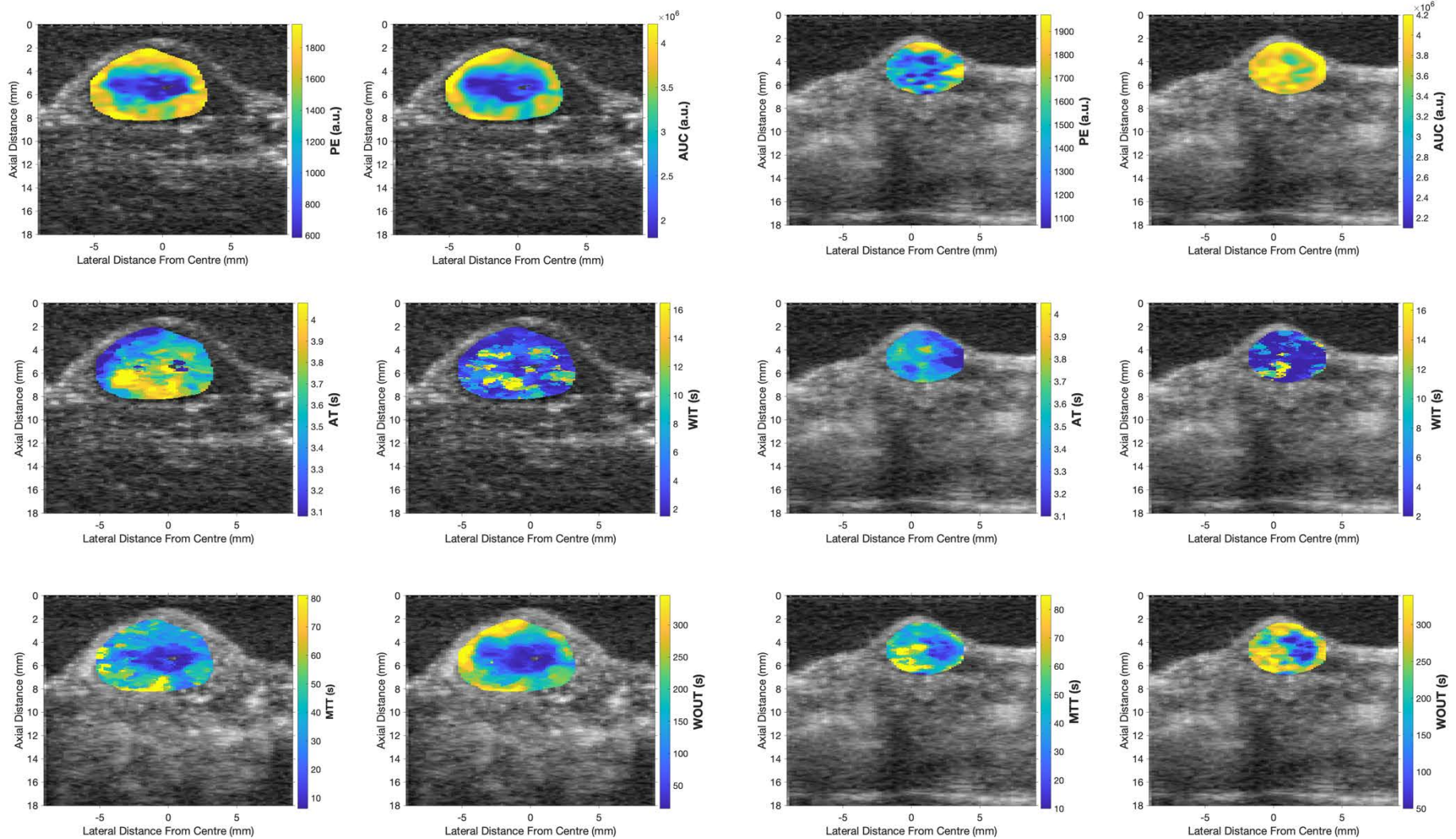


Figure 4-12 : Spatial metric maps of the central tumour slice ROI in a C33A (left) and HN5 tumour (right) overlaid on contrast mode images. The rim/core perfusion pattern of the C33A tumour is evident, especially in PE and AUC maps, while the HN5 tumour shows a more spatially homogenous perfusion pattern

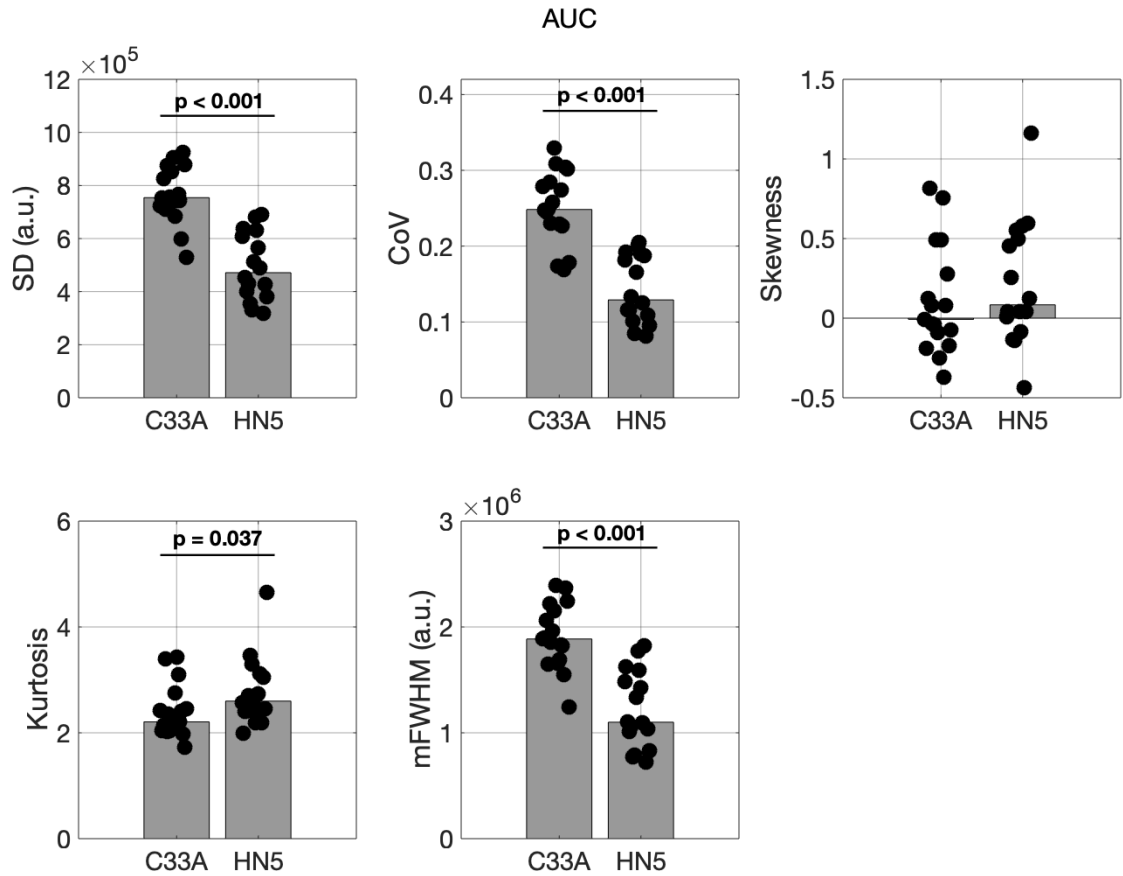


Figure 4-13: Intratumour heterogeneity of AUC for C33A and HN5 tumours. Heterogeneity is characterised using SD, CoV, skewness, kurtosis and mFWHM of pixel-wise AUC. C33A tumours had greater intratumour heterogeneity demonstrated by the significantly bigger SD, CoV, and mFWHM, and smaller kurtosis value.

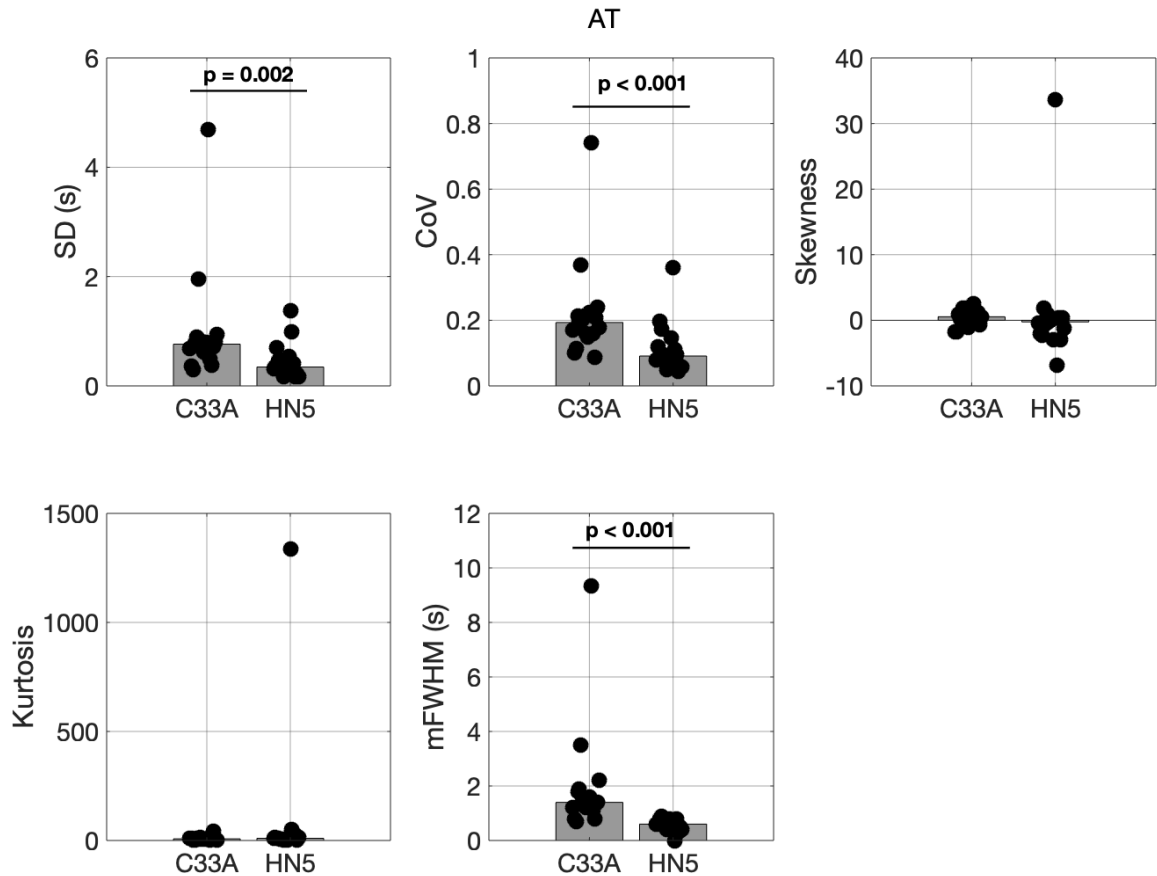


Figure 4-14 :Intratumour heterogeneity of AT for C33A and HN5 tumours. Heterogeneity is characterised using SD, CoV, skewness, kurtosis and mFWM of pixel-wise AT. C33A tumours had greater intratumour heterogeneity demonstrated by the significantly bigger SD, CoV and mFWM.

#### 4.3.3.3 Correlation of metrics

Correlations between whole-ROI DCE-US metrics for the two tumour models are shown in, Table 4-3, Table 4-4, and Figure 4-15 . PE and AUC were positively correlated in both models, with r values of 0.61 and 0.92 for C33A and HN5 tumours respectively. The 95% CIs of the two correlations overlapped, meaning the correlations cannot be considered significantly different from each other. Each tumour model revealed correlations that were not found in the other. C33A tumours showed a positive correlation of WIT and MTT ( $r = 0.68$ ), in contrast to a non-significant correlation across the HN5 tumours. The MTT was calculated from the arrival time, and thus included the wash-in time (and the time required for the contrast signal to fall to 65% of PE). A significant correlation could reflect

that the observed slow wash-in, and thus long WIT, of the C33A tumours constituted a substantial proportion of the overall MTT.

HN5 tumours showed a showed a positive correlation between amplitude-based and time-based metrics (Table 4-4). PE and AUC were correlated to MTT ( $r = 0.72$  and  $0.74$  respectively) and WOUT ( $r = 0.67$  and  $0.69$  respectively), indicating that tumours with high enhancement displayed persisting enhancement. MTT and WOUT were also positively correlated ( $r = 0.72$ ). This is expected since they are calculated from overlapping intervals of the TAC, and both are related to microbubble wash-out from the ROI.

*Table 4-3 : Correlation matrix of Whole-ROI TAC metrics in C33A tumours. The Pearson correlation coefficient is presented with 95 % CIs. Statistically significant correlations are shown in bold*

	AT	WIT	MTT	WOUT	AUC
PE	-0.08 [-0.57,0.38]	-0.39 [- <b>0.72,0.34</b> ]	0.05 [-0.70,0.61]	-0.12 [-0.548,0.43]	0.62 [0.36,0.86]
AT		0.14 [- <b>0.29,0.54</b> ]	0.4 [-0.03,0.73]	0.18 [-0.34,0.64]	0.37 [-0.22,0.64]
WIT			<b>0.68</b> [0.50,0.92]	-0.01 [-0.32,0.56]	-0.26 [-0.67,0.44]
MTT				0.28 [-0.08,0.718]	0.22 [-0.35,0.73]
WOUT					0.05 [-0.25,0.37]

Table 4-4 : Correlation of Whole - ROI TAC metrics in HN5 tumours. The Pearson correlation coefficient is presented with 95 % CI. Significant correlations are shown in bold

	AT	WIT	MTT	WOUT	AUC
PE	0.061 [-0.34,0.30]	0.12 [-0.47,0.51]	<b>0.72</b> [0.51,0.90]	<b>0.67</b> [0.30,0.87]	<b>0.92</b> [0.83,0.98]
AT		-0.12 [-0.43,0.43]	0.21 [-0.41,0.69]	-0.14 [-0.57,0.41]	-0.11 [-0.40,0.07]
WIT			0.13 [-0.54,0.67]	0.18 [-0.62,0.68]	0.02 [-0.62,0.48]
MTT				<b>0.72</b> [0.47,0.92]	<b>0.74</b> [0.30,0.94]
WOUT					<b>0.68</b> [0.37,0.92]

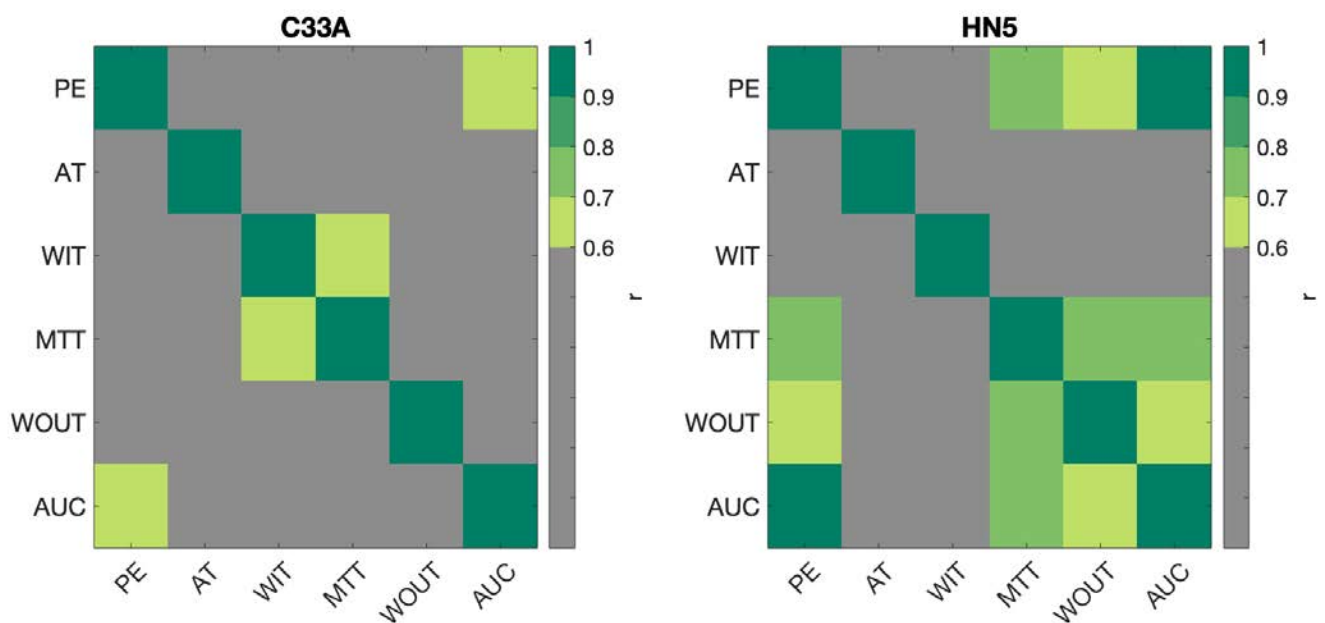


Figure 4-15: Correlation matrices between DCE -US metrics calculated from the whole-ROI TAC, showing the significant correlations in the C33A model (left) and HN5 model (right). Non-significant correlations are not shown (in grey)

The Pearson correlation coefficient of pixel-wise DCE-US metrics was calculated in each tumour, and the median correlation value was computed for each tumour model, shown in Figure 4-16. This analysis revealed similar correlations to what was seen using whole-ROI TAC metrics. All C33A tumours and HN5 tumours showed a positive correlation between PE and AUC (median  $r = 0.84$  and  $0.66$  respectively). HN5 tumours, however, exhibited a significantly lower correlation ( $p < 0.001$ ). To understand this difference, a scatter plot of PE vs AUC for a C33A tumour with strong correlation between the metrics, and a HN5 tumour with a low correlation coefficient is shown in Figure 4-17. The two tumours had a similar number of pixels, but the HN5 tumour had a narrower range of PE and AUC values. PE was also correlated to MTT (median  $r = 0.57$  and  $0.67$  for C33A and HN5 tumours, respectively) and to WOUT (median  $r = 0.77$  and  $0.78$  for C33A and HN5 tumours, respectively), in agreement with the correlation seen for whole-ROI metrics in HN5 tumours.

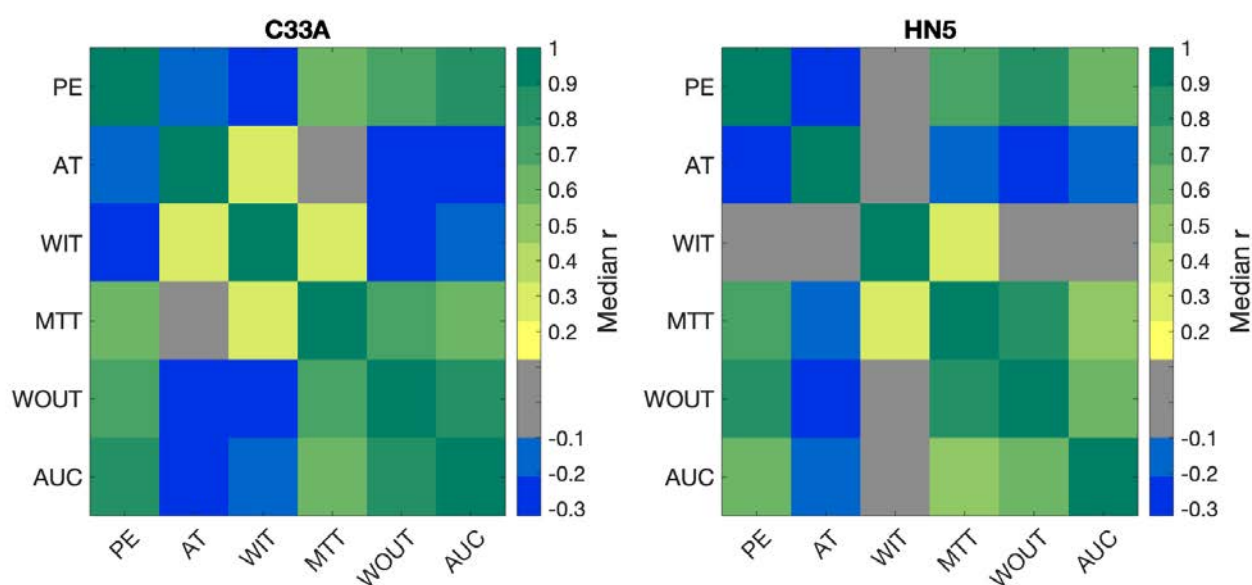


Figure 4-16: Correlation matrices of pixel-wise DCE-US metrics, shown as the median correlation coefficient obtained from all tumours in the model. Significant correlations are shown for C33A model (left) and HN5 model (right) with non-significant correlations not shown (in grey).

Likewise, AUC revealed similar correlations as seen in whole-ROI TAC metrics. AUC was correlated to MTT (median  $r = 0.66$  and  $0.54$  for C33A and HN5 models respectively) with higher correlations seen in the C33A tumour model ( $p = 0.037$ ).

The correlation of AUC with WOUT was also significantly higher ( $p < 0.0001$ ) in the C33A model (median  $r = 0.88$ ) compared to the HN5 tumours (median  $r = 0.66$ ). Both C33A and HN5 tumour models also showed a correlation between time-based metrics MTT and WOUT (median  $r = 0.67$  and  $0.80$  respectively), with lower correlation for the C33A model ( $p = 0.049$ ). MTT and WIT were weakly correlated (median  $r = 0.29$  and  $0.27$  for C33A and HN5 tumours respectively).

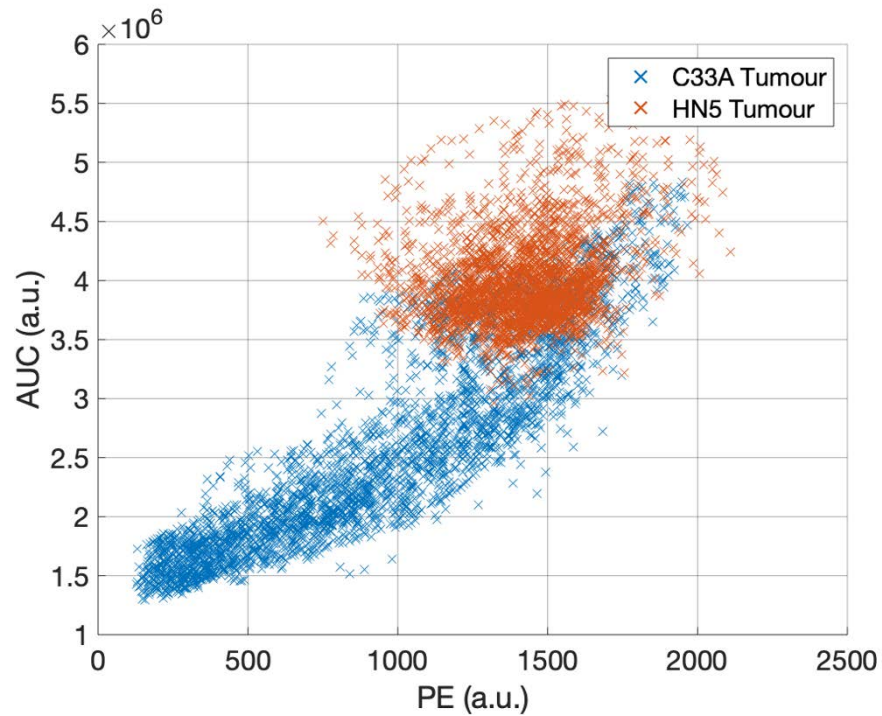


Figure 4-17: Scatter plot of pixel-wise PE and AUC values for a C33A tumour (blue) showing a strong correlation ( $r = 0.90$ ), and a HN5 tumour (orange) with a weaker correlation ( $r = 0.23$ ), suggested to be because of the smaller range of values.

Pixel-wise correlations between DCE-US metrics revealed additional correlations that were not apparent using the whole-ROI analysis. These correlations were not always present in the two tumour models nor in all tumours of a model and were typically weak correlations. C33A and HN5 tumours showed a weak negative correlation of AT with PE (median  $r = -0.17$  and  $-0.24$ ) and AUC (median  $r = -0.25$  and  $-0.20$ ). AT and WIT were correlated in C33A tumours (median  $r = 0.26$ ). AT was negatively correlated to MTT for HN5 tumours only (median  $r = -0.17$ ) and with WOUT in both models (median  $r = -0.3$  for both). WIT was weakly negatively correlated with PE, WOUT and AUC in C33A tumours (median  $r = -$

0.22, -0.22, & - 0.16 respectively). The correlations of pixel-wise TAC metrics for all tumours are shown in Appendix A2.

#### 4.3.3.4 Correspondence of DCE-US imaging with CD31 staining

DCE-US metric maps of three C33A tumours and the corresponding CD31 + hematoxylin-stained sections are shown in *Figure 4-18* for two treated and one control tumour. Examples shown here present the best morphological agreement between stained section and the tumour imaging slice (*Figure 4-18*: ultrasound contrast image). At this endpoint, DCE-US showed mainly rim enhancement in the tumours, and minimal enhancement in the tumour core ( *Figure 4-18*: AUC map). This corresponded with CD31 staining results; vessels were mainly detected in the tumour periphery, while the tumour core showed no CD31 or hematoxylin staining ( *Figure 4-18*: CD31 staining), indicating a non-viable core which corresponds to the non-enhanced centre of the tumour.

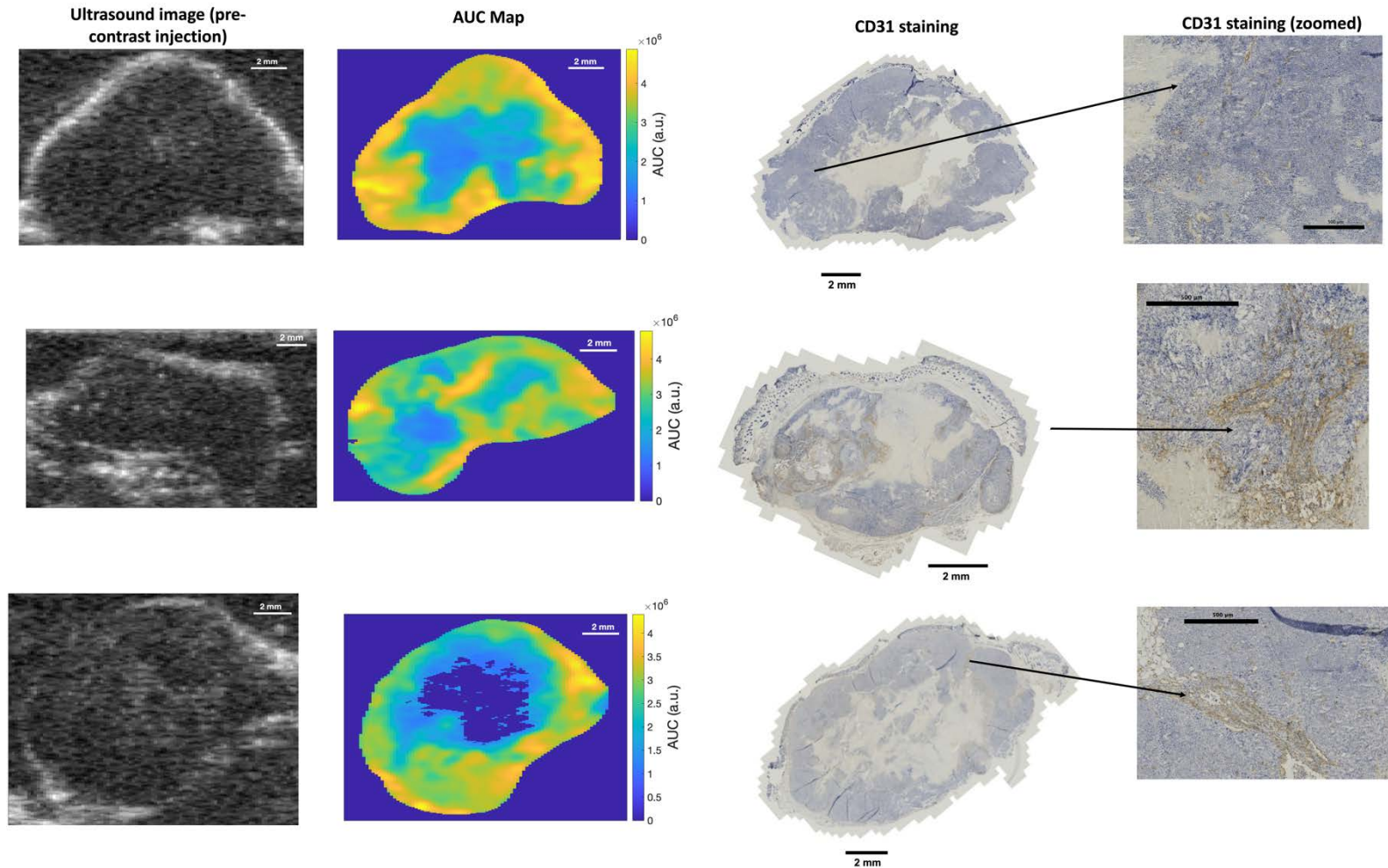


Figure 4-18 : Spatial correspondence of DCE-US imaging and CD31. Shown here are the ultrasound images (first column), AUC maps (second column), CD31(brown) + haematoxylin (blue) stained tumour slice (third column) and a zoomed region of high CD31staining (fourth column) for three C33A tumours (top: control, middle: 10 Gy, bottom 20 Gy). Regions of high AUC mainly in the tumour rim correspond to viable tumour and regions with identified vessels, while the tumour core shows poor AUC enhancement and corresponds to non-viable tumour tissue.

## 4.4 Discussion

The work described in this chapter aimed to identify and characterise *in vivo* tumour models of head and neck and cervical cancer that can be used to evaluate DCE-US imaging for radiotherapy response assessment. This involved investigation of the tumourigenicity, the radioresponse, and the vascular properties of subcutaneously grown xenograft tumour models.

Subcutaneous xenograft tumour models propagated in athymic nude mice are practical for studying DCE-US in the context of radiotherapy. Subcutaneous tumour engraftment is of mild burden on the mouse's health, and allows for accurate tumour irradiation with minimal side effects [185]. Furthermore, the location of tumours on the flank and lack of hair facilitates tumour monitoring and ultrasound imaging. Athymic nude mice also have higher radioresistance compared to other immunosuppressed strains [186], providing higher radioprotection of normal tissue. Nevertheless, the practicality of the subcutaneous xenograft tumour model limits its ability to recapitulate the in-situ tumour environment. Generally the mouse-derived tumour microenvironment differs from the original human tumour microenvironment [187]. For example, the vascular network of tumour H&N xenografts was more dense, with a shorter distance between tumour cells and the nearest vessel, compared to the original tumour [188]. Further, the ectopic model introduces differences in the tumour microenvironment compared to orthotopic implantation [170]. A comparison of orthotopic and a subcutaneous H&N model showed higher vascular density and angiogenic activity in the former [189], which can play a crucial part in the tumour's radioresponse. Despite these differences, tumour xenografts can exhibit similar perfusion levels as the original human tumours, and similar response to treatment [187].

Moreover, the immunocompromised status of the mouse strain alters the radiation-induced immune response, another important component of the tumour's radioresponse [101]. However, in this regard, athymic nude mice are

less immunosuppressed than other immunodeficient mice and still retain some elements of the immune system that can generate an immune response in the tumour. For example, athymic nude mice have active macrophages [190], which were reported to cause a pro-tumour radiation response in another nude mouse strain with similar immunodeficiency [191]. On the other hand, an innate anti-tumour immunogenic response can confound estimations of tumour growth and response to treatment. A host reaction against some melanoma xenografts in nude mice led to greater radiocurability, indicated by a lower tumor control dose 50% (TCD50) than what was expected *in vitro* [192]. This was suggested to be related to poorer tumorigenicity, rather than a radiation-induced response, supported by the greater number of cells needed to establish tumours compared to irradiated athymic mice with depleted immune function [192]. A host immune response was also indicated for in a H&N (FaDu) xenograft model based on the higher number of cells needed to propagate tumours in athymic mice compared to whole body irradiated mice [193]. This only rarely led to visible tumour regression or growth inhibition but may still confound natural tumour growth. Thus, the residual immunity of athymic nude mice is useful for mimicking radiation-induced tumour immune response but may also diminish tumorigenicity of some xenograft models.

#### 4.4.1 *Establishing in vivo tumour models of head & neck and cervical cancer*

##### 4.4.1.1 ME-180 tumour model

The first tumorigenicity study of ME-180 tumours grown in athymic nude showed 100% tumour uptake, but severe ulceration led to tumour collapse in all tumours. Using a lower number of tumour cells did reduce the ulceration rate in a subsequent study, with 50% of tumours ulcerating. Adopting this tumour model would require a large number of mice to account for ulcerating and subsequent culling of mice, which contradicts ethical animal research guidelines. Ulceration-induced tumour collapse also confounds the evaluation of radiation-induced volume changes using calliper measurements to assess radioresponse. The poor tumorigenicity observed is in agreement with the report of extensive tumour necrosis caused by an inflammatory response in ME-180 tumours grown in athymic nude mice in the thigh [194], and ties in with the previously discussed

effect of the host's residual immunity on tumour growth. Yet, ME-180 tumours have been grown *in vivo* previously at the ICR in athymic nudes by injecting  $2.5 \times 10^6$  cells with no reported tumour ulceration [195]. One possible explanation for this difference are genetic changes in the mouse colony maintained at the ICR.

The volumes of ME-180 tumours in the high and low cell number studies were calculated using different equations because of difficulty in measuring tumour depth in the low cell number study. This was, however, unlikely to affect the comparison of tumour growth between the two cohorts. The tumour volume was calculated using both equations for the high cell number study and showed similar trends in tumour growth, with tumour collapse confirmed using both equations.

#### 4.4.1.2 C33A tumour model

The initial tumourigenicity study of C33A tumours showed excellent tumour uptake (100%) and uniform growth within the study cohort. However, the tumour uptake and growth were considerably lower in the imaging study. The lower tumourigenicity may be explained by the difference in animal age at the time of cell injection, with 7 to 8 weeks old mice in the pilot study and 10 weeks old in the imaging investigation. Older athymic mice have a greater number of active T-cells [196] and NK cells [197], which can reduce the tumour uptake rate and delay the onset of growth [197]. C33A tumours from all remaining cohorts showed good agreement with the C1 pilot study. A few animals exhibited metastatic tumour growth in lymph nodes near the tumour underneath the arm, which was confirmed at the time of animal termination. This is in agreement with the reported metastasis of subcutaneous C33A tumours, where C33A tumours were found in lymph nodes close to the primary tumour in 16 out of 22 animals and coincided with enlarging of lymph nodes [198].

Based on the pilot study, the growth characteristics of C33A tumours were considered suitable and encouraged further investigation of the model's radioresponse to determine the optimal radiation dose. A range of doses from 10

to 25 Gy was examined. There was variation in intertumour response for each dose, with tumours regrowing at varying rates. However, only radiation with 25 Gy led to complete response defined as complete or near complete regression with no regrowth in 3 out of 18 tumours (17%), with the other treated tumours showing heterogeneous responses. Thus, 25 Gy was considered the optimal radiation dose. The radiation dose could have been increased to the maximum set out by the Home Office project licence limit of 30 Gy, but this was expected to increase the radiation-induced skin irritation, which was already apparent with 25 Gy, and lead to overtreatment (> 30 Gy) in a tumour subvolume.

Interestingly, the C33A cell line was reported to be the most radiosensitive cervical cancer cell line *in vitro* [179-182]. *In vitro* radiosensitivity of the C33A cell line has been characterised using clonogenic assays, which showed a surviving fraction of 0.1 at 4 Gy [180], surviving fraction at 2 Gy (SF2) values of 0.5 [181] and 0.34 [182] and radiation dose of 0.9 Gy for survival fraction of 0.37 (D37 value) [183], and using the MTS viability assay [179] which showed a viability of 30% at 4 Gy. But the tumour model displayed radioresistance *in vivo*, which may be explained by the poor perfusion of the tumour assessed using DCE-US, as discussed below.

#### 4.4.1.3 HN5 tumour model

Local experience with the *in vivo* tumour growth and radioresponse of HN5 xenografts made it a practical model to use, with no need for tumourigenicity or radioresponse studies before beginning DCE-US imaging studies. HN5 tumours had consistent tumour growth properties between studies and was similar to growth reported by others [174]. Ulceration was observed in 15 of 46 tumours. This was expected and was an improvement on the ulceration rate seen previously at the ICR of ~60% [174]. Severe ulceration cases, requiring animal termination or leading to complete tumour collapse, occurred in 7 tumours out of 46 across all studies. While not desirable, this was a tolerable rate. It is important to note that ulceration can occur in response to radiation [199], but in this model ulceration seemed as likely in irradiated and untreated tumours. Instead, the probability of ulceration seemed to be related to the depth of the tumour.

Superficial tumours growing within the skin layer were more prone to ulceration, than tumours located deeper, as tumours outgrew the skin's ability to stretch, leading to skin rupture [200, 201].

The radiosensitivity of HN5 cell line has been characterised *in vitro* and *in vivo*. Clonogenic assays showed a surviving fraction at 2 Gy (SF2) of 0.53 [174], ~ 0.6 [175] or around 0.75 [202]. *In vivo*, intramuscular HN5 tumours in male nude mice treated with 5 x 5 Gy fractions exhibited minimal tumour regression and regrew at a slower rate than control tumours at around day 20 [202]. Treatment of subcutaneous HN5 tumours with a single fraction of 20 Gy at the ICR resulted in growth inhibition within 1 week, and a 86 % survival rate 60 days after radiation [174].

HN5 tumours were irradiated with 20 and 25 Gy in this work. This was based on the radioresponse seen with 20 Gy which led to tumour regression with no regrowth in only 1 tumour out of 7 [174]. Increasing the dose to 25 Gy aimed to increase the proportion of tumours with complete response. Complete or near complete regression was achieved in 8 of 24 treated tumours (~ 33 %). No discernible difference could be made between the two radiation doses. HN5 tumours were more radioresponsive *in vivo* compared to C33A tumours, despite HN5 cells being more radioresistant *in vitro* [174, 176, 202]. Higher *in vivo* radiosensitivity of HN5 tumours than what is expected *in vitro* has been previously reported [176], and could be explained by the better perfusion of HN5 tumours prior to radiation as assessed by DCE-US.

#### 4.4.2 Characterisation of tumour vasculature

The functional vasculature in the C33A and HN5 tumour models was examined prior to radiotherapy using DCE-US imaging. The aim of the analysis was to understand the tumour vascular structure and function, and to highlight features of importance for overall radioresponse. A number of studies have shown that the presence of perfused tumour vasculature, indicative of normoxia, is correlated with a positive radiotherapy outcome [70, 71, 73], while other studies have observed that good tumour perfusion can be a result of high angiogenic

activity, and thus reflect an aggressive hypoxic tumour phenotype with poor response [74, 75]. A detailed review of this literature is presented in section 1.3.1. The discussion here only aims to describe the perfusion characteristics of the two models without discussing the individual tumour response. Single central slice whole-ROI TAC metrics were used to assess the overall perfusion of the tumour, while spatial metric maps and histogram analysis for that slice were used to characterise the intratumour vascular heterogeneity. Both analyses assume that characteristics measured for the central slice are representative of those for the whole tumour. The relationship between this 2D analysis and a full 3D approach is explored in chapter 7.

#### 4.4.2.1 C33A tumour model

DCE-US imaging revealed heterogeneous perfusion in C33A tumours, characterised by a rim/core perfusion pattern, a phenotype frequently seen in subcutaneously propagated tumour models [131, 134, 203], in which the core of the tumour is less perfused than its rim. This perfusion pattern was captured by the whole-ROI TAC and the metric maps. The slow contrast wash-in within the tumour core compared to the rim produced a biphasic wash-in pattern in the whole-ROI TAC, leading to long WIT and low PE. PE, AUC and AT pixel-wise metric maps further demonstrated the rim/core perfusion pattern, which led to large standard deviation and coefficient of variation for these metrics.

Based on the literature discussed above, the slower wash-in and lower enhancement in the tumour core compared to the rim may suggest that it contains less vessels, or smaller and collapsed vessels. Reduced blood flow within the core can also be due to an increased flow resistance because of the presence of abnormal tumour vasculature [102], coupled with highly permeable vessels creating elevated interstitial fluid pressure [63]. Furthermore, the longer wash-in time and MTT may also be a consequence of disorganised vasculature. [204] looked at the kinetics of a tracer agent in simulated vascular structures of different organisation. The transit time was defined as the time for tracer to travel from entry point to the terminal vessels of a model and is equivalent to WIT here. The transit time of a kidney model, an example of an organised vascular structure,

was quicker than that in a tumour model with a chaotic vascular network, despite models having a similar vascular volume and flow rate. The disorganised tumour model also has a wider distribution of transit times [204], an observation similar to the large intratumoural heterogeneity of AT calculated from pixel-wise TACs seen here. The wider distribution of transit times in chaotic vascular networks was reported in another study [205] and was strongly correlated to the shape parameter of disruption-replenishment TACs fitted to the lognormal model. The shape parameter describes the steepness of the TAC between the initial signal increase after disruption and the signal plateau at steady state condition; a small shape parameter is obtained from a steeper curve. More chaotic vascular networks had larger shape parameter [205]. This result indicates that the vascular organisation in a ROI can be inferred from the whole-ROI TAC curve. An analogous argument can be made for bolus TAC based on the results presented here: the whole-ROI TACs for C33A tumours showed gradual signal increase between initial contrast arrival and maximum enhancement (Figure 4-8, Figure 4-9), which is associated with disorganised flow within the tumour core, and a wide distribution of blood flow speeds demonstrated as large intratumoural heterogeneity of AT calculated from pixel-wise TACs (Figure 4-14).

Poor or disorganised perfusion within the tumour core inhibits sufficient oxygen delivery, which can lead to hypoxia. The presence of this perfusion pattern in C33A tumours, as inferred by DCE-US imaging before treatment, can explain the *in vivo* radioresistance of the model, despite the high *in vitro* radiosensitivity reported in the literature.

#### 4.4.2.2 HN5 tumour model

DCE-US imaging of HN5 tumours revealed good perfusion. HN5 tumours showed more homogeneous perfusion compared to C33A tumours. This was reflected in the whole-ROI TAC, which exhibited quicker wash-in up to PE, followed by quick wash-out (Figure 4-8). Concurrently, histogram analysis of pixel-wise metric maps revealed lower intratumoural heterogeneity. The homogeneity in amplitude metrics and time-based metrics may indicate that microvessels in HN5 tumours are of similar sizes and functionality throughout the tumour.

The good perfusion of this tumour model agrees with the low levels of hypoxia seen at similar tumour volumes using pimonidazole staining [174]. Moreover, it can explain the enhanced radioresponse of the model compared to C33A tumours, despite the HN5 cell line being described as radioresistant in *vitro* [174, 202] and its HPV negative status.

#### 4.4.2.3 Correlation of DCE-US metrics

Correlation analysis using whole-ROI and pixel-wise TAC metrics revealed several key correlations for several metrics. PE and AUC were positively correlated in both tumour models using the two analysis methods. This was presumed since both metrics can be considered surrogates of blood volume. HN5 tumours had a lower correlation coefficient between pixel-wise PE and AUC compared to C33A tumours, which might be the result of the smaller range of PE and AUC values within HN5 tumours ( Figure 4-17). A smaller range of values may make the effect of noise on metric estimation more pronounced and hide any correlation.

Interestingly, PE and AUC, showed a moderate positive correlation with time-based metrics MTT and WOUT. This was present in HN5 tumours for both analyses (Figure 4-15) while it could only be detected using pixel-wise TAC metrics in the C33A tumours (Figure 4-16). One reason for the lack of correlation in whole-ROI metrics is that the long WIT in C33A tumours means that it makes up a substantial proportion of the MTT and may obscure the effect of microbubbles wash-out from the ROI on the MTT. This explanation is supported by the fact that WIT and MTT were positively correlated in C33A tumours ( $r = 0.68$ ). The weaker correlation of pixel-wise WIT and MTT in C33A and HN5 tumours compared to the whole-ROI metrics correlation in the C33A model may be due to uncertainty in the metric calculation in the pixel-wise TAC compared to whole-ROI TAC as a result of greater noise.

The positive correlations between PE or AUC with MTT and WOUT means that regions of high contrast enhancement (high PE / AUC) have slower contrast

wash-out (long MTT / WOUT). These regions are hypothesised to be regions with large vascular volumes offering low flow resistance that would thus continue to be enhanced as the concentration of circulating microbubbles decreases. Numerical modelling of microbubble flow through different vascular volumes reported an increase in the mean transit time with increasing vascular volume, noting the longer path that the microbubbles have to travel to leave the region of interest [206]. However, this was a simplistic model and did not account for the tortuous vessels that are expected in the tumour. For future analysis, it is important to remember that changes in MTT and WOUT could be indicative of changes in the PE and AUC, and thus vascular volume.

Moreover, AT and WIT calculated from pixel-wise TACs showed a positive correlation in the C33A model. This was somewhat expected and can be understood by examining the flow of microbubbles in pixels at tumour centre. For a pixel within the tumour centre, AT is dictated by the flow of microbubbles from the injection site through the tumour to the site of the pixel, which was demonstrated to be substantially prolonged compared to the tumour periphery due to slower flow in the centre and the longer distance required to travel. WIT is the time from arrival of contrast agent in the pixel to the time of maximum of enhancement and depends on flow rate within the pixel. Since the pixel volume is small, blood flow within the pixel (affecting WIT) would not be expected to vary substantially from the input blood flow to the pixel (affecting AT), and thus the metrics would be correlated.

In contrast to the late time-based metrics, a negative correlation of AT and WIT was established with PE and AUC. While the correlation was weak, it is sensible; low blood flow rate (defined as blood volume per time) within a region will lead to long AT and WIT and small PE and AUC values. This relationship was reported in a microvessel phantom using contrast power doppler imaging [207], where the flow rate was negatively correlated to arrival time (named onset time in the study) and wash-in time, and positively correlated with AUC and PE.

#### 4.4.2.4 Biological validation of DCE-US imaging

Biological validation of DCE-US was sought by comparing endpoint imaging with CD31 and haematoxylin staining of vessels. Tumours at the endpoint were poorly vascularised as indicated by the lack of contrast enhancement and CD31 staining in most of the tumour core. The observed spatial correspondence of these regions in AUC metrics and staining sections ( Figure 4-18 ) supports the biological validation of DCE-US imaging. Moreover, tumour regions with no contrast enhancement had no viable tissue as evident by haematoxylin staining. Tumour cell death in these regions could have been caused by the lack of vascular supply, which may happen due to tumour growth or radiation damage.

## 4.5 Limitations

The poor tumour growth of the ME-180 model precluded its use, therefore only the C33A tumour model was used as a proxy for cervical cancer. C33A is HPV-negative, making it quite distinct from the typical presentation of cervical cancer clinically and other cervical cell lines such as SiHa, CaSki, and HeLa. Exploring and optimizing another model that had not been previously used at the ICR would have been time intensive and was not possible within the scope of this project. Similarly, the HN5 model suffers ulceration, and an exploration of an alternative head and neck tumour model with a lower degree of ulceration would be appropriate. However, the local expertise and knowledge about this model, particularly in the context of radiotherapy treatment, meant it was the most practical model to use.

The initial radiation of 10 Gy used in the C3 study was only carried out at a volume of 200 mm<sup>3</sup> versus 150 mm<sup>3</sup> for later radiation doses. The radioresponse with 10 Gy at the smaller treatment volume was not tested, and it is possible that the difference in tumour volume may have contributed to the minimal radiation response seen at 10 Gy. However, radiation with larger doses of 15 and 20 Gy was still not sufficient to produce the desired radioresponse and therefore it is unlikely that 10 Gy would have had a suitable response at the smaller treatment volume.

It is possible that the comparison of DCE-US metrics before treatment for HN5 and C33A tumour models was confounded by the significant difference in their treatment volumes at this point. C33A tumours had larger volumes, which may have contributed to the poorer perfusion seen in the model. The difference was probably caused by the lack of experience with measuring tumour volumes in the initial C5 study. However, the difference in mean volume between HN5 and C33A cohorts of 20 mm<sup>3</sup> was small, and is unlikely to significantly affect the vascular properties of the tumours as it has been reported that the ratio of vascular volume to viable tumour tissue within this volume range is almost constant [169]. More importantly, the difference in DCE-US metrics between the models was seen in later imaging studies (Chapter 7) where the mean volume of the C33A and HN5 cohorts were not significantly different. It should be noted that the difference in volume at radiation was also unlikely to be the reason for the difference in radioresponse as C33A tumours displayed a greater level of radioresistance in all studies conducted as part of this thesis.

The characterisation of tumour vasculature was performed using 2D DCE-US, which was the only DCE-US imaging technique available at the time. 2D imaging may not be reflective of the vascularisation of the whole tumour volume as it only sampled a central slice of the tumour. Further work using 3D DCE-US will assess vascular properties of the whole tumour volume.

DCE-US analysis of the vascular properties discussed here requires further histopathological validation prior to treatment. As the purpose of the experiments carried out during the thesis was to assess radioresponse based on eventual tumour growth, histopathological analysis carried out after tumours reached the project licence limits was prioritised. Validation of DCE-US was limited by the poor vascularisation status of the tumours at this timepoint, which did not allow quantification of the vascular density or comparison of metric maps with vascular morphology. Further, histopathology could not be successfully carried out for HN5 tumours in this study, which tended to collapse and release fluid when attempts were made to section them.

## 4.6 Conclusion

The work described here characterised two models of cervical and head and neck cancer that can be employed in subsequent studies. The growth and radiation response patterns were characterised for C33A and HN5 tumours. HN5 tumours showed better radioresponse. The perfusion status of the models was assessed using DCE-US imaging prior to treatment and revealed greater perfusion in the HN5 tumours with smaller intratumour heterogeneity. Correlations between DCE-US metrics were identified, the most important of which is the correlation of PE and AUC with MTT and WOUT. Finally, the spatial correspondence of AUC metric maps and the CD31 stained tumour sections confirms that DCE-US is measuring the underlying tumour vasculature.

# 5 CHAPTER Preliminary investigation of DCE-US for assessment of response to radiotherapy

## 5.1 Introduction

Radiation – induced vascular changes occur within a shortly period after treatment as reviewed in section 1.3.2. Several methods and imaging modalities have been used to measure these changes, but the ability of detecting such changes using DCE-US remains to be explored. In addition, the correlation of vascular changes and radioresponse needs confirmation. The two characterised models of head and neck (H&N) and cervical cancer can be used to examine DCE-US imaging for the assessment of radiotherapy response. The established heterogeneous intertumour radioresponse allows comparison of DCE-US measured vascular changes with radioresponse. Further, validation of DCE-US as an imaging biomarker of response requires assessment of its precision. Thus, this chapter presents a preliminary investigation of DCE-US imaging for the assessment of response to radiotherapy.

## 5.2 Study Aim & Design

The aims of the work described in this chapter were to investigate (1) the potential for pretreatment DCE-metrics to predict tumour response to radiation, (2) post-treatment changes in DCE-metrics that would allow early (within 48 hours of treatment) prediction of response and how this relates to changes in tumour size (the current clinical measure of response), and (3) the repeatability of the measurement of 2D DCE-US metrics. Specifically, the analysis examined differences in the pretreatment DCE-US metrics between groups of tumours that had partial or complete response to treatment and differences in the changes in DCE-US metrics between groups measured in a region of interest covering the whole tumour (whole-ROI), and in spatially and functionally defined subregions of the tumour before and after treatment (sub-ROIs). Changes in the distribution

of pixel-based metrics (histogram analysis) were also investigated. The repeatability of these metrics was assessed at the final imaging timepoint. All these experiments were done early during the period of the PhD before the 3D DCE-US methods had been developed.

### 5.3 Methods

This investigation into the DCE-US metrics and their relationship to treatment response was carried out using both the C33A and HN5 tumour models using data from studies C5 and H1 (see Table 4-1). Irradiation was performed at a tumour volume of  $150 \text{ mm}^3$  and 2D DCE-US imaging was carried out shortly before irradiation and 48 hours afterwards. Pretreatment DCE-US was carried out 24 hours before irradiation for C33A tumours, and around 3 to 6 hours before irradiation for HN5 tumours. The change in the pretreatment imaging timepoint was made to reduce the likelihood of tumour growth between imaging and radiation, as discussed in 3.2.1

Tumour response was evaluated based on tumour volume following radiation. Repeatability of 2D DCE-US was assessed by carrying out two DCE-US image acquisitions at the study endpoint. The study timeline is shown in Figure 5-1. The evaluation of repeatability presented here also used data from studies C2, C3 and C4 (Table 4-1), for which repeat imaging was also performed at the study endpoint.

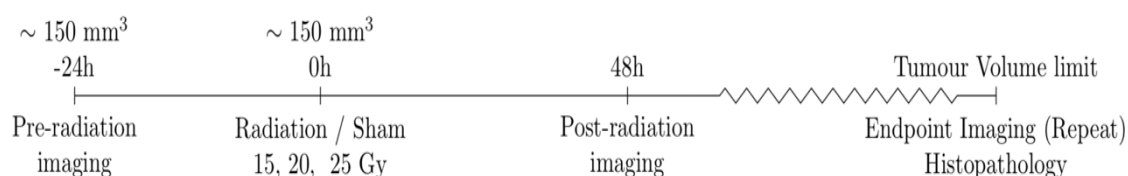


*Figure 5-1 : Timeline of studies. For HN5 tumours the, pre-radiation timepoint was done on the same day once animals recovered from the anaesthetics used for DCE-US imaging.*

### 5.3.1 *Experimental setup*

#### 5.3.1.1 2D DCE-US imaging

Animals were anaesthetised using Hypnorm™/Hypnovel™. Cannulation and imaging setup was as described in section 3.2.2 and 2D DCE-US imaging was carried out using the Aplio scanner as described in section 3.2.4.

#### 5.3.1.2 Repeat 2D DCE-US

2D DCE-US image acquisitions were performed to calculate the variation of DCE-US at endpoint imaging. Only two acquisitions were possible based on the allowed volume for intravenous injection within 24 hours. Both acquisitions were carried out as for the other two timepoints (pre-treatment and 48 hours post treatment). Following the first acquisition, saline was injected to flush remaining microbubbles in the cannula. In addition, the tumour was exposed to ultrasound with a high MI of 1.24 to destroy residual microbubbles. The transducer was translated manually to cover the whole tumour volume. The two contrast injections were separated by 15 to 20 minutes and used microbubbles from the same vial.

#### 5.3.1.3 Irradiation of mouse xenograft tumours

Single fraction radiation was delivered as detailed in 3.4. C33A tumours (C5) were irradiated with 15 or 20 Gy, while HN5 tumours (H1) received a dose of 20 or 25 Gy.

### 5.3.2 *DCE-US analysis for assessment of radioresponse*

DCE-US images from the first two imaging timepoints were analysed using whole-ROI analysis (section 3.3.1.1), metric maps (section 3.3.1.2) subregion analysis (section 3.3.1.3), and histogram characterisation (section 3.3.1.4). The change in metrics between the timepoints was calculated as shown in equation 3–1. Differences in DCE-US metrics pre–radiation and the change in the metrics were compared between response groups using the Mann–Whitney U test.

Significance of the change in metrics between the timepoints for each tumour were assessed using the Wilcoxon signed rank test.

### 5.3.3 Repeatability of DCE-US imaging analysis

#### 5.3.3.1 Variation of whole-ROI metrics

The variation in whole-ROI metrics between repeat injections was calculated as:

$$Variation_M(\%) = \frac{M_2 - M_1}{0.5 \times (M_2 + M_1)} \times 100 \% \quad \text{Equation 5 - 1}$$

where  $M_2$  and  $M_1$  represent the metrics calculated from the second and first injection, respectively. The absolute variation was also calculated to evaluate the magnitude of variation without regard to the sign of the variation.

#### 5.3.3.2 Variation of whole-ROI metrics due to noise

TACs are affected by noise inherent in ultrasound images and introduced through tissue motion, which can contribute to the metric variation. Fitted mathematical models can remove the noise and are hypothesised to improve repeatability of metrics. To assess this, the whole-ROI TACs generated from the raw data were fitted to two mathematical models of perfusion, the Gamma and the Arditi models which were previously developed by the ultrasound team [155]. The relative quality of the fit was assessed using the adjusted coefficient of determination ( $R^2$ ) value and the root mean square error (RMSE). The model with the superior fitting was used to calculate whole-ROI DCE-US metrics for the two injections and the variation was calculated as for the raw data TACs.

There was also an opportunity to reduce TAC noise using the Savitzky-Golay filter which removes TAC noise by fitting segments of the TAC to a polynomial model [208]. This analysis was carried out in a subset of tumours ( $n = 10$ ) by Zhiting Xu, a visiting Master's student, using dedicated software [208] with a graphical interface shown in Figure 5-2. The software also performed motion

compensation on the data, using the skin boundary in the B-mode images. Due to software compatibility issues, only the displayed video data could be used, hence the Savitzky-Golay filter was applied to video data TAC. The metrics and the variation from the filtered and experimental video TACs were compared. The metrics calculated by the software were PE, AUC, AT, WIT, and MTT.



Figure 5-2: Screenshot of the software used for Savitzky-Golay filtering. The tumour ROI is outlined in green on the contrast image (left image). The white ROI in the B-mode image (right image) was used to perform motion estimation. The experimental and filtered (the line with smoother appearance) TACs are shown in the panel on the right side, with the parameters calculated below.

### 5.3.3.3 Variation of whole-ROI metrics TACs due to ROI delineation

The variation in whole-ROI metrics due to ROI drawing was calculated by comparing metrics from two ROI delineations for one acquisition done in a subset of tumours (n = 7). Next, the variation in whole-ROI metrics between two repeat acquisitions, analysed using the same or different ROIs, was compared.

### 5.3.3.4 Variation of histogram analysis

Histograms were generated from metric maps of each acquisition as detailed in section 3.3.1.4 and the histogram shape parameters were estimated. The variation in histogram parameters was calculated using equation 5-1, except for

skewness. This is because the skewness can change sign, making the numerator large and the denominator small and leading to artificially high variation. The variation in skewness was calculated as the difference in skewness between the two injections divided by the absolute value of skewness of the first injection.

#### 5.3.3.5 Spatial repeatability of DCE-US

The repeatability of the spatial pattern of perfusion was evaluated using metric maps. To ensure spatial correspondence, metric maps obtained from the two acquisitions were spatially registered. Spatial registration was determined using the normalised cross correlation of raw data contrast images before contrast injection and was then applied to the metric maps. The similarity of metrics maps was assessed using pixels that were encompassed in both ROIs and were perfused in both acquisitions (as detailed in section 3.3.1.2). The similarity of the metric maps was assessed using the cross-correlation coefficient.

## 5.4 Results

### 5.4.1 *Characterisation of radiation response*

#### 5.4.1.1 HN5 tumour model

Sixteen animals of 18 animals that were inoculated from the H1 study developed tumours that grew to the desired treatment volume of 150 mm<sup>3</sup>. Ten animals were treated and 6 were controls and the tumour growth curves are shown in Figure 5-3. Based on tumour growth post treatment, 4 animals were classified as complete responders. These were tumours that regressed and remained at a tumour volume below the treatment volume for at least 80 days after radiation and showed no signs of regrowth at the time of animal sacrifice. Three animals, 2 control tumours and 1 treated, had be culled within 14 days of radiation due to weight loss or other distress signs. The treated tumour was classed as a partial responder as it did not show the degree of volume regression seen in complete responders. Two more mice, with 1 treated and 1 control tumour, were culled before license size limits, as the tumours were impeding the animal's movement. The treated tumour was also classed as partial responder. Three tumours

regressed with the onset of ulceration, and two were culled due to the severity of the ulceration. As this regression occurred later than volume regression seen in complete responders, it was not considered indicative of response and the tumours were classed as partial responders. A summary of the response groups is provided in Table 5-1. Table 5-1: Numbers of HN5 tumours that showed complete or partial response at each radiation dose.

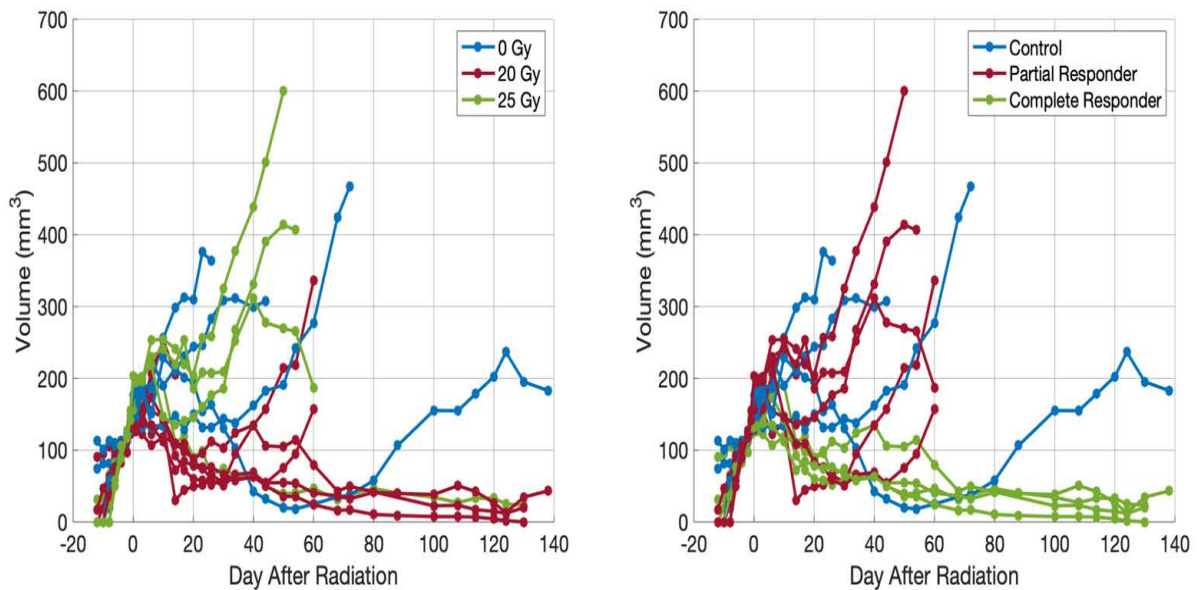


Figure 5-3: HN5 tumour growth measured using callipers. Radiation treatment was carried out at day = 0 when tumours were approximately 150 mm<sup>3</sup>. Individual tumours are grouped according to radiation dose (left) or response (right). Complete responders are tumours that showed no regrowth for at least 80 days after radiation

Table 5-1: Numbers of HN5 tumours that showed complete or partial response at each radiation dose.

Radiation Dose (Gy)	Complete response	Partial response
20	3	2
25	1	3

#### 5.4.1.2 C33A tumour model

All mice in the C5 study developed tumours that grew to the treatment target volume. Twelve tumours were irradiated and 6 served as controls, with the growth curves shown in Figure 5-4. Tumours tended to grow quicker in one

dimension, which did not allow substantial volume increase before animals had to be culled due to Home Office licence size limits. While none of the tumours showed complete response as defined above, responses groups were defined based on the tumour model's behaviour. Complete response was defined as a sustained slowed tumour growth or regression for 20 days after irradiation. All other treated tumours were defined as partial responders. The response groups are summarised in Table 5-2.

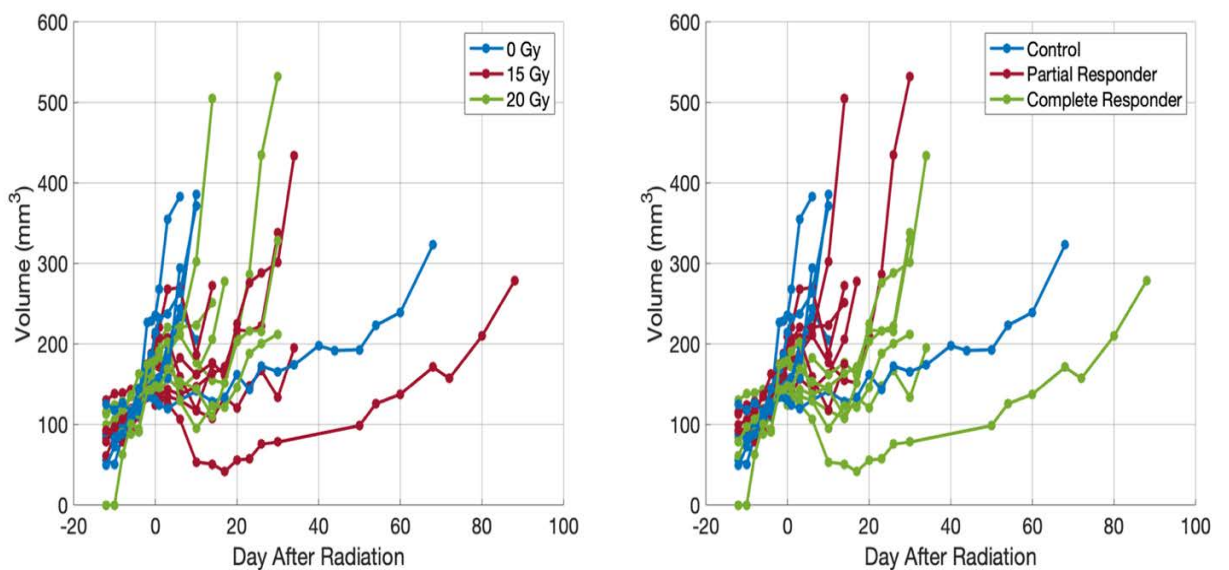


Figure 5-4: C33A tumour growth measured using callipers. Radiation treatment was carried out at day = 0 when tumours were approximately 150 mm<sup>3</sup>. Individual tumours are grouped according to radiation dose (left) and response (right).

Table 5-2: Numbers of C33A tumours that showed a complete or partial response at each radiation dose.

Radiation Dose (Gy)	Full response	Partial response
15	5	1
20	2	4

#### 5.4.2 Association of radioresponse with pretreatment DCE-US metrics

For the HN5 cancer model, complete responders had a shorter wash-in time (WIT) than partial and control tumours before treatment. This was true for whole–

ROI WIT, percentile, and subregion analysis as shown in *Figure 5-5*. Whole-ROI WIT was lower in the complete response group (median WIT of 2.2 s) than in the partial response (median WIT of 2.9 s,  $p = 0.016$ ) and control groups (median WIT of 3.0 s,  $p = 0.010$ ). Sub-ROIs of high WIT, defined through subregion analysis, also had significantly shorter WIT in complete responders compared to partial responders or control tumours for the 10% ( $p = 0.048, 0.019$  respectively), 20% ( $p = 0.019, 0.010$ ), 40% ( $p = 0.038, 0.010$ ) and 50% sub-ROIs ( $p = 0.019, 0.010$ ). Moreover, percentile analysis of the WIT also showed significant differences, with smaller WIT for complete responders compared to partial responders or control tumours for the 15th and 20th percentiles ( $p = 0.010$  for both percentiles). When compared to control tumours, this was also true for the 5th and 10th percentiles ( $p = 0.010$ ).

There was no significant difference in the whole-ROI wash-in time for all treated tumours (partial and complete responders combined) compared with control tumours ( $p = 0.14$ ) before treatment, confirming that there was no selection bias between treated and control tumours. However, a significant difference was identified when 5th ( $p = 0.026$ ), 10th ( $p = 0.026$ ) and 15th ( $p = 0.036$ ) percentiles were analysed. No other pretreatment DCE-US metric was significantly different between response groups and there were no differences in the histogram parameters.

For the C33A cancer model, there were no pretreatment differences in any of DCE-US metrics between response groups, obtained using whole-ROI, subregion or percentile analysis. Nor was there any difference in the histogram parameters of DCE-US metrics.

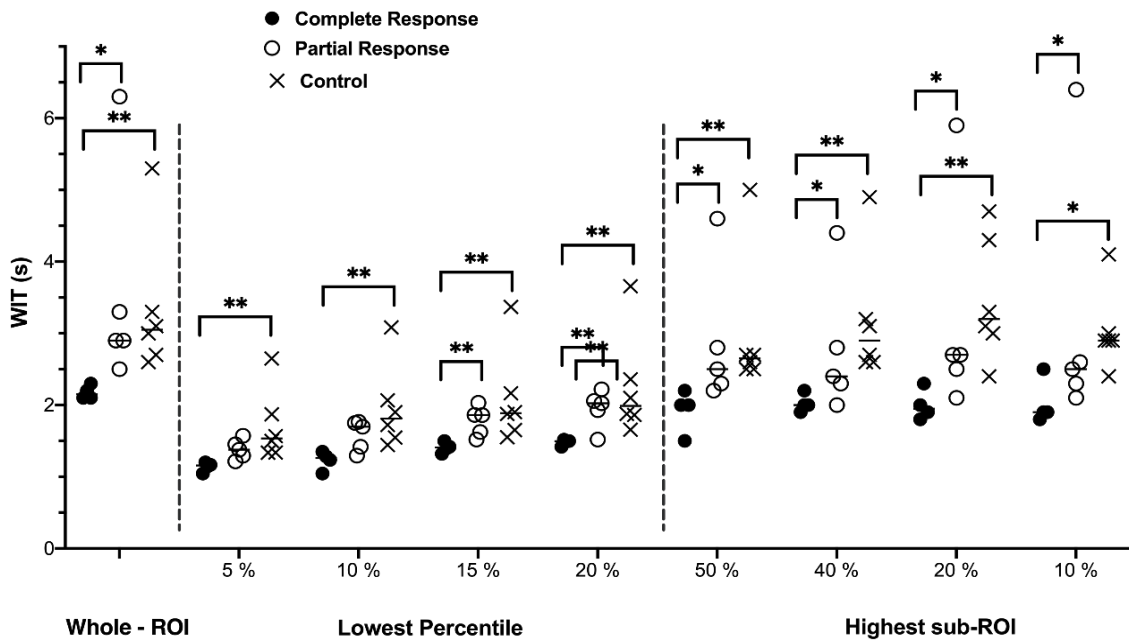


Figure 5-5: WIT before treatment for the HN5 cancer model showing significantly lower wash-in time in complete responders compared to partial responders and controls using whole ROI WIT (left), WIT of the 5<sup>th</sup> - to 20<sup>th</sup> percentiles (middle) and the WIT from subregion analysis (right). There were significant differences between complete responders and control tumours for all percentiles investigated.

### 5.4.3 Association of radioresponse with changes in DCE-US metrics

#### 5.4.3.1 HN5 tumour model

The change in whole-ROI DCE-US metrics from pre- to post-treatment for HN5 tumours is shown in Figure 5-6. Two tumours were excluded from the WOUT analysis as the imaging duration was not long enough to capture amplitude decrease to 30 %, while contrast wash – in was not saved in WIT in two tumours, and the WIT and AT were excluded. Only the change in AUC was significantly different between the response groups and control tumours. Partial responders had a significantly smaller decrease in AUC compared to complete responders ( $p = 0.038$ ) and control tumours ( $p = 0.002$ ). Both complete responders and controls had a decrease in AUC with no significant difference between the two groups, whereas partial responders exhibited no significant change relative to the pretreatment value.

It was not possible to test the changes in a metric from pre- to post-treatment for the complete response group separately due to its small sample number (n = 4). No significant changes were identified in the partial response group. However, when the partial and complete responder groups were analysed together, a significant decrease in PE (p = 0.006), MTT and WOUT (p = 0.037), and AUC (p = 0.010) following radiation was detected. Tumours in the control group also showed a significant decrease in PE and AUC (p = 0.031 for both).

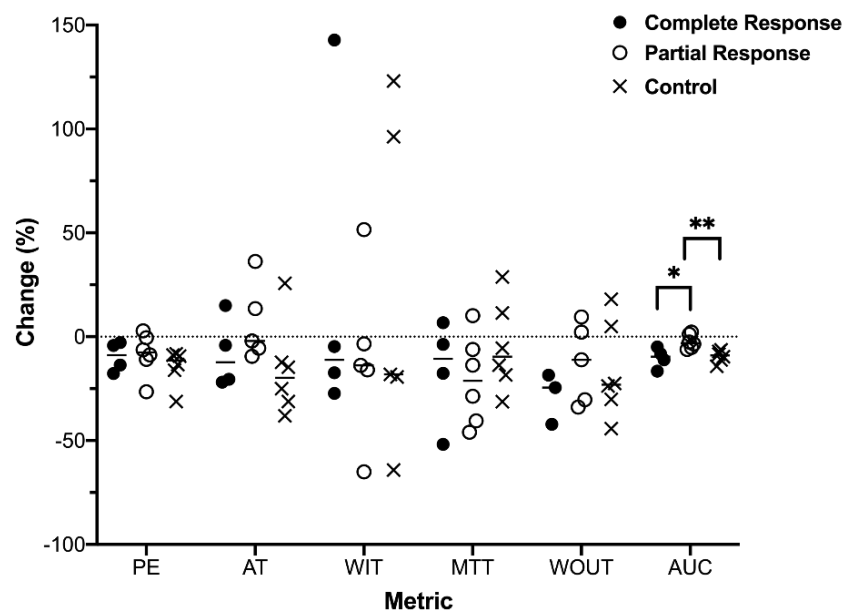
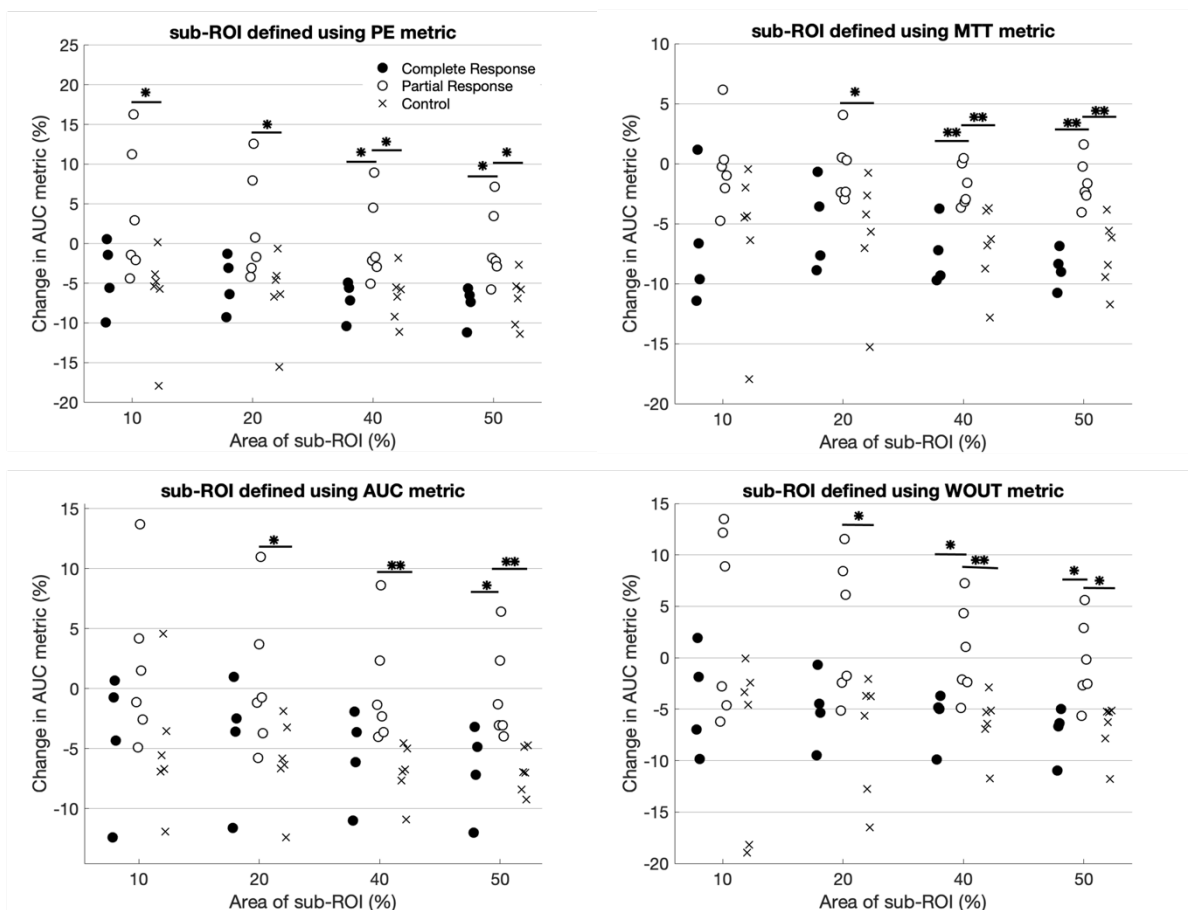


Figure 5-6: Percent change in DCE-US metrics between pre-treatment and 48 hours post radiation in the HN5 tumour model using whole-ROI analysis. Significant differences in the change in AUC were observed between complete and partial responders, and partial responders and control tumours.

Metrics obtained from functional sub-ROIs defined using PE, AUC, MTT and WOUT reflected the same changes in AUC seen in the whole-ROI analysis. Referring to Figure 5-7, sub-ROIs comprised of pixels with the highest WOUT at 40% and 50% thresholds showed a significantly bigger decrease in AUC of complete responders compared to partial responders (p = 0.038 and p = 0.019, respectively). Control and partial responders showed significant differences for the 20% (p = 0.026), 40% (p = 0.0043) and 50% sub-ROIs (p = 0.015). MTT defined sub-ROIs at all levels showed significant differences between tumour groups. Complete and partial responders had significant differences at 40% and 50% sub-ROIs (p = 0.010 for both) while control tumours and partial responders

were significantly different for the 20% ( $p = 0.026$ ), 40% ( $p = 0.002$ ) and 50% sub-ROIs ( $p = 0.004$ ). The 40% and 50% sub-ROIs defined from PE also revealed a significant difference between complete responders and partial responders ( $p = 0.019$  for both), while a significant difference between partial and control tumours was detected for all PE sub-ROIs ( $p = 0.026$  for 10%, 20% and 50% sub-ROIs and  $p = 0.015$  for 40% sub-ROI). For AUC defined sub-ROIs, complete and partial responders only had a significant difference for the biggest sub-ROI at 50% ( $p = 0.019$ ) while partial responders and control tumours were different for 50% ( $p = 0.002$ ), 40% ( $p = 0.002$ ), and 20% ( $p = 0.026$ ) sub-ROIs. Spatial sub-ROI analysis, where the sub-ROI in the post-treatment images was generated from the translation of the pretreatment sub-ROI did not show any significant differences between groups.



*Figure 5-7: Subregion analysis of HN5 tumours. Sub-ROIs defined using PE, AUC, MTT, or WOUT detected significant differences in the change of AUC between complete and partial responders, as well as between partial responders and control tumours.*

Histogram analysis of HN5 tumours revealed an increase in intratumour heterogeneity of PE, AUC, AT and WOUT posttreatment. This was observed in all groups, and no significant differences were detected between the different groups. When all groups were analysed together, PE, SD and CoV, skewness and mFWHM increased significantly ( $p = 0.006$ ,  $0.002$ ,  $0.002$  and  $0.010$ , respectively) while the kurtosis decreased ( $p = 0.004$ ), indicating increased heterogeneity. Similarly, the SD, CoV, and mFWHM of AUC increased ( $p = 0.004$ ,  $0.004$ ,  $0.019$ ). The CoV ( $p = 0.002$ ) and skewness ( $p = 0.004$ ) of WOUT increased significantly. Finally, the mFWHM of AT increased ( $p = 0.002$ ). Changes in the histogram parameters are represented in Appendix A3

#### 5.4.3.2 C33A tumour model

Imaging data was acquired for 16 C33A tumours. The imaging data for two tumours during wash-in appeared corrupted upon data transfer from the scanner, preventing the estimation of all metrics, and these tumours were excluded. Another tumour was excluded from the AT and WIT analysis because of missing data.

The change in whole-ROI DCE-US metrics pre- and post-treatment is shown in Figure 5-8. The change in WOUT was significantly different between partial and complete responders ( $p = 0.016$ ), with complete responders exhibiting a decrease in WOUT following radiotherapy, whereas WOUT increased in partial responders, which was also significantly different from the decrease in WOUT in control tumours ( $p = 0.009$ ). No other whole-ROI metrics showed a significant difference between any of the groups. The change in AUC in partial responders compared to control tumours approached significance ( $p = 0.052$ ). Combining treated tumours, as was done for HN5 tumours complete and partial responders, also did not reveal any trends.

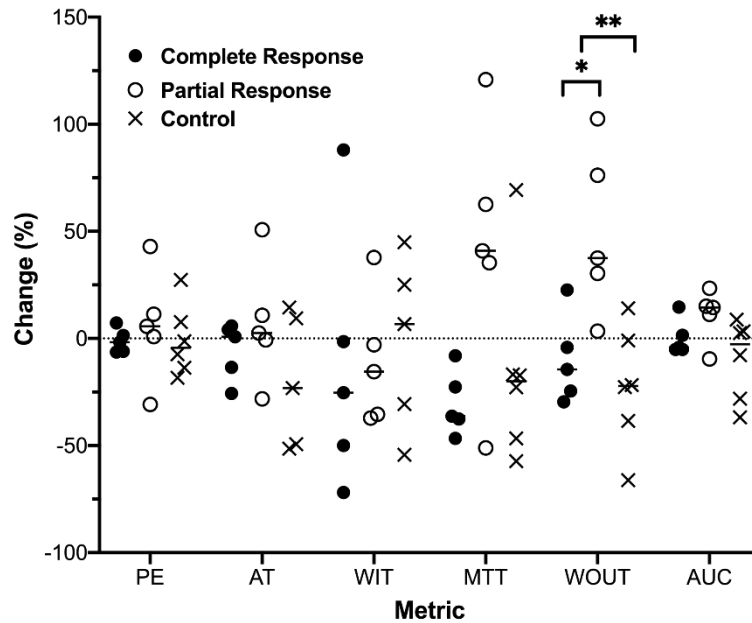


Figure 5-8: Percent change in DCE-US metrics between pre-treatment and 48 hours post radiation in the C33A tumour model using whole-ROI analysis. Significant differences in the change in WOUT were observed between complete and partial responders, and partial responders and control tumours.

As demonstrated in Figure 5-9, subregion analysis similarly revealed significant differences in the change of DCE-US metrics according to response. As seen in whole-ROI WOUT, functional sub-ROIs defined from all metrics showed an increase in WOUT in partial responders compared to a decrease in complete responders and control tumours. The most significant difference between complete and partial responders was obtained using the 50% AT sub-ROI ( $p = 0.008$ ). Additionally, significant decreases in MTT and AUC in complete responders compared to partial responders were identified in sub-ROIs defined from PE, MTT, WOUT and AUC. The most significant difference for MTT and AUC were detected in the 40% and 50% WOUT sub-ROIs ( $p = 0.016$  for both).

DCE-US metrics from spatial sub-ROIs similarly revealed a significant decrease in WOUT and AUC in complete responders and control tumours compared to partial responders. Again, the largest significant difference in the change of WOUT was calculated from 40% and 50% AT sub-ROIs ( $p = 0.008$ ) while the difference in AUC was most significant using the 40% MTT sub ROI ( $p = 0.016$ ), as shown in Figure 5-9.

Analysis of the histograms of DCE-US metrics also revealed differences between groups. Complete responders showed an increase in the skewness of WOUT distribution, that was significantly different to partial responders ( $p = 0.029$ ) which showed a decrease in skewness. Partial responders also showed a decrease in the kurtosis of WOUT which was significantly different to the increase seen in control tumours ( $p = 0.032$ ). The magnitude of the change however was small for both groups. An example of how the WOUT histogram skewness changes with treatment in complete and partial responders is shown in Figure 5-10. The change in the WOUT skewness and kurtosis for response groups is shown in Figure 5-11.

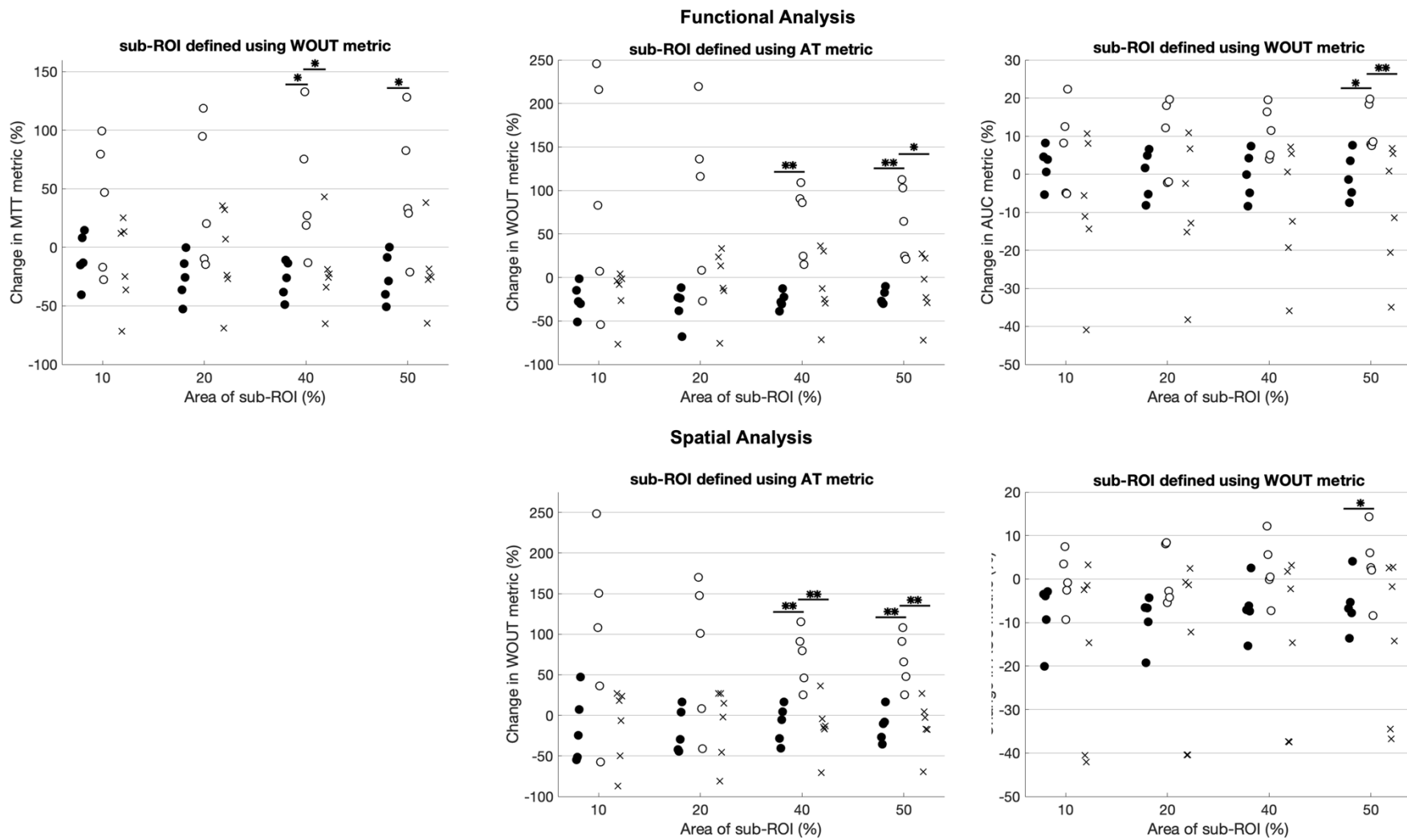


Figure 5-9: Subregion analysis of C33A tumours. The change in MTT (left), WOUT (middle) and AUC (right) with the greatest significance are shown for functional (top) and spatial subregion analysis (bottom).

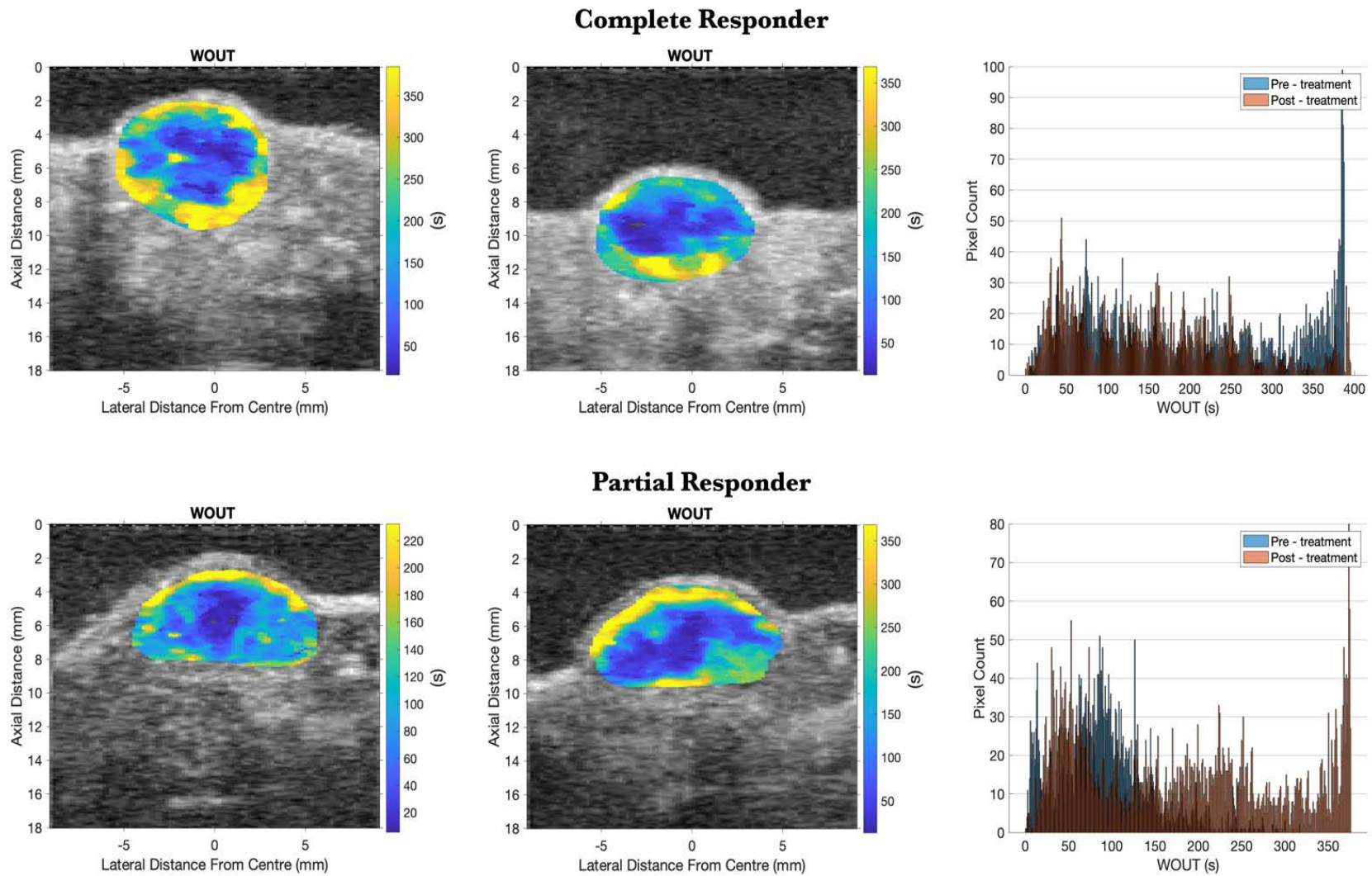


Figure 5-10: Representative WOUT metric maps in C33A tumours pre- and post-treatment. The top row shows a complete responder demonstrating a decrease in WOUT and increase in histogram skewness, while the partial responder (bottom) showed an increase in WOUT following radiation and the distribution became more negatively skewed.

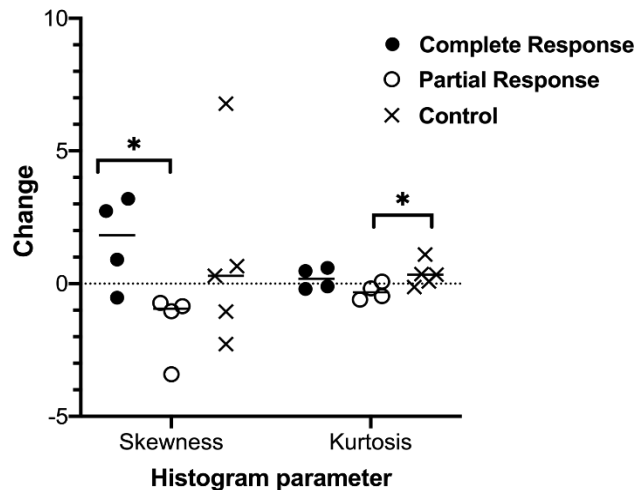


Figure 5-11: Change in WOUT histogram parameters in C33A tumours, showing a significant difference in change in skewness of complete and partial responders, and kurtosis between partial and control tumours.

#### 5.4.4 Tumour volume changes following treatment

To examine whether the detected change in DCE-US metrics preceded changes in tumour volume which could be used to stratify response, early tumour volume changes were compared between response groups. The change in tumour volume 2, 4 and 6 days after treatment was calculated as the difference in the volume at those timepoints and the volume at treatment, divided by the latter. In the HN5 model, complete responders showed a significantly bigger decrease in tumour volume compared to partial responders ( $p = 0.038$ ) on day 2, as shown in Figure 5-12 - left. The difference was not apparent on days 4 and 6, when some tumours in the partial response group started to regress.

The change in the tumour volume of C33A tumours shortly after radiation is shown in Figure 5-12 - right. A significant difference in the decrease in tumour volume of complete and partial responders is present at day 6 ( $p = 0.002$ ). The decrease in tumour volume of complete responders was also significantly different than control tumours at day 4 ( $p = 0.022$ ) and day 6 ( $p = 0.008$ ).

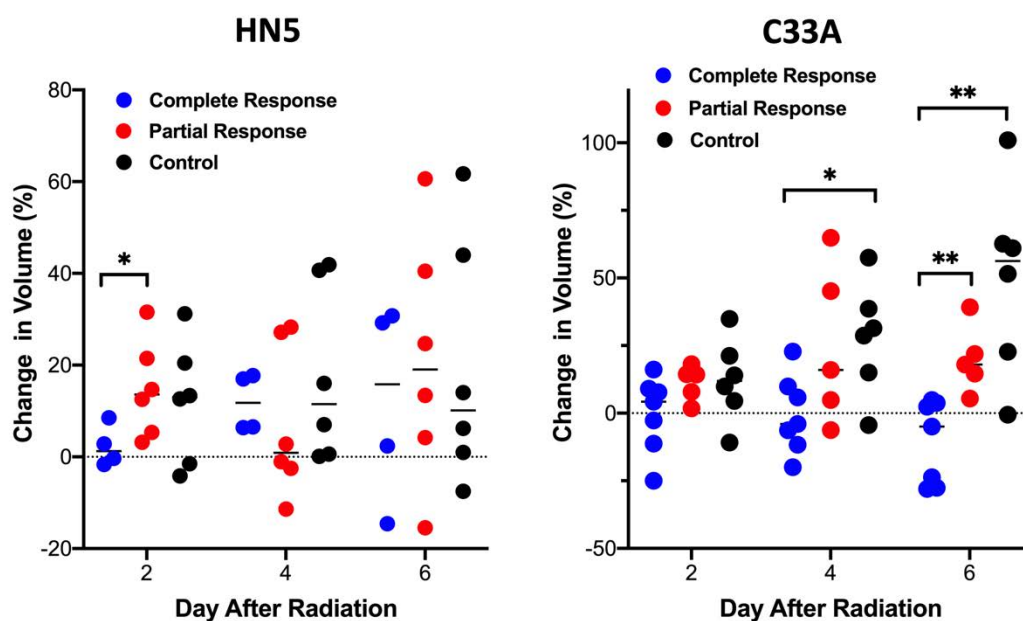


Figure 5-12: Tumour volume changes shortly following irradiation in HN5 (left) and C33A (right) models. The bar represents the median change for each response group. In the HN5 model, differences in the tumour volume change between complete and partial responders are present at day 2, while they are only detected at day 6 for the C33A model.

#### 5.4.5 Repeatability of 2D DCE-US

Repeat contrast agent injections were performed in 24 mice at endpoint imaging. This included C33A tumours (n = 18 compiled from C2, C3, C4 and C5 studies) and HN5 tumours (n = 6 from H1 study). Separate analysis of C33A or HN5 tumours did not reveal any differences in the variation according to tumour model, thus the results presented here combine tumour models. The mean tumour volume at the point of imaging was 322 mm<sup>3</sup> with an interquartile range of 226 – 408 mm<sup>3</sup>, as some animals had large tumours approaching the size limit, while others were not yet at the size limit but were impeding the animal's movement due to growth near the leg.

##### 5.4.5.1 Variation of whole-ROI DCE-US metrics

The absolute and signed variation, defined as the difference divided by the mean expressed as a percentage, of DCE-US metrics obtained from whole-ROI analysis for two repeat acquisitions is shown in Figure 5-13 and Table 5-3.

Evaluation of the mean absolute variation indicates the magnitude of the mean discrepancy between the two injections irrespective of the sign, whereas the mean signed variation indicates if there was a systematic difference between the two injections. The mean absolute variation for all metrics was lower than 35 %. AUC had the lowest variation of 7.9 % while WIT had the highest variation at 33 %. PE and AT significantly decreased ( $p = 0.041, 0.019$ ) while WIT and MTT increased ( $p = 0.0003, 0.004$ ) between the first and second injection.

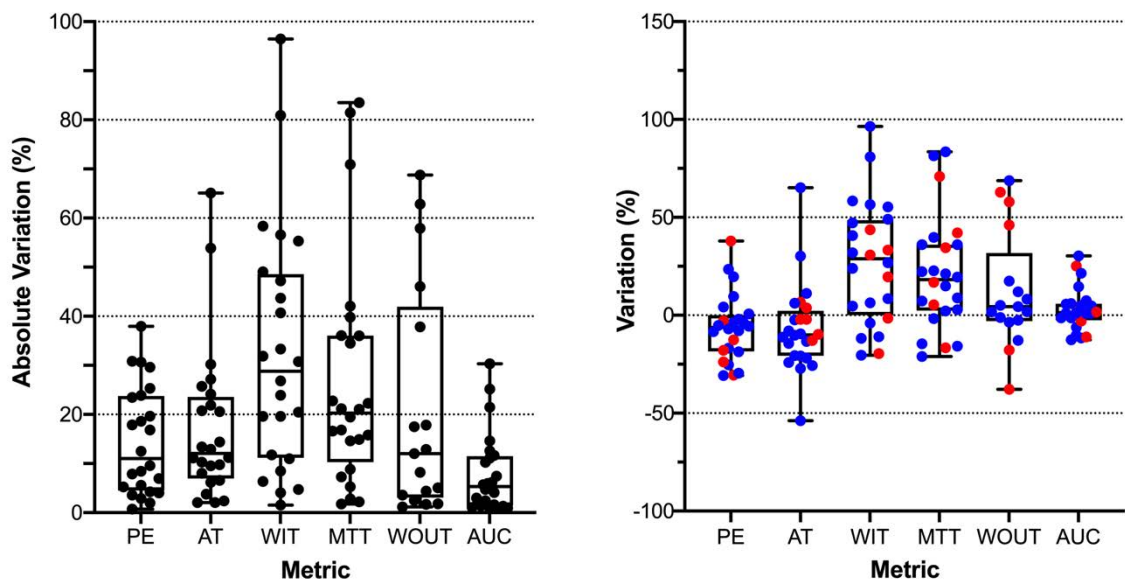


Figure 5-13: Absolute (left) and signed variation (right), defined as the difference divided by the mean of the two acquisitions, expressed as a percentage, for DCE-US metrics calculated using whole-ROI analysis. The horizontal line is the median variation, the box indicates the interquartile range, and the whiskers correspond to the minimum and maximum variations, each data point represents the variation measured in one tumour. The signed variation plot distinguishes HN5 tumours (red) and C33A tumours (blue). PE and AT decreased at the second acquisition, while WIT and MTT increased.

Table 5-3: Mean absolute and signed variation [interquartile range] of DCE-US metrics obtained from whole-ROI analysis from two acquisitions obtained with the same set-up.

METRIC	Abs variation (%)	Signed variation (%)
PE	15 [5.0 23]	-6.5 [-18 -1.3]
AT	17 [7.7 22]	-6.9 [-21 -0.59]
WIT	33 [11 48]	27 [3.1 48]
MTT	27 [13 36]	21 [2.6 36]
WOUT	21 [3.6 38]	12 [2.6 36]
AUC	7.9 [1.5 11]	3.1 [-1.8 5.8]

#### 5.4.5.2 Variation improvement using model fitting and TAC filtering

The quality of fit metrics of the Arditi and Gamma models are shown in Table 5-3, demonstrating better fitting with the Arditi model as indicated by the greater  $R^2$  value and lower root mean squared error (RMSE). In addition, the Gamma model failed to fit one TAC. The variation of whole-ROI DCE-US metrics derived from the Arditi model, and the raw TAC is shown in Figure 5-14. There were no significant differences in the variation of any metrics between the two methods.

Table 5-3: Mean coefficient of determination ( $R^2$ ) and root mean squared error (RMSE) of fit metrics  $\pm$  standard deviation of perfusion models for raw data TACs.

MODEL	ARDITI	GAMMA
$R^2$	$0.992 \pm 0.004$	$0.977 \pm 0.014$
RMSE	$24.3 \pm 4.52$	$45.2 \pm 12.2$

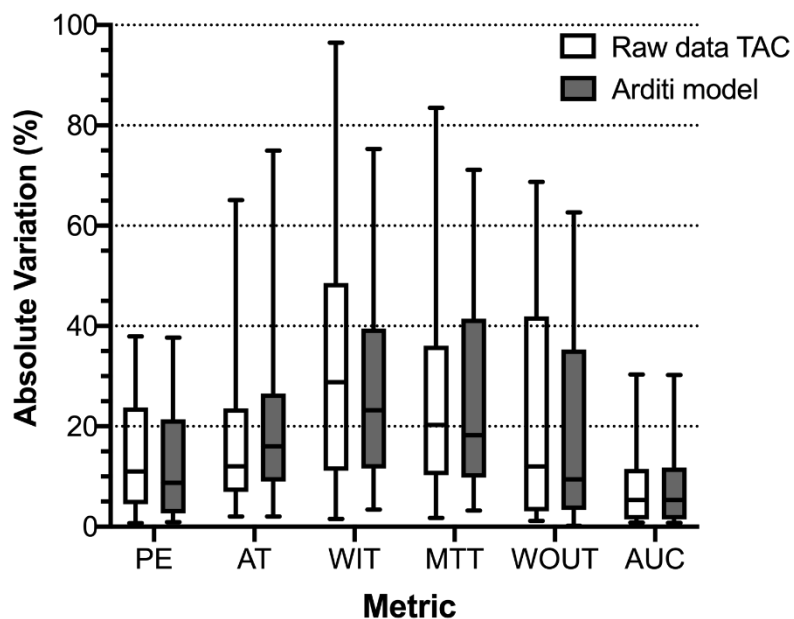


Figure 5-14: Absolute variation of DCE-US metrics derived from the raw data TAC and the Arditi model. There were no significant differences between the variation in the metrics calculated directly from the TAC or when using the Arditi model.

Moreover, Bland-Altman plots were used to compare the two attempted-repeat values of whole-ROI metrics derived from the two methods, looking for bias. All metrics had a significant bias, indicated by a mean difference and 95% confidence interval (CI 95 %) not overlapping with zero, shown in Figure 5-15. AT had the smallest bias as a percentage of the metric value. Note the difference in the WIT increases as the mean WIT increases. This indicates inaccurate fitting of the model for TACs with longer wash-in and an example, for one of the long wash-in times, is given in Figure 5-16.

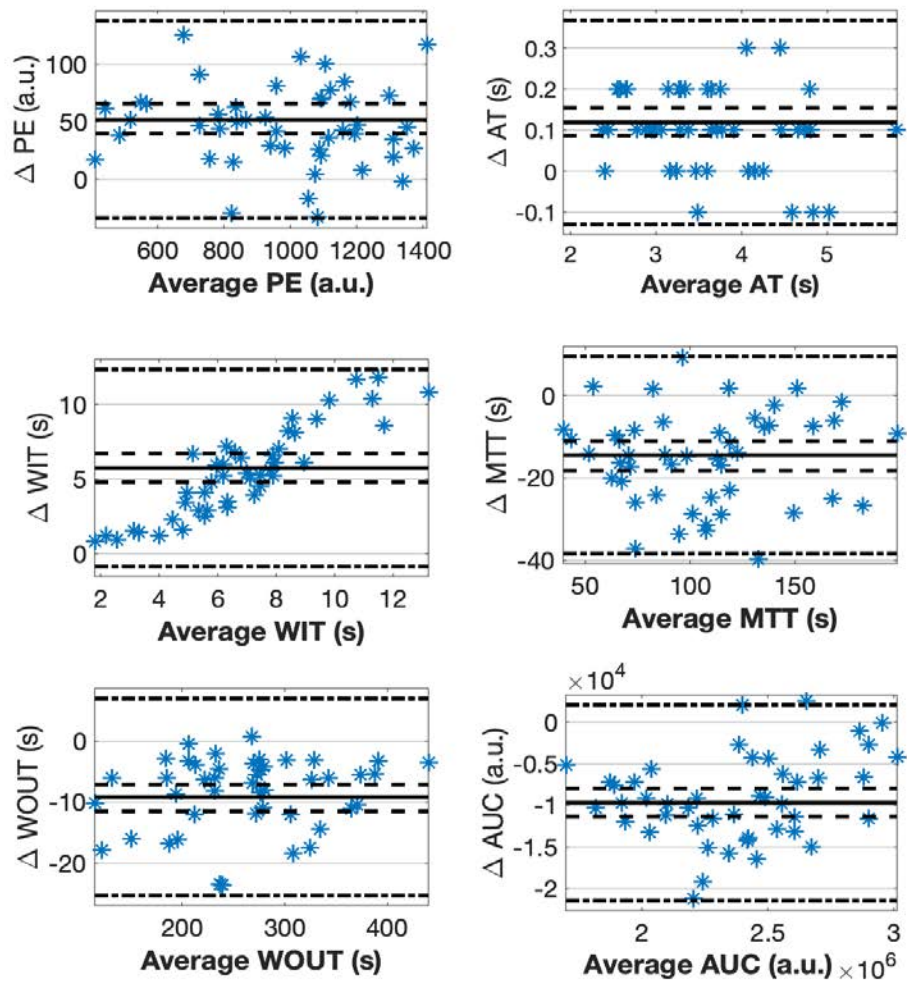


Figure 5-15: Bland Altman plots of metrics calculated from the raw data TAC or fitted to the Arditi model. The difference is calculated as metric from raw TAC -metric from Arditi fit. Each data points represents a comparison from one injection (2 per tumour). The mean difference is represented with a solid line, the 95% CI of the mean difference with long dash lines, and short and long dash line is the limit of agreement.

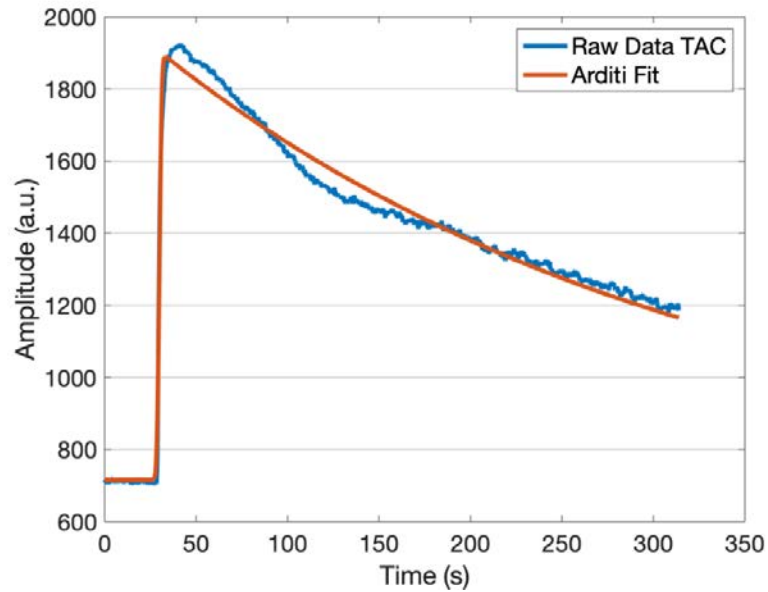


Figure 5-16: Ardití model fitted to the TAC curve of a C33A tumour, showing poor fitting for the wash-in part of the TAC close to the peak.

The variation of metrics calculated from video data TACs analysed with Savitzky-Golay filter and without filtering is shown in Figure 5-17. Filtering decreased the variation in MTT (median variation 9.1 % vs 22 %,  $p = 0.027$ ) while it increased the variation in AUC (median variation of 32 % vs 23 %,  $p = 0.014$ ).

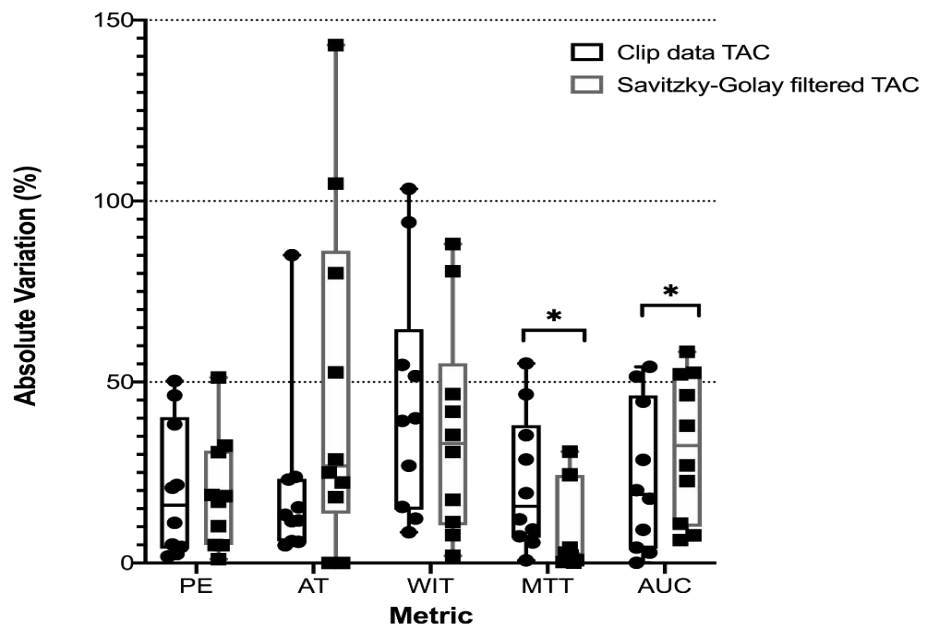


Figure 5-17: Variation of whole-ROI metrics from experimental video TACs (black, circles) and Savitzky-Golay filtered TACs (grey, square). Each data point represents one animal.

Bland-Altman plots, shown in Figure 5-18, revealed a significant bias for all metrics, with Savitzky-Golay filtering. In fact, although WIT variation no longer demonstrated a value dependent bias, PE, MTT and AUC were found to have a proportional bias that had not existed in the analysis with metrics derived from the best fit Arditi model.

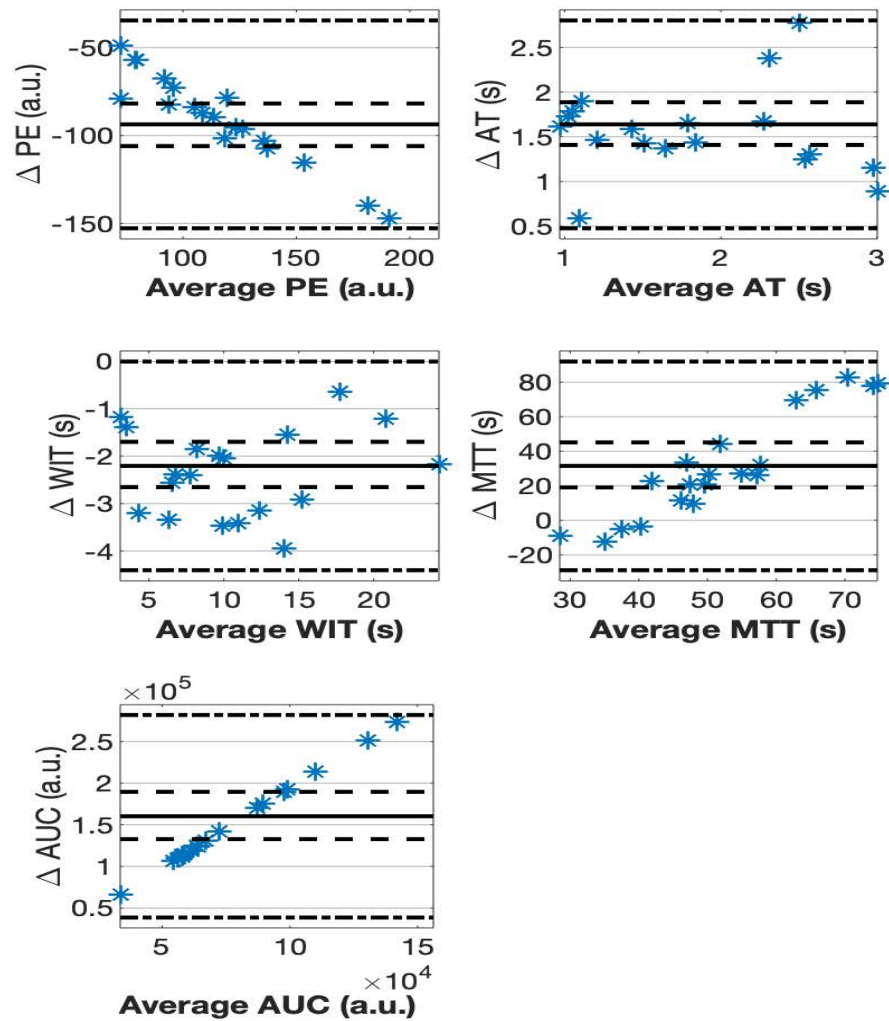


Figure 5-18: Bland Altman plot of metrics derived using the Savitzky-Golay (S-G) filter and video data TACs. The difference is calculated as video TAC metric - S-G metric. Each data points represents comparison from one injection (2 per tumour). The mean difference is represented with a solid line, the CI % 95 with long dash lines, and short and long dash lines are the limits of agreement.

#### 5.4.5.3 Variation of whole-ROI DCE-US metrics due to ROI delineation

The variation between whole-ROI metrics calculated from one DCE-US acquisition using two differently drawn ROIs (each regarded as a reasonable

delineation of the tumour cross-sectional ROI) is shown in Figure 5-19 . The mean variation in all metrics was lower than 3 %. One repeat ROI delineated showed a large variation in the WOUT of 16 %. The WOUT maps generated over the areas covered by the two ROIs are shown in Figure 5-20 . The variation in the WOUT was likely due to a long WOUT near the tumour boundary, which was included in one ROI and not the other.

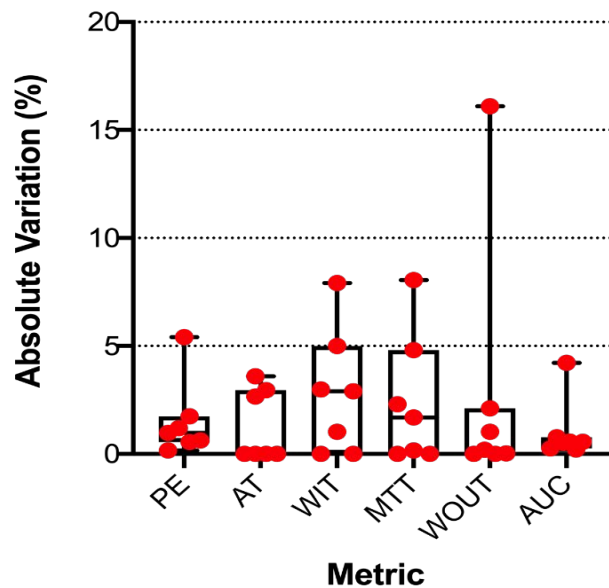


Figure 5-19: Absolute variation of TAC metrics of the same injection analysed with different ROIs. Each data point represents one tumour.

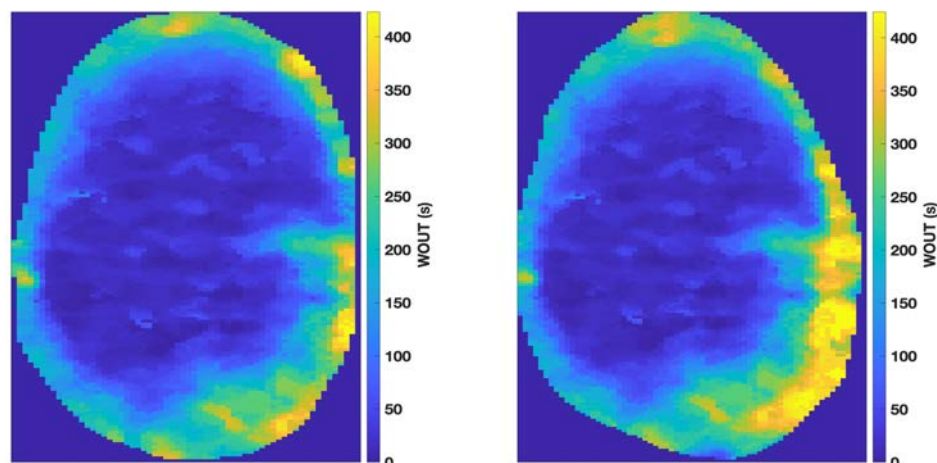


Figure 5-20: WOUT maps analysed with two ROIs drawn on the same image independently. The whole-ROI WOUT had a variation of 16 %, which can be seen to have been because of pixels at the tumour edge with high WOUT, which were included in one ROI (right) but not the other (left).

Next, the variation in whole-ROI metrics from two injections analysed using the same or different ROIs was compared and is shown in Figure 5-21. Only AUC was significantly different between the two methods, with smaller variation when drawing ROI independently for each injection ( $p = 0.047$ ). However, the mean variation is 6 % for same-ROI vs 5.4 % for different-ROI analysis, indicating only a small difference.

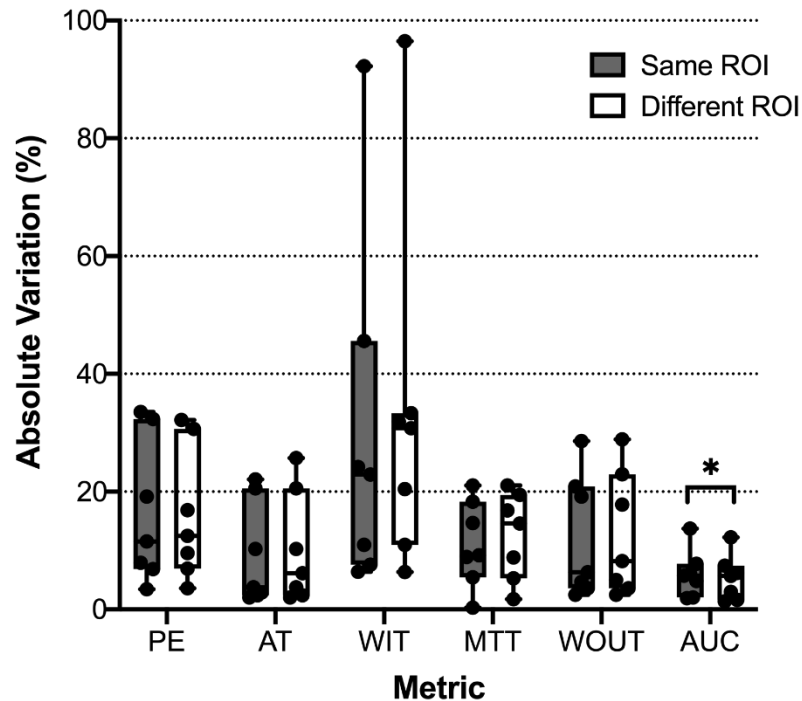


Figure 5-21: Absolute variation of whole-ROI metrics from 2 repeat injections analysed using the same ROI (grey bar) or with ROIs drawn independently (white bar).

#### 5.4.5.4 Variation of intratumour heterogeneity

The absolute and signed variation in the all-histogram parameters except skewness are shown in Figure 5-22 and Table 5-4. In some tumours, the variation in skewness between two injections was greater than 300%. This was seen in histograms with skewness close to zero (small denominator), leading to a perceived large variation. Therefore, the estimation of variation in skewness was deemed unreliable. The variation in skewness is shown in the Appendix A4 with an example of a large variation calculated despite minimal change in the histogram. Kurtosis showed the greatest variation in all metrics. AUC histogram

parameters had the smallest variation while WIT had the largest variation, which was in agreement with the whole-ROI analysis. A significant change in histogram parameters of AT, WIT and MTT between injections was identified, indicating a change in the distribution of the metric. AT had a significant increase in the SD, CoV and mFWHM ( $p= 0.004, 0.001, 0.001$  respectively). WIT had a significant increase in SD and mFWHM ( $p = 0.004, 0.0008$ ). These changes agree with the observed increase in whole-ROI WIT. Meanwhile, MTT had a decrease in CoV and kurtosis ( $p = 0.006, 0.040$ ). A representative example of these changes is shown in Figure 5-23.

*Table 5-4: Absolute median variation [interquartile range] (%) of histogram parameters for DCE-US metrics. Significant changes between the two injections are shown in bold.*

METRIC	SD	COV	SKEWENESS	KUR	MFWHM
PE	-2.17 [-10.1 3.46]	4.14 [-7.56 12.3]	20.2 [-5.00 31.4]	1.75 [-7.57 13.9]	3.59 [-10.2 5.02]
AT	<b>30.6</b> <b>[6.39 50.4]</b>	<b>37.5</b> <b>[19.1 60.9]</b>	-40.6 [-194 85.0]	-11.0 [-62.1 22.8]	<b>30.2</b> <b>[7.83 51.1]</b>
WIT	<b>20.9</b> <b>[0.26 39.2]</b>	-4.14 [-12.3 11.1]	-2.58 [-26.4 25.0]	-1.89 [-39.2 23.1]	<b>22.9</b> <b>[13.9 50.8]</b>
MTT	-0.34 [-20.2 14.0]	<b>-7.59</b> <b>[-16.9 -2.84]</b>	-24.1 [-92.5 12.2]	<b>-22.7</b> <b>[-49.4 14.0]</b>	4.87 [-17.3 26.9]
WOUT	2.13 [-3.49 17.3]	-4.5 [-13.1 3.43]	-44.7 [-100.0 14.8]	-13.2 [-30.7 -0.29]	4.33 [-3.54 27.5]
AUC	1.26 [-5.29 10.9]	2.44 [-8.46 13.7]	23.4 [-13.8 157]	0.32 [-13.9 25.4]	0.67 [-5.93 13.9]

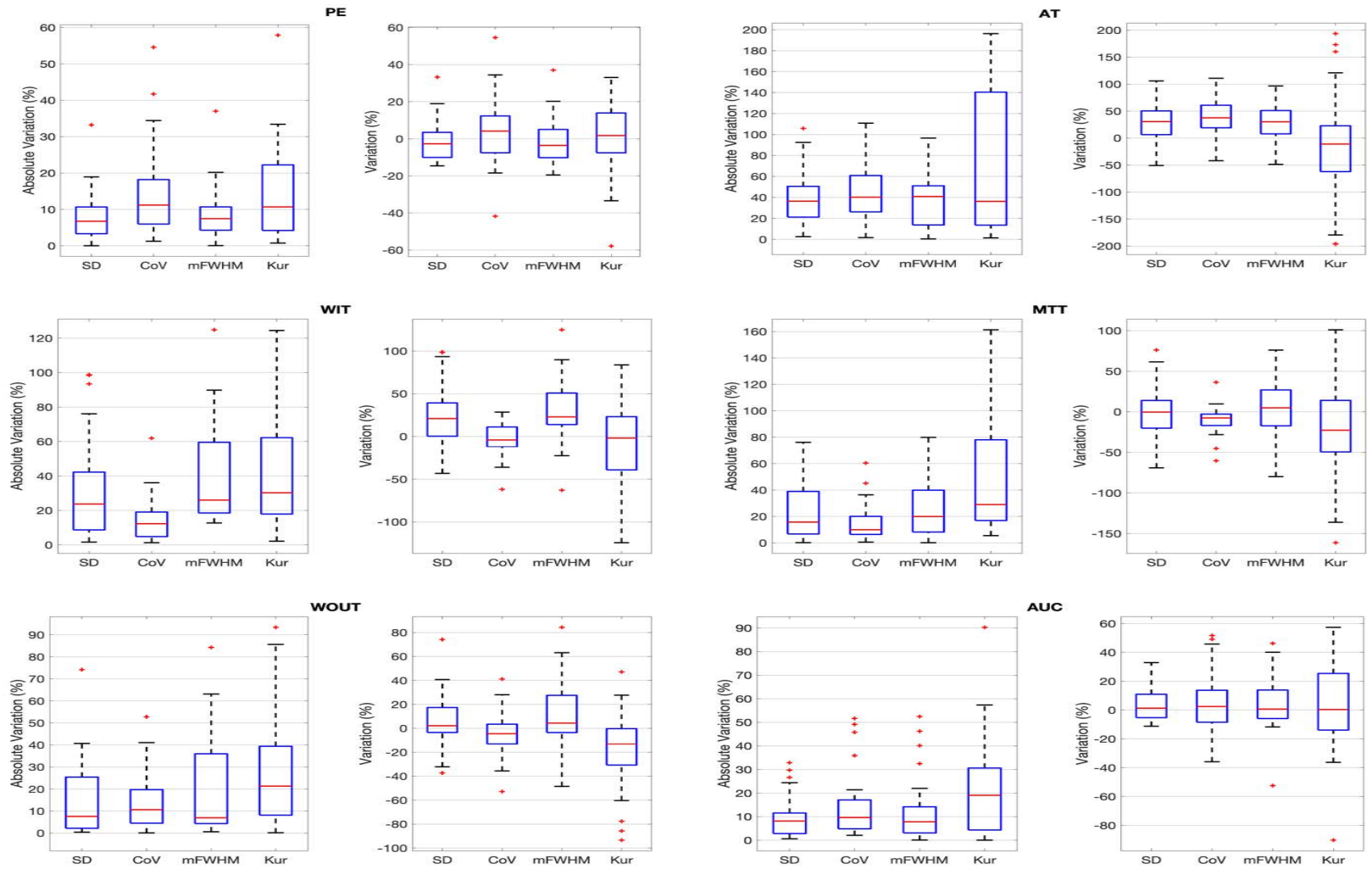


Figure 5-22 : Absolute and signed variation in histogram parameters of DCE - US metrics obtained from two acquisitions.

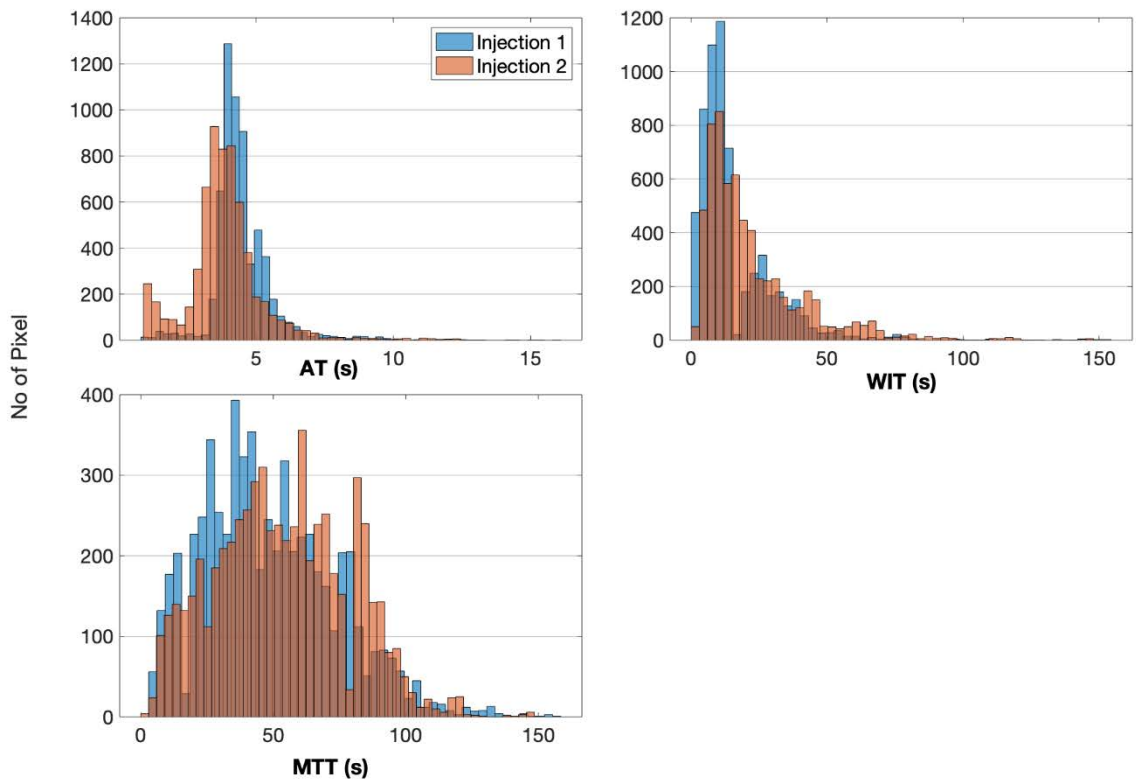


Figure 5-23: A representative example of histogram distributions of AT, WIT and MTT for two repeat DCE-US acquisitions. AT has increased heterogeneity, as measured by CoV, SD and mFWHM, for the second injection compared to the first. WIT had increased SD and mFWHM. MTT tended to have decreased CoV and kurtosis for the second injection compared to the first.

#### 5.4.5.5 Spatial repeatability of DCE-US metric maps

The spatial correlation of metric maps obtained from two DCE-US acquisitions is shown in Figure 5-24. Similar to the whole-ROI and histogram analysis, amplitude-based metrics had a greater correlation coefficient than time metrics, indicating better spatial repeatability. Again, WIT had the lowest average correlation of all metrics. Example metric maps of PE, for the best and worst correlation (which would be a better correlation than even the best of WIT) are shown in Figure 5-25 .

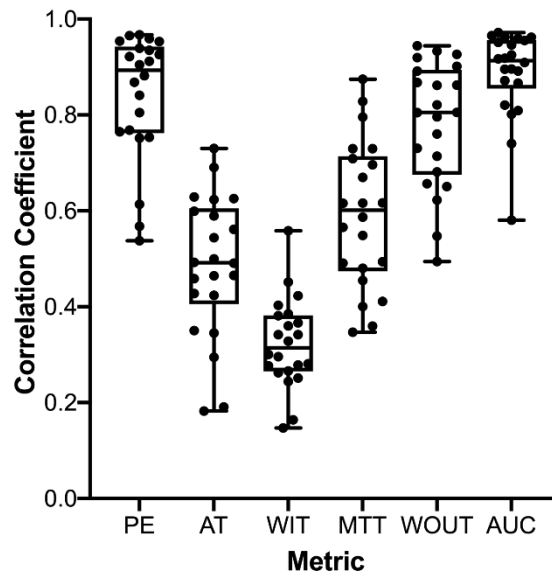


Figure 5-24: Correlation coefficient of metric maps obtained from two DCE-US acquisitions. Each point represents one tumour.

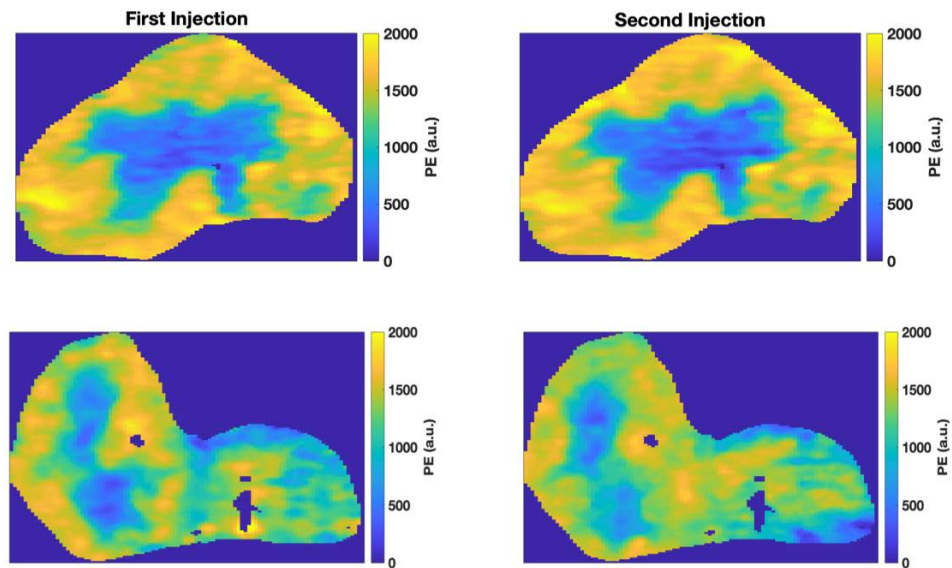


Figure 5-25: Spatial correlation of repeat injections. The top row shows PE maps of a tumour with a high correlation coefficient (0.96) and the bottom row shows a different tumour with a low correlation coefficient (0.54). The greater correlation obtained in the top maps is demonstrated by the similarity of the spatial pattern, while there are discernible differences in the centre of the bottom maps leading to the lower correlation.

## 5.5 Discussion

### 5.5.1 Radioresponse of cervical and head and neck tumour models

The H1 study used radiation doses of 20 and 25 Gy, which both produced partial and complete responses, as desired. Response was defined as tumour regression to below the treatment volume that was sustained for more than 80 days (Figure 5-3). For the C33A tumour model (C5 study), none of the tumours achieved complete response, according to this definition (Figure 5-4). C33A tumours were classified as partial and complete responders using the same criteria as the HN5 tumours but using a shorter period (20 days) for clarity, i.e., to avoid confusion between the relative responsive within tumour models. The implications of having no complete responders in the C33A study are discussed below.

### 5.5.2 Association of radioresponse with pretreatment DCE-US metrics

Pre-treatment perfusion was assessed using DCE-US metrics of the whole-ROI, sub-ROIs (defined using pixels with highest TAC metric values), and analysis of histogram percentiles (5th to 20th). The analysis aimed to uncover the association of radioresponse with tumour perfusion assessed prior to radiotherapy. Both poor and good tumour perfusion have been found to predict tumour control following radiotherapy (see section 1.3.1). In the HN5 tumour model, complete responders had shorter WIT (or quicker wash-in), compared to partial responders and control tumours, which was evident with all three analysis methods (Figure 5-5). Inspection of tumour enhancement pattern was discussed in chapter 4, where it was observed that the quick wash-in HN5 tumours was related to a spatially homogenous enhancement pattern. Tumour regions with longer wash-in had lower PE. Therefore, shorter WIT can be indicative of quick blood flow. The negative correlation between the WIT and flow rate has been confirmed in a microvessel phantom [207]. HN5 tumours with quicker blood flow, indicated by short WIT, are expected to be well-perfused and are hypothesised to suffer less hypoxia and thus be more radiosensitive. This finding is in agreement with the clinical studies of head and neck cancer demonstrating a correlation of high blood flow prior to treatment with favourable outcome ,

assessed using perfusion CT [77] and DCE-MRI [78]. Furthermore, WIT calculated for sub-ROIs and histogram analysis revealed stronger significance than that observed for whole-ROI analysis, confirming the importance of investigating intratumour perfusion heterogeneity.

Moreover, it should be noted that WIT can be a measure of tumour volume. Microbubbles travel longer distances to reach the centre of larger tumours with larger cross sections, increasing the WIT. While there were no significant differences in the tumour volume between HN5 response groups at treatment, the significant result of WIT may be a combined measure of tumour volume and blood flow, making it a more sensitive metric than PE or AUC which do not depend on the tumour volume.

Conversely, no DCE-US metrics, including WIT, were significantly different according to response in the C33A model. C33A tumours did not achieve complete tumour regression like HN5 tumours, and hence there was not as a distinct discrimination between response groups. Further, there was larger intertumour heterogeneity in WIT metric in C33A cohort (mean WIT of 10.4 s  $\pm$  standard deviation of 8.0 s) compared to the HN5 cohort (mean WIT 3.1 s  $\pm$  standard deviation of 1.1 s). The wider distribution of WIT values, with greater overlap between response groups, would decrease the predictive power of the metric

### *5.5.3 Association of radioresponse with changes in DCE-US metrics*

The change in tumour vasculature after radiation was evaluated using DCE-US imaging. Whole-ROI analysis provides DCE-US metrics representing the average perfusion of the imaged tumour slice. Subregion analysis can capture vascular changes that occur within subregions of the tumour and may not be evident in the whole-ROI metrics. Histogram analysis based on metric maps allows investigation of intratumour vascular spatial heterogeneity.

HN5 tumours showed a decrease in whole-ROI PE and AUC, 48 hours post treatment, regardless of whether tumours were treated. Additionally, a decrease

in MTT and WOUT for treated tumours was observed. This was accompanied by an increase in the heterogeneity of the metrics apparent from the increase in SD, CoV and mFWHM histogram parameters. The decrease in PE reflects a decrease in the vascular volume and the decrease in AUC reflects a decrease in vascular volume/and or blood flow within the tumour, which may be caused by different mechanisms for the different groups. Control tumours growing at a faster rate than can be supported by the vascularisation rate will become less perfused at their core, while the tumour rim may still be perfused by surrounding normal vasculature. The result of this growth behaviour is a decrease in the overall tumour vascular volume per unit tumour volume averaged across the whole-ROI, and an increase in intratumour perfusion heterogeneity. Whereas, treated tumours may have suffered vascular damage, also leading to a decrease in vascular volume per unit tumour volume. The decrease in MTT and WOUT in all tumours could be explained similarly, as these metrics are correlated with PE and are thereby correlated to vascular volume.

Although all tumours showed a decrease in AUC, the decrease was significantly greater in complete responders and control tumours compared to partial responders (Figure 5-6). A decrease in vascular volume was expected based on the literature discussed earlier of vascular damage. While vascular damage has not been directly assessed in HN5 tumours, HIF-1 signal, visualised using PET imaging, in HN5 tumours increased 6 days after radiation with 8 Gy indicating more hypoxia [87]. An increase in HIF-1 signal 2 days after radiation was concurrent with a decrease in ultrasound Doppler signal in another tumour model, and hence reduced vascular volume, supporting the presence of vascular damage. Assessment of vascular changes using functional sub-ROIs revealed the same decrease in AUC in complete responders. There was no difference in the p-values of the results to suggest either method was more sensitive.

C33A complete responders displayed a decrease in whole-ROI WOUT following radiation, compared to an increase in partial responders (Figure 5-8). A similar decrease was also observed in control tumours, which can be justified as discussed above for control HN5 tumours. It is hypothesised that vascular damage occurs predominately in small vessels with long wash out that influence

overall WOUT but have too small a vascular volume to impact whole-ROI AUC or PE. This is supported by additional findings of the model; using functional sub-ROIs, the change in WOUT could be detected with higher significance from sub-ROIs with the largest AT (Figure 5-9). As discussed in Chapter 4, C33A tumours showed slow wash-in and low PE within the tumour core, implying the presence of micro-vessels. Moreover, the increase in WOUT skewness in complete responders (Figure 5-11) demonstrates a heterogenous radiation-induced vascular response within the tumour, with selective elimination of pixels with slow wash-out, rather than a uniform decrease in wash-out across the imaged tumour slice.

Furthermore, the literature reports selective radiation-induced disruption of vessels with poor flow dynamics [102] or small immature vessels with no pericyte bounding [104]. Microvessels with smaller diameters (5 – 15  $\mu\text{m}$ ) suffered more damage than larger vessels at radiation doses of up to 15 Gy, but with larger doses of 20 Gy, larger vessels (up to 35  $\mu\text{m}$ ) were also damaged [105]. As C33A tumours were irradiated with both doses, there might still be a preferential radiation response in smaller vessels.

The results of both cancer models indicate correlation of vessel disruption in tumours with better radioresponse. The concomitant decrease in WOUT and AUC are in alignment since these metrics are correlated, as discussed in Chapter 4. However, there are several differences between the two tumour models which may influence their vascular radiation response. Firstly, HN5 and C33A tumours had significant differences in their perfusion metrics at the pre-radiation timepoint, as presented in Chapter 4, which can affect the vascular response to radiation [209]. For example, the greater intratumour vascular heterogeneity of C33A tumours pre-radiation may explain why the tumour model exhibited significant changes in heterogeneity that were not observed in HN5 tumours. Secondly, some HN5 tumours displayed a complete response with tumour regression and no evidence of regrowth, while this was not the case for the C33A model, meaning that their radioresponse is not comparable.

Spatial sub-ROI analysis was unable to capture significant differences seen in whole-ROI analysis or functional sub-ROI analysis. This may point to a spatial mismatch of spatial sub-ROIs between the two imaging timepoints which can be a result of poor reproducibility of transducer position relative to the centre of the tumour.

#### *5.5.4 Repeatability of 2D DCE-US imaging*

Analysis of whole-ROI TAC metrics revealed that the greatest repeatability was observed in a metric based on vascular volume, AUC (Figure 5-13). The good repeatability of AUC allows more precise estimation of changes induced by radiotherapy and therefore, potentially, a more accurate assessment of response using AUC compared to using other metrics. This may help understand the results for the HN5 model presented in this chapter that found significant differences in the AUC but not in the PE, i.e., changes in PE may not have been detectable due to the greater variation associated with its measurement. This result is in agreement with a study of repeatability in melanoma xenograft mouse model imaged with SonoVue<sup>®</sup> contrast agent and the Aplio scanner [210] which reported AUC as the most reliable parameter with a coefficient variation of 15.79 % calculated from three injections. The study concluded that AUC is suitable for assessing antiangiogenic treatment based on the level of change in tumour perfusion associated with treatment reported elsewhere and the variation estimated in their study. However, they also reported similar repeatability of WIT. This may be because they calculated metrics using a fitted model that removes TAC noise. The study also did not report a significant systematic change in the WIT between injections, which was observed here and would increase the variation. The variation of DCE-US metrics observed in the current study is in agreement with that reported of less than 34 % for all metrics in a murine colon cancer model [57].

The good repeatability of AUC compared to PE may be because PE is dependent on the initial concentration of microbubbles, while AUC represents the total volume of microbubbles seen in the TAC, at different concentrations, which are influenced by the size and structure of vessels, and blood flow. Changes in the

initial concentration of microbubbles, which can occur because of variability in injection, may therefore have a larger influence on PE. The effect of the injection rate on PE has been shown previously [211, 212], with a decrease of 55% observed when the time for a manual injection was increased from 2 s to 10 s in an epidermoid carcinoma xenograft [54]. Variation in the injection time in the current study is expected between repeat injections.

Metrics that were solely based on temporal characteristics of the TAC showed greater variation compared to PE and AUC, indicating lower precision in measuring blood flow. One source of the measured variation in time-based metrics is the systematic change in the metrics at the second injection, at which AT decreased and WIT and MTT increased (Figure 5-13). As discussed in Chapter 4, AT measured from the whole-ROI is largely dominated by blood flow of the mouse body circulation, while WIT measures blood flow within the tumour. A decrease in AT in the second injection means that blood flow was quicker from the injection site to the tumour boundary, and the increase in WIT suggests that blood flow within the tumour was slower than for the first injection. The increase in MTT is likely caused by the increased WIT, given that no change was observed in WOUT. The increase in WIT and MTT reported here contrasts with an observed decrease in the time to peak and MTT in the fourth injection in a colon cancer mouse model performed under gaseous anaesthesia [213].

The variation in DCE-US time metrics could be a result of a change in physiological functions of the mouse, such as the heart rate. CEUS imaging of the duodenum in healthy dogs showed a negative correlation between the heart rate and time to peak, equivalent to the sum of WIT and AT [214], which was suggested to explain the higher interday variation in WIT compared to the relatively low variation in AUC and PE. The authors also report that calculating the time to peak from the arrival time (i.e., WIT in the current study), rather than from the time of injection, improved the repeatability of the measurement by minimizing its dependence on the systemic blood flow properties. However, the authors reported smaller intraday variation of WIT (coefficient of variation of 2.27 %) compared to that found in this study. The difference may be species-dependent, with small animals, such as mice, being more sensitive to

anaesthesia-induced changes than dogs. In nude mice, a decrease in the time to peak in an epidermoid carcinoma model coincided with an increase in heart rate [215]. The heart rate was not measured in the current study, but it is possible that it increased at the time of second injection. Hypnorm™/Hypnovel™ anaesthetics have been shown to increase heart rate in rats [216]. The temporal profile of these changes during animal imaging is unknown. In another study, an increase in heart rate was suggested to be due to an increased volume load from the saline and microbubbles injection [215]. An increased heart rate can lead to a decrease in AT.

There was a systematic difference in PE between injections, with an overall decrease in PE for the second injection compared to the first. This difference was only marginally significant ( $p = 0.049$ ), but this finding contradicts reports of increased PE and AUC following repeat injections. PE and AUC was reported to increase continually over four injections, separated by 15 mins with no high MI disruption in between, using SonoVue® contrast agent in a colon tumour mouse model [213]. In contrast, the PE and AUC calculated in the renal cortex did not increase, indicating that this effect may be caused by changes specific to the tumour microvasculature. Others [215] have demonstrated a small non-significant increase in PE for the second injection (using B-mode imaging) in an epidermoid carcinoma tumour model in nude mice. This effect coincided with a measured increased heart rate, which was hypothesised to increase the microbubble concentration, and a decrease in liver PE which may indicate saturation of microbubble uptake by Kupffer cells, leaving more freely circulating microbubbles. Saturation of Kupffer cells was speculated in the study because of the high microbubble concentration used, approximately x 3 times the typically used concentration, which was needed for B-mode imaging and may therefore not be relevant in the studies reported herein. Different results have also been reported across species. In healthy cats [217], the PE and AUC of SonoVue in renal cortex, medulla and spleen increased for the second injection of SonoVue, which was suggested to be due to reduced filtering by pulmonary macrophages, or possible interaction of microbubbles with the vasculature leading to vasodilation and greater vessel filling.

A clinical investigation reported an increase in AUC by a factor 3.5 for the second injection in the aorta and the liver with SonoVue [218]. It was suggested that this was due to pulmonary macrophages being saturated by microbubbles from the first injection and thus having diminished filtering capacity at the second injection. A similar effect may be present in immunosuppressed athymic mice, but this requires confirmation.

An interaction between insonified microbubbles and microvasculature has not been confirmed in any study assessing imaging repeatability but rupture of capillaries in mouse muscle and intestine has been reported with Optison™ doses close to the human clinical dose and an MI of 0.4 [219]. Capillary rupture was evident from the increased haemorrhaging and dye extravasation. If a similar effect was present in this study, disrupted capillaries would be expected to have slower blood flow due to leakage, which can explain observed increase in WIT and decrease in PE. MI is an acoustic field parameter (spatial peak, temporal peak negative pressure divided by the square root of frequency, derated by an assumed attenuation coefficient and depth to the spatial peak) that is indicative of the likelihood of acoustic cavitation and is displayed on the screens of diagnostic imaging systems. Increased likelihood of cavitation may be regarded, for microbubbles, as increased amplitude of oscillation of the microbubbles. For a fixed frequency, depth, etc. (transducer and focus settings), MI is used as a display-screen surrogate for acoustic pressure, and hence capillary disruption due to microbubble activity is more likely to occur when a high MI is applied between injections to destroy residual microbubbles.

In addition to biological factors influencing TACs, breathing motion may be an additional source of signal variation [152], leading to the appearance of noise in the TAC and variation in metric quantification. Here, the effect on noise on whole-ROI-derived metrics was investigated by reducing or removing noise, using one of two approaches: fitting TACs to the Arditi model or filtering with the Savitzky-Golay filter. The metrics determined using these methods were significantly different from those of the experimental TACs, as demonstrated by Bland-Altman plots ( Figure 5-15, Figure 5-18), and the variation was reduced only using Savitzky-Golay filtering for MTT (Figure 5-17). These results do not

support the use of either Arditi model or filtering and imply TAC noise is not a major source for variability for whole-ROI metrics.

The effect of ROI delineation on the variation was revealed to be minimal (Figure 5-19). Yet, in one case, different ROI delineations had a variation greater than 10%. In this case, the tumour was enhanced only at the periphery (Figure 5-20), making the whole-ROI metrics more affected by changes in the delineation of the ROI at the tumour boundary. In general, this demonstrates the ROI delineation is robust, but care must be taken in identifying the tumour boundary, which can be done by inspecting the enhancement pattern using video data. Analysing repeat injections using the same ROI did not improve the repeatability and in fact increased the variation of AUC marginally (Figure 5-21). Therefore, independent delineation of repeat injections is valid and desirable, and would compensate for shifts in the position of the tumour due to respiration and probe repositioning after high MI scanning.

Variation in the histograms of metric maps reflected similar changes to those observed for ROI analysis (Figure 5-22). PE and AUC remained the most repeatable metrics, while the WIT was the least repeatable. Skewness and kurtosis had the highest variations of the histogram parameters. The large variation of kurtosis may be because it is calculated from the metric raised to the fourth power of the metric value, making it more sensitive to changes in the distribution. It was not possible to reliably assess the repeatability of histogram skewness due to artificially high variation when the skewness was close to zero, causing outliers in PE, AUC, AT and WOUT calculation. This suggests that the calculation of changes in the skewness may be unreliable if the histogram is initially not skewed, and care must be taken interpreting the results.

As with whole-ROI, the change in the histogram distribution of AT and WIT was directional, showing an increase in SD and mFWHM in the second injection. The observed increase in the CoV of AT implies that there is increased intratumour heterogeneity in AT. This is hypothesized to be because of opposing effects on AT in different regions of the tumour. As discussed in Chapter 4, AT for pixels near the tumour periphery is mostly dependent on the blood flow to the tumour

through major vessels, similar to the whole-ROI AT, which was shown to decrease in the second injection, while contrast arrival in the tumour centre depends on both its arrival at the tumour (systemic circulation) and its perfusion within the tumour (local microcirculation), similar to whole-ROI WIT, which was shown to increase. The decrease in AT at the periphery versus the increase at the core can explain the increased CoV. The WIT histogram shifted to longer WIT values, consistent with the increase in whole-ROI WIT and leading to an increase in SD. As a result of the increase in WIT, the MTT increased, leading to decreased CoV.

Finally, the spatial repeatability PE and AUC was good compared to other metrics (Figure 5-24). The lower repeatability of WIT, AT and MTT is a result of their susceptibility to motion noise in pixel-wise TACs.

## **5.6 Limitations**

The pilot study provided encouraging results as to the suitability of DCE-US imaging to assess tumor response to radiotherapy. In both head and neck and cervical cancer models, some DCE-US metrics had significant changes 48 hours after treatment that were different between complete and partial responders. While these results are promising and establish analysis methods for further studies, there are several limitations to this study.

First, the studies reported here involved a small sample number for each tumour model. Hence these results must be validated with a bigger number of animals.

The pretreatment wash-in time (WIT) was found to be significantly different between complete responders and partial responders, indicating its potential as a predictive biomarker. It must be noted that when comparing the treated group with the control group, the treated group had significantly smaller wash-in time in the histogram percentiles, but not using whole-ROI or subregion analysis. This may indicate a selection bias between the groups; while animals were randomised according to tumour volume and growth rate as much as possible, randomisation according to pretreatment metrics to ensure similarity between

control and treated tumours should also be considered for future studies. As this study was focused on the difference between complete and partial responders, this selection bias does not confound the main findings.

The Aplio™ scanner is well established and widely used for clinical contrast imaging. However, even the raw data generated has undergone unspecified processing, which may have introduced non-linearity in the signal, affecting quantification of DCE-US metrics [220]. Moving towards research-based scanners, such as the Verasonics™ system, with programmable signal-processing, can provide more reliable quantification of the DCE-US signal. This is further discussed in chapter 7.

Relying on a single tumour plane for quantification is flawed, due to the discussed heterogeneity of the vasculature and its response. Indeed, heterogeneity in vascular response was even observed within the imaged tumour slice, evident by the change in the histogram shape parameters and subregion analysis. 3D DCE-US imaging is hypothesised to provide more accurate quantification of tumour perfusion and its changes, and this will be described in chapter 7.

The discussed analysis provides an understanding of the level of variation inherent in 2D DCE-US imaging of tumours and revealed several sources of variation that need to be explored further. Overall, AUC appears to be the most repeatable metric. The higher variation in PE indicates that variability due to the manual injection of microbubbles may be significant. Future studies, discussed in chapter 6 and 7, used a controlled injection which was shown to improve repeatability in kidneys [163] and tumours [212].

Further, the variability in AT and WIT was speculated to be caused by changes in the heart and breathing rate of the mouse. Physiological animal monitoring was not carried out in this study, due to constraints with the animal setup for imaging. Monitoring of the heart and breathing rate during imaging should be done to evaluate their influence on the change in TAC metrics over repeat injections. This will also be relevant to longitudinal imaging to ensure that measured changes in

DCE-US metrics are reflective of changes in tumour perfusion and are not artefactual.

Next, as suggested by the literature, the increase in AT and WIT and decrease in PE may be caused by rupture of the tumour endothelium. This may be tissue-specific since evidence of the change is not present in all organs or tumour models. To better understand the observed change, the repeatability of DCE-US imaging was assessed in a normal tissue, the kidney, to determine if these effects are tumour-specific and is discussed in chapter 6.

Furthermore, the repeatability assessment carried out here did not consider the interday variability of DCE-US. Changes in cannula, microbubbles' vial and imaging plane, as would happen with longitudinal imaging, are all expected to contribute to the variation. Interday variation is challenging to assess in a tumour model due to expected growth of the tumour and changes in vasculature, between timepoints. Therefore, interday variability was also examined in the kidney which is expected to have minimal change between imaging timepoints and is discussed in chapter 6.

## **5.7 Conclusion**

The experiments described in this chapter provide encouraging evidence for the ability of DCE-US imaging to examine pretreatment vascular features and radiation-induced vascular changes that are important for overall tumour response. The variation observed between repeat DCE-US warrants further investigation of the precision of DCE-US imaging.

# 6 CHAPTER Repeatability of the 2D and 3D DCE-US time-amplitude curve metrics of the renal vasculature

## 6.1 Introduction

The repeatability of DCE-US imaging in tumours reported in Chapter 5 warrants further investigation to identify and potentially eliminate the sources of variation seen in some metrics. Improved technical precision enables more reliable detection of biological changes and therefore increases the utility of an imaging biomarker [47].

The repeatability of DCE-US imaging between timepoints (interday repeatability), which is needed for reliable longitudinal monitoring of vasculature is expected to be greater than the variation reported in Chapter 5 where repeat imaging was carried out on the same day (intraday repeatability). This is because several additional sources of variation may be introduced, including changes in the microbubble vial and/or batch, the cannula, the patency of cannulation, and the challenge of reproducing the 2D imaging slice from one day to the next. Misalignment of the tumour scan position in liver metastases led to a median variation between -15% - 16% in bolus TAC metrics [145], while a misalignment of the scan position by 2 mm in a xenograft breast cancer model caused a variation ranging from 6.4 – 40.3 % in DCE-US metrics [131]. It is expected that 3D DCE-US imaging of the entire subject volume (i.e., the whole tumour) can overcome this source of variation and is hypothesised to improve the interday repeatability. A 3D DCE-US imaging technique was developed at the ICR using continuous sweeping of a 1D ultrasound transducer to image a volume of interest. The main limitations associated with the technique, relative to 2D DCE-US using the same array, are the reduced temporal sampling of the TAC and that different points on the TAC are associated with different locations in the tumour. *In vitro* study of this 3D DCE-US method showed that, for flow in large simulated blood vessels and anisotropic flow along aligned bundles of simulated microvessels in

phantoms, the TACs at the lower sampling rate (1.5 Hz) were similar to the well-sampled 2D TACs (10 Hz), so long as, when the mechanical scan direction was parallel to the flow direction, corrections were made to account for the different time of acquisition of the different 2D scan planes in the 3D dataset with variation within the measurement repeatability [165]. Unfortunately, a phantom that is stable over time but with isotropic or heterogeneous flow direction from one location to another (i.e., tumour-like) did not exist with which to compare the performance and study the reproducibility and repeatability of 3D and 2D DCE-US. In this chapter, the mouse kidney is employed for that purpose.

Interday DCE-US repeatability is ideally evaluated in a tissue with vasculature that is stable across a few days to avoid confounding vascular changes. It is possible that due to the rapid proliferation of tumour cells and resulting tumour growth, the tumour vasculature is not stable over a few days, and therefore a normal tissue model is needed. The kidney was chosen for the evaluation of repeatability based on its high blood flow, which permits the use of a smaller injection volume for DCE-US imaging and thus makes it possible to perform three injections within one day. Further, the perfusion of the kidney is spatially heterogeneous, both in vascular volume and (as mentioned above) flow direction and could to some extent mimic the heterogeneity present in tumours, providing a suitable model for the evaluation of mechanically swept 3D DCE-US of tumours. Heterogeneity in the kidney arises from the different perfusion in the renal cortex versus the renal medulla (Figure 6-1). Following intravenous injection, contrast agent first enhances the cortex and then gradually fills the outer and inner medulla [221], and has lower peak enhancement [222, 223] in the medulla since that includes a smaller proportion (10 %) of the total renal blood flow [223]. An additional advantage of employing the kidney as a model is that, using the apparatus described below, both kidneys could be imaged, increasing the number of ROIs that could be used to examine the repeatability.

The kidney has been used as model of normal tissue repeatability in several other studies. Specifically for the evaluation of the capability of 3D DCE-US, a rat kidney model reported a standard deviation of 10 % for the reperfusion time between kidney imaging slices, which was defined as the time to reach 20 % of

peak intensity following a disruption pulse in a disruption-replenishment sequence. In contrast, repeat calculations of the reperfusion time from the whole kidney volume had a standard deviation of only 3 %, even in the presence of transducer offsets [151].

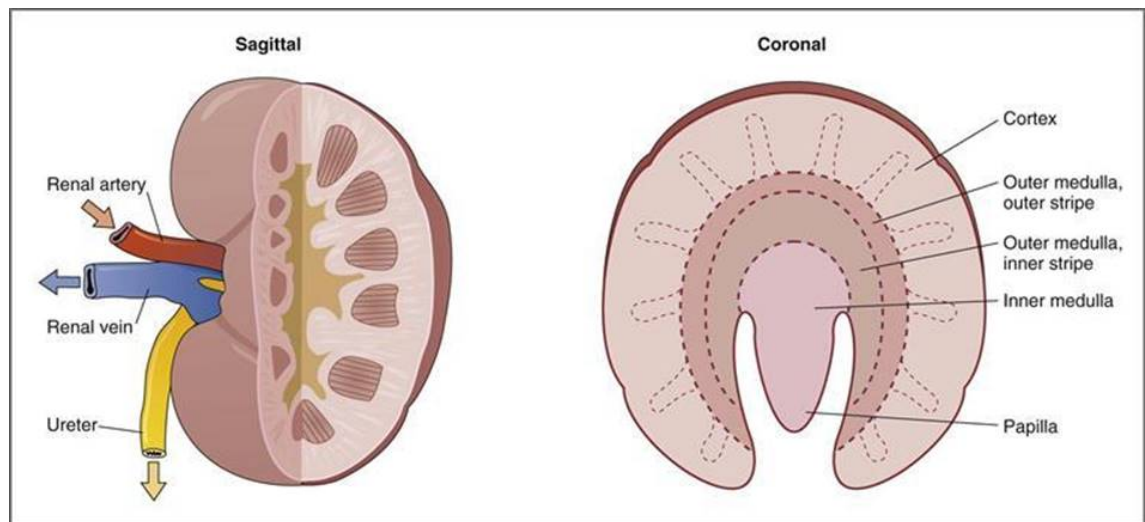


*Figure 6-1: Anatomical structure of the kidney from [224]. In this study, DCE-US imaging was carried out with the imaging plane of the transducer aligned with the coronal plane shown on the right.*

### 6.1.1 Aims

The work described in this chapter aimed to assess the repeatability (intraday and interday) of mechanically swept 3D DCE-US and determine the improvement that it offers, if any, over 2D DCE-US. Additionally, DCE-US metrics of repeat injections were compared to determine if there was a systematic change in DCE-US metrics between repeat injections to determine if the observed systematic changes observed in chapter 5 between repeat injections are tumour-specific.

## 6.2 Materials & Methods

### 6.2.1 Study design

The study cohort included six mice, 3 each for 2D and 3D DCE-US imaging. Imaging and DCE-US data acquisition were carried out at three timepoints per mouse, separated by 6 to 10 days. Not all mice were imaged on the same days due to time constraints imposed by concurrent studies. The study timepoints are given in Table 6-1. The focal length used was 20 mm and animals were set up such that the centre of one the kidneys (typically the left) was at 20 mm.

Animals were between 10 – 14 weeks old and 19 – 30 g when imaged. This is in line with the characteristics of tumour-bearing mice used for radioresponse studies (Chapters 4,5, and 7).

*Table 6-1 : Summary of study timepoints.*

<b>Numbers of mice</b>	<b>Timepoints: Days</b>
<b>2D: 3</b>	1: 0
<b>3D: 3</b>	2: 6 or 9
	3: 16 or 19

### 6.2.2 Animal setup

Mice were anaesthetised using a ketamine-xylazine–acepromazine combination (4 µL/g) injected intraperitoneally. Mice were imaged in the prone position to view both kidneys. The animal setup and procedure for cannulation were as described in section 3.2.2

### 6.2.3 DCE-US imaging

3D DCE-US imaging was performed as described in section 3.2.5. 2D imaging used the same setup, including the water bath and the motion platform holder, but without running the motion controller. The 2D imaging cross section was chosen to be the largest kidney cross sectional area for each kidney, wherever possible. A volume of 30  $\mu\text{L}$  of contrast agent was injected using an infusion pump with a rate of 2.18 mL/min for each acquisition, with three injections per imaging timepoint. To remove residual microbubbles after an injection, the cannula was flushed with 10 – 15  $\mu\text{L}$  of saline and the kidney was scanned with a voltage of 15 V, the highest voltage possible with the scanner to produce maximum MI, to destroy remaining microbubbles for a period of 5 minutes. Repeat injections were separated by 15 minutes. An example of a typical contrast enhancement imaged with 2D imaging at the centre kidney cross sections shown in Figure 6-2 .

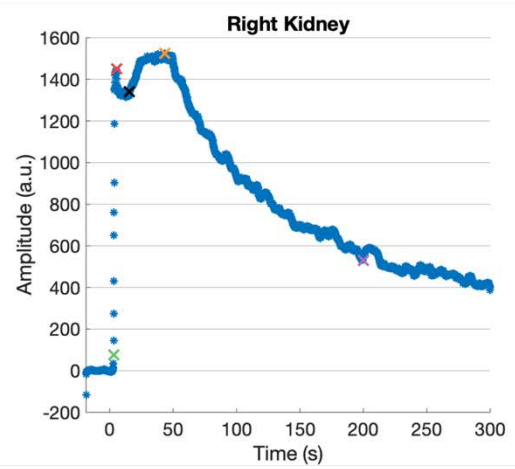
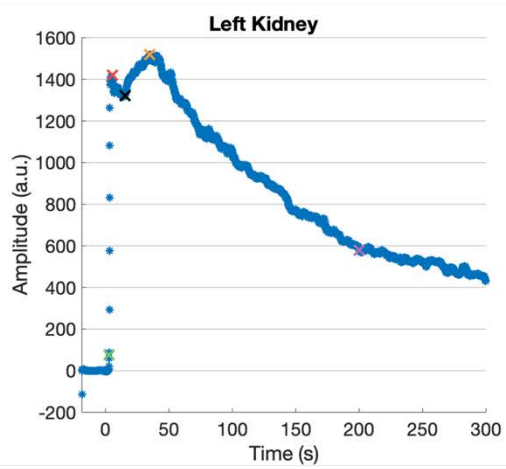
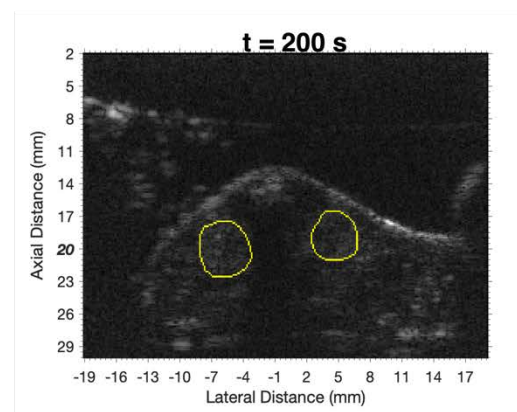
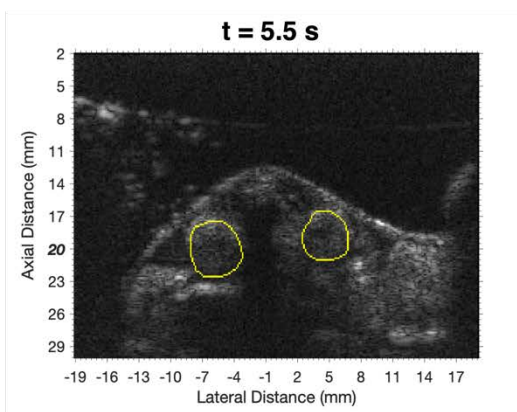
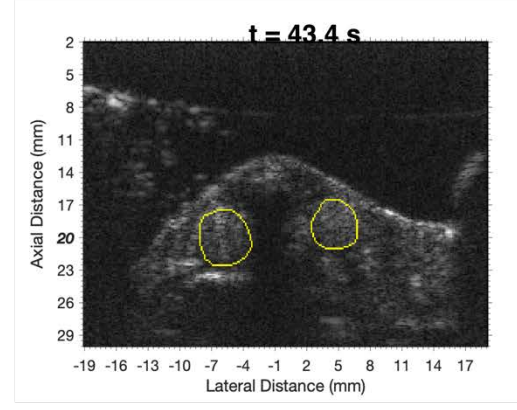
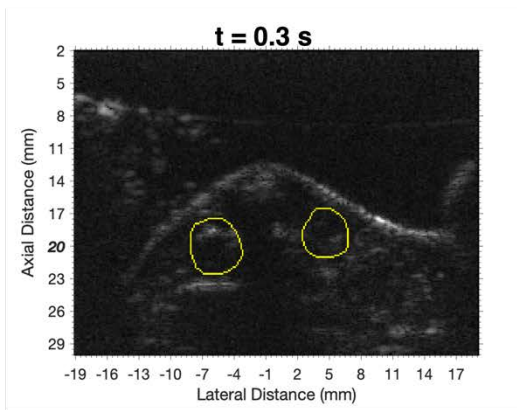
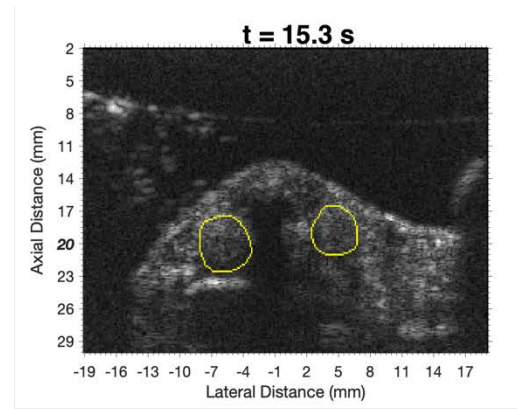
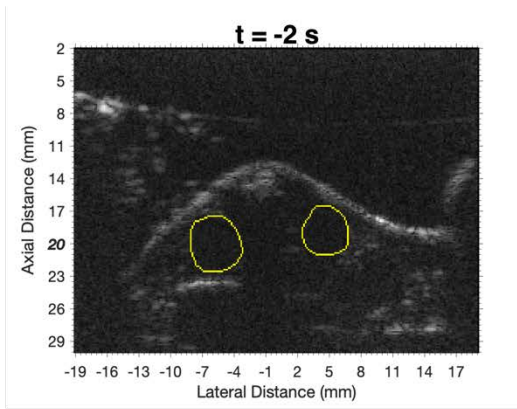


*Figure 6-2: Representative example of 2D DCE-US imaging of the centre cross section of the left and right kidney (outlined in yellow), with the corresponding TACs shown below. Contrast frames shown correspond to the marked timepoints on the TAC;  $t = -2$  s is the time before contrast injection,  $t = 0.3$  s is the arrival time (green cross), with contrast seen in the cortex.  $t = 5.5$  s shows maximum enhancement in the cortex and minimal enhancement in the medulla (red cross).  $t = 15.3$  s shows decreased enhancement (black cross),  $t = 43.4$  s corresponds to the peak enhancement with enhancement seen in the cortex and medulla (yellow cross), and  $t = 200$  s represents contrast wash-out (purple cross).*

#### 6.2.4 DCE-US analysis

The kidneys' cross-sectional outline was delineated in each imaging slice, and the DCE-US metrics were calculated from whole-ROI TACs in 2D imaging, and whole-VOI TACs in 3D imaging with motion compensation and temporal filtering as detailed in section 3.3.2. Image acquisitions that had incomplete injection of the contrast volume by the pump or, for 3D DCE-US, delayed start of transducer motion causing contrast agent wash-in to be missed, were excluded from the analysis.

#### 6.2.5 Intraday variation

Intraday variation describes the repeatability of DCE-US imaging carried out on the same day (at one imaging timepoint), without animal repositioning, using the same cannula and the same vial of contrast agent. The variation between two injections was calculated according to equation 5-1 (see Chapter 5). For each day, for each kidney, for each TAC metric, 3 values of the intraday variation were calculated (i.e., Inj 1 vs Inj 2, Inj 2 vs Inj 3, Inj 1 vs Inj 3) and the mean intraday variation was calculated. This method was used instead of using the coefficient of variation because of the limited sample number. For an animal with a complete imaging dataset, 3 values of intraday variation per kidney were obtained from the 3 imaging timepoints.

#### 6.2.6 Interday variation

Interday variation describes the repeatability of DCE-US imaging carried out (on different days) with animal repositioning, a new cannula and a new vial of contrast

agent, with the assumption that there is no change in functional vasculature between the timepoints. Care was taken to acquire DCE-US data in matched time sessions (morning or afternoon) for each day. The interday variation between the  $n^{\text{th}}$  injection carried out on consecutive days for all injections (e.g., Inj 1 (day 0) vs Inj 1 (day 6), Inj 1 (day 6) vs Inj 1 (day 16), Inj 2 (day 0) vs Inj 2 (day 6), etc.) was calculated using equation 5 -1 and the mean interday variation was calculated. The variation was calculated between matched injections to account for potential effect of repeated injections at one imaging timepoint. For an animal with a complete imaging dataset, 2 values of interday variation per kidney were obtained from the 3 imaging timepoints.

### *6.2.7 Variation of TAC*

Another measure of repeatability was sought by examining the shape of the TAC, which was found to vary in this experiment. The similarity of the TAC shape was evaluated using normalized cross correlation of one TAC with another. A correlation coefficient of TACs was calculated for intraday and interday imaging in the same manner as intraday and interday (TAC metric) variation.

### *6.2.8 Statistical testing*

DCE-US metrics from the three injections on the same day were assessed using the non-parametric signed Wilcoxon rank test to identify any systematic changes. The intraday and interday variation for each imaging method (2D or 3D) were compared using the Mann Whitney U test to assess whether interday variation was increased due to the additional sources of variations. The intraday and interday variation were compared between the imaging methods using the Mann Whitney U test to assess if 3D imaging improves the intra- or interday repeatability. The coefficients of correlation between TACs were assessed using the same tests.

## 6.3 Results

### 6.3.1 DCE-US metrics from repeat injections

Figure 6-3 shows DCE-US metrics (normalised to the first injection) from three repeat injections performed on the same day obtained from 2D and 3D imaging, showing several significant differences between the first injection and consecutive injections. There was a trend in increasing PE between repeat injections, compared to the first injection PE increased at the 2<sup>nd</sup> and 3<sup>rd</sup> injection in 3D imaging ( $p = 0.011$ ,  $0.004$ , respectively), and at the 3<sup>rd</sup> injection in 2D imaging ( $p = 0.002$ ). AUC increased between the 1<sup>st</sup> and 3<sup>rd</sup> injection only for 2D imaging ( $p = 0.001$ ), remaining stable for 3D imaging. For 3D imaging only, MTT and WOUT both decreased significantly at the 2<sup>nd</sup> injection ( $p = 0.004$  and  $p = 0.005$ ) and 3<sup>rd</sup> injection ( $p = 0.0001$  and  $0.0006$ ), compared to the 1<sup>st</sup> injection. AT increased significantly for the 3<sup>rd</sup> injection ( $p = 0.002$ ) in 3D imaging. WIT for 2D imaging decreased at the 3<sup>rd</sup> injection ( $p = 0.048$ ).

The TACs presented in Figure 6-4 demonstrate the trends observed above for TAC metrics derived from 3D imaging and 2D imaging, i.e., greater PE for repeat injections, the quicker contrast washout for repeat injections in whole-VOI TACs ( Figure 6-4 – left), and the quicker wash-in time in whole-ROI TACs ( Figure 6-4 – right). There were no systematic changes between repeat injections on different days, i.e., there was no significant difference in any TAC metric measured at the first imaging timepoint compared to those measured at the later imaging timepoints (data not shown).

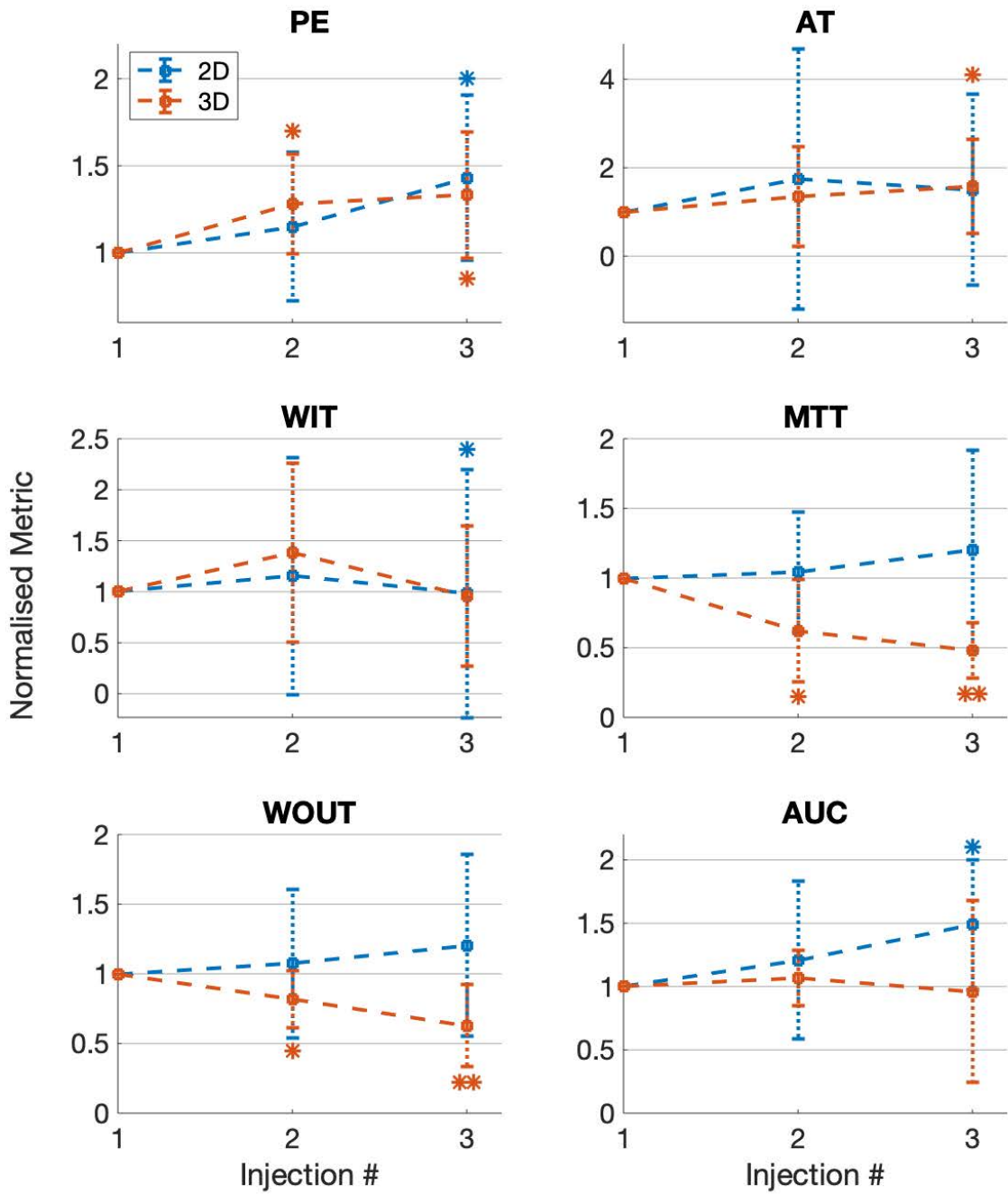


Figure 6-3: Mean DCE-US metrics (across 6 kidneys on 3 days) from 2D (blue) and 3D (orange) imaging for three consecutive injections. Metrics are shown normalised to their value for the 1<sup>st</sup> injection. Error bars represent the standard deviation of this normalised value over the 6 kidneys for each injection. Asterisks denote statistical significance in the change from the first injection (\*  $p < 0.05$ , \*\*  $p < 0.001$ ) and are shown in the same colour for each method.

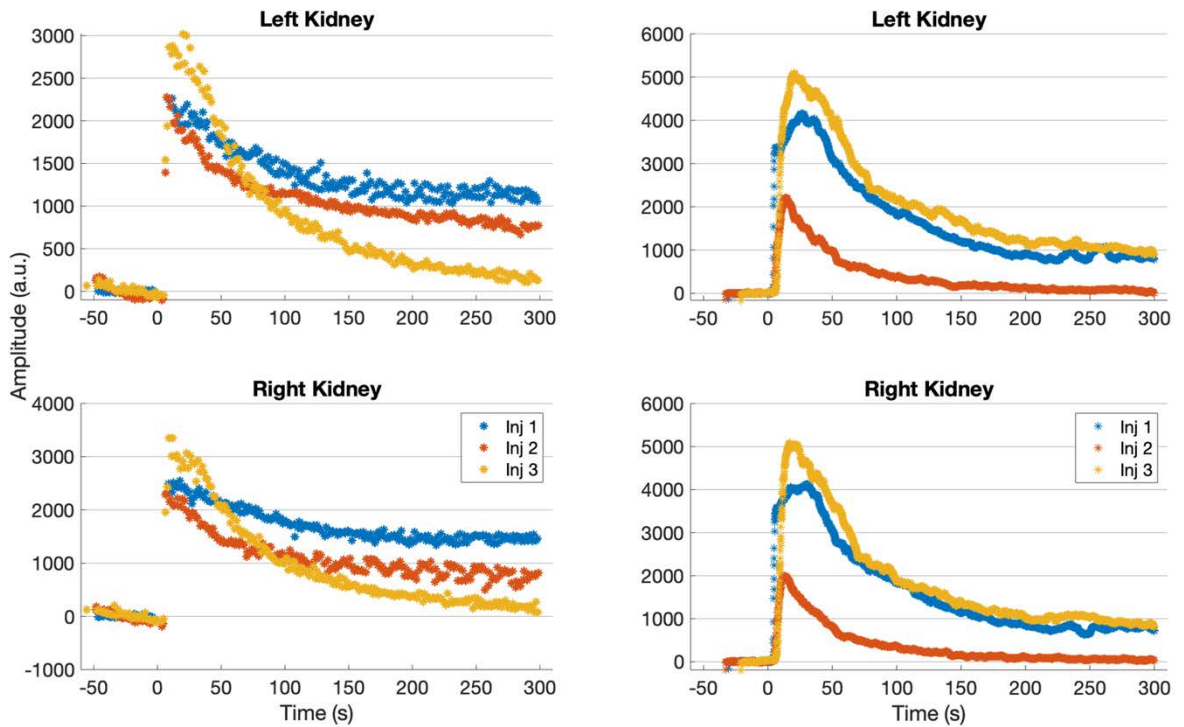


Figure 6-4 : Repeat TACs (whole-VOI) of the kidney volume (left) and (whole-ROI) of the biggest kidney cross section (right) for the left (top) and right (bottom) kidney in two mice. Three TACs are shown representing three consecutive injections in the same imaging session. Whole-VOI TACs show an increase in PE and decrease in MTT and WOUT between injection 1 and consecutive injections. Whole-ROI TACs demonstrated an increase in PE and a decrease in WIT between consecutive injections.

### 6.3.2 Comparison of intraday and interday absolute variation

The absolute intraday and interday variations of metrics obtained from 2D and 3D DCE-US are shown in Figure 6-5 . There were no significant differences between the absolute interday and intraday variation for 2D DCE-US. 3D DCE-US had significantly greater intraday variation in MTT compared to interday ( $p = 0.0081$ ). No other metrics showed a significant difference in intraday and interday variation for 3D imaging.

### 6.3.3 Comparison of 2D and 3D DCE-US absolute variation

3D imaging had greater intraday absolute variation of MTT compared to 2D imaging ( $p = 0.032$ ). No other DCE-US metrics showed a significant difference

between 3D and 2D in the intraday absolute variation. With the exception of AUC, 3D imaging had smaller interday absolute variation compared to 2D imaging. However, the difference in variation was only significant for WOUT (0.002).

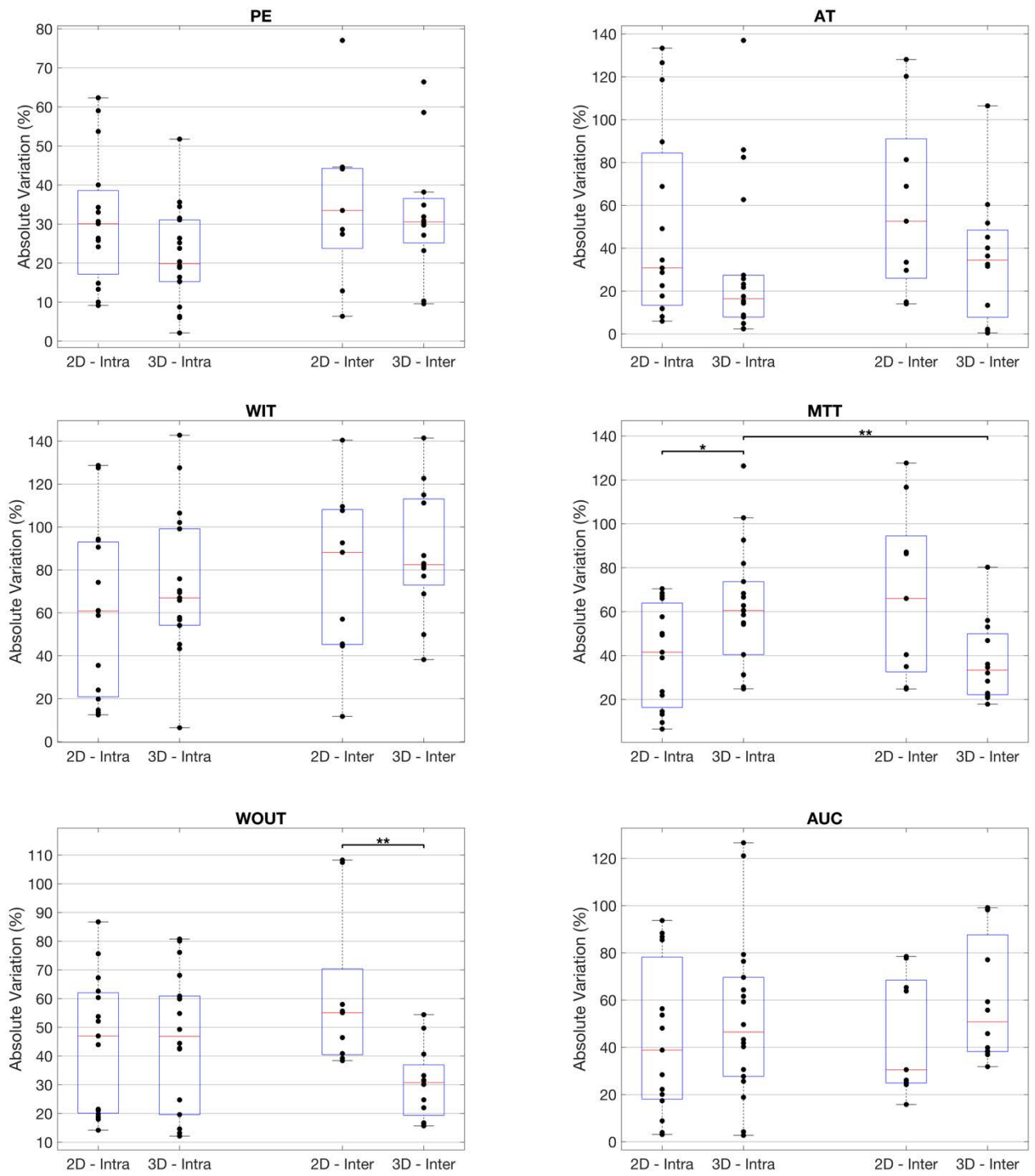


*Figure 6-5: Intraday and interday absolute variation of DCE-US metrics obtained from whole-ROI (2D) and whole-VOI TAC (3D) imaging. Each datapoint corresponds to the variation calculated in one kidney.*

### 6.3.4 Correlation between TACs

The intraday and interday correlations between TACs for 2D and 3D imaging are shown in Figure 6-6. The correlations between TACs were not significantly different between 2D and 3D imaging, whether the TACs were obtained on the same day on different days, but there was a trend for better interday TAC correlation using 3D imaging ( $p = 0.07$ ); specifically, for 2D imaging, interday correlation coefficients tended to be lower than intraday values, whereas this did not happen for 3D imaging. Additionally, low correlation coefficients corresponded to the highest variation seen in DCE-US metrics. For example, the lowest correlation of 0.85 for interday with 2D imaging (Figure 6-6 -right) was found for TACs that had a variation of 120 % in MTT and 78 % in AUC (Figure 6-5).

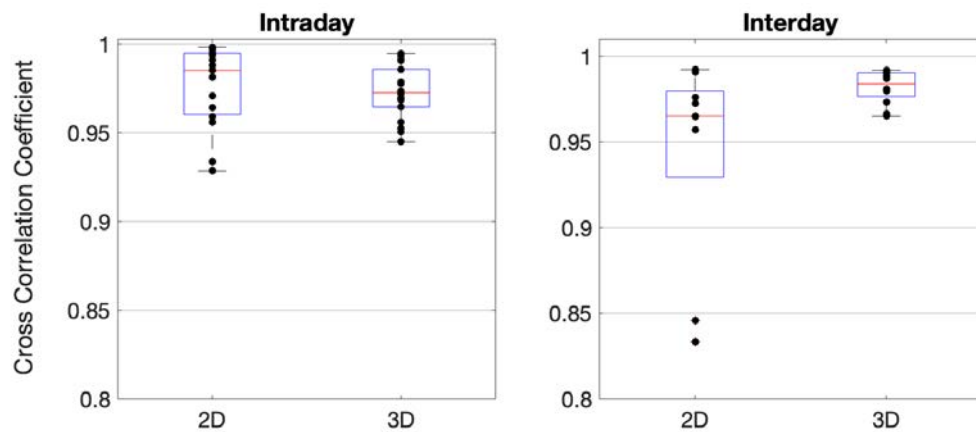


Figure 6-6: Correlation of TACs compared intra- and inter- day for 2D and 3D imaging.

## 6.4 Discussion

Reliable longitudinal monitoring of functional vasculature using DCE-US imaging requires good technical repeatability. 3D DCE-US imaging was hypothesised to be more precise than 2D DCE-US in quantifying tumour vascular changes as it examines the heterogenous whole tumour volume vasculature, and it overcomes the variability resulting from trying to reproduce an imaging slice within a tumour

from one imaging timepoint to the next. The intraday and interday variation of 2D and 3D DCE-US imaging was investigated in the kidney. Imaging of normal tissue provides a way of examining interday repeatability as, unlike in a tumour, few/no changes in the vasculature would be expected between timepoints. The kidney was chosen because its vascular volume is sufficient to allow imaging with a volume of contrast agent small enough to permit three injections to be given in each imaging session whilst adhering to the maximum volume of fluid that can be injected, as prescribed by Home Office project license constraints. Further, the kidney could be identified relatively easily with B-mode imaging, and the animal could be positioned to image two kidneys at once.

Repeat injections had systematic changes in PE, MTT, WOUT and AUC (Figure 6-3). Increases in PE were observed for 3D and 2D imaging and in AUC for 2D imaging. These increases are in agreement with the increase in peak enhancement and AUC seen in the feline renal cortex and medulla [217] using 2D DCE-US imaging, which was suggested to be due to reduced filtering of microbubbles by pulmonary macrophages, or a possible interaction of microbubbles with the vasculature leading to vasodilation and greater blood volume. An alternative cause for the increased PE and AUC may be the effects of the anaesthetic agent. Ketamine-xylazine-acepromazine causes a reduction in mean arterial pressure and heart rate at the onset of anaesthesia, followed by a gradual increase up to normal levels as the mouse wakes up [225]. An increase in blood pressure and heart rate between consecutive injections could lead to the observed changes.

A significant decrease in MTT and WOUT with repeat injections was observed using 3D imaging, but not with 2D imaging. A decrease in WOUT was also observed in the renal cortex of feline kidneys [217]. This may explain why the change was not observed with 2D imaging, since the centre kidney cross section that is imaged in the 2D setting has a bigger proportion of medulla tissue than cortex, and therefore the whole-ROI TAC would have a larger contribution from the medulla and may not capture changes specific to the cortex unlike 3D imaging which includes the whole cortex tissue.

The intraday repeatability of 2D DCE-US imaging of the kidney in mice has been reported previously by Dizeux et al [213]. Using controlled injections of SonoVue® microbubbles, coefficients of variation, calculated as the standard deviation of four injections divided by their mean of 4 – 12.8 % were reported, substantially lower than the variation observed here (median variation > 20 % in all metrics). However, whilst Dizeux et al calculated the CV for the cortex only, in the current study the variation was calculated for the entirety of the kidney ROI or VOI, because it was difficult to accurately delineate the cortex. DCE-US metrics derived from the cortex had better repeatability than those of the medulla in feline kidneys [223] which may explain the observed lower variation in the study by Dizeux et al. Moreover, the authors used a saline flush of 80 µL following injection of the microbubbles, which is said to improve mixing of the contrast agent-blood solution and can minimise variation in the injected microbubbles volume. Unlike the present study, no systematic variation in any of the metrics was observed in the kidney cortex over a series of four injections. Likely reasons for the discrepancy include the different effects of the inhalable anaesthetic they used, compared to the injectable anaesthetic used here, and that they did not use a high MI insonation sweep between injections as used here to clear residual contrast agent, which is suggested to induce changes in the capillaries [217, 219]. Further work is required to confirm the biological or physiological cause behind these changes.

Interestingly, the intraday variation in DCE-US metrics for both 2D and 3D imaging of the kidney was generally found to be greater than the variation in the tumour data reported in Chapter 5. This was despite injections being performed manually for the tumours compared to using a syringe pump for the kidneys; Dizeu et al. [11] found that manual injections caused more variability in the time to peak (equivalent to the sum of AT +WIT) and the wash-in and wash-out rates in mouse kidneys than did injections controlled with a syringe pump. In the current study, even though DCE-US was expected to be more repeatable in the kidney than in tumour, the differences in repeatability may be related to several other difference between the experiments, such as the different imaging scanners (Aplio versus Verasonics), the different volume of injection, the use of two repeats

compared to one, and the different anaesthetics agent. The repeatability of tumour 3D DCE-US imaging was explored subsequently (Chapter 7) to elucidate some of these factors.

Overall, there was some, but relatively little, evidence to support the hypothesis that longitudinal (interday) 3D imaging was more repeatable than longitudinal 2D imaging. Only WOUT demonstrated better interday variation with 3D imaging than with 2D (Figure 6-5), indicating the ability of 3D imaging to minimise the variation introduced when attempting to reproduce a single imaging position for successive timepoints. Also, no metrics showed increased interday variation compared to intraday using either 2D or 3D imaging methods. For 2D imaging, where the imaging plane was fixed for intraday but not interday, this also suggests that reproducing the central imaging plane does not contribute significantly to the variation. The similarity between interday and intraday repeatability implies that the vial of microbubbles and the cannula, which change between imaging timepoints, have little influence on the variation in metrics. Instead, the main sources of variation are present when imaging on the same day. The suspected sources of variation include microbubbles preparation and resuspension [152], subject physiological changes and the systematic change in metrics between repeat injections. Indeed, intraday variation of MTT was significantly higher than interday, because of the large systematic decrease in MTT observed over repeat injections during one period of anaesthesia. WOUT also had large systematic reduction with each sequential injection during a single period of anaesthesia and its intraday variation was also larger than its interday variation, albeit not significantly so. No other study comparing inter and intraday variation of DCE-US could be found in the literature.

## **6.5 Limitations**

The main limitation of the studies is the small number of animals included. This is exacerbated by the inclusion of two kidneys from each subject, meaning that the two data points from each mouse are not independent, and the results should be interpreted with caution.

For the kidney to be a useful model for assessing DCE-US repeatability, it should not include sources of variation that are not present in a tumour. Three such sources have been considered. First, locating the kidney using B-mode imaging was found to be more difficult than subcutaneous tumours, which may have led to poorer image slice reproducibility and increased interday variation. However, this did not appear to have increased the interday variation compared to the intraday variation. Next, the smaller injection volume used per acquisition for the kidney may have caused a proportionally larger variation in the number of microbubbles injected. Finally, the heterogenous perfusion pattern within the kidney, which was crucial to imitate the fact the heterogenous tumour perfusion, has a spatio-temporal enhancement pattern that may not be relevant to DCE-US imaging of some tumours. The early enhancement in the cortex followed by slower enhancement in the medulla produced a second peak in the TAC (Figure 6-2), which can affect quantification and thus the repeatability of PE and WIT. Such an effect has not been observed in any TACs of the tumour models used here. Additionally, higher levels of enhancement in the shallowest subregion of the kidney cortex might have caused attenuation of contrast signal in the deeper regions of the kidney, which introduces another source of variation in the form of a depth-dependent TAC shape. A subregion analysis of centre kidney cross section (2D) TAC demonstrating the attenuation effect within the kidney is shown in Figure 6-7.

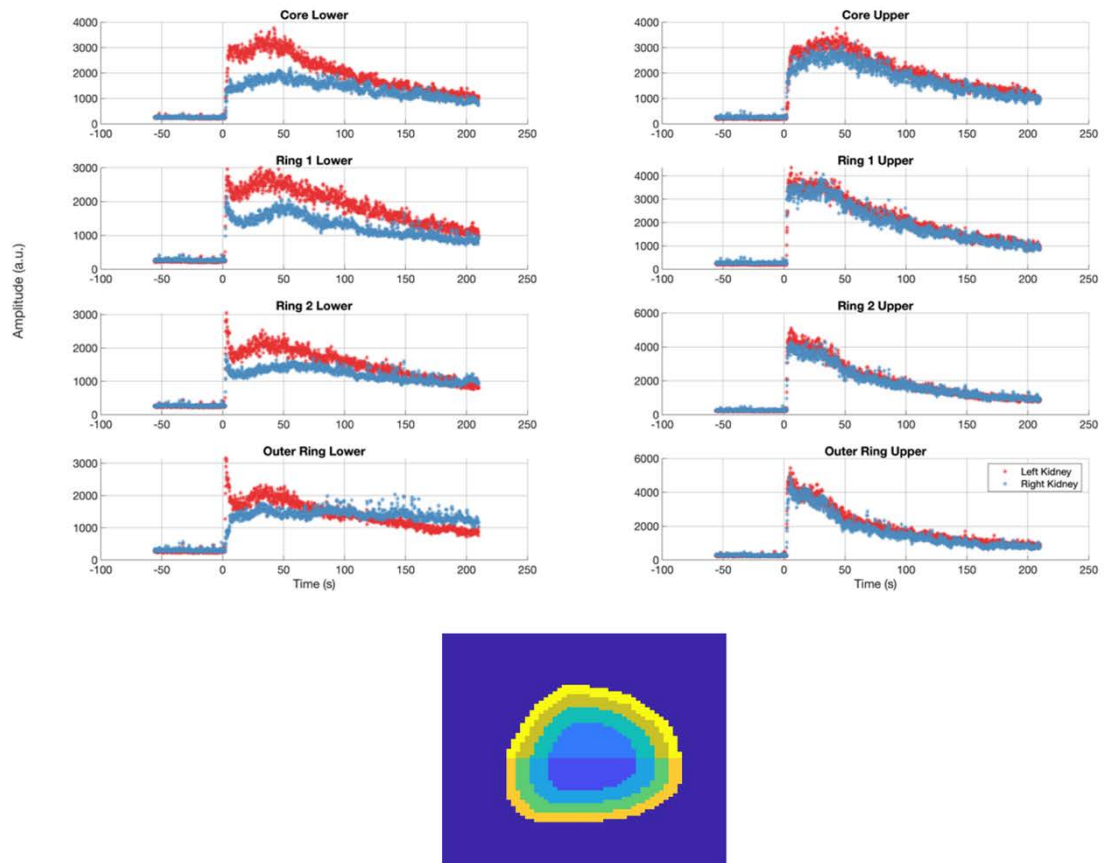


Figure 6-7: Example TACs from 2D imaging of a central kidney slice. The ROI, which covered the whole kidney cross section excluding the kidney boundary, was divided into 8 annular subregions of equal areas. The subregions most distal to the ultrasound transducer ('Outer Ring Lower' and 'Ring 2 Lower') display attenuation as an increase in signal at wash-in followed by a decrease. The subregions are shown in the bottom diagram, with each sub-ROI drawn in a different colour and the distal half of the tumour indicated by darker colours.

## 6.6 Conclusions

The discussed work establishes the repeatability of the proposed 3D DCE-US imaging technique, both intra- and interday using the kidney as a normal tissue model. The results will be helpful for contextualising the vascular changes observed with 3D DCE-US imaging in tumours following radiotherapy and the repeatability of the imaging in tumours. Using the kidney as a tissue model with spatial vascular heterogeneity, it was not possible to confirm the improvement in interday variability by using 3D DCE-US imaging compared to 2D imaging. Furthermore, interday variability was comparable to intraday variability.

# 7 CHAPTER 3D DCE-US for assessment of response to radiation

## 7.1 Introduction

2D DCE-US imaging was able to detect vascular changes that are associated to radioresponse (see Chapter 5). Overall, DCE-US revealed greater vascular damage in the tumours with better response assessed based on tumour regression or growth delay. The difference detected following radiation and the differences between response groups were of a small magnitude, (maximum median change of 40 % for C33A model and 20 % in HN5 model). One reason for the small measured change is the uncertainty associated with 2D DCE-US imaging. This is a result of large intratumour vascular heterogeneity with poor reproducibility of imaging position between timepoints. The importance of intratumour heterogeneity was confirmed through the histogram analysis which demonstrated that radiation-induced vascular changes are not uniform, presumed to be due to the heterogenous radiosensitivity of the vasculature, discussed in section 1.3. These observations lead to the conclusion that changes monitored in the central tumour cross section are unlikely to reflect vascular changes in the rest of the tumour volume, and instead longitudinal imaging of the tumour volume can detect vascular changes more accurately. Three dimensional (3D) DCE-US imaging achieves this and is therefore hypothesised to provide more useful biomarkers of response.

Studies using volumetric contrast enhanced-ultrasound imaging have demonstrated large intratumour heterogeneity of the vasculature and the effect that this can have on calculating vascular changes. In a clinical study of metastatic liver tumours, bolus TAC metrics (PE, AUC and, time to peak (TP)) and disruption replenishment TAC metrics (relative blood volume, relative blood flow) had intratumour coefficients of variation between 0.3 - 0.52 [145]. In a preclinical study with a colon cancer xenograft model, the same DCE-US metrics had coefficients of variation greater than 0.5, and as high as 2.86 [226]. Significant changes in these metrics after anti-angiogenic treatment were around

50 - 60 %, measured using 3D imaging. 2D imaging was unable to identify treatment -induced vascular changes because the changes were of a similar order of magnitude as the intratumour heterogeneity. Changes calculated in the central tumour plane, over- or under-estimated the results of 3D imaging by 57- or 3-fold, respectively. Another study using colon cancer xenograft models reported a significant difference in the change in 3D-DCE US metrics PE and AUC, between responding and non-responding tumours [227]. Using a xenograft breast cancer model, an intratumour variation of 6.1 – 40.3 % in the peak intensity, AUC, and TP metrics obtained was obtained [131].

### *7.1.1 Aims*

Based on the encouraging preliminary findings outlined in Chapter 5, it was hypothesised that 3D DCE-US can detect vascular changes associated with response to radiotherapy. The experiments described in this chapter aimed to:

- 1- Assess the change in 3D DCE-US metrics and their association with radioresponse in the previously established models of head and neck (H&N) and cervical cancer.
- 2- Compare TAC metrics measured using 2D and 3D DCE-US imaging for the assessment of response to radiotherapy.
- 3- Assess the repeatability of 3D DCE-US imaging in tumours.
- 4- Biological validation of 3D DCE-US imaging with CD31 staining of vasculature

## **7.2 Materials & Methods**

### *7.2.1 Study design*

The use of 3D DCE-US imaging was examined in the C33A cervical cancer model (C6 and C7 studies, n = 32 tumours in total) and HN5 head and neck cancer model (H2 and H3 studies, n = 28 tumours in total). Radiotherapy was delivered as described in section 3.4, with a 25 Gy dose for C33A tumours and either a 20 or 25 Gy dose for HN5 tumours. 3D DCE-US imaging was carried out 24 hours before radiotherapy and repeated 72 hours and 1 week post treatment. In the C6 study, which was the first 3D DCE-US radioresponse study carried out, imaging

was also performed 24 hours post treatment, but this timepoint was omitted from later studies due to the observed adverse effects of repeated anaesthetics within a short time interval (48 h).

Anaesthesia for imaging was achieved using Hypnorm™–Hypnovel™ in study C6, while all later studies used a combination of ketamine–xylazine–acepromazine (KXA), as described in section 3.2.2. Further, in the C6 study the focal length was adjusted between imaging sessions, and between animals, to keep tumours of differing depths at the transmit focus. This resulted in a range of focal lengths, which ranged from 9 mm to 20 mm, throughout the study. For subsequent studies, a constant focal length was maintained to minimise this as a potential source of variation. The tumour centre was kept near the focal length of 20 mm, through adjustments of animal positioning and the water bath offset.

### *7.2.2 3D DCE-US imaging*

Three-dimensional imaging was carried out as described in section 3.2.5 using a Verasonics Vantage™ scanner and a Philips ATL L7-4 transducer and continuous transducer translation in the elevational axis along a distance of 20 mm. Sonazoid™ contrast microbubbles were injected using an injection pump for a controlled injection speed and pressure. A flow rate of 2.18 mL/min was used.

### *7.2.3 DCE-US image analysis*

The selection of frames containing the tumour volume and the motion correction were carried out as described in section 3.3.2.1. To assess the benefit of 3D imaging as opposed to 2D imaging, DCE-US metrics of perfusion were obtained for the tumour centre mimicking the 2D imaging reported in chapter 5, and for the tumour volume, representing the global perfusion of the tumour.

#### 7.2.3.1 Centre tumour–ROI and whole-VOI analysis

TACs representing the perfusion of an imaged tumour slice (centre tumour-ROI TACs), and a TAC of the tumour volume (whole-VOI TAC) were generated as described in section 3.3.2.3. DCE-US metrics, Peak enhancement (PE), arrival time (AT), wash-in time (WIT), modified transit time (MTT), wash-out time (WOUT), and the area under the curve (AUC), were calculated at each timepoint from the TACs.

#### 7.2.3.2 Metric maps and histogram analysis

Intratumoural heterogeneity was characterised using histograms derived from pixel-wise metric maps of each tumour ROI as described in section 3.3.2.4. Histograms of all pixels in whole-ROIs (from each tumour slice) were combined to generate a tumour volume histogram. The histogram distribution was described using standard deviation (SD), coefficient of variation (CoV), modified full-width half-maximum (mFWHM), skewness and kurtosis as introduced in section 3.3.2.6. Here again, the histogram parameters of the centre tumour-ROI were examined to assess 3D compared to 2D imaging.

The change in a metric at a timepoint following treatment compared to pretreatment was calculated as the difference in the metric at the two timepoints divided by the pretreatment metric, using equation 3 – 2. Significant changes in the metrics between pre- and post-treatment were identified using the Wilcoxon signed-rank test, while differences in the change of the metrics between response groups, or between treated and control tumours, were assessed using the Mann-Whitney U test. Pretreatment DCE-US metrics of centre tumour–ROI and whole-VOI were also compared between response groups.

#### 7.2.4 *Comparison of DCE-US quantification between studies*

To elucidate any differences between the results in this chapter and those of earlier studies (see Chapter 5), the centre tumour-ROI metrics acquired using 3D imaging and the Verasonics Vantage scanner at pretreatment were compared to

those of earlier studies (whole-ROI acquired using 2D imaging using the Aplio scanner), for each tumour model using the Mann Whitney U test.

#### *7.2.5 Agreement of whole-VOI and centre tumour-ROI TAC metrics*

The DCE-US metrics of the centre tumour-ROI and whole-VOI and their changes following treatment were compared to examine their agreement in the two tumour models. A ratio of centre-tumour metric (or change) to whole-VOI metric was calculated at each timepoint. Agreement between the methods is indicated by a value of 1, while greater values indicate overestimation of central plane changes, and vice versa. Significant differences in the metrics, indicating either over- or underestimation by the centre-tumour ROI, was assessed with the Wilcoxon signed-rank test.

#### *7.2.6 3D DCE-US repeatability*

The repeatability of 3D DCE-US imaging was assessed at the experimental endpoint when tumours approached the size limit set out by the Home Office project licence. Two acquisitions were carried out, using the same settings as used for all other timepoints. Following the first acquisition, saline was injected manually to flush out any microbubbles left in the dead space of the cannula. In addition, the tumour was scanned with voltage of 15 V, the highest voltage possible with the scanner to produce maximum MI to destroy remaining microbubbles, for a period of 5 minutes with continuous transducer translation. The two contrast injections were separated by 15 to 20 minutes and used microbubbles from the same vial. The variation in centre tumour-ROI and whole-VOI DCE-US metrics, as well as histogram parameters from two repeat acquisitions, was calculated as the difference in the two metric values divided by their average (equation 5 -1). Additionally, the repeatability of metric maps of the centre slice was assessed using the correlation coefficient as described in section 5.3.3.5. Here the centre tumour slice was taken as the middle slice without attempting to correlate the most similar ROIs; this was deemed adequate based on visual comparison of the chosen slices.

### 7.2.7 Validation of 3D DCE-US imaging with histopathology

Biological validation of DCE-US imaging was carried out at endpoint imaging. Excised tumours were cut in half, fixed in formalin, and stained with CD31 and haematoxylin counterstain as described in section 3.5.6. The agreement of CD31 staining and the DCE-US metric maps was assessed visually between the stained section and the most similar imaged tumour slice.

## 7.3 Results

### 7.3.1 Characterisation of radiation response

#### 7.3.1.1 HN5 tumour model

Growth of HN5 tumours in H2 and H3 studies is shown in Figure 7-1. All treated tumours regressed after radiation treatment. Complete and partial responders were differentiated based on survival of 80 days or longer following radiotherapy. This corresponded to 6 complete responders and 5 partial responders. Three animals with treated tumours were culled within 10 days of treatment because of weight loss or severe ulceration, or did not recover from anaesthesia, and were excluded from the analysis.

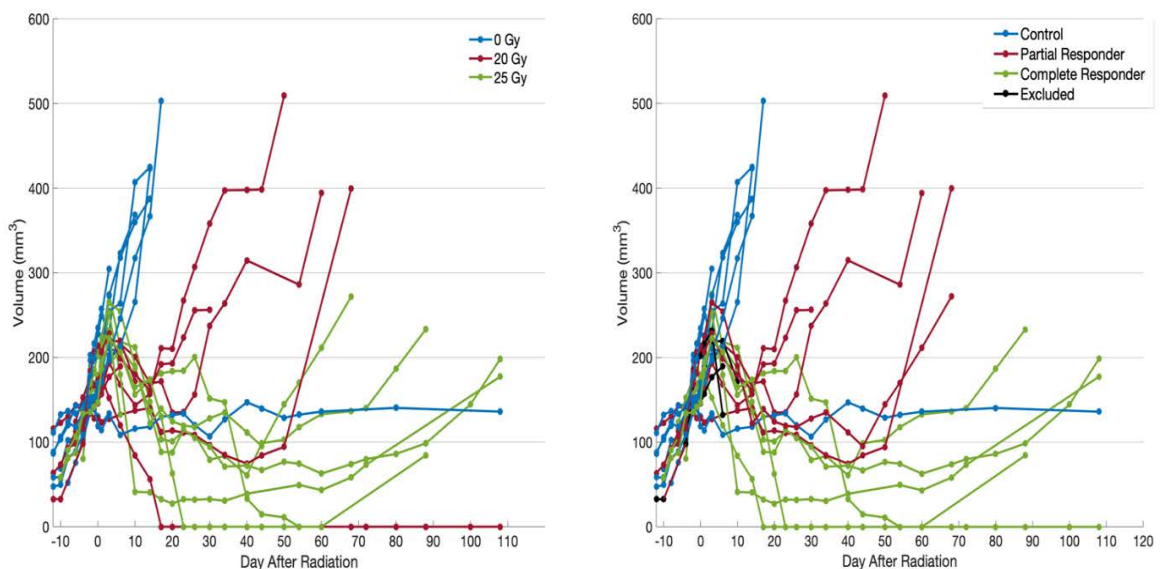
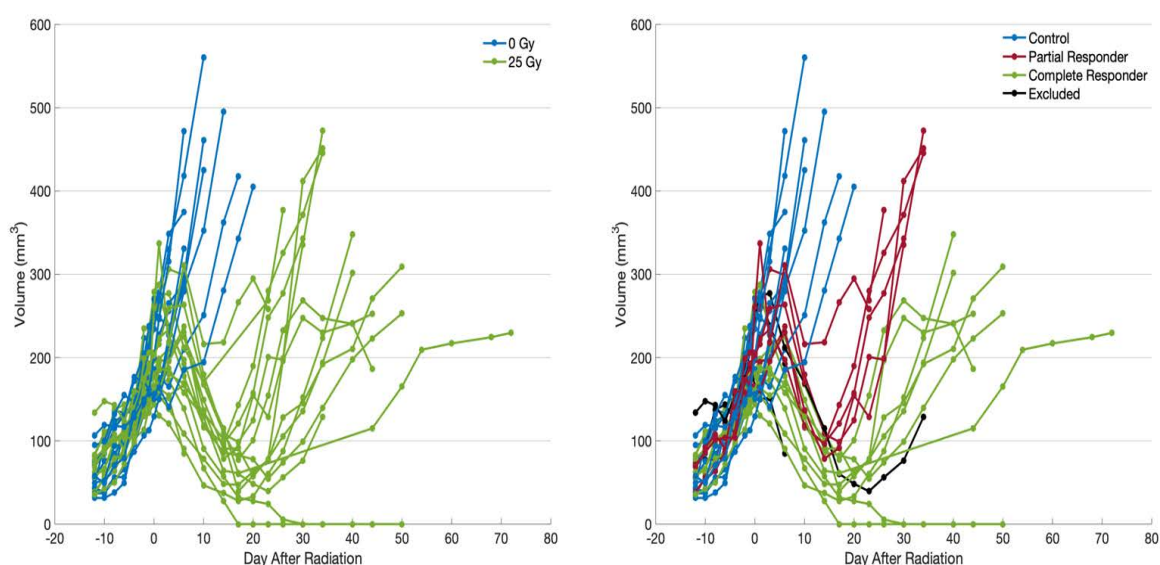


Figure 7-1: HN5 tumour growth measured using callipers. Irradiation was carried out at day = 0 at a tumour volume of 150 mm<sup>3</sup>. Individual tumours are grouped according to radiation dose (left) or response (right). Treated tumours that regrew to the tumour licence limit within 80 days of radiation were classified as partial responders, and tumour and complete responders are tumours that did not reach the license limit before 80 days.

### 7.3.1.2 C33A tumour model

Growth of C33A tumours irradiated with 25 Gy in C6 and C7 studies is shown in Figure 7-2. As for the HN5 model, all treated tumours regressed. Complete or partial response was designated based on survival for 40 days or longer after irradiation. Nine tumours were classed as complete responders and six as partial responders. Three treated tumours were culled due to weight loss before day 40 and therefore excluded from the analysis.



*Figure 7-2: C33A tumour growth measured using callipers. Irradiation was carried out at day = 0 at a tumour volume of 150 mm<sup>3</sup>. Individual tumours are grouped according to radiation dose (left) or response (right). Treated tumours that regrew to the tumour licence limit within 40 days of radiation were classified as partial responders, and tumour and complete responders are tumours that did not reach the license limit before 40 days.*

### 7.3.2 Agreement of whole-VOI and centre tumour-ROI TAC metrics

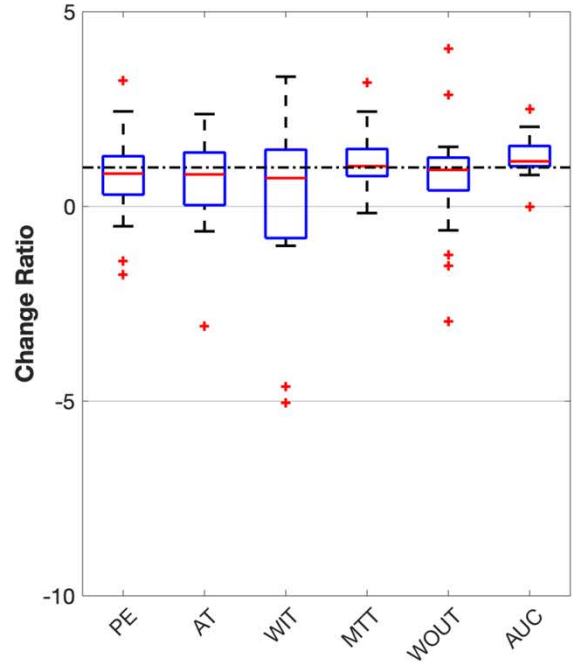
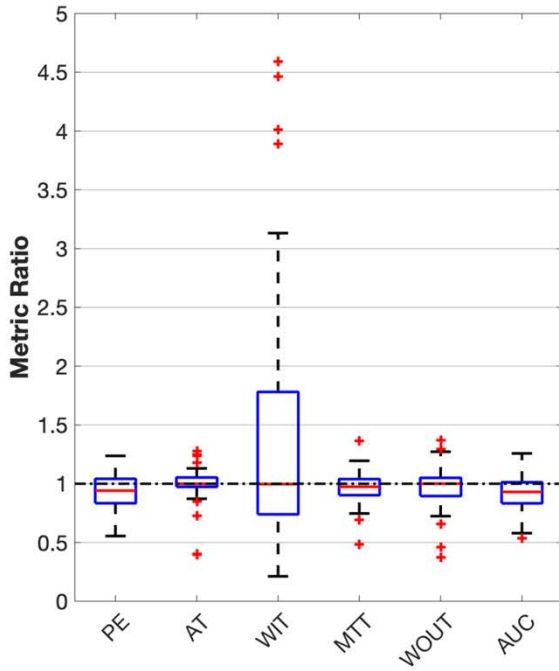
The ratio of DCE-US metrics calculated from the centre tumour-ROI and whole-VOI TACs, representing 2D and 3D DCE-US respectively, and the ratio of respective changes between imaging timepoint is shown in Figure 7-3 and in Table 7-1. The ratios are calculated using DCE-US metrics and their change from all imaging timepoints. PE and AUC metrics calculated from centre tumour-ROI were significantly smaller than those metrics of the whole-VOI in HN5 tumours ( $p$

= 0.015, 0.002 respectively) and C33A tumours (p = 0.006, <0.0001, respectively). The centre tumour-ROI AT was also significantly longer than whole-VOI AT in C33A tumours (p = 0.006). In both models, the disagreement in the change in a metric calculated from centre tumour-ROI and whole-VOI was either similar to or larger than the disagreement in the value of the metric, demonstrated by ratios with greater deviation from 1. Underestimation or overestimation of the metrics and their changes was possible using the centre tumour-ROI, as shown in the box and whiskers plot in Figure 7-3. The largest disagreement was observed in change in WIT (ratios of 0.73 and 0.55 for HN5 and C33A models, respectively), meaning that perfusion quantification using centre tumour-ROI underestimated the change in WIT.

*Table 7-1: Ratio of the value and change in DCE-US metrics obtained from centre tumour-ROI TAC and whole-VOI TAC. Ratios are presented as the median [lower quartile upper quartile] for head and neck (HN5) and cervical (C33A) xenograft tumours. Values closest to 1 indicate greater average agreement between metrics of the two TACs.*

METRIC	HN5		C33A	
	Metric value (ratio)	Metric change (ratio)	Metric value (ratio)	Metric change (ratio)
PE	0.94 [0.83 1.04]	0.84 [0.30 1.29]	0.96 [0.87 1.06]	1.02 [0.19 1.53]
AT	1.00 [0.97 1.05]	0.82 [ 0.03 1.39]	1.03 [0.98 1.09]	0.98 [0.43 1.23]
WIT	1.00 [0.74 1.78]	0.73 [-0.81 1.46]	1.02 [0.79 1.32]	0.55 [-0.12 1.00]
MTT	0.97 [0.90 1.04]	1.03 [0.78 1.47]	1.00 [0.93 1.09]	0.96 [0.13 2.03]
WOUT	1.00 [0.89 1.05]	0.94 [0.41 1.25]	1.00 [0.88 1.13]	0.87 [ 0.11 1.33]
AUC	0.93 [ 0.83 1.01]	1.16 [1.03 1.55]	0.92 [0.83 1.03]	0.93 [0.24 1.34]

### HN5



### C33A

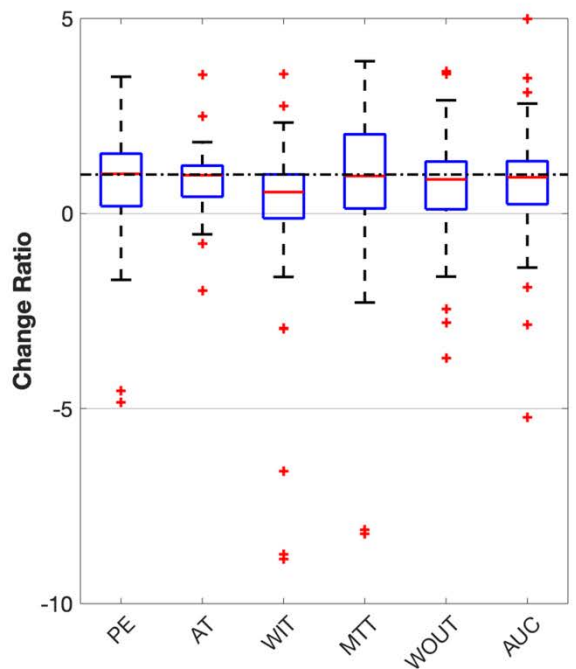
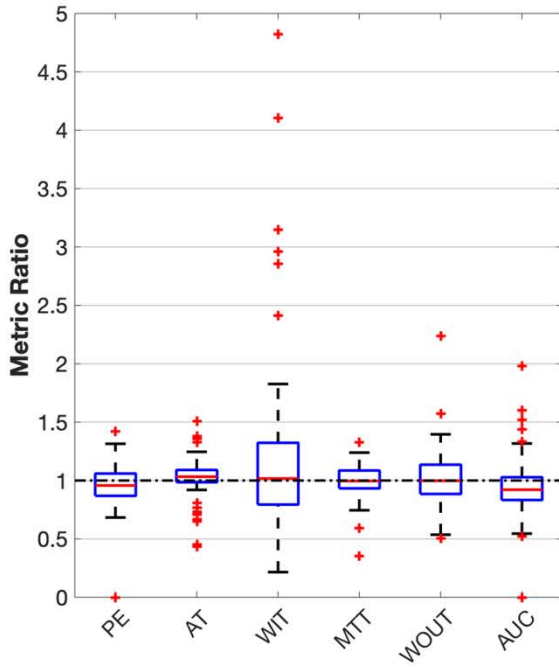


Figure 7-3: The difference in DCE-US metrics calculated using centre tumour-ROI and whole-VOI TACs. The ratios of the metrics (left) for HN5 tumours (top) and C33A tumours (bottom) and the respective change from pretreatment (right) are shown. The box and whisker plots show the median ratio and the interquartile range. For visualisation, outliers greater than 5 or lower than -10 are not shown. The black dashed line represents a ratio of 1, indicating perfect agreement.

### *7.3.3 Association of radioresponse with pretreatment DCE-US metrics*

No significant differences in pretreatment metrics could be detected between response groups in HN5 tumours. In the C33A cohort, partial responders had longer pretreatment WOUT compared to control tumours based on the whole-VOI ( $p = 0.024$ ). This data is not shown.

### *7.3.4 Association of radioresponse with changes in whole-VOI TAC metrics*

The change in whole-VOI TAC metrics of HN5 tumours is shown in Figure 7-4. There were 5 acquisitions out of a total of 48 datasets for which AT could not be calculated due to insufficient temporal sampling, and these were excluded from AT, WIT and MTT analysis. Analysis of all HN5 tumours, treated and control combined, showed a decrease in PE ( $p = 0.018, 0.039$ ), MTT ( $p = 0.0002, 0.0001$ ), WOUT ( $p = 0.0002, 0.002$ ) and AUC ( $p = 0.0001, 0.0011$ ), 72 hours and 1 week post - treatment respectively, while AT decreased at the 1-week timepoint only ( $p = 0.024$ ). The change in treated tumours was not significantly different from the change in control tumours, nor were changes between complete responders and partial responders significant.

The change in whole-VOI DCE-US metrics for C33A tumours is shown in Figure 7-5 (right). There were also 13 cases of failed AT calculation in the whole-VOI and centre tumour-ROI TACs out of the 88 DCE-US acquisitions which led to the exclusion of AT, WIT and MTT. Treated tumours were observed to have decreased WIT, MTT, WOUT and AUC 72 hours ( $p = 0.001, 0.0034, 0.0006, 0.0043$ , respectively), and 1 week following radiation ( $p = 0.001, 0.001, 0.0005, 0.011$ , respectively). The decrease in MTT was also apparent at the 24-hour timepoint ( $p = 0.047$ ). The decrease in WIT, MTT and WOUT metrics of treated tumours was significantly different from the change observed in control tumours at the 72-hour timepoint ( $p = 0.0003, 0.030, 0.043$ , respectively) and in MTT and WOUT at the 1-week timepoint ( $p = 0.034, 0.0011$ , respectively). Complete responders had a significantly bigger decrease in WIT at the 72-hour timepoints compared to partial responders ( $p = 0.048$ ) and control tumours ( $p = 0.0002$ ).

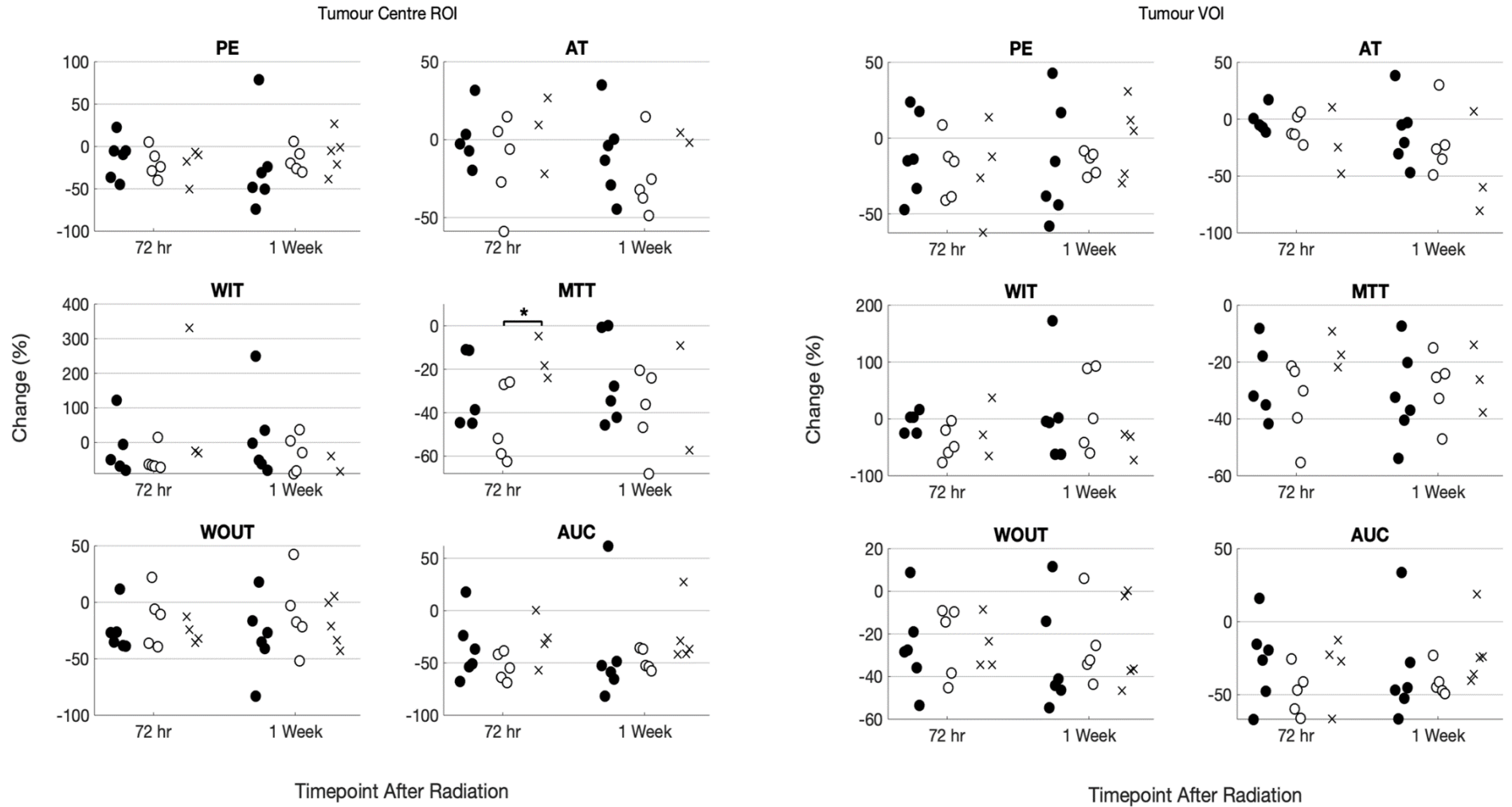


Figure 7-4: Change in DCE-US metrics of HN5 tumours obtained from centre tumour-ROI (left) and whole-VOI (right) TACs for complete responders (filled circle), partial responders (open circle) and control tumours (cross). Treated and control tumours exhibited a decrease in PE, AUC, MTT and WOUT from pretreatment at both post-treatment imaging timepoints.

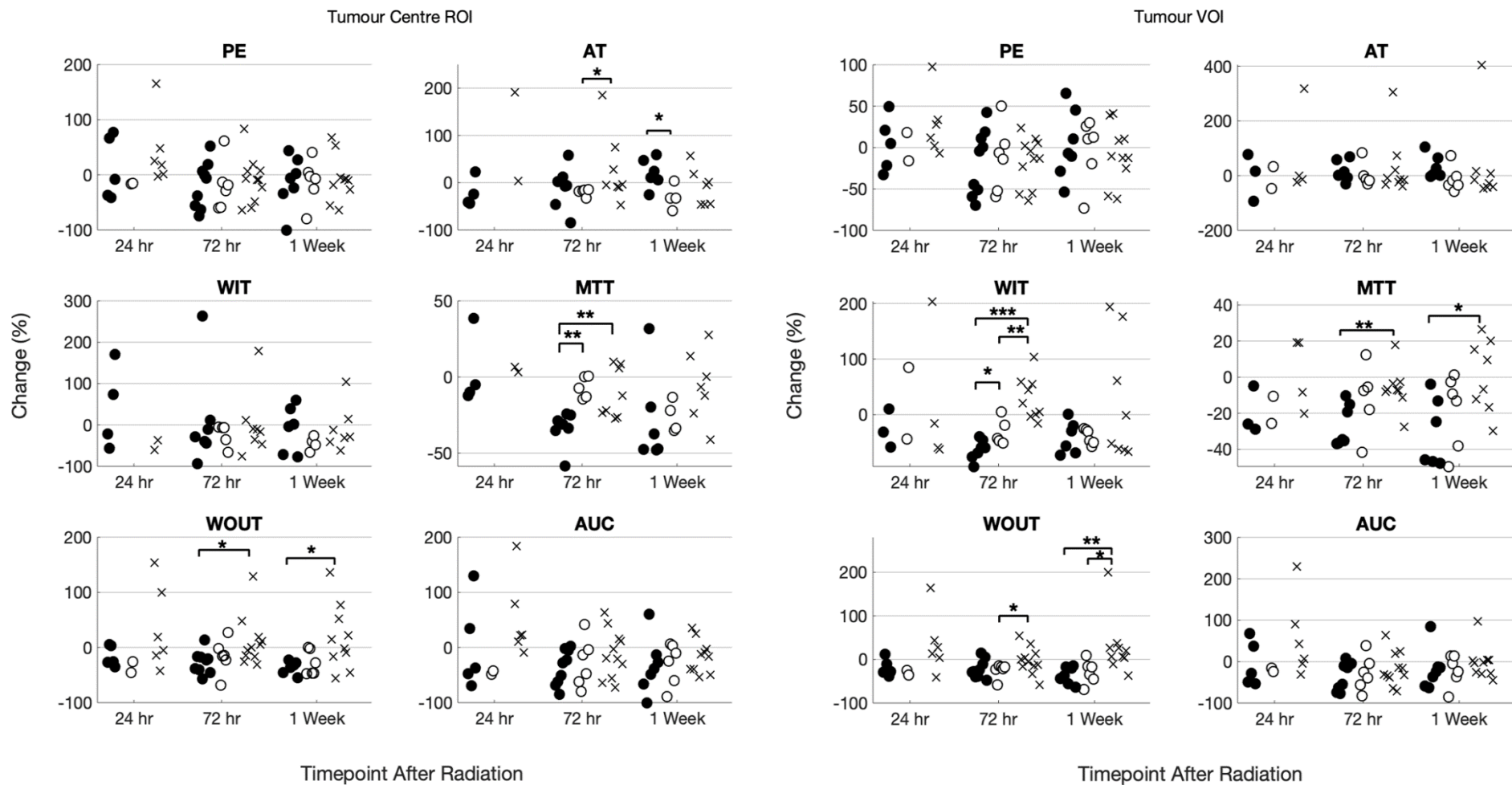


Figure 7-5: Change in DCE-US metrics of C33A tumours obtained from centre tumour-ROI (left) and whole-VOI (right) TACs for complete responders (filled circle), partial responders (open circle) and control tumours (cross). Irradiated tumours exhibited a decrease in WIT, MTT and WOUT 72 hours and 1 week following radiation.

### 7.3.5 Association of radioresponse with changes in centre tumour-ROI TAC metrics

The change in DCE-US metrics of the centre tumour-ROI TAC was calculated for comparison with 2D DCE-US imaging. This is shown for HN5 tumours in Figure 7-4 (left). As with whole-VOI TAC metrics, analysis of treated and control tumours showed a decrease in PE ( $p = 0.002, 0.0174$ ), MTT ( $p = 0.0002, 0.0005$ ), WOUT ( $p = 0.0007, 0.0072$ ) and AUC ( $p = 0.0003, 0.0013$ ) from pretreatment at 72-hour and 1 week post imaging timepoints respectively. No differences in the changes could be detected between treated and control tumours, nor between complete and partial responders. Partial responders had a significantly bigger decrease in MTT than control tumours ( $p = 0.036$ ).

The change in DCE-US metrics of the centre tumour-ROI TAC for C33A tumours is shown in Figure 7-5 (left). There was one case of failed calculation of PE, with PE and AUC set to zero at this timepoint to indicate no perfusion, and the time-based metrics excluded. Imaging 72 hours after radiation showed a decrease in MTT, WOUT and AUC in treated tumours ( $p = 0.0024, 0.0052$  &  $0.0034$ , respectively) compared to pretreatment, which was not observed in control tumours. Complete responders had a significantly greater decrease in MTT than partial responders ( $p = 0.0025$ ) or control tumours ( $p = 0.0037$ ). Complete responders also had a significantly bigger decrease in WOUT compared to control tumours ( $p = 0.015$ ). One week following radiation, the decrease in the aforementioned metrics persisted in treated tumours ( $p = 0.0059, 0.0005$ , &  $0.0046$ , respectively) but the difference in the WOUT change between complete responders and control tumours was no longer significant ( $p = 0.05$ ). Complete responders revealed an increase in AT compared to a decrease for partial responders ( $p = 0.019$ ). No significant changes could be detected in centre tumour-ROI metrics 24 hours following radiotherapy, likely because of the small sample number.

### *7.3.6 Comparison of pretreatment DCE-US metrics with preliminary studies*

The preliminary study of HN5 tumours (H1 study) described in Chapter 5 revealed a significant difference in the change in AUC between complete and partial responders following treatment, which was not observed here. Similarly, the preliminary study of C33A tumours (C5 study) showed a significant difference in the change of WOUT between complete and partial responders, not observed here. To evaluate the discrepancy in the results between the studies, the pretreatment DCE-US metrics obtained in H1 and C5 studies were compared to centre tumour–ROI metrics obtained using 3D DCE-US imaging of each tumour model. The pretreatment DCE-US metrics for HN5 studies are shown in Figure 7-6 - left. H2 and H3 cohorts were analysed together. All metrics were significantly different between H1 and H2+H3 studies ( $p < 0.0005$ ). Interestingly, H2+H3 cohort tumours had a larger PE but smaller AUC. The smaller AUC is in agreement with the quicker MTT and WOUT. HN5 tumours of the H2 and H3 studies had longer AT and WIT. Example TACs from a H1 tumour and a H2 tumour demonstrating these differences are shown in Figure 7-7.

The pretreatment DCE-US metrics for the C33A studies are shown in Figure 7-6 - right. C6 and C7 were compared separately to isolate the effect of the change in anaesthetic agents. C5 and C6 cohorts, both imaged using Hypnorm™–Hypnovel™ revealed a significant difference in all metrics except AT. The difference in other metrics between C5 and C6 and C7 cohorts was similar to that observed in HN5 tumours: C6 and C7 tumours had greater PE and smaller AUC, quicker MTT and WOUT and longer WIT compared to the preliminary C5 study. C6 and C7 cohorts, both imaged using 3D DCE-US but different anaesthetics showed differences in PE, AT, MTT and AUC. Tumours in the C7 study imaged under anaesthesia with a ketamine–xylazine–acepromazine combination had greater PE, longer AT, longer MTT and greater AUC than C6 study tumours. The difference in metrics due to the change of anaesthetics, however, is of a smaller magnitude than the difference caused by changing scanners and imaging techniques.

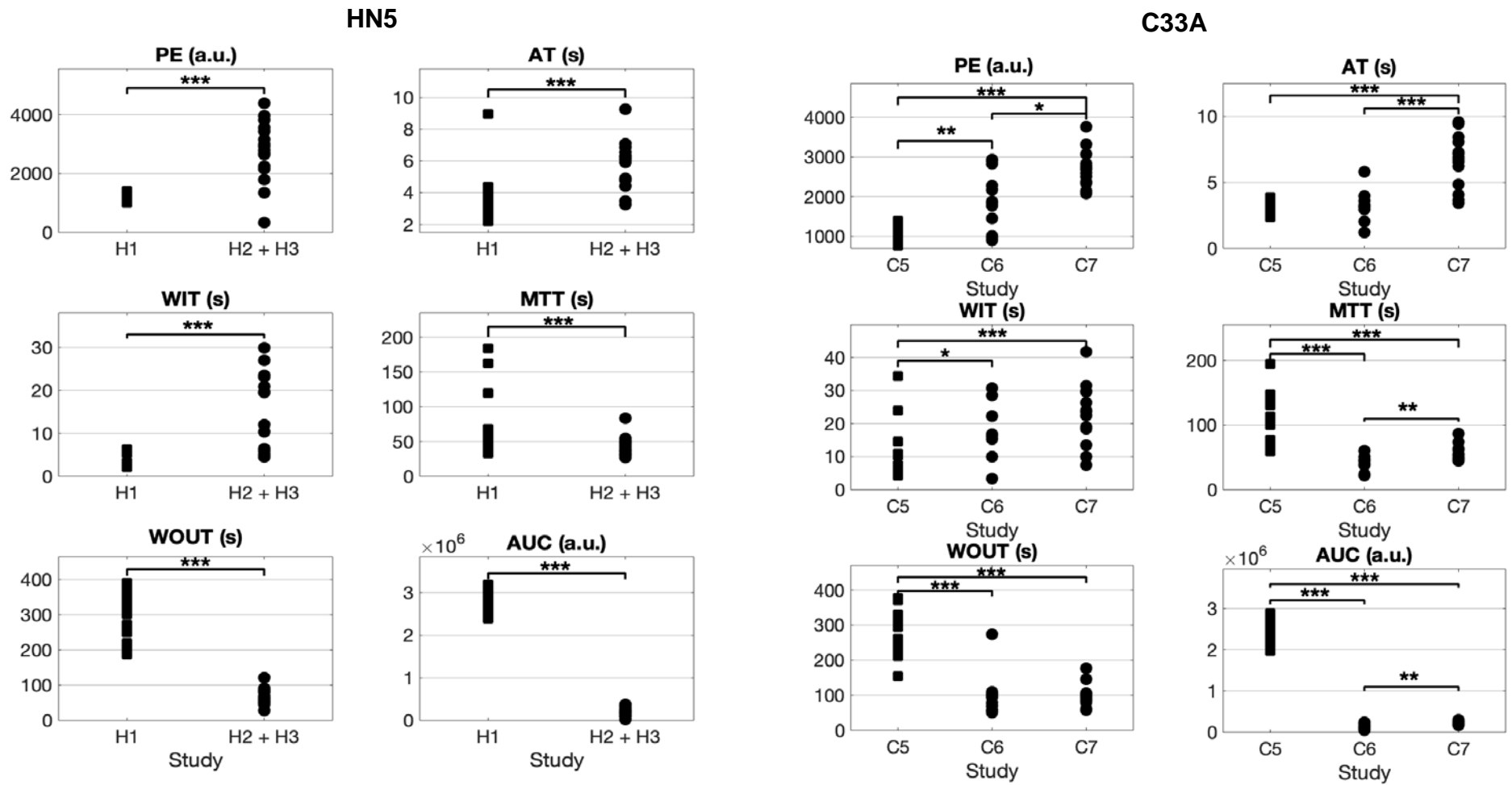


Figure 7-6: Comparison of DCE-US metrics obtained from the tumour centre using the 2D imaging with the Aprio (H1, C5, black squares) and 3D imaging with the Verasonics (H2 + H5, C6, C7, black circles), for HN5 tumours (left) and C33A tumours (right).

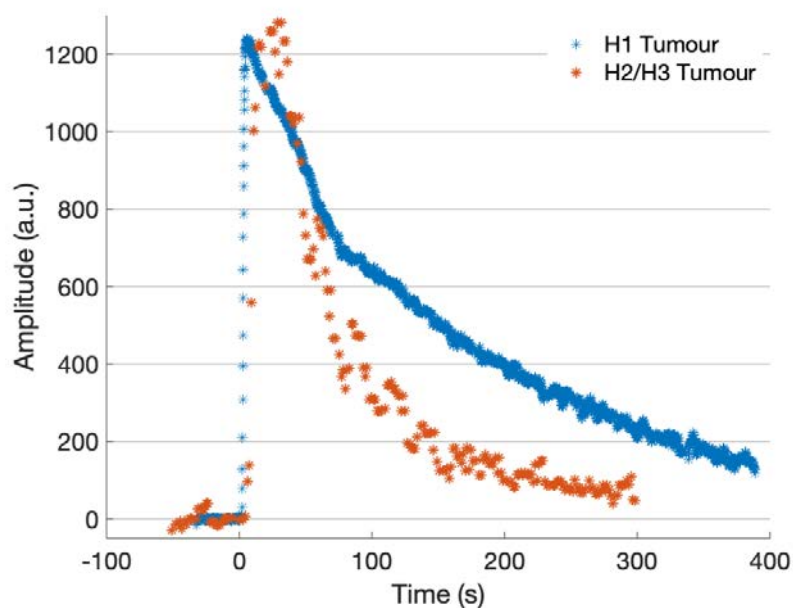


Figure 7-7: Representative TACs of a whole-tumour ROI of an H1 tumour (blue) and centre tumour whole-ROI of an H2 tumour (orange), showing longer WIT, greater PE, quicker MTT and WOUT and smaller AUC in the latter cohort.

### 7.3.7 Association of radioresponse with changes in DCE-US metrics histogram distribution

Some changes in the histogram distribution of DCE-US metrics were significantly different between response groups in the HN5 tumour model and are shown in Figure 7-8. Changes are given as the difference in the histogram metric before and after treatment divided by the pretreatment metric (equation 3 – 2). Seventy-two hours after treatment, the standard deviation (SD) of PE calculated from the centre tumour-ROI increased in complete responders compared to partial responders and control tumours ( $p = 0.052$ ,  $0.0095$  respectively). The skewness of AUC histogram of the whole-VOI in complete responders became more negative compared to partial responders and control tumours ( $p = 0.052$ ,  $p = 0.019$  respectively). At the 1-week imaging timepoint, there were no differences in centre tumour-ROI histogram distribution. Meanwhile, the WIT distribution for the VOI showed a decrease in SD for partial responders compared to complete responders and control tumours ( $p = 0.017$  and  $0.016$ , respectively). A similar

decrease in coefficient of variation (CoV) of MTT compared to an increase in complete responders was present ( $p = 0.017$ ) as shown in Figure 7-8.

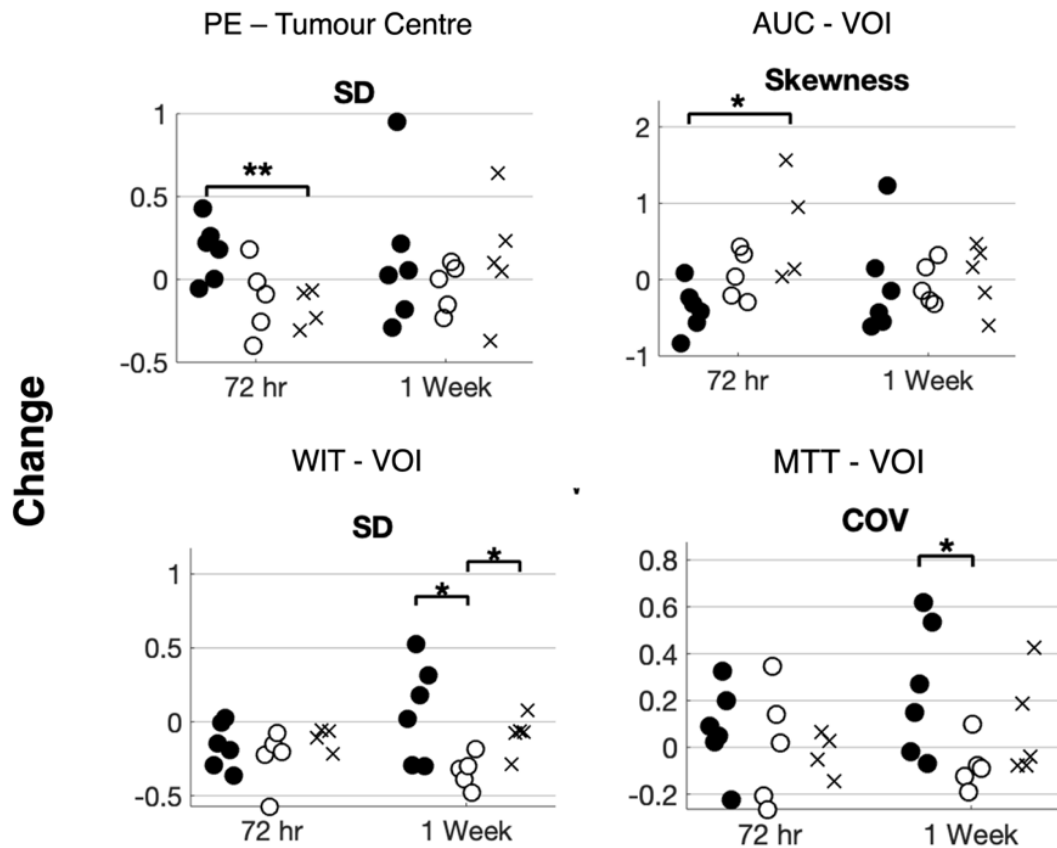
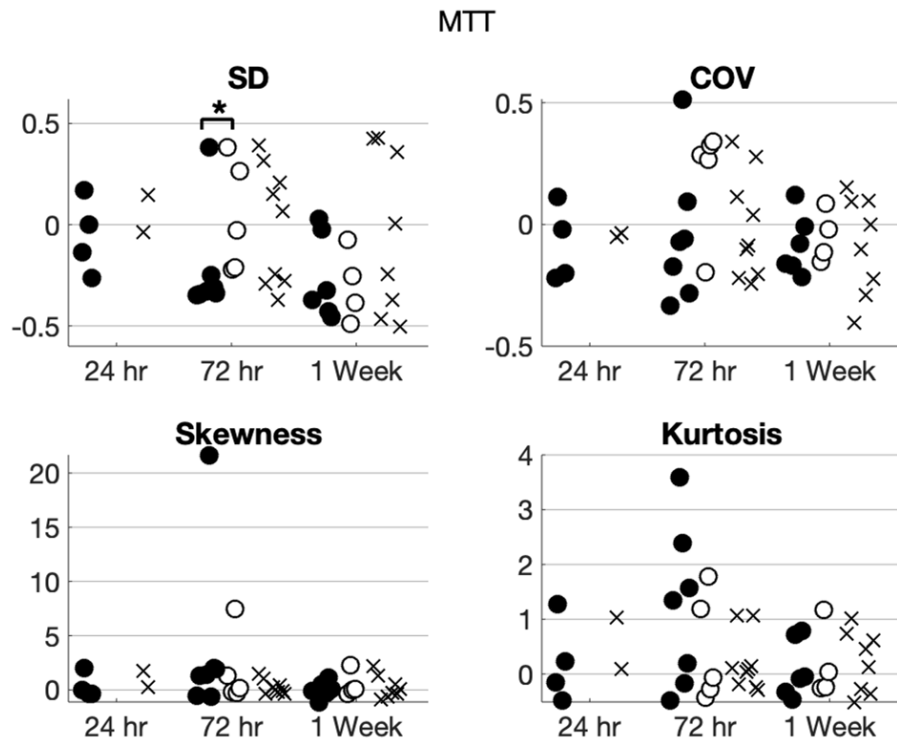


Figure 7-8 : Change in the histogram distribution of DCE-US metrics in HN5 tumours. Presented here are the most significant changes from centre tumour-ROI (left) and whole-VOI (right) for complete responders (filled circle), partial responders (open circle) and control tumours (cross)

For C33A tumours, histogram analysis of the centre tumour-ROI revealed a significant decrease in SD of MTT in complete responders compared to partial responders ( $p = 0.030$ ) 72 hours after radiation, in line with the decrease in centre tumour-ROI TAC. These changes are presented in Figure 7-9 . VOI histogram analysis revealed several differences between treated tumours and control tumours. Irradiated tumours showed a significant decrease in SD of AT compared to control tumours at both imaging timepoints ( $p = 0.019, 0.0116$ ) and a decrease in SD of WOUT at 1 week ( $p = 0.0021$ ). Differences in complete responders and partial responders were not observed. Complete responders had a significant increase in skewness and kurtosis of WIT ( $p = 0.025$  both) and MTT ( $p = 0.016, 0.011$ ) at the 72-hour timepoint compared to control tumours.

## Tumour Centre Histogram



## Tumour Volume Histogram

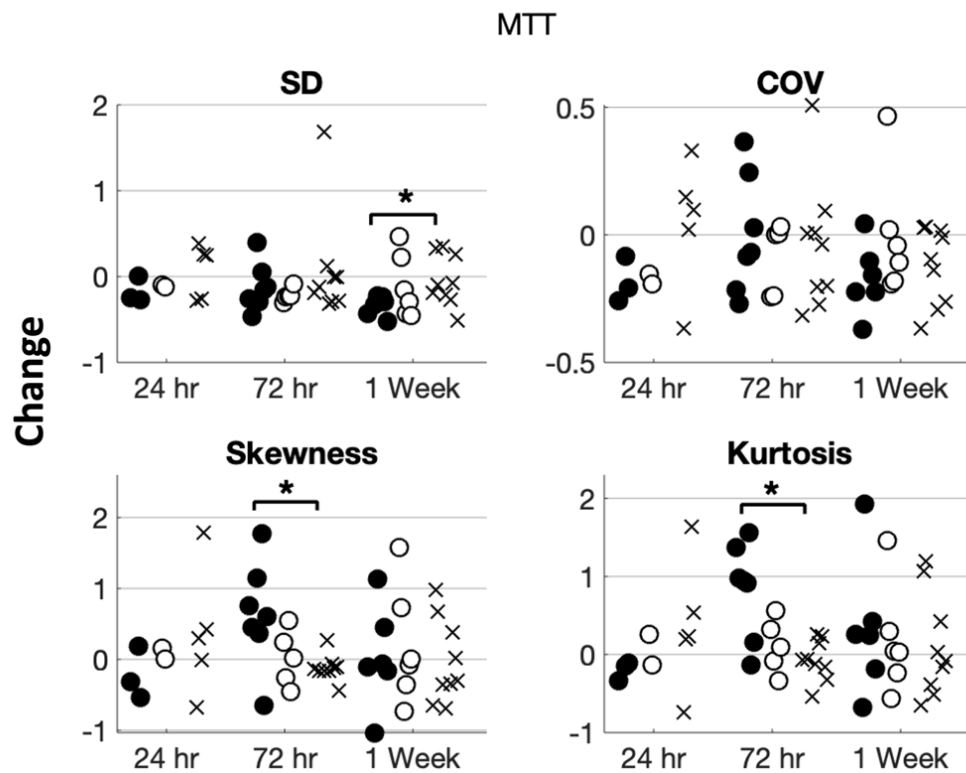


Figure 7-9 : Changes in the histogram distribution of MTT for the centre tumour-ROI (top) and the tumour volume whole-VOI (bottom) in C33A tumours 24 hours, 72 hours or 1 week post irradiation in complete responders (filled circle), partial responders, and control tumours (cross).

### *7.3.8 Combining tumour models*

Analysis of tumours of both models together did not elucidate any clearer distinctions between response groups than analysis of each model separately, but still maintained the difference between treated tumours and controls. Complete response was defined as survival at day 50, the median survival day of both cohorts. The resulting figures are shown in Appendix A5.

### *7.3.9 Tumour volume changes following radiation*

The tumour volume was examined at imaging timepoints to examine whether DCE-US can detect important changes in the tumour vasculature, between complete and partial responders, before a difference in the tumour volume is observed. The change in volume from treatment day to each imaging timepoint is presented in Figure 7-10. HN5 complete responders and partial responders did not show a tumour volume decrease before day 7 and had no significant difference in the change in volume at any of the imaging timepoints. At day 3, C33A complete responders had a significantly slower tumour growth rate compared to control tumours ( $p = 0.02$ ), and a significant difference compared to both control tumours and partial responders ( $p = 0.0007, 0.049$ , respectively) at day 7 as they start to regress. Additional analysis of days between the imaging timepoints showed that the significant difference between complete and partial responders is present by day 4 ( $p = 0.02$ ).

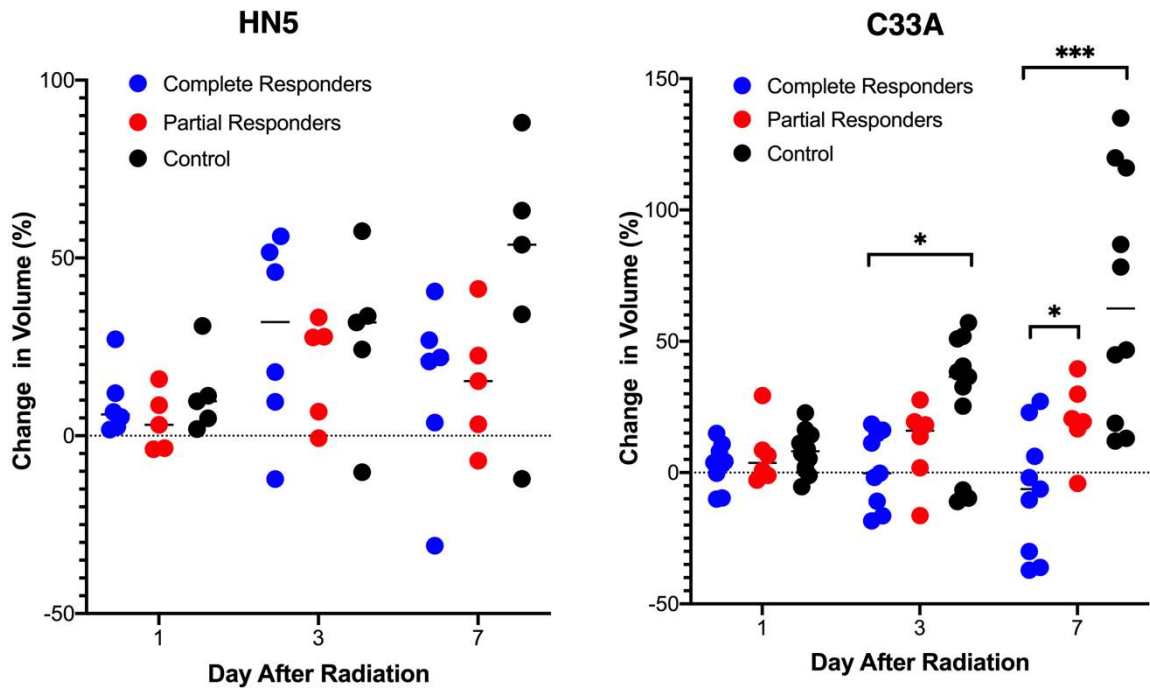


Figure 7-10: Tumour volume changes in HN5 tumours (left) and C33A tumours (right). No difference was observed in complete and partial responders in HN5 tumours by day 7, while C33A complete responders had a significant decrease in volume compared to control tumours by day 3 and compared to partial responders by day 7.

### 7.3.10 Repeatability of 3D DCE-US imaging

#### 7.3.10.1 Repeatability of centre tumour-ROI & whole-VOI TAC metrics

The repeatability of DCE-US metrics and histogram parameters of the whole-VOI and the centre tumour-ROI was assessed using the variation of the metric between two repeat image acquisitions acquired at the study endpoint. Thirteen pairs of repeat imaging acquisitions were available from both C33A and HN5 tumours.

The absolute and signed variation of whole-VOI and centre tumour-ROI TAC metrics are shown in Figure 7-11 and Table 7-2. The greatest variations were always observed in 2D centre tumour-ROI metrics compared to whole-VOI metrics (except for AUC with a variation of 76% in whole-VOI compared to 71% in the centre-ROI). The average PE for whole-ROI and whole-VOI appeared to systematically decrease for the second injection ( $p = 0.068$  and  $0.057$ ) and similarly for whole-ROI AT ( $p = 0.054$ ). The WOUT of whole-VOI ( $p = 0.05$ ) and centre-ROI AUC ( $p = 0.013$ ) also decreased.

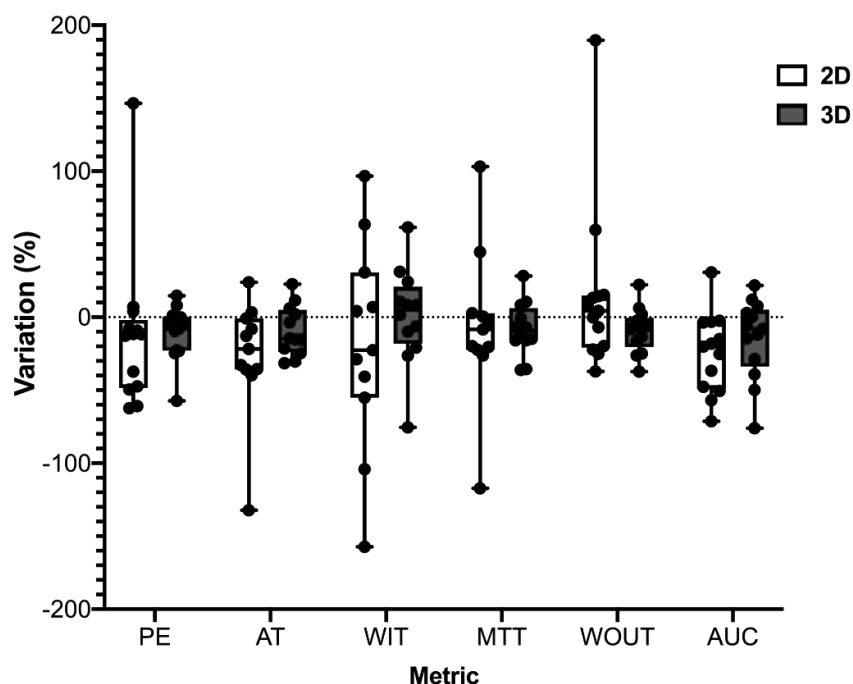


Figure 7-11: Variation of 2D (centre tumour-ROI, white bar) and 3D (whole-VOI, grey bar) DCE-US metrics of two repeat imaging acquisitions. Each animal is represented by one data point.

Comparison of the absolute values of the variation of centre tumour ROI and whole-VOI TAC metrics showed less variation, and hence better repeatability, for PE ( $p = 0.013$ ), AT ( $p = 0.042$ ), and WIT ( $p = 0.024$ ) using whole-VOI analysis. Meanwhile, comparison of the variation in metrics obtained with different scanners showed that the variation of AUC was significantly lower when measured using the Aplio scanner than the variation of the centre tumour-ROI and whole-VOI AUC ( $p = 0.0015, 0.027$  respectively).

### 7.3.10.2 Repeatability of histogram analysis

The variation of histogram parameters obtained from the VOI, and the centre tumour -ROI is shown in Figure 7-12. Skewness is not shown as it suffers large outlier variation (as discussed in section 5.4.5.4). The absolute variation is shown as none of the parameters were shown to have a systematic change between injections, except for SD and mFWHM of PE, which decrease in agreement with the decrease in whole-ROI analysis. Kurtosis was the most variable for all metrics. PE and AUC showed generally lower variation than time-based metrics,

in agreement with the ROI analysis. The repeatability of whole-VOI and centre tumour ROI - based histogram parameters was compared and revealed better repeatability of whole-VOI CoV for PE and AUC ( $p = 0.012, 0.024$  respectively).

*Table 7-2 : Mean absolute and signed variation [interquartile range] (%) of DCE-US metrics obtained from centre tumour-ROI (2D) and whole-VOI (3D) analysis of two repeat acquisitions.*

<b>Metric</b>	<b>ABS</b>		<b>SIGNED</b>	
	2D	3D	2D	3D
<b>PE</b>	36.0	14.0	- 11.7	-10.3
	[8.5 52.4]	[4.4 22.8]	[ -48.0 -4.8]	[-22.8 0.1]
<b>AT</b>	31.5	16.5	-26.6	-9.44
	[9.2 35.8]	[8.8 23.6]	[-35.8 -2.7]	[-23.0 4.0]
<b>WIT</b>	55.5	23.7	-18.8	0.65
	[24.2 88.3]	[8.3 28.7]	[-51.6 24.7]	[-15.3 17.6]
<b>MTT</b>	33.5	15.8	-6.0	-8.00
	[4.4 40.0]	[7.6 22.1]	[-21.8 2.2]	[-15.9 4.0]]
<b>WOUT</b>	32.0	13.5	15.0	-8.9
	[8.2 28.0]	[5.3 22.9]	[-20.3 14.6]	[-18.2 -1.5]
<b>AUC</b>	29.3	21.3	-24.6	-14.5
	[12.1 48.3]	[7.1 31.2]	[-48.3 -3.4]	[-31.2 4.0]

### 7.3.10.3 Repeatability of the spatial distribution of metrics

The correlation coefficient of metrics maps of the centre tumour-ROI of two repeat acquisitions is shown in Figure 7-13. PE and AUC had the highest correlation on average, while WIT was the lowest. Compared with the spatial repeatability obtained with DCE-US imaging with the Aplio scanner, PE, WOUT and AUC ( $p = 0.046, 0.007, <0.001$ ) had lower repeatability while the spatial repeatability of AT and WIT was improved with the Verasonics scanner ( $p = 0.0001, 0.0001$ ).

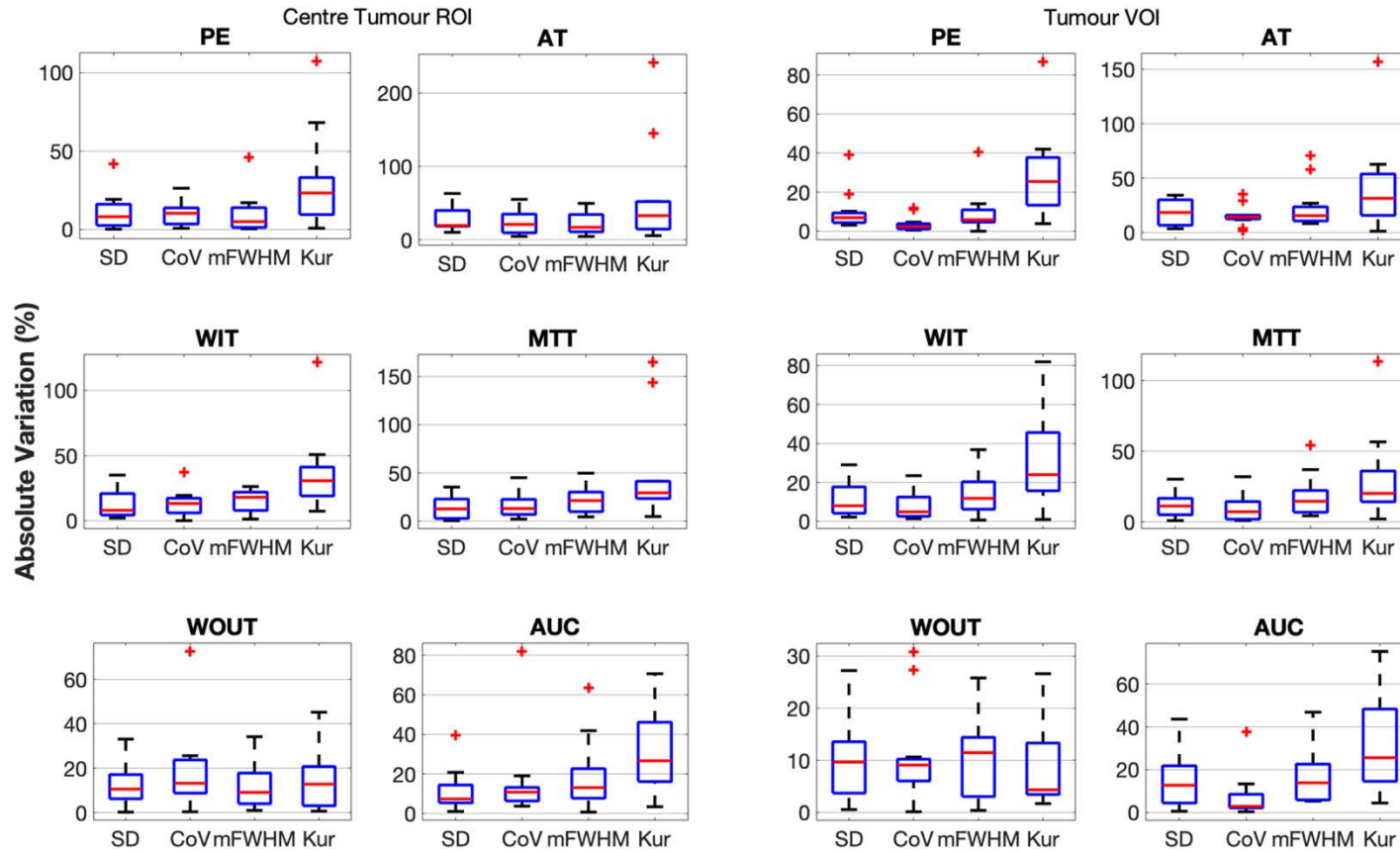


Figure 7-12: Absolute variation of histogram parameters of DCE-US metrics from two acquisitions for centre tumour-ROI (left) and whole-tumour VOI (right).

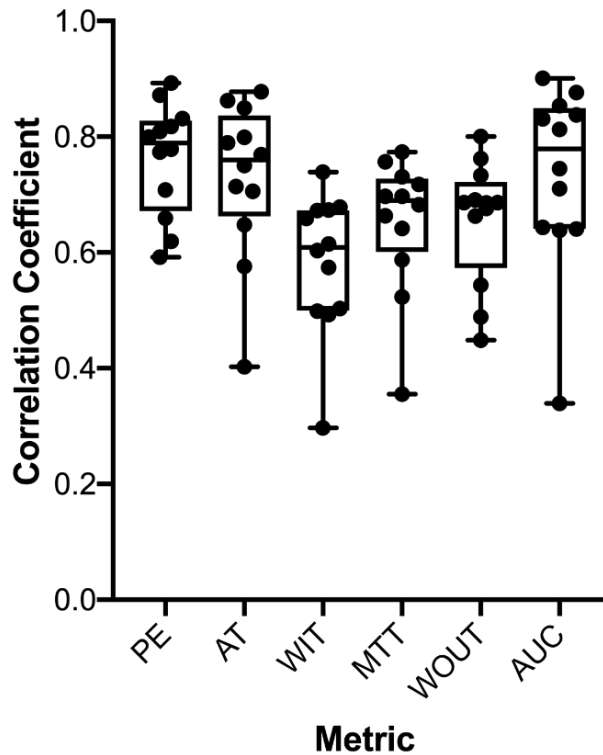


Figure 7-13: Correlation coefficient of metric maps of the central tumour whole-ROI obtained from two DCE-US acquisitions. Each point represents one animal.

### 7.3.11 Correspondence of DCE-US imaging with CD31 staining

DCE-US AUC maps of treated HN5 and C33A tumours with the corresponding CD31 + haematoxylin-stained sections are shown in Figure 7-14. The DCE-US metric maps are presented for the tumour slice with the best morphological agreement with the stained tumour section. At this endpoint, DCE-US showed mainly rim enhancement in the tumours, and minimal enhancement in the tumour core (Figure 7-14– AUC map). This corresponded with CD31 staining results; vessels were mainly detected in the tumour periphery, while the tumour core showed no CD31 or haematoxylin staining ( Figure 7-14– CD31 staining) indicating a non-viable core which corresponds to the non-enhanced core. The presented HN5 tumour has a larger non-enhanced core, which corresponded to a bigger necrotic core in the stained sections, compared to the C33A tumour.

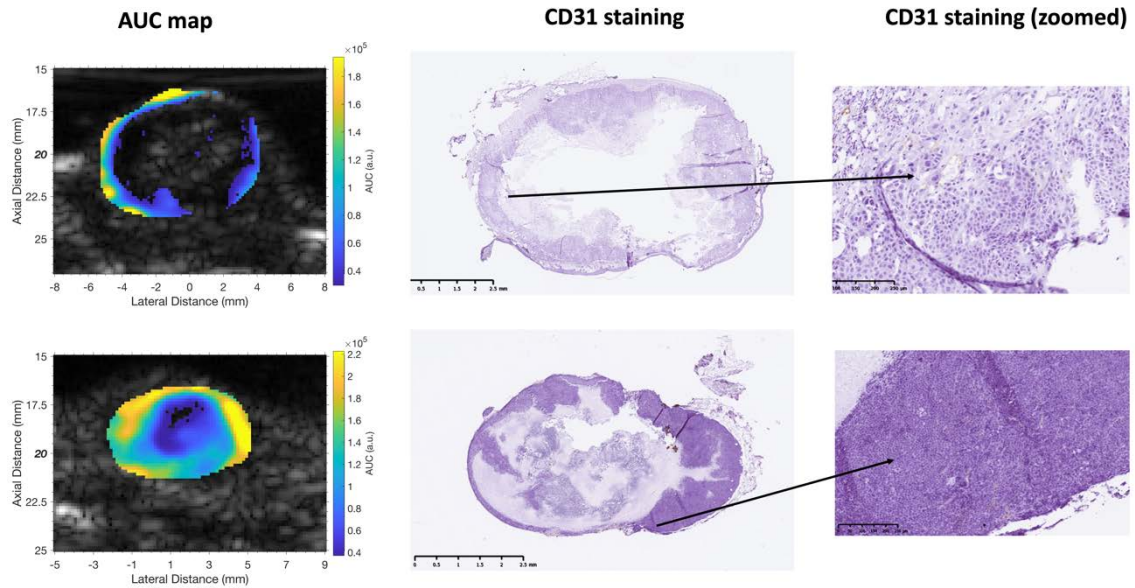


Figure 7-14: Spatial correspondence of DCE-US imaging and CD31 in a HN5 (top) and C33A (bottom) tumour. Shown here are AUC maps (first column), CD31(brown) + haematoxylin (purple) stained tumour slice (second column) and a zoomed region with CD31 staining (fourth column).

## 7.4 Discussion

The experiments described investigated the use of 3D DCE-US imaging to assess tumour vascular changes associated with response to radiation. The advantages of 3D imaging are, firstly, its ability to detect changes in the whole tumour volume, rather than relying on a subregion of the tumour to inform these changes, and secondly, improved technical precision of longitudinal imaging by reliably reproducing the imaging volume. These factors were hypothesized to improve examination of the heterogenous tumour vasculature and potentially provide an imaging biomarker for the non-invasive assessment of response to radiation.

### 7.4.1 Comparison of DCE-US quantification between studies

The DCE-US metrics at pretreatment obtained for both tumour models in this study demonstrated significant differences from the respective preliminary study discussed in chapter 5. There are several key differences between the studies that should be noted.

First, different anaesthetic agents had to be used in the two studies, because Hypnorm™ was no longer available. Anaesthesia modulates the physiological status of the animal, including blood pressure, heart rate and respiration rate, which can influence DCE-US quantification [152]. The effect of the change of anaesthetic agents was examined by comparing DCE-US metrics of C33A tumours in the C6 and C7 studies which were imaged with Verasonics scanner 3D DCE-US using Hypnorm™/Hypnovel™ and KXA anaesthesia respectively. This revealed significant differences in PE, AT, MTT and AUC. Quicker AT in C6, which is indicative of faster systematic blood flow, can be explained by the reported increase in heart rate caused by Hypnorm™/Hypnovel™ [216] compared to a reduction with KXA [225]. Similar differences in haemodynamic modulation caused by the anaesthetics agent may describe the difference in MTT, AUC and PE, but this remains to be explored. Additionally, the time between imaging and the induction of anaesthesia was different between the cohorts as the C7 study also involved elastography imaging carried out before DCE-US imaging. The magnitude of the difference between these cohorts was substantially smaller than the change observed in cohorts imaged with different scanners, and, more importantly, the increase in MTT, WOUT and AUC in the C7 cohort with the KXA anaesthetic, contrasts with the net decrease in these metrics compared to the C5 cohort imaged with the Aplio scanner. This implies the presence of a far more dominant factor driving these differences.

Significant differences were founded in PE, WIT, MTT, WOUT, and AUC between the C5 and C6 studies, which were imaged under Hypnorm™/Hypnovel™ using the Aplio and Verasonics scanner respectively. The injection method was changed between studies; contrast injection was done manually in study C5 and using an automated injection using a pump with constant pressure and speed in study C6. The speed of the injection was similar for the two methods, but differences in the injection pressure could influence the concentration and size distribution of injected microbubbles [152]. Furthermore, the difference in the scanner imaging parameters can explain the observed differences in DCE-US quantification. The Aplio scanner used a centre frequency of 8 MHz, compared to 4.08 MHz used by the Verasonics scanner. The latter frequency is closer to

the resonance frequency of Sonazoid microbubbles [164, 228]. Imaging closer to the resonance frequency increases the microbubbles' nonlinear response, which produces the contrast signal. The frequency used in the Aplio scanner, which was greater than the resonance frequency, would require larger pressures to drive the nonlinear response [229]. Both effects will influence the amplitude-based metrics, which could be therefore expected to be different between scanners. This was the case for PE, which was greater for the Verasonics scanner. Despite greater PE, AUC was smaller when measured with the Verasonics due to quicker MTT and WOUT. The most likely explanation for this is greater bubble disruption. With 3D imaging, a larger volume of tissue, and thus volume of microbubbles, were exposed to the ultrasound pulse. Even though the mechanical index used for 3D imaging with the Verasonics ( $MI = 0.15$ ) was lower than that for 2D imaging ( $MI = 0.3$ ), it is sufficient to cause disruption [164] and combined with the larger volume of exposure, may have reduced the MTT and WOUT.

#### *7.4.2 Association of radioresponse with 3D DCE-US imaging*

In the HN5 tumour model, DCE-US metrics obtained from the centre tumour-ROI and the whole-VOI indicated a decrease in the tumour perfusion over time, regardless of treatment or response. The reduced perfusion was in agreement with the results of a preliminary study (H1). Despite the overall decrease in all tumours, the preliminary study showed a significantly bigger decrease in whole-ROI AUC in complete responders compared to partial responders, indicating greater vascular damage, or reduced perfusion in the complete responders. This was not observed in studies described in this chapter. Further, the preliminary study showed a significant difference in WIT at pretreatment, with complete responders having shorter WIT, suggesting better perfusion. This was also not observed in the current study. The different observations between studies for the HN5 model may be attributed to the difference in DCE-US quantification discussed above. Longer WIT was observed in H2 and H3 cohorts compared to H1 tumours. This change may have confounded differences in WIT between well-perfused complete responders and partial responders with poorer perfusion

at pretreatment. Additionally, the difference between cohorts may have been an effect of the small sample number of both cohorts, due to tumour ulceration.

3D DCE-US imaging of the C33A cervical tumour model revealed that radiation caused vascular disruption up to 1 week following treatment, evident by the decrease in MTT, WOUT, and AUC in treated tumours. This result is in agreement with the established vascular disruption induced by large-dose single-fraction radiation early following treatment. Significant differences between complete and partial responding C33A tumours 72 hours after radiation were observed (Figure 7-5). Complete responders had greater decrease in MTT derived from the centre tumour-ROI. A decrease in MTT implies a decrease in vascular volume, based on the observed pixel-wise correlation of MTT with vascular volume-related metrics, PE and AUC (see section 4.3.3.3). Whole-VOI analysis showed a greater decrease in WIT in complete responders. The decrease in WIT indicates faster blood flow within the tumour, which may be the result of the disruption of small microvasculature with slow blood flow. Moreover, the decrease in MTT was not spatially uniform, as indicated by an increase in the skewness of MTT distribution calculated from tumour volume in complete responders (Figure 7-9). Taking these results together, it can be hypothesised that C33A complete responders undergo greater vascular damage, and the damage occurs in smaller vessels preferentially. This hypothesis agrees with observed damage reported in normal tissue microvasculature [230], where it was observed that radiation-damaged capillaries were shut and blood was rerouted to larger vessels with quicker flow.

The significant change in WIT was only observed through whole-VOI analysis and not in centre tumour-ROI. The difference between the results may be explained by the large discrepancy in the measured change of the two methods. The WIT change ratio of 0.55 had the greatest deviation from 1 between DCE-US metrics. This ratio implies that the change in WIT calculated using the centre tumour-ROI underestimated the change occurring in the whole tumour volume. A possible contributing factor to the difference observed may be the imprecise calculation of WIT with the low temporal resolution, leading to inaccurate estimation of WIT in the centre tumour-ROI. The whole-ROI WIT metric was not

observed to show a difference associated with response in the preliminary 2D imaging study carried out using a higher frame rate.

Finally, a promising result of this study is that the significant changes observed in MTT and WIT that could be used to differentiate tumour radioresponse were detected within 72 hours of treatment, before a difference could be detected in the tumour volume changes between these response groups. This is encouraging in the context of developing DCE-US imaging as an early response biomarker. Detection of vascular changes using DCE-US before volume changes are observed between responding and non-responding tumours was reported in in rat colon cancer model treated with chemotherapy [231] and antiangiogenic therapy [232], with DCE-US changes occurring several days before volume changes. The result reported here is novel for the evaluation of radiotherapy treatment using DCE-US imaging.

Similar to the HN5 tumour model, 3D imaging (C6 and C7) studies of the C33A tumour model also revealed significant differences from the preliminary 2D imaging study (C5). Using the Aplio scanner, complete responders showed a greater decrease in WOUT compared to partial responders, while the current study only showed a significant difference in the WOUT of complete responders compared to control tumours. Again, the discrepancy may be due to the greater bubble disruption leading to quicker washout in all tumours regardless of response. Another possible reason is the increased radiation dose used in the current study, which led to improved radioresponse of all treated tumours. Therefore, partial and complete responders may not be equivalent between studies and may have undergone different biological changes following radiation.

#### *7.4.3 Repeatability of 3D DCE-US imaging*

Examination of 3D DCE-US repeatability showed better repeatability of whole-VOI PE, AT and WIT compared to centre tumour-ROI analysis, demonstrating the potential benefit of 3D DCE-US imaging. However, the repeatability of AUC from whole-VOI and centre tumour-ROI using the Verasonics scanner was significantly less than that obtained using 2D imaging with the Aplio scanner in

the preliminary study. The difference in repeatability may be related to the difference in DCE-US quantification between scanners, discussed above. It is also expected due to the lower temporal resolution with 3D DCE-US, making the approximation of the area under the curve less accurate. This is supported by the observation of larger AUC variation in the kidney using 3D imaging compared to 2D with the Verasonics scanner (see chapter 6), although the difference was not significant. The poorer repeatability of AUC may also explain why no difference in AUC could be detected between response groups in the HN5 tumour model.

Moreover, lower spatial repeatability was observed for PE, WOUT and AUC metric maps obtained with 3D DCE-US compared to the preliminary study, which can again be explained by the lower temporal resolution. Interestingly, AT and WIT had greater spatial repeatability compared to the Aplio scanner. This may be a result of the motion correction applied here, which would make a substantial improvement to TAC noise. Further, the criteria for calculation of pixel-wise AT and WIT was stricter in this study due to the limited temporal resolution. This may have removed outliers and erroneous estimations which would corrupt the correlation.

## **7.5 Limitations**

The examination of the HN5 tumour model was hindered by the small sample number, as a result of ulceration. More ulceration was observed here than what was expected based on the preliminary study, a result of a variation in the depth of the injection, and time limitations did not allow for incorporation of additional animals. Further, it was difficult to stratify complete and partial responders in this cohort since all treated tumours responded and survived for longer than 40 days. Response was based on an arbitrary threshold of survival at day 80, which may not be reflective of a true difference in response.

Histopathology was not performed at any imaging timepoints following radiotherapy to confirm the biological basis of changes seen in DCE-US metrics. However, visual assessment of DCE-US metric maps at endpoint imaging and CD31 staining of the excised tumours revealed good spatial correspondence

supporting the biological validation of 3D DCE-US. Future work should examine histopathological readouts that can be used to assess perfusion at short timepoints after radiation to confirm the changes observed with DCE-US imaging.

The presented analysis examines the change in each DCE-US metric at each timepoint independently. A multi-metric, multi-timepoint analysis integrating these separate changes is expected to reflect radiation-induced vascular changes more comprehensively and will be investigated in future work. The analysis also did not consider the change in perfusion metrics for each tumour ROI or using a subregion analysis of the highest perfused volume, similar to that presented in chapter 5, and this will also be attempted.

All the studies discussed in the introduction used volumetric matrix arrays to image the tumour volume. Such transducers are not widely available, and thus volumetric imaging achieved through transducer translation, as is carried out here, can increase the accessibility of 3D DCE-US imaging but has a limited volume rate. There may be improved estimation of time-based metrics for the whole-VOI if a matrix array which can achieve a higher volume rate is used.

# 8 CHAPTER Conclusion

## 8.1 Conclusions

The work reported in this thesis aimed to investigate the potential of imaging metrics measured using dynamic contrast enhanced ultrasound (DCE-US) imaging as early imaging biomarkers of tumour response to radiotherapy in head and neck (H&N) and cervical cancer. Preclinical H&N and cervical tumour models were employed to study the repeatability of the imaging modality, as part of its technical assessment [47], and the association of DCE-US measured vascular changes with overall tumour response.

### 8.1.1 Characterisation of *in vivo* models of H&N and cervical cancer

**Chapter 4** explored *in vivo* models that can be reliably used to assess the stated aims. The examined models were based on cancer cell lines that had previously grown *in vivo* at the ICR. Tumorigenicity assessment of C33A & ME-180 cervical cancer cell lines showed good tumor growth in the former and a high rate of ulceration in the latter, making it an unsuitable *in vivo* tumour model. Tumorigenicity of close to 100% could be achieved in athymic nude mice inoculated with C33A cancer cells. Examination of the radiosensitivity of C33A tumours radiation doses from 10 – 25 Gy, demonstrated that the desired intertumour heterogenous radioresponse was achieved using 25 Gy. This dose produced minimal radiation-induced side effects, skin erythema which quickly resolved was observed. The tumorigenicity (close to 100%) and radioresponse of HN5 H&N model that was previously observed at ICR, was confirmed in this study, with a dose of 20 Gy and 25 Gy achieving both partial and complete response.

The functional vasculature of the two tumour models was assessed using 2D DCE-US. The C33A tumour model had a well-enhanced rim and lower enhancement in the core, representing a rim/core pattern of tumour vasculature,

while HN5 tumours exhibited more spatially homogenous enhancement. Overall, C33A tumours were less perfused than HN5 tumours. This was quantified by the lower whole-ROI PE, AUC, and longer WIT of C33A tumours, as well greater intratumour spatial heterogeneity. The poor enhancement in C33A tumours indicates poor perfusion at pretreatment, which can explain the lower-than-expected *in vivo* radiosensitivity based on the cell line's *in vitro* radiosensitivity. The relationship between DCE-US metrics and the tumour vasculature was confirmed at endpoint imaging of the tumours using histopathological markers of vasculature and cell viability. Regions in the tumour section with CD31 staining and viable cells showed good spatial correspondence to regions of high AUC in the metric map, indicating the presence of vascular volume. Based on this work, it was concluded that the C33A model is typically less perfused compared to HN5 tumours, with a non-viable core which necessitates high doses of radiation to induce a complete response. Both models, however, were considered suitable for *in vivo* studies of DCE-US metrics.

The relationship between the different DCE-US metrics was assessed to confirm what metrics were interdependent and are thus expected to show similar trends and inform on the same vascular properties. The most consistent correlation obtained from both tumour models and using pixel-wise and whole-ROI metrics was the positive correlation of PE and AUC with MTT and WOUT, indicating that MTT and WOUT are influenced by the blood volume in addition to their relationship with blood velocity. The weak correlation of AT and WIT with AUC and PE indicated that these time-based metrics were not strongly influenced by blood volume and may be more likely to be influenced by the mouse physiology and the structure of the vasculature.

### *8.1.2 Assessment of 2D DCE-US metrics for use as imaging biomarkers of radiotherapy response*

**Chapter 5** described the examination of DCE-US using 2D imaging with the Aplio scanner. DCE-US imaging was carried out prior to and 48 hours after radiation. In the HN5 tumour model, complete responders were identified based on complete tumour regression with no regrowth. All treated and control tumours

showed a decrease in whole-ROI PE, AUC, indicating decreased vascular volume at the later imaging timepoint. This was confirmed by comparing the pattern of perfusion, using maps of PE, between pretreatment and endpoint imaging. HN5 tumours tended to be homogeneously enhanced pretreatment but had a non-perfused core at endpoint.

This study showed that when the whole-ROI was considered, complete responders had a greater decrease in AUC and WOUT than partial responders in HN5 and C33A tumours, respectively, indicating a greater disruption of vascular volume (vascular damage) in complete responders. Results from chapter 4 showed that WOUT and MTT are related to blood volume-based metrics (PE and AUC). The same trend, negative decreases in complete responders relative to the change in partial responder was observed for PE and AUC in both models and MTT in the C33A model. Functional subregion analysis examined the change in DCE-US metrics in the tumour subregion with the highest perfusion, an analysis equivalent to commonly used 'hotspot' analysis. In HN5 tumours this showed the same result as whole-ROI analysis with a decrease in AUC in the subregion for complete responders. In C33A tumours, high perfusion subregions revealed a decrease in MTT, WOUT and AUC. Indicating that subregion analysis may be more sensitive to changes in DCE-US metrics in response to treatment. However, since AUC and MTT are strongly correlated to WOUT, subregion analysis may not be able to provide more predictive imaging biomarkers of response compared to whole-ROI analysis. The hypothesised decrease in vascular volume in both models, inferred by changes in DCE-US metrics, agrees with the reported evidence of vascular damage following high-dose single fraction radiation. Histogram analysis based on pixel-wise metric maps can be used to inspect intratumour heterogeneity and showed that complete response in the C33A model was associated with an increase in the skewness of the WOUT distribution, which suggests that the decrease in the whole-ROI WOUT was driven by the elimination of pixels (i.e., they no longer contained functioning vasculature) with long WOUT.

It should be noted that C33A tumours were treated with 15 or 20 Gy and complete tumour regression was not achieved with either dose and therefore these results

showing that DCE-US can measure differences between complete and partial responders were particularly encouraging in terms of the potential of DCE-US metrics to detect changes in vasculature in response to treatment.

The repeatability of DCE-US imaging was assessed in tumours of both models at endpoint imaging. The most repeatable metric using whole-ROI analysis was AUC (median variation 8%) while WIT had the lowest repeatability (median variation 33 %). The superior repeatability of AUC compared to PE may explain why changes in the vascular volume could only be detected from the AUC in HN5 tumours. DCE-US metrics changed systematically between injections; a decrease in PE and AT and an increase in WIT and MTT was observed in the second DCE-US acquisition. Changes in AT were likely a result of changes in the mouse body blood flow which can be caused by temporally variable hemodynamic effects of the anaesthesia. Meanwhile, the increase in WIT and MTT and decrease in PE may indicate lower blood flow or volume within the tumour. The reason for this remains unclear but could indicate an interaction with microbubbles from the first injection with the functional vasculature, causing transient changes. Other sources of variation relating to data and image analysis were considered. The contribution to the variation in whole-ROI metrics due to the uncertainty of ROI delineation was found not to be significant. Similarly, calculating DCE-US metrics from fitted models, rather than raw TAC that includes motion noise, did not provide an improvement in the repeatability.

Variation in histogram metrics were of similar magnitude as whole-ROI metrics. The histogram distribution of pixel-wise DCE-US metrics showed the highest repeatability in AUC and lowest for WIT, in agreement with whole-ROI analysis. Similar to the whole-ROI WIT, the SD and mFWHM of WIT distribution increased in the second acquisition. Meanwhile, AT had an increase in heterogeneity, despite the overall decrease in AT across the tumour. The explanation put forward is that pixel-wise AT is dependent on different factors according to the spatial location of pixels. AT in pixels near the periphery is primarily a measure of blood flow outside the tumour and should have quicker AT. Pixels in the tumour core depend on blood outside the tumour and blood flow within the tumour from periphery to the core, which increased as per whole-ROI WIT. The different

effects on pixel-wise AT led to an increase in the heterogeneity of AT. Moreover, the repeatability of spatial metric maps revealed moderately good to excellent correlation between repeat DCE-US imaging.

The overall conclusion of the preliminary results presented here is that DCE-US imaging could detect changes in the tumour functional vasculature that are associated with overall tumour response to radiotherapy, using whole-ROI and histogram analysis. The variation in DCE-US metrics between repeat acquisitions was of the same order of magnitude as observed changes following radiation, and therefore improvement in measurement repeatability is of crucial importance for the development of imaging biomarkers measured using 2D DCE-US.

### *8.1.3 Assessment of 3D DCE-US metrics for use as imaging biomarkers of radiotherapy response*

The 3D DCE-US imaging technique used in this thesis was developed in-house using the Verasonics Vantage scanner. It was hypothesised that 3D imaging increases the precision of the measurement of DCE-US imaging metrics by evaluating vascular changes in the entire tumour volume, thereby improving repeatability of measurements across multiple days.

**Chapter 6** examined the repeatability of 2D and 3D DCE-US imaging carried out on the same (intra) day and on different (inter) days in the kidney, as a model of normal tissue, with no expected changes in the vasculature between imaging days. Comparison of 2D and 3D DCE-US intraday repeatability of whole-ROI or whole-VOI metrics showed no improvement using 3D DCE-US, and in fact showed greater variation in MTT with 3D DCE-US. The increased variation is assumed to be related to the systematic decrease in MTT observed over the three repeat injections, which was not observed with 2D DCE-US. In contrast, 3D imaging improved the interday repeatability of WOUT in comparison to 2D imaging. This supports the hypothesised improved precision that can be achieved using 3D imaging to overcome the variation introduced by changes in the imaging position. The repeatability of both 2D and 3D imaging was worse than that obtained with the Aplio 2D scanner. This could indicate kidney-specific sources

of variation, including kidney flow modulations due to the increase in total blood volume with repeat contrast injections. The repeatability of tumour 3D DCE-US imaging obtained in chapter 7 was also better than kidney repeatability, supporting the presence of additional sources of variation relating to the kidney.

Finally, **Chapter 7** presented studies of the use of 3D DCE-US imaging to predict and assess radioresponse. Vascular changes were assessed using TACs obtained from the central tumour whole-ROI, equivalent to the previously used 2D DCE-US and TACs of the tumour volume (whole-VOI). Radiation-induced vascular changes in HN5 tumours could not be identified since both treated and control tumours exhibited a similar decrease in vascular volume demonstrated by a decrease in PE, MTT and WOUT, AUC of centre tumour-ROI and whole-VOI from pretreatment, 72 hours and 1 week post treatment. While this was also observed in the preliminary study of the model, a significant difference in the magnitude of decrease in AUC could still be observed between complete and partial responders in the earlier study. This was not observed here and may be a result of the lower repeatability of AUC measurement with 3D imaging. Additionally, the centre tumour-ROI and whole-VOI AUC at pretreatment was significantly smaller than AUC in the preliminary study and therefore the change may have been relatively smaller and therefore more difficult to detect.

3D DCE-US imaging study of the C33A cervical cancer model used a radiation dose for 25 Gy to elicit complete response. Vascular disruption in treated tumours was apparent 72 hours and up to 1 week following radiation, evident by a decrease in MTT, WOUT and AUC of the centre tumour-ROI, which was not detected in control tumours. A significantly bigger decrease in MTT was observed in complete responders compared to partial responders, which is related to WOUT in which a difference was observed between complete and partial responders in the preliminary study of chapter 5. An increase in the skewness of MTT distribution was observed, which implies that the decrease in the centre-ROI MTT was caused by the change in pixels with high MTT. DCE-US metrics derived for the whole-VOI, showed the same decrease in MTT, WOUT and AUC at both timepoints following treatment, in addition to a decrease in WIT. The decrease in WIT represents enhanced tumour flow speed, discussed in chapter

4, which can be due to the disruption of vessels with poor flow that would prolong the whole-VOI wash-in.

C33A complete responders had a larger decrease in WIT compared to partial responders. This was only observed using tumour whole-VOI analysis and not in the tumour central whole-ROI. The change in WIT in the centre tumour ROI showed the largest variation from the change in whole-VOI of all metrics, indicating the unreliability of quantifying the change in this metric through a single tumour slice to represent vascular changes of the whole tumour. Additionally, whole-VOI WIT had better repeatability than the central tumour whole-ROI.

DCE-US metrics obtained in this study using the Verasonics scanner were different than metrics obtained in the preliminary study with the Aplio scanner; a shorter MTT & WOUT, smaller AUC, higher PE, and longer WIT were observed. Differences in the amplitude metrics PE and AUC were expected due to differences in the amplitude quantification between the imaging parameters of the two scanners and contrast modes used. The difference in MTT and WOUT, however, suggests that greater volume of sonicated tissue for 3D DCE-US caused greater bubble disruption, leading to quicker bubble disappearance in the tumour volume. The clear differences in MTT and WOUT contributed to the inability of 3D imaging to detect changes in the metric relevant to response, specifically in AUC for the HN5 model. This highlights the importance of standardising imaging settings to achieve similar contrast disruption and amplitude quantification when conducting longitudinal investigations. Repeatability of intraday measurements of 3D DCE-US was examined at the endpoint. Similar to the results of 2D DCE-US imaging repeatability, the variation in centre tumour-ROI and whole-VOI metrics between repeat acquisitions were of the same order as the measured radiation-induced vascular changes, which further supports the need for future work to improve repeatability of DCE-US, using both 2D and 3D imaging. These changes are specific to single high dose irradiation of these murine models. In a clinical context, changes in the vasculature may be smaller, or more gradual, as radiotherapy for H&N and cervical cancer is predominantly given in 2 Gy fractions.

## 8.2 Summary

The work of this thesis provides encouraging evidence to support the use of DCE-US imaging for assessing vascular changes associated with response to radiotherapy. Changes in MTT, WOUT and AUC metrics implied vascular disruption, in agreement with the reported radiation induced vascular damage discussed in the introduction and shown in other studies using DCE-US. Using 2D DCE-US significant differences between complete and partial were identified in MTT, WOUT and AUC, which indicated more vascular disruption in tumours with better response. 3D DCE-US imaging further revealed that a decrease in WIT is associated with response, which could not be detected with 2D imaging. A decrease in WIT suggests improved tumour blood flow which can be a result of the selective disruption of smaller vessels. Changes in the distribution of pixel-wise metrics observed through histogram analysis supports the presence of a heterogenous impact on the vasculature. Examination of the repeatability of DCE-US showed that the measurement variation associated with DCE-US is of the same order as the measured significant changes, and hence improving repeatability can provide a notable effect on the biological validation and the utility of DCE-US imaging for measurement of response.

## 8.3 Future work

### 8.3.1 *Biological validation of DCE-US imaging*

The timepoint chosen for histopathological comparison of DCE-US metrics was not ideal as tumours at this volume lacked vascularisation, and therefore it was not possible to perform a quantitative comparison of vascular density and DCE-US metrics. Nor could the relationship of vascular morphology and DCE-US metrics be explored. Histopathology is also needed to confirm the observed vascular changes at the early timepoints following radiation. Future work should include histopathological examination of treated tumours at timepoints corresponding to the imaging timepoints.

Furthermore, Pimonidazole (hypoxia) and Hoechst (perfusion) staining were incorporated in the endpoint imaging protocol but have not been examined yet due to time constraints. Hoechst staining is able to identify functional vasculature, unlike CD31 staining of endothelial cells which would include non-functional vasculature and can therefore be a better histopathological correlate. Inspection of the correlation of hypoxia with DCE-US would support the use of DCE-US in assessing hypoxia, another important factor of radioresponse which can serve as an important predictor.

### *8.3.2 Technical validation of DCE-US*

The precision of DCE-US, quantified only through repeatability here, suggests work is required to improve repeatability to enable detection of vascular changes using DCE-US metrics. It was clear that repeat injections in one imaging session introduce a bias in DCE-US metrics. This effect should be considered when comparing DCE-US longitudinally (and preclinically) and indicates that changes in DCE-US metrics between timepoints should be measured from matched injections, i.e., comparison of the first injections. One source of variation, speculated but not confirmed, was the effect of changes in animal physiological status. The employed animal setup and equipment here only allowed monitoring of the respiration rate, which was noted to possibly change substantially between repeat DCE-US acquisitions because of the anaesthesia. It is unlikely that this effect exists in the context of clinical DCE-US imaging, and in the clinical context of treatment response monitoring repeat injections are also likely to be at least several days apart. However, physiological variations day-to-day in patients may also exist and future work as part of the translation DCE-US into the clinic for assessment of response could study the effect of variation in, for example, blood pressure, respiration rate or hydration.

Moreover, approaches to normalise tumour DCE-US metrics using a reference tissue should be explored. Normalised metrics do not suffer the variation caused by changes in the contrast injection volume or speed, i.e., the input function. However, it can be difficult to obtain such a signal within the imaging field of view. Future work should investigate the best approach, which may mean an additional

transducer is required, to obtain some normalisation measure, perhaps from a normal tissue such as the kidney or a large blood vessel.

Another aspect of technical validation was unintentionally noted in this work, that of the reproducibility of DCE-US. Reproducibility refers to the precision of imaging carried out with different scanners, in different centres, and different users. Here the two scanners used displayed significant differences in the quantification of DCE-US metrics. Methods of standardising the obtained DCE-US metrics between different scanners may be of vital importance in some settings where it is not possible to guarantee the use of the same type or make of scanner each time a patient is scanned.

### *8.3.3 DCE-US data analysis*

Multi-metric, or multi-timepoint analysis can provide a more accurate evaluation of vascular changes rather than relying on a single metric, which can in turn improve assessment of response using DCE-US. This analysis did not fully explore methods of examining intratumour spatial heterogeneity, including texture analysis of metric maps. This is an exciting prospect considering the demonstrated good to excellent spatial repeatability in some of the metrics. The data obtained in the work described in this thesis provides the opportunity for future investigation of metrics of changes in spatial heterogeneity.

### *8.3.4 Radiotherapy fractionation*

Single fraction large radiation done in this thesis is of limited clinical utility, particularly for H&N and cervical cancer. Stereotactic body radiotherapy is not clinical standard but has been explored in the treatment of oligometastases [9, 233]. Future work should focus on clinically fractionated radiotherapy treatment schedules. Fractionated radiotherapy does not induce endothelial cell apoptosis, and conversely has been shown to improve tumour perfusion [95, 234] and lead to tumour reoxygenation [95, 101]. Consequently, we may expect to see significant increases in metrics such as AUC, WOUT, PE and MTT in complete responders compared to partial responders.

# Bibliography

- [1] M. C. Joiner, and A. v. d. Kogel, *Basic Clinical Radiobiology*, 4 ed., London: CRC Press, 2013.
- [2] D. E. Johnson, B. Burtneß, C. R. Leemans *et al.*, "Head and neck squamous cell carcinoma," *Nature Reviews Disease Primers*, vol. 6, no. 1, pp. 92, 2020/11/26, 2020.
- [3] E. E. Vokes, R. R. Weichselbaum, S. M. Lippman *et al.*, "Head and Neck Cancer," *New England Journal of Medicine*, vol. 328, no. 3, pp. 184-194, 1993/01/21, 1993.
- [4] S.-A. Yeh, "Radiotherapy for Head and Neck Cancer," *Seminars in Plastic Surgery*, vol. 24, no. 2, pp. 127-136, 2010.
- [5] C. R. Uk. "Head and neck cancers statistics," <https://www.cancerresearchuk.org/health-professional/cancer-statistics/statistics-by-cancer-type/head-and-neck-cancers>.
- [6] T. R. C. o. R. (RCR), *Radiotherapy dose fractionation*, Royal College of Radiologists (RCR), 2019.
- [7] J. J. Caudell, J. F. Torres-Roca, R. J. Gillies *et al.*, "The future of personalised radiotherapy for head and neck cancer," *The Lancet Oncology*, vol. 18, no. 5, pp. e266-e273, 2017/05/01/, 2017.
- [8] S. A. Bhide, and C. M. Nutting, "Recent advances in radiotherapy," *BMC Medicine*, vol. 8, no. 1, pp. 25, 2010/04/28, 2010.
- [9] D. Alterio, G. Marvaso, A. Ferrari *et al.*, "Modern radiotherapy for head and neck cancer," *Seminars in Oncology*, vol. 46, no. 3, pp. 233-245, 2019/06/01/, 2019.
- [10] S. A. S. Raktoe, H. Dehnad, C. P. J. Raaijmakers *et al.*, "Origin of Tumor Recurrence After Intensity Modulated Radiation Therapy for Oropharyngeal Squamous Cell Carcinoma," *International Journal of Radiation Oncology\*Biophysics\*Physics*, vol. 85, no. 1, pp. 136-141, 2013/01/01/, 2013.
- [11] H. Bollen, J. van der Veen, A. Laenen *et al.*, "Recurrence Patterns After IMRT/VMAT in Head and Neck Cancer," *Frontiers in oncology*, vol. 11, pp. 720052-720052, 2021.
- [12] R. Zukauskaitė, C. R. Hansen, C. Brink *et al.*, "Analysis of CT-verified loco-regional recurrences after definitive IMRT for HNSCC using site of origin

estimation methods," *Acta Oncologica*, vol. 56, no. 11, pp. 1554-1561, 2017/11/02, 2017.

- [13] L. J. Peters, and G. H. Fletcher, "Causes of failure of radiotherapy in head and neck cancer," *Radiother Oncol*, vol. 1, no. 1, pp. 53-63, Aug, 1983.
- [14] P. Silva, J. J. Homer, N. J. Slevin *et al.*, "Clinical and biological factors affecting response to radiotherapy in patients with head and neck cancer: a review," *Clinical Otolaryngology*, vol. 32, no. 5, pp. 337-345, 2007/10/01, 2007.
- [15] E.-L. Göttgens, C. Ostheimer, P. N. Span *et al.*, "HPV, hypoxia and radiation response in head and neck cancer," *The British journal of radiology*, vol. 92, no. 1093, pp. 20180047-20180047, 2019.
- [16] D. Atwell, J. Elks, K. Cahill *et al.*, "A Review of Modern Radiation Therapy Dose Escalation in Locally Advanced Head and Neck Cancer," *Clinical Oncology*, vol. 32, no. 5, pp. 330-341, 2020/05/01/, 2020.
- [17] B. Lacas, J. Bourhis, J. Overgaard *et al.*, "Role of radiotherapy fractionation in head and neck cancers (MARCH): an updated meta-analysis," *Lancet Oncol*, vol. 18, no. 9, pp. 1221-1237, Sep, 2017.
- [18] M. Saksø, K. Jensen, M. Andersen *et al.*, "DAHANCA 28: A phase I/II feasibility study of hyperfractionated, accelerated radiotherapy with concomitant cisplatin and nimorazole (HART-CN) for patients with locally advanced, HPV/p16-negative squamous cell carcinoma of the oropharynx, hypopharynx, larynx and oral cavity," *Radiother Oncol*, vol. 148, pp. 65-72, Jul, 2020.
- [19] H. Mirghani, and P. Blanchard, "Treatment de-escalation for HPV-driven oropharyngeal cancer: Where do we stand?," *Clinical and Translational Radiation Oncology*, vol. 8, pp. 4-11, 2018.
- [20] C. C. Wu, D. P. Horowitz, I. Deutsch *et al.*, "De-escalation of radiation dose for human papillomavirus-positive oropharyngeal head and neck squamous cell carcinoma: A case report and preclinical and clinical literature review," *Oncol Lett*, vol. 11, no. 1, pp. 141-149, Jan, 2016.
- [21] B. S. Chera, R. J. Amdur, R. Green *et al.*, "Phase II Trial of De-Intensified Chemoradiotherapy for Human Papillomavirus-Associated Oropharyngeal Squamous Cell Carcinoma," *Journal of clinical oncology : official journal of the American Society of Clinical Oncology*, vol. 37, no. 29, pp. 2661-2669, 2019.
- [22] A. M. Chen, C. Felix, P.-C. Wang *et al.*, "Reduced-dose radiotherapy for human papillomavirus-associated squamous-cell carcinoma of the oropharynx: a single-arm, phase 2 study," *The Lancet. Oncology*, vol. 18, no. 6, pp. 803-811, 2017.
- [23] S. Marur, S. Li, A. J. Cmelak *et al.*, "E1308: Phase II Trial of Induction Chemotherapy Followed by Reduced-Dose Radiation and Weekly Cetuximab in

Patients With HPV-Associated Resectable Squamous Cell Carcinoma of the Oropharynx- ECOG-ACRIN Cancer Research Group," *Journal of clinical oncology : official journal of the American Society of Clinical Oncology*, vol. 35, no. 5, pp. 490-497, 2017.

- [24] H. Quon, and A. A. Forastiere, "Controversies in Treatment Deintensification of Human Papillomavirus–Associated Oropharyngeal Carcinomas: Should We, How Should We, and for Whom?," *Journal of Clinical Oncology*, vol. 31, no. 5, pp. 520-522, 2013/02/10, 2013.
- [25] B. O'Sullivan, S. H. Huang, L. L. Siu *et al.*, "Deintensification Candidate Subgroups in Human Papillomavirus–Related Oropharyngeal Cancer According to Minimal Risk of Distant Metastasis," *Journal of Clinical Oncology*, vol. 31, no. 5, pp. 543-550, 2013/02/10, 2013.
- [26] A. J. Rosenberg, and E. E. Vokes, "Optimizing Treatment De-Escalation in Head and Neck Cancer: Current and Future Perspectives," *The oncologist*, vol. 26, no. 1, pp. 40-48, 2021.
- [27] M. Arbyn, E. Weiderpass, L. Bruni *et al.*, "Estimates of incidence and mortality of cervical cancer in 2018: a worldwide analysis," *The Lancet Global Health*, vol. 8, no. 2, pp. e191-e203, 2020.
- [28] A. Psyrrri, and D. DiMaio, "Human papillomavirus in cervical and head-and-neck cancer," *Nature Clinical Practice Oncology*, vol. 5, no. 1, pp. 24-31, 2008/01/01, 2008.
- [29] C. R. Uk. "Cervical cancer statistics," <https://www.cancerresearchuk.org/health-professional/cancer-statistics/statistics-by-cancer-type/cervical-cancer>.
- [30] H. Lyng, and E. Malinen, "Hypoxia in cervical cancer: from biology to imaging," *Clinical and translational imaging*, vol. 5, no. 4, pp. 373-388, 2017.
- [31] P. J. Hoskin, "Hypoxia dose painting in prostate and cervix cancer," *Acta Oncologica*, vol. 54, no. 9, pp. 1259-1262, 2015/10/21, 2015.
- [32] S. Kilic, B. Cracchiolo, M. Gabel *et al.*, "The relevance of molecular biomarkers in cervical cancer patients treated with radiotherapy," *Annals of Translational Medicine*, vol. 3, no. 18, pp, 2015.
- [33] J. Overgaard, "Hypoxic radiosensitization: adored and ignored," *J Clin Oncol*, vol. 25, no. 26, pp. 4066-74, Sep 10, 2007.
- [34] J. Overgaard, "Hypoxic Radiosensitization: Adored and Ignored," *Journal of Clinical Oncology*, vol. 25, no. 26, pp. 4066-4074, 2007/09/10, 2007.
- [35] I. S. Dayes, and S. Abuzallouf, "Local tumour control in women with carcinoma of the cervix treated with the addition of nitroimidazole agents to

radiotherapy: a meta-analysis," *The British Journal of Radiology*, vol. 78, no. 933, pp. 777-782, 2005/09/01, 2005.

- [36] "Biomarkers and surrogate endpoints: preferred definitions and conceptual framework," *Clin Pharmacol Ther*, vol. 69, no. 3, pp. 89-95, Mar, 2001.
- [37] J. Meehan, M. Gray, C. Martínez-Pérez *et al.*, "Precision Medicine and the Role of Biomarkers of Radiotherapy Response in Breast Cancer," *Front Oncol*, vol. 10, pp. 628, 2020.
- [38] N. Lee, H. Schoder, B. Beattie *et al.*, "Strategy of Using Intratreatment Hypoxia Imaging to Selectively and Safely Guide Radiation Dose De-escalation Concurrent With Chemotherapy for Locoregionally Advanced Human Papillomavirus-Related Oropharyngeal Carcinoma," *Int J Radiat Oncol Biol Phys*, vol. 96, no. 1, pp. 9-17, Sep 1, 2016.
- [39] E. A. Eisenhauer, P. Therasse, J. Bogaerts *et al.*, "New response evaluation criteria in solid tumours: Revised RECIST guideline (version 1.1)," *European Journal of Cancer*, vol. 45, no. 2, pp. 228-247, 2009/01/01/, 2009.
- [40] A. B. Miller, B. Hoogstraten, M. Staquet *et al.*, "Reporting results of cancer treatment," *Cancer*, vol. 47, no. 1, pp. 207-14, Jan 1, 1981.
- [41] R. L. Wahl, H. Jacene, Y. Kasamon *et al.*, "From RECIST to PERCIST: Evolving Considerations for PET response criteria in solid tumors," *Journal of nuclear medicine : official publication, Society of Nuclear Medicine*, vol. 50 Suppl 1, no. Suppl 1, pp. 122S-50S, 2009.
- [42] A. Sadeghi-Naini, O. Falou, J. M. Hudson *et al.*, "Imaging innovations for cancer therapy response monitoring," *Imaging in Medicine*, vol. 4, no. 3, pp. 311-327, 2012.
- [43] G. De Rubis, S. Rajeev Krishnan, and M. Bebawy, "Liquid Biopsies in Cancer Diagnosis, Monitoring, and Prognosis," *Trends in Pharmacological Sciences*, vol. 40, no. 3, pp. 172-186, 2019/03/01/, 2019.
- [44] M. J. Duffy, E. W. McDermott, and J. Crown, "Blood-based biomarkers in breast cancer: From proteins to circulating tumor cells to circulating tumor DNA," *Tumor Biology*, vol. 40, no. 5, pp. 1010428318776169, 2018/05/01, 2018.
- [45] F. J. Hilke, F. Muyas, J. Admard *et al.*, "Dynamics of cell-free tumour DNA correlate with treatment response of head and neck cancer patients receiving radiochemotherapy," *Radiotherapy and Oncology*, vol. 151, pp. 182-189, 2020.
- [46] C. D. Marcus, V. Ladam-Marcus, C. Cucu *et al.*, "Imaging techniques to evaluate the response to treatment in oncology: Current standards and perspectives," *Critical Reviews in Oncology/Hematology*, vol. 72, no. 3, pp. 217-238, 2009/12/01/, 2009.

- [47] J. P. O'Connor, E. O. Aboagye, J. E. Adams *et al.*, "Imaging biomarker roadmap for cancer studies," *Nat Rev Clin Oncol*, vol. 14, no. 3, pp. 169-186, Mar, 2017.
- [48] H. Cliffe, C. Patel, R. Prestwich *et al.*, "Radiotherapy response evaluation using FDG PET-CT—established and emerging applications," *The British Journal of Radiology*, vol. 90, no. 1071, pp. 20160764, 2017/03/01, 2017.
- [49] N. Helsen, T. Van den Wyngaert, L. Carp *et al.*, "FDG-PET/CT for treatment response assessment in head and neck squamous cell carcinoma: a systematic review and meta-analysis of diagnostic performance," *European Journal of Nuclear Medicine and Molecular Imaging*, vol. 45, no. 6, pp. 1063-1071, 2018/06/01, 2018.
- [50] M. G. Isles, C. McConkey, and H. M. Mehanna, "A systematic review and meta-analysis of the role of positron emission tomography in the follow up of head and neck squamous cell carcinoma following radiotherapy or chemoradiotherapy," *Clinical Otolaryngology*, vol. 33, no. 3, pp. 210-222, 2008/06/01, 2008.
- [51] A. Campbell, L. M. Davis, S. K. Wilkinson *et al.*, "Emerging Functional Imaging Biomarkers of Tumour Responses to Radiotherapy," *Cancers*, vol. 11, no. 2, pp. 131, 2019.
- [52] K. Lehtiö, O. Eskola, T. Viljanen *et al.*, "Imaging perfusion and hypoxia with PET to predict radiotherapy response in head-and-neck cancer," *International Journal of Radiation Oncology\*Biology\*Physics*, vol. 59, no. 4, pp. 971-982, 2004/07/15/, 2004.
- [53] J. M. Bernstein, J. J. Homer, and C. M. West, "Dynamic contrast-enhanced magnetic resonance imaging biomarkers in head and neck cancer: Potential to guide treatment? A systematic review," *Oral Oncology*, vol. 50, no. 10, pp. 963-970, 2014/10/01/, 2014.
- [54] H. Quon, and D. M. Brizel, "Predictive and Prognostic Role of Functional Imaging of Head and Neck Squamous Cell Carcinomas," *Seminars in Radiation Oncology*, vol. 22, no. 3, pp. 220-232, 2012/07/01/, 2012.
- [55] B. Liu, Z. Sun, W.-L. Ma *et al.*, "DCE-MRI Quantitative Parameters as Predictors of Treatment Response in Patients With Locally Advanced Cervical Squamous Cell Carcinoma Underwent CCRT," *Frontiers in Oncology*, vol. 10, 2020-October-29, 2020.
- [56] J. P. B. O'Connor, S. P. Robinson, and J. C. Waterton, "Imaging tumour hypoxia with oxygen-enhanced MRI and BOLD MRI," *Br J Radiol*, vol. 92, no. 1095, pp. 20180642, Mar, 2019.
- [57] L. Zhu, L. Zhu, H. Shi *et al.*, "Evaluating early response of cervical cancer under concurrent chemo-radiotherapy by intravoxel incoherent motion MR imaging," *BMC cancer*, vol. 16, pp. 79-79, 2016.

- [58] M. Ghadimi, and A. Sapra, "Magnetic resonance imaging contraindications," *StatPearls [Internet]*, 2021.
- [59] T. J. Fraum, D. R. Ludwig, M. R. Bashir *et al.*, "Gadolinium-based contrast agents: a comprehensive risk assessment," *Journal of Magnetic Resonance Imaging*, vol. 46, no. 2, pp. 338-353, 2017.
- [60] C. I. Board, *Magnetic resonance imaging (MRI) equipment, operations and planning in the NHS*, The Royal College of Radiologists (RCR), 2017.
- [61] S. Ursino, L. Faggioni, F. Guidoccio *et al.*, "Role of perfusion CT in the evaluation of functional primary tumour response after radiochemotherapy in head and neck cancer: preliminary findings," *The British Journal of Radiology*, vol. 89, no. 1065, pp. 20151070, 2016/09/01, 2016.
- [62] T. I. Banks, R. von Eyben, D. Hristov *et al.*, "Pilot study of combined FDG-PET and dynamic contrast-enhanced CT of locally advanced cervical carcinoma before and during concurrent chemoradiotherapy suggests association between changes in tumor blood volume and treatment response," *Cancer Med*, vol. 7, no. 8, pp. 3642-3651, Aug, 2018.
- [63] D. Cosgrove, and N. Lassau, "Imaging of perfusion using ultrasound," *European Journal of Nuclear Medicine and Molecular Imaging*, vol. 37, no. 1, pp. 65-85, 2010/08/01, 2010.
- [64] W. K. Chong, V. Papadopoulou, and P. A. Dayton, "Imaging with ultrasound contrast agents: current status and future," *Abdom Radiol (NY)*, vol. 43, no. 4, pp. 762-772, Apr, 2018.
- [65] S. Rockwell, I. T. Dobrucki, E. Y. Kim *et al.*, "Hypoxia and radiation therapy: past history, ongoing research, and future promise," *Current molecular medicine*, vol. 9, no. 4, pp. 442-458, 2009.
- [66] C. Liu, Q. Lin, and Z. Yun, "Cellular and molecular mechanisms underlying oxygen-dependent radiosensitivity," *Radiat Res*, vol. 183, no. 5, pp. 487-96, May, 2015.
- [67] H. E. Barker, J. T. E. Paget, A. A. Khan *et al.*, "The tumour microenvironment after radiotherapy: mechanisms of resistance and recurrence," *Nature reviews. Cancer*, vol. 15, no. 7, pp. 409-425, 2015.
- [68] R. Huang, and P.-K. Zhou, "HIF-1 signaling: A key orchestrator of cancer radioresistance," *Radiation Medicine and Protection*, vol. 1, no. 1, pp. 7-14, 2020/03/01/, 2020.
- [69] N. A. Mayr, W. T. C. Yuh, V. A. Magnotta *et al.*, "Tumor perfusion studies using fast magnetic resonance imaging technique in advanced cervical cancer: A new noninvasive predictive assay," *International Journal of Radiation Oncology\*Biophysics\*Physics*, vol. 36, no. 3, pp. 623-633, 1996/10/01/, 1996.

- [70] N. A. Mayr, W. T. C. Yuh, J. C. Arnholt *et al.*, "Pixel analysis of MR perfusion imaging in predicting radiation therapy outcome in cervical cancer," *Journal of Magnetic Resonance Imaging*, vol. 12, no. 6, pp. 1027-1033, 2000/12/01, 2000.
- [71] N. A. Mayr, J. Z. Wang, D. Zhang *et al.*, "Longitudinal Changes in Tumor Perfusion Pattern during the Radiation Therapy Course and its Clinical Impact in Cervical Cancer," *International Journal of Radiation Oncology\*Biology\*Physics*, vol. 77, no. 2, pp. 502-508, 2010/06/01/, 2010.
- [72] Y. Yamashita, T. Baba, Y. Baba *et al.*, "Dynamic Contrast-enhanced MR Imaging of Uterine Cervical Cancer: Pharmacokinetic Analysis with Histopathologic Correlation and Its Importance in Predicting the Outcome of Radiation Therapy1," *Radiology*, vol. 216, pp. 803-9, 10/01, 2000.
- [73] J. A. Loncaster, B. M. Carrington, J. R. Sykes *et al.*, "Prediction of radiotherapy outcome using dynamic contrast enhanced MRI of carcinoma of the cervix," *International Journal of Radiation Oncology • Biology • Physics*, vol. 54, no. 3, pp. 759-767, 2002.
- [74] A. F. DeVries, J. Griebel, C. Kremser *et al.*, "Tumor microcirculation evaluated by dynamic magnetic resonance imaging predicts therapy outcome for primary rectal carcinoma," *Cancer Res*, vol. 61, no. 6, pp. 2513-6, Mar 15, 2001.
- [75] A. F. DeVries, C. Kremser, P. A. Hein *et al.*, "Tumor microcirculation and diffusion predict therapy outcome for primary rectal carcinoma," *International Journal of Radiation Oncology\*Biology\*Physics*, vol. 56, no. 4, pp. 958-965, 2003/07/15/, 2003.
- [76] P. J. Hoskin, M. I. Saunders, K. Goodchild *et al.*, "Dynamic contrast enhanced magnetic resonance scanning as a predictor of response to accelerated radiotherapy for advanced head and neck cancer," *Br J Radiol*, vol. 72, no. 863, pp. 1093-8, Nov, 1999.
- [77] L. Preda, S. F. Calloni, M. E. M. Moscatelli *et al.*, "Role of CT Perfusion in Monitoring and Prediction of Response to Therapy of Head and Neck Squamous Cell Carcinoma," *BioMed Research International*, vol. 2014, pp. 917150, 2014/07/21, 2014.
- [78] D. P. Noij, M. C. de Jong, L. G. Mulders *et al.*, "Contrast-enhanced perfusion magnetic resonance imaging for head and neck squamous cell carcinoma: a systematic review," *Oral Oncol*, vol. 51, no. 2, pp. 124-38, Feb, 2015.
- [79] A. Shukla-Dave, N. Y. Lee, J. F. A. Jansen *et al.*, "Dynamic contrast-enhanced magnetic resonance imaging as a predictor of outcome in head-and-neck squamous cell carcinoma patients with nodal metastases," *International journal of radiation oncology, biology, physics*, vol. 82, no. 5, pp. 1837-1844, 2012.

- [80] B. P. Venkatesulu, L. S. Mahadevan, M. L. Aliru *et al.*, "Radiation-Induced Endothelial Vascular Injury: A Review of Possible Mechanisms," *JACC. Basic to translational science*, vol. 3, no. 4, pp. 563-572, 2018.
- [81] M. Garcia-Barros, F. Paris, C. Cordon-Cardo *et al.*, "Tumor Response to Radiotherapy Regulated by Endothelial Cell Apoptosis," *Science*, vol. 300, no. 5622, pp. 1155, 2003.
- [82] J.-P. Truman, M. García-Barros, M. Kaag *et al.*, "Endothelial Membrane Remodeling Is Obligate for Anti-Angiogenic Radiosensitization during Tumor Radiosurgery," *PLOS ONE*, vol. 5, no. 8, pp. e12310, 2010.
- [83] S. Bodo, C. Campagne, T. H. Thin *et al.*, "Single-dose radiotherapy disables tumor cell homologous recombination via ischemia/reperfusion injury," *The Journal of Clinical Investigation*, vol. 129, no. 2, pp. 786-801, 02/01/, 2019.
- [84] S. K. Kasoji, J. N. Rivera, R. C. Gessner *et al.*, "Early Assessment of Tumor Response to Radiation Therapy using High-Resolution Quantitative Microvascular Ultrasound Imaging," *Theranostics*, vol. 8, no. 1, pp. 156-168, 2018.
- [85] M. R. Horsman, T. Nielsen, L. Østergaard *et al.*, "Radiation administered as a large single dose or in a fractionated schedule: Role of the tumour vasculature as a target for influencing response," *Acta Oncologica*, vol. 45, no. 7, pp. 876-880, 2006/01/01, 2006.
- [86] D. W. N. Kim, J. Huamani, K. J. Niermann *et al.*, "Noninvasive Assessment of Tumor Vasculature Response to Radiation-Mediated, Vasculature-Targeted Therapy Using Quantified Power Doppler Sonography," *Journal of Ultrasound in Medicine*, vol. 25, no. 12, pp. 1507-1517, 2006/12/01, 2006.
- [87] D. L. Schwartz, J. Bankson, L. Bidaut *et al.*, "HIF-1-dependent stromal adaptation to ischemia mediates in vivo tumor radiation resistance," *Molecular cancer research : MCR*, vol. 9, no. 3, pp. 259-270, 2011.
- [88] A. El Kaffas, A. Giles, and G. J. Czarnota, "Dose-dependent response of tumor vasculature to radiation therapy in combination with Sunitinib depicted by three-dimensional high-frequency power Doppler ultrasound," *Angiogenesis*, vol. 16, no. 2, pp. 443-454, 2013/04/01, 2013.
- [89] A. Salem, R. A. Little, A. Latif *et al.*, "Oxygen-enhanced MRI Is Feasible, Repeatable, and Detects Radiotherapy-induced Change in Hypoxia in Xenograft Models and in Patients with Non-small Cell Lung Cancer," *Clinical Cancer Research*, 2019.
- [90] A. Jani, F. Shaikh, S. Barton *et al.*, "High-Dose, Single-Fraction Irradiation Rapidly Reduces Tumor Vasculature and Perfusion in a Xenograft Model of Neuroblastoma," *International Journal of Radiation Oncology\*Biophysics\*Physics*, vol. 94, no. 5, pp. 1173-1180, 2016/04/01/, 2016.

- [91] J. Bussink, J. H. A. M. Kaanders, P. F. J. W. Rijken *et al.*, *Changes in Blood Perfusion and Hypoxia after Irradiation of a Human Squamous Cell Carcinoma Xenograft Tumor Line*: BIOONE, 2000.
- [92] V. Demidov, A. Maeda, M. Sugita *et al.*, "Preclinical longitudinal imaging of tumor microvascular radiobiological response with functional optical coherence tomography," *Scientific Reports*, vol. 8, no. 1, pp. 38, 2018/01/08, 2018.
- [93] P. L. Olive, "Radiation-induced reoxygenation in the SCCVII murine tumour: evidence for a decrease in oxygen consumption and an increase in tumour perfusion," *Radiotherapy and Oncology*, vol. 32, no. 1, pp. 37-46, 1994/07/01/, 1994.
- [94] H. D. Roh, Y. Boucher, S. Kalnicki *et al.*, "Interstitial Hypertension in Carcinoma of Uterine Cervix in Patients: Possible Correlation with Tumor Oxygenation and Radiation Response," *Cancer Research*, vol. 51, no. 24, pp. 6695, 1991.
- [95] N. Crockart, B. F. Jordan, C. Baudelet *et al.*, "Early reoxygenation in tumors after irradiation: Determining factors and consequences for radiotherapy regimens using daily multiple fractions," *International Journal of Radiation Oncology\*Biophysics*, vol. 63, no. 3, pp. 901-910, 2005/11/01/, 2005.
- [96] L. J. Rich, and M. Seshadri, "Photoacoustic monitoring of tumor and normal tissue response to radiation," *Sci Rep*, vol. 6, pp. 21237, Feb 17, 2016.
- [97] K. D. Castle, and D. G. Kirsch, "Establishing the Impact of Vascular Damage on Tumor Response to High-Dose Radiation Therapy," *Cancer research*, vol. 79, no. 22, pp. 5685-5692, 2019.
- [98] M. García-Barros, T. H. Thin, J. Maj *et al.*, "Impact of stromal sensitivity on radiation response of tumors implanted in SCID hosts revisited," *Cancer research*, vol. 70, no. 20, pp. 8179-8186, 2010.
- [99] J. H. Tsai, S. Makonnen, M. Feldman *et al.*, "Ionizing radiation inhibits tumor neovascularization by inducing ineffective angiogenesis," *Cancer Biology & Therapy*, vol. 4, no. 12, pp. 1395-1400, 2005/12/01, 2005.
- [100] J. M. Brown, D. J. Brenner, and D. J. Carlson, "Dose escalation, not "new biology," can account for the efficacy of stereotactic body radiation therapy with non-small cell lung cancer," *International journal of radiation oncology, biology, physics*, vol. 85, no. 5, pp. 1159-1160, 2013.
- [101] K. M. Arnold, N. J. Flynn, A. Raben *et al.*, "The Impact of Radiation on the Tumor Microenvironment: Effect of Dose and Fractionation Schedules," *Cancer Growth and Metastasis*, vol. 11, pp. 1179064418761639, 2018.
- [102] R. J. Gillies, P. A. Schornack, T. W. Secomb *et al.*, "Causes and effects of heterogeneous perfusion in tumors," *Neoplasia (New York, N.Y.)*, vol. 1, no. 3, pp. 197-207, 1999.

- [103] J. P. B. O'Connor, C. J. Rose, J. C. Waterton *et al.*, "Imaging intratumor heterogeneity: role in therapy response, resistance, and clinical outcome," *Clinical cancer research : an official journal of the American Association for Cancer Research*, vol. 21, no. 2, pp. 249-257, 2015.
- [104] F.-H. Chen, C.-S. Chiang, C.-C. Wang *et al.*, "Radiotherapy decreases vascular density and causes hypoxia with macrophage aggregation in TRAMP-C1 prostate tumors," *Clinical cancer research : an official journal of the American Association for Cancer Research*, vol. 15, no. 5, pp. 1721-1729, 2009.
- [105] O. V. Solesvik, E. K. Rofstad, and T. Brustad, "Vascular changes in a human malignant melanoma xenograft following single-dose irradiation," *Radiat Res*, vol. 98, no. 1, pp. 115-28, Apr, 1984.
- [106] P. Heon Joo, J. G. Robert, H. Susanta *et al.*, "Radiation-Induced Vascular Damage in Tumors: Implications of Vascular Damage in Ablative Hypofractionated Radiotherapy (SBRT and SRS)," *Radiation Research*, vol. 177, no. 3, pp. 311-327, 1/1, 2012.
- [107] S.-L. Peng, C.-F. Chen, H.-L. Liu *et al.*, "Analysis of parametric histogram from dynamic contrast-enhanced MRI: application in evaluating brain tumor response to radiotherapy," *NMR in Biomedicine*, vol. 26, no. 4, pp. 443-450, 2013/04/01, 2013.
- [108] H. J. Baek, H. S. Kim, N. Kim *et al.*, "Percent change of perfusion skewness and kurtosis: a potential imaging biomarker for early treatment response in patients with newly diagnosed glioblastomas," *Radiology*, vol. 264, no. 3, pp. 834-43, Sep, 2012.
- [109] L. Alic, M. van Vliet, P. A. Wielopolski *et al.*, "Regional heterogeneity changes in DCE-MRI as response to isolated limb perfusion in experimental soft-tissue sarcomas," *Contrast Media & Molecular Imaging*, vol. 8, no. 4, pp. 340-349, 2013/07/01, 2013.
- [110] D. J. Rakhit, H. Becher, M. Monaghan *et al.*, "The clinical applications of myocardial contrast echocardiography," *European Journal of Echocardiography*, vol. 8, no. 3, pp. s24-s29, 2007.
- [111] K. Lv, H. Zhai, Y. Jiang *et al.*, "Prospective assessment of diagnostic efficacy and safety of Sonazoid(TM) and SonoVue(®) ultrasound contrast agents in patients with focal liver lesions," *Abdom Radiol (NY)*, vol. 46, no. 10, pp. 4647-4659, Oct, 2021.
- [112] K. Hatanaka, M. Kudo, Y. Minami *et al.*, "Sonazoid-Enhanced Ultrasonography for Diagnosis of Hepatic Malignancies: Comparison with Contrast-Enhanced CT," *Oncology*, vol. 75, pp. 42-7, Dec 2008
- [113] C. F. Dietrich, C. P. Nolsøe, R. G. Barr *et al.*, "Guidelines and Good Clinical Practice Recommendations for Contrast-Enhanced Ultrasound (CEUS) in the

Liver-Update 2020 WFUMB in Cooperation with EFSUMB, AFSUMB, AIUM, and FLAUS," *Ultrasound Med Biol*, vol. 46, no. 10, pp. 2579-2604, Oct, 2020.

- [114] T. K. Kim, S. Y. Noh, S. R. Wilson *et al.*, "Contrast-enhanced ultrasound (CEUS) liver imaging reporting and data system (LI-RADS) 2017 - a review of important differences compared to the CT/MRI system," *Clin Mol Hepatol*, vol. 23, no. 4, pp. 280-289, Dec, 2017.
- [115] E. Terzi, M. Iavarone, M. Pompili *et al.*, "Contrast ultrasound LI-RADS LR-5 identifies hepatocellular carcinoma in cirrhosis in a multicenter retrospective study of 1,006 nodules," *Journal of Hepatology*, vol. 68, no. 3, pp. 485-492, 2018/03/01/, 2018.
- [116] P. Frinking, T. Segers, Y. Luan *et al.*, "Three Decades of Ultrasound Contrast Agents: A Review of the Past, Present and Future Improvements," *Ultrasound Med Biol*, vol. 46, no. 4, pp. 892-908, Apr, 2020.
- [117] H.-y. Zhai, P. Liang, J. Yu *et al.*, "Comparison of Sonazoid and SonoVue in the Diagnosis of Focal Liver Lesions: A Preliminary Study," *Journal of Ultrasound in Medicine*, vol. 38, no. 9, pp. 2417-2425, 2019/09/01, 2019.
- [118] H.-J. Kang, J. M. Lee, J. H. Yoon *et al.*, "Contrast-enhanced US with Sulfur Hexafluoride and Perfluorobutane for the Diagnosis of Hepatocellular Carcinoma in Individuals with High Risk," *Radiology*, vol. 297, no. 1, pp. 108-116, 2020/10/01, 2020.
- [119] I. Boca, S. M. Ducea, and A. I. Ciurea, "Contrast-Enhanced Ultrasonography in the Diagnosis and Treatment Modulation of Breast Cancer," *Journal of Personalized Medicine*, vol. 11, no. 2, 2021.
- [120] J. Y. Lee, Y. Minami, B. I. Choi *et al.*, "The AFSUMB Consensus Statements and Recommendations for the Clinical Practice of Contrast-Enhanced Ultrasound using Sonazoid," *Journal of medical ultrasound*, vol. 28, no. 2, pp. 59-82, 2020.
- [121] C.-C. Shen, Y.-H. Chou, and P.-C. Li, "Pulse Inversion Techniques in Ultrasonic Nonlinear Imaging," *Journal of Medical Ultrasound*, vol. 13, no. 1, pp. 3-17, 2005/01/01/, 2005.
- [122] A. L. Klibanov, "Ultrasound Contrast: Gas Microbubbles in the Vasculature," *Invest Radiol*, vol. 56, no. 1, pp. 50-61, Jan, 2021.
- [123] C. F. Dietrich, M. A. Averkiou, J. M. Correas *et al.*, "An EFSUMB introduction into Dynamic Contrast-Enhanced Ultrasound (DCE-US) for quantification of tumour perfusion," *Ultraschall Med*, vol. 33, no. 4, pp. 344-51, Aug, 2012.
- [124] J. M. Hudson, R. Williams, B. Lloyd *et al.*, "Improved flow measurement using microbubble contrast agents and disruption-replenishment: clinical application to tumour monitoring," *Ultrasound Med Biol*, vol. 37, no. 8, pp. 1210-21, Aug, 2011.

- [125] S. Turco, P. Frinking, R. Wildeboer *et al.*, "Contrast-Enhanced Ultrasound Quantification: From Kinetic Modeling to Machine Learning," *Ultrasound in Medicine & Biology*, vol. 46, no. 3, pp. 518-543, 2020/03/01/, 2020.
- [126] N. Weidner, J. Folkman, F. Pozza *et al.*, "Tumor Angiogenesis: A New Significant and Independent Prognostic Indicator in Early-Stage Breast Carcinoma," *JNCI: Journal of the National Cancer Institute*, vol. 84, no. 24, pp. 1875-1887, 1992.
- [127] N. Mori, S. Mugikura, S. Takahashi *et al.*, "Quantitative Analysis of Contrast-Enhanced Ultrasound Imaging in Invasive Breast Cancer: A Novel Technique to Obtain Histopathologic Information of Microvessel Density," *Ultrasound Med Biol*, vol. 43, no. 3, pp. 607-614, Mar, 2017.
- [128] H. Zhuang, Z. G. Yang, H. J. Chen *et al.*, "Time-intensity curve parameters in colorectal tumours measured using double contrast-enhanced ultrasound: correlations with tumour angiogenesis," *Colorectal Disease*, vol. 14, no. 2, pp. 181-187, 2012/02/01, 2012.
- [129] S. Pitre-Champagnat, I. Leguerney, J. Bosq *et al.*, "Dynamic Contrast-Enhanced Ultrasound Parametric Maps to Evaluate Intratumoral Vascularization," *Investigative Radiology*, vol. 50, no. 4, pp. 212-217, 2015.
- [130] J. Zhuo, W. Fu, and S. Liu, "Correlation of Contrast-Enhanced Ultrasound with Two Distinct Types of Blood Vessels for the Assessment of Angiogenesis in Lewis Lung Carcinoma," *Ultraschall Med*, vol. 35, no. 05, pp. 468-472, 2014.
- [131] K. Hoyt, A. Sorace, and R. Saini, "Quantitative mapping of tumor vascularity using volumetric contrast-enhanced ultrasound," *Investigative radiology*, vol. 47, no. 3, pp. 167-174, 2012.
- [132] P. Zhang, Y. Chen, J. Liu *et al.*, "Quantitative Evaluation of Combretastatin A4 Phosphate Early Efficacy in a Tumor Model with Dynamic Contrast-Enhanced Ultrasound," *Ultrasound in Medicine & Biology*, vol. 44, no. 4, pp. 840-852, 2018/04/01/, 2018.
- [133] A. Shah, N. Bush, G. Box *et al.*, "Value of combining dynamic contrast enhanced ultrasound and optoacoustic tomography for hypoxia imaging," *Photoacoustics*, vol. 8, pp. 15-27, 2017/12/01/, 2017.
- [134] A. Bar-Zion, M. Yin, D. Adam *et al.*, "Functional Flow Patterns and Static Blood Pooling in Tumors Revealed by Combined Contrast-Enhanced Ultrasound and Photoacoustic Imaging," *Cancer Research*, vol. 76, no. 15, pp. 4320-4331, 2016.
- [135] M. Butler, A. Perperidis, J. M. Zahra *et al.*, "Differentiation of Vascular Characteristics Using Contrast-Enhanced Ultrasound Imaging," *Ultrasound Med Biol*, vol. 45, no. 9, pp. 2444-2455, Sep, 2019.

- [136] K. Mahéo, S. Chevalier, S. Vibet *et al.*, "Non-invasive quantification of tumor vascular architecture during docetaxel-chemotherapy," *Breast Cancer Research and Treatment*, vol. 134, no. 3, pp. 1013-1025, 2012/08/01, 2012.
- [137] M. Galiè, M. D'Onofrio, M. Montani *et al.*, "Tumor Vessel Compression Hinders Perfusion of Ultrasonographic Contrast Agents," *Neoplasia*, vol. 7, no. 5, pp. 528-536, 2005/05/01/, 2005.
- [138] J. R. Eisenbrey, C. C. Wilson, R. J. Ro *et al.*, "Correlation of ultrasound contrast agent derived blood flow parameters with immunohistochemical angiogenesis markers in murine xenograft tumor models," *Ultrasonics*, vol. 53, no. 7, pp. 1384-1391, 2013/09/01/, 2013.
- [139] P. S. Sidhu, V. Cantisani, C. F. Dietrich *et al.*, "The EFSUMB Guidelines and Recommendations for the Clinical Practice of Contrast-Enhanced Ultrasound (CEUS) in Non-Hepatic Applications: Update 2017 (Short Version)," *Ultraschall Med*, vol. 39, no. 02, pp. 154-180, 2018.
- [140] N. Lassau, J. Bonastre, M. Kind *et al.*, "Validation of dynamic contrast-enhanced ultrasound in predicting outcomes of antiangiogenic therapy for solid tumors: the French multicenter support for innovative and expensive techniques study," *Invest Radiol*, vol. 49, no. 12, pp. 794-800, Dec, 2014.
- [141] N. Lassau, S. Koscielny, L. Albiges *et al.*, "Metastatic renal cell carcinoma treated with sunitinib: early evaluation of treatment response using dynamic contrast-enhanced ultrasonography," *Clin Cancer Res*, vol. 16, no. 4, pp. 1216-25, Feb 15, 2010.
- [142] M. Lamuraglia, B. Escudier, L. Chami *et al.*, "To predict progression-free survival and overall survival in metastatic renal cancer treated with sorafenib: Pilot study using dynamic contrast-enhanced Doppler ultrasound," *European Journal of Cancer*, vol. 42, no. 15, pp. 2472-2479.
- [143] J. M. Hudson, R. Williams, C. Tremblay-Darveau *et al.*, "Dynamic contrast enhanced ultrasound for therapy monitoring," *Eur J Radiol*, vol. 84, no. 9, pp. 1650-7, Sep, 2015.
- [144] N. Arteaga-Marrero, J. F. Mainou-Gomez, C. Brekke Rygh *et al.*, "Radiation treatment monitoring with DCE-US in CWR22 prostate tumor xenografts," *Acta Radiologica*, pp. 0284185118798167, 2018.
- [145] A. El Kaffas, R. M. S. Sigrist, G. Fisher *et al.*, "Quantitative Three-Dimensional Dynamic Contrast-Enhanced Ultrasound Imaging: First-In-Human Pilot Study in Patients with Liver Metastases," *Theranostics*, vol. 7, no. 15, pp. 3745-3758, 2017.
- [146] F.-j. Dong, J.-f. Xu, D. Du *et al.*, "3D analysis is superior to 2D analysis for contrast-enhanced ultrasound in revealing vascularity in focal liver lesions – A

retrospective analysis of 83 cases," *Ultrasonics*, vol. 70, pp. 221-226, 2016/08/01/, 2016.

- [147] A. Sridharan, J. R. Eisenbrey, P. Machado *et al.*, "Quantitative analysis of vascular heterogeneity in breast lesions using contrast-enhanced 3-D harmonic and subharmonic ultrasound imaging," *IEEE transactions on ultrasonics, ferroelectrics, and frequency control*, vol. 62, no. 3, pp. 502-510, 2015.
- [148] H. Fukuda, K. Numata, K. Hara *et al.*, "Comparison of vascularity observed using contrast-enhanced 3D ultrasonography and pathological changes in patients with hepatocellular carcinoma after sorafenib treatment," *Journal of Cancer*, vol. 9, no. 13, pp. 2408-2414, 2018.
- [149] Y. Lu, B. Liu, Y. Zheng *et al.*, "Application of real-time three-dimensional contrast-enhanced ultrasound using SonoVue for the evaluation of focal liver lesions: a prospective single-center study," *American journal of translational research*, vol. 10, no. 5, pp. 1469-1480, 2018.
- [150] W.-R. Jia, L. Tang, D.-B. Wang *et al.*, "Three-dimensional Contrast-enhanced Ultrasound in Response Assessment for Breast Cancer: A Comparison with Dynamic Contrast-enhanced Magnetic Resonance Imaging and Pathology," *Scientific Reports*, vol. 6, pp. 33832, 09/22/online, 2016.
- [151] S. Feingold, R. Gessner, I. M. Guracar *et al.*, "Quantitative volumetric perfusion mapping of the microvasculature using contrast ultrasound," *Investigative radiology*, vol. 45, no. 10, pp. 669-674, 2010.
- [152] M. X. Tang, H. Mulvana, T. Gauthier *et al.*, "Quantitative contrast-enhanced ultrasound imaging: a review of sources of variability," *Interface focus*, vol. 1, no. 4, pp. 520-539, 2011.
- [153] T. P. Gauthier, M. Chebil, P. Peronneau *et al.*, "In vitro evaluation of the impact of ultrasound scanner settings and contrast bolus volume on time-intensity curves," *Ultrasonics*, vol. 52, no. 1, pp. 12-19, 2012/01/01/, 2012.
- [154] T. P. Gauthier, M. A. Averkiou, and E. L. S. Leen, "Perfusion quantification using dynamic contrast-enhanced ultrasound: The impact of dynamic range and gain on time-intensity curves," *Ultrasonics*, vol. 51, no. 1, pp. 102-106, 2011/01/01/, 2011.
- [155] J. Fromageau, N. Tunariu, and J. C. Bamber, "Evaluation of adaptive perfusion models in dynamic contrast-enhanced ultrasound (DCE-US)." pp. 1311-1314.
- [156] M. Doury, "Quantification of tissue perfusion using contrast-enhanced ultrasound : toward robust exam comparison

Quantification de la perfusion tissulaire en échographie de contraste : vers la comparaison robuste d'examen," Université Pierre et Marie Curie - Paris VI, 2017.

- [157] M. M. Tomayko, and C. P. Reynolds, "Determination of subcutaneous tumor size in athymic (nude) mice," *Cancer Chemotherapy and Pharmacology*, vol. 24, no. 3, pp. 148-154, 1989/09/01, 1989.
- [158] A. B. Iversen, M. Busk, and M. R. Horsman, "Induction of hypoxia by vascular disrupting agents and the significance for their combination with radiation therapy," *Acta Oncologica*, vol. 52, no. 7, pp. 1320-1326, 2013/10/01, 2013.
- [159] M. Hasegawa, H. Niibe, N. Mitsuhashi *et al.*, "Hyperfractionated and Hypofractionated Radiation Therapy for Human Malignant Glioma Xenograft in Nude Mice," *Japanese Journal of Cancer Research*, vol. 86, no. 9, pp. 879-884, 1995/09/01, 1995.
- [160] M. Martinho Costa, A. Shah, I. Rivens *et al.*, "Photoacoustic imaging for the prediction and assessment of response to radiotherapy in vivo," *bioRxiv*, 2018.
- [161] H. Menke, and P. Vaupel, "Effect of injectable or inhalational anesthetics and of neuroleptic, neuroleptanalgesic, and sedative agents on tumor blood flow," *Radiat Res*, vol. 114, no. 1, pp. 64-76, Apr, 1988.
- [162] P. C. Sontum, "Physicochemical Characteristics of Sonazoid™, A New Contrast Agent for Ultrasound Imaging," *Ultrasound in Medicine & Biology*, vol. 34, no. 5, pp. 824-833, 2008/05/01/, 2008.
- [163] T. Payen, A. Coron, M. Lamuraglia *et al.*, "Echo-Power Estimation from Log-Compressed Video Data in Dynamic Contrast-Enhanced Ultrasound Imaging," *Ultrasound in Medicine and Biology*, vol. 39, no. 10, pp. 1826-1837, 2013.
- [164] E. Moghimirad, J. Bamber, and E. Harris, "Plane wave versus focused transmissions for contrast enhanced ultrasound imaging: the role of parameter settings and the effects of flow rate on contrast measurements," *Phys Med Biol*, vol. 64, no. 9, pp. 095003, Apr 23, 2019.
- [165] Z. X. Elahe Moghimirad, Hong Ding, Jeffery Bamber, Emma Harris, "Evaluation of performance trade-offs when using mechanically swept 1D linear arrays for 3D DCE-US," 2022.
- [166] J. B. A. Maintz, and M. A. Viergever, "A survey of medical image registration," *Medical Image Analysis*, vol. 2, no. 1, pp. 1-36, 1998/03/01/, 1998.
- [167] MathWorks. "xcorr2," 2022;  
<https://uk.mathworks.com/help/signal/ref/xcorr2.html>.
- [168] M. Bazalova, and E. E. Graves, "The importance of tissue segmentation for dose calculations for kilovoltage radiation therapy," *Medical physics*, vol. 38, no. 6, pp. 3039-3049, 2011.

- [169] K. A. Smith, S. A. Hill, A. C. Begg *et al.*, "Validation of the fluorescent dye Hoechst 33342 as a vascular space marker in tumours," *British journal of cancer*, vol. 57, no. 3, pp. 247-253, 1988.
- [170] B. Méry, C. Rancoule, J. B. Guy *et al.*, "Preclinical models in HNSCC: A comprehensive review," *Oral Oncol*, vol. 65, pp. 51-56, Feb, 2017.
- [171] J. D. Boone, Z. C. Dobbin, J. M. Straughn, Jr. *et al.*, "Ovarian and cervical cancer patient derived xenografts: The past, present, and future," *Gynecol Oncol*, vol. 138, no. 2, pp. 486-91, Aug, 2015.
- [172] C. J. Lin, J. R. Grandis, T. E. Carey *et al.*, "Head and neck squamous cell carcinoma cell lines: established models and rationale for selection," *Head Neck*, vol. 29, no. 2, pp. 163-88, Feb, 2007.
- [173] R. J. Kimple, M. A. Smith, G. C. Blitzer *et al.*, "Enhanced Radiation Sensitivity in HPV-Positive Head and Neck Cancer," *Cancer Research*, vol. 73, no. 15, pp. 4791-4800, 2013.
- [174] S. C. Brüningk, "Analysis and simulation of combination treatments of radiation and focused ultrasound mediated heating," University of London, 2018.
- [175] M. McLaughlin, H. E. Barker, A. A. Khan *et al.*, "HSP90 inhibition sensitizes head and neck cancer to platin-based chemoradiotherapy by modulation of the DNA damage response resulting in chromosomal fragmentation," *BMC Cancer*, vol. 17, no. 1, pp. 86, 2017/01/31, 2017.
- [176] H. E. Barker, R. Patel, M. McLaughlin *et al.*, "CHK1 Inhibition Radiosensitizes Head and Neck Cancers to Paclitaxel-Based Chemoradiotherapy," *Molecular Cancer Therapeutics*, vol. 15, no. 9, pp. 2042, 2016.
- [177] K. Skok, L. Gradišnik, U. Maver *et al.*, "Gynaecological cancers and their cell lines," *Journal of Cellular and Molecular Medicine*, vol. 25, no. 8, pp. 3680-3698, 2021/04/01, 2021.
- [178] E. M. Burd, "Human papillomavirus and cervical cancer," *Clinical microbiology reviews*, vol. 16, no. 1, pp. 1-17, 2003.
- [179] M. V. Bose, G. Gopal, G. Selvaluxmy *et al.*, "Dominant negative Ubiquitin-conjugating enzyme E2C sensitizes cervical cancer cells to radiation," *International Journal of Radiation Biology*, vol. 88, no. 9, pp. 629-634, 2012/09/01, 2012.
- [180] W.-H. Su, P.-C. Chuang, E.-Y. Huang *et al.*, "Radiation-Induced Increase in Cell Migration and Metastatic Potential of Cervical Cancer Cells Operates Via the K-Ras Pathway," *The American Journal of Pathology*, vol. 180, no. 2, pp. 862-871, 2012/02/01/, 2012.

- [181] A. Saxena, C. Yashar, D. D. Taylor *et al.*, "Cellular response to chemotherapy and radiation in cervical cancer," *Am J Obstet Gynecol*, vol. 192, no. 5, pp. 1399-403, May, 2005.
- [182] J. P. Banáth, S. H. MacPhail, and P. L. Olive, "Radiation Sensitivity, H2AX Phosphorylation, and Kinetics of Repair of DNA Strand Breaks in Irradiated Cervical Cancer Cell Lines," *Cancer Research*, vol. 64, no. 19, pp. 7144-7149, 2004.
- [183] Y. Cheng, F. Li, E. Mladenov *et al.*, "The yield of DNA double strand breaks determined after exclusion of those forming from heat-labile lesions predicts tumor cell radiosensitivity to killing," *Radiotherapy and Oncology*, vol. 116, no. 3, pp. 366-373, 2015/09/01/, 2015.
- [184] B. Efron, "Bootstrap confidence intervals: Good or bad?," *Psychological Bulletin*, vol. 104, no. 2, pp. 293-296, 1988.
- [185] J. Kahn, P. J. Tofilon, and K. Camphausen, "Preclinical models in radiation oncology," *Radiation Oncology*, vol. 7, no. 1, pp. 223, 2012/12/27, 2012.
- [186] Envigo, *Radiosensitivity of immunodeficient mice in oncology studies*, Envigo, 2017.
- [187] A. G. Taghian, and H. D. Suit, "Animal systems for translational research in radiation oncology," *Acta Oncol*, vol. 38, no. 7, pp. 829-38, 1999.
- [188] S. Lauk, A. Zietman, S. Skates *et al.*, "Comparative Morphometric Study of Tumor Vasculature in Human Squamous Cell Carcinomas and Their Xenotransplants in Athymic Nude Mice<sup>1</sup>," *Cancer Research*, vol. 49, no. 16, pp. 4557-4561, 1989.
- [189] S. Kim, "Animal models of cancer in the head and neck region," *Clinical and experimental otorhinolaryngology*, vol. 2, no. 2, pp. 55-60, 2009.
- [190] C. Cheers, and R. Waller, "Activated Macrophages in Congenitally Athymic "Nude" Mice and in Lethally Irradiated Mice," *The Journal of Immunology*, vol. 115, no. 3, pp. 844, 1975.
- [191] K. I. Jones, J. Tiersma, A. E. Yuzhalin *et al.*, "Radiation combined with macrophage depletion promotes adaptive immunity and potentiates checkpoint blockade," *EMBO molecular medicine*, vol. 10, no. 12, pp. e9342, 2018.
- [192] E. K. Rofstad, "Local Tumor Control following Single Dose Irradiation of Human Melanoma Xenografts: Relationship to Cellular Radiosensitivity and Influence of an Immune Response by the Athymic Mouse<sup>1</sup>," *Cancer Research*, vol. 49, no. 12, pp. 3163-3167, 1989.

- [193] A. L. Zietman, H. D. Suit, J. R. Ramsay *et al.*, "Quantitative studies on the transplantability of murine and human tumors into the brain and subcutaneous tissues of NCr/Sed nude mice," *Cancer Res*, vol. 48, no. 22, pp. 6510-6, Nov 15, 1988.
- [194] A. L. Epstein, F.-M. Chen, and C. R. Taylor, "A Novel Method for the Detection of Necrotic Lesions in Human Cancers," *Cancer Research*, vol. 48, no. 20, pp. 5842, 1988.
- [195] D. Zietkowski, "High resolution magnetic resonance spectroscopy of cervical cancer: correlation of changes in mobile lipid resonances with cellular processes," University of London, 2010.
- [196] I. Szadvari, O. Krizanova, and P. Babula, "Athymic nude mice as an experimental model for cancer treatment," *Physiol Res*, vol. 65, no. Suppl 4, pp. S441-s453, Dec 21, 2016.
- [197] J. C. Romijn, "Growth of tumor cells with different sensitivities for murine natural killer cells in young and adult athymic nude mice," *Exp Cell Biol*, vol. 53, no. 1, pp. 24-31, 1985.
- [198] U. Donat, J. Rother, S. Schäfer *et al.*, "Characterization of Metastasis Formation and Virotherapy in the Human C33A Cervical Cancer Model," *PLOS ONE*, vol. 9, no. 6, pp. e98533, 2014.
- [199] P. Workman, E. O. Aboagye, F. Balkwill *et al.*, "Guidelines for the welfare and use of animals in cancer research," *British Journal Of Cancer*, vol. 102, pp. 1555, 05/25/online, 2010.
- [200] U. o. B. C. A. C. a. U. Program, *UBC ACC Guideline on Rodents with Ulcerated Subcutaneous Tumours: Protocol Requirements, Monitoring, Managing and Humane Endpoints (2018)*, 2018.
- [201] D. M. Easty, G. C. Easty, R. L. Carter *et al.*, "Ten human carcinoma cell lines derived from squamous carcinomas of the head and neck," *British journal of cancer*, vol. 43, no. 6, pp. 772-785, 1981.
- [202] M. A. Torres, U. Raju, D. Molkenkine *et al.*, "AC480, formerly BMS-599626, a pan Her inhibitor, enhances radiosensitivity and radioresponse of head and neck squamous cell carcinoma cells in vitro and in vivo," *Investigational New Drugs*, vol. 29, no. 4, pp. 554-61, Aug 2011
- [203] E. K. Rofstad, K. Galappathi, and B. S. Mathiesen, "Tumor interstitial fluid pressure-a link between tumor hypoxia, microvascular density, and lymph node metastasis," *Neoplasia (New York, N.Y.)*, vol. 16, no. 7, pp. 586-594, 2014.
- [204] R. Karshafian, P. N. Burns, and M. R. Henkelman, "Transit time kinetics in ordered and disordered vascular trees," *Physics in Medicine and Biology*, vol. 48, no. 19, pp. 3225-3237, 2003/09/16, 2003.

- [205] J. Hudson, R. Williams, R. Karshafian *et al.*, "Quantifying Vascular Heterogeneity Using Microbubble Disruption-Replenishment Kinetics in Patients With Renal Cell Cancer," *Investigative radiology*, vol. 49, 11/11, 2013.
- [206] L. Boyer, I. Leguerney, S. Randall Thomas *et al.*, "Study of the reliability of quantification methods of dynamic contrast-enhanced ultrasonography: numerical modeling of blood flow in tumor microvascularization," *Phys Med Biol*, vol. 63, no. 17, pp. 17nt01, Aug 23, 2018.
- [207] P. Ugolini, A. Delouche, A. Herment *et al.*, "In vitro flow quantification with contrast power Doppler imaging," *Ultrasound Med Biol*, vol. 26, no. 1, pp. 113-20, Jan, 2000.
- [208] S. Peng, H. Ding, T. Fu *et al.*, "Savitzky-Golay filter based contrast-enhanced ultrasound quantification in hepatic tumors: Methodology and its correlation with tumor angiogenesis," *Clinical Hemorheology and Microcirculation*, vol. 73, pp. 271-282, 2019.
- [209] M. W. Dewhirst, R. Oliver, C. Y. Tso *et al.*, "Heterogeneity in tumor microvascular response to radiation," *International Journal of Radiation Oncology\*Biophysics*, vol. 18, no. 3, pp. 559-568, 1990/03/01/, 1990.
- [210] M. Gauthier, I. Leguerney, J. Thalmensi *et al.*, "Estimation of intra-operator variability in perfusion parameter measurements using DCE-US," *World journal of radiology*, vol. 3, no. 3, pp. 70-81, 2011.
- [211] M. Palmowski, W. Lederle, J. Gaetjens *et al.*, "Comparison of conventional time-intensity curves vs. maximum intensity over time for post-processing of dynamic contrast-enhanced ultrasound," *European Journal of Radiology*, vol. 75, no. 1, pp. e149-e153, 2010/07/01/, 2010.
- [212] J.-M. Hyvelin, I. Tardy, C. Arbogast *et al.*, "Use of Ultrasound Contrast Agent Microbubbles in Preclinical Research: Recommendations for Small Animal Imaging," *Investigative Radiology*, vol. 48, no. 8, pp. 570-583, 2013.
- [213] A. Dizeux, T. Payen, G. Barrois *et al.*, "Reproducibility of Contrast-Enhanced Ultrasound in Mice with Controlled Injection," *Molecular Imaging and Biology*, vol. 18, no. 5, pp. 651-658, 2016/10/01, 2016.
- [214] K. Nisa, S. Y. Lim, M. Shinohara *et al.*, "Repeatability and reproducibility of quantitative contrast-enhanced ultrasonography for assessing duodenal perfusion in healthy dogs," *The Journal of veterinary medical science*, vol. 79, no. 9, pp. 1585-1590, 2017.
- [215] A. Rix, M. Palmowski, F. Gremse *et al.*, "Influence of Repetitive Contrast Agent Injections on Functional and Molecular Ultrasound Measurements," *Ultrasound in Medicine & Biology*, vol. 40, no. 10, pp. 2468-2475, 2014/10/01/, 2014.

- [216] "A comparison of propofol with other injectable anaesthetics in a rat model for measuring cardiovascular parameters," *Laboratory Animals*, vol. 27, no. 3, pp. 250-257, 1993/07/01, 1993.
- [217] E. Stock, K. Vanderperren, H. Haers *et al.*, "Quantitative Differences Between the First and Second Injection of Contrast Agent in Contrast-Enhanced Ultrasonography of Feline Kidneys and Spleen," *Ultrasound in Medicine & Biology*, vol. 43, no. 2, pp. 500-504, 2017/02/01/, 2017.
- [218] J. Skrok, "Markedly increased signal enhancement after the second injection of SonoVue compared to the first—a quantitative normal volunteer study."
- [219] D. L. Miller, and J. Quddus, "Diagnostic ultrasound activation of contrast agent gas bodies induces capillary rupture in mice," *Proceedings of the National Academy of Sciences of the United States of America*, vol. 97, no. 18, pp. 10179-10184, 2000.
- [220] C. Strouthos, M. Lampaskis, V. Sboros *et al.*, "Indicator dilution models for the quantification of microvascular blood flow with bolus administration of ultrasound contrast agents," *IEEE Transactions on Ultrasonics, Ferroelectrics, and Frequency Control*, vol. 57, no. 6, pp. 1296-1310, 2010.
- [221] S. C. Tenant, and C. M. Gutteridge, "The clinical use of contrast-enhanced ultrasound in the kidney," *Ultrasound (Leeds, England)*, vol. 24, no. 2, pp. 94-103, 2016.
- [222] H. Schweiger, S. Ohlerth, and B. Gerber, "Contrast-enhanced ultrasound of both kidneys in healthy, non-anaesthetized cats," *Acta Veterinaria Scandinavica*, vol. 57, no. 1, pp. 80, 2015/11/25, 2015.
- [223] E. Stock, L. Duchateau, J. H. Saunders *et al.*, "Repeatability of Contrast-Enhanced Ultrasonography of the Kidneys in Healthy Cats," *Ultrasound in Medicine & Biology*, vol. 44, no. 2, pp. 426-433, 2018/02/01/, 2018.
- [224] Doctorlib. "Physiology 5th Ed. ANATOMY AND BLOOD SUPPLY," 2022; <https://doctorlib.info/physiology/physiology-2/51.html>.
- [225] S. Buitrago, T. E. Martin, J. Tetens-Woodring *et al.*, "Safety and Efficacy of Various Combinations of Injectable Anesthetics in BALB/c Mice," *Journal of the American Association for Laboratory Animal Science*, vol. 47, no. 1, pp. 11-17, //, 2008.
- [226] H. Wang, D. Hristov, J. Qin *et al.*, "Three-dimensional Dynamic Contrast-enhanced US Imaging for Early Antiangiogenic Treatment Assessment in a Mouse Colon Cancer Model," *Radiology*, vol. 277, no. 2, pp. 424-434, 2015.
- [227] J. Zhou, H. Zhang, H. Wang *et al.*, "Early prediction of tumor response to bevacizumab treatment in murine colon cancer models using three-

dimensional dynamic contrast-enhanced ultrasound imaging," *Angiogenesis*, vol. 20, no. 4, pp. 547-555, 2017.

- [228] S. Kotopoulos, M. Popa, M. Mayoral Safont *et al.*, "SonoVue(®) vs. Sonazoid™ vs. Optison™: Which Bubble Is Best for Low-Intensity Sonoporation of Pancreatic Ductal Adenocarcinoma?," *Pharmaceutics*, vol. 14, no. 1, Jan 1, 2022.
- [229] L. Hoff, "Nonlinear response of Sonazoid. Numerical simulations of pulse-inversion and subharmonics." pp. 1885-1888 vol.2.
- [230] G. S. Dimitrievich, K. Fischer-Dzoga, and M. L. Griem, "Radiosensitivity of vascular tissue. I. Differential radiosensitivity of capillaries: a quantitative in vivo study," *Radiat Res*, vol. 99, no. 3, pp. 511-35, Sep, 1984.
- [231] R. Taiji, H. Nishiofuku, T. Tanaka *et al.*, "Useful Parameters in Dynamic Contrast-enhanced Ultrasonography for Identifying Early Response to Chemotherapy in a Rat Liver Tumor Model," *Journal of Clinical Imaging Science*, vol. 11, pp. 15.
- [232] A. Broillet, J. Hantson, C. Ruegg *et al.*, "Assessment of microvascular perfusion changes in a rat breast tumor model using SonoVue™ to monitor the effects of different anti-angiogenic therapies," *Academic Radiology*, vol. 12, no. 5, Supplement, pp. S28-S33, 2005/05/01/, 2005.
- [233] E. J. Lehrer, R. Singh, M. Wang *et al.*, "Safety and Survival Rates Associated With Ablative Stereotactic Radiotherapy for Patients With Oligometastatic Cancer: A Systematic Review and Meta-analysis," *JAMA Oncology*, vol. 7, no. 1, pp. 92-106, 2021.
- [234] V. A. Potiron, R. Abderrahmani, K. Clément-Colmou *et al.*, "Improved Functionality of the Vasculature during Conventionally Fractionated Radiation Therapy of Prostate Cancer," *PLOS ONE*, vol. 8, no. 12, pp. e84076, 2014.

## Appendix

## A1. Intratumour heterogeneity

Histogram parameters, standard deviation (SD), coefficient of variation (CoV), modified full-width half maximum (mFWHM), skewness, and kurtosis of pixel wise PE, WIT, MTT, and WOUT, are shown for C33A tumours (C5 study) and HN5 tumours (H1) study at the pretreatment imaging timepoint discussed in chapter 4

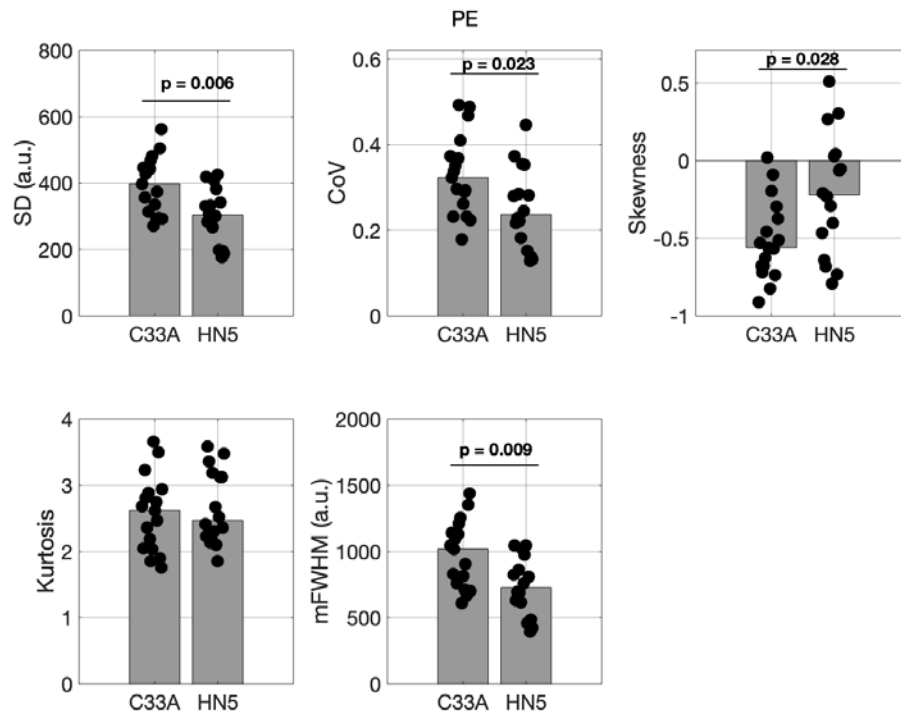


*Figure A1-1: Intratumour heterogeneity of PE for C33A and HN5 tumours. Heterogeneity is characterised using SD, CoV, skewness, kurtosis and mFWHM of pixel-wise PE. C33A tumours had greater intratumour heterogeneity demonstrated by the significantly bigger SD, CoV, and mFWHM.*

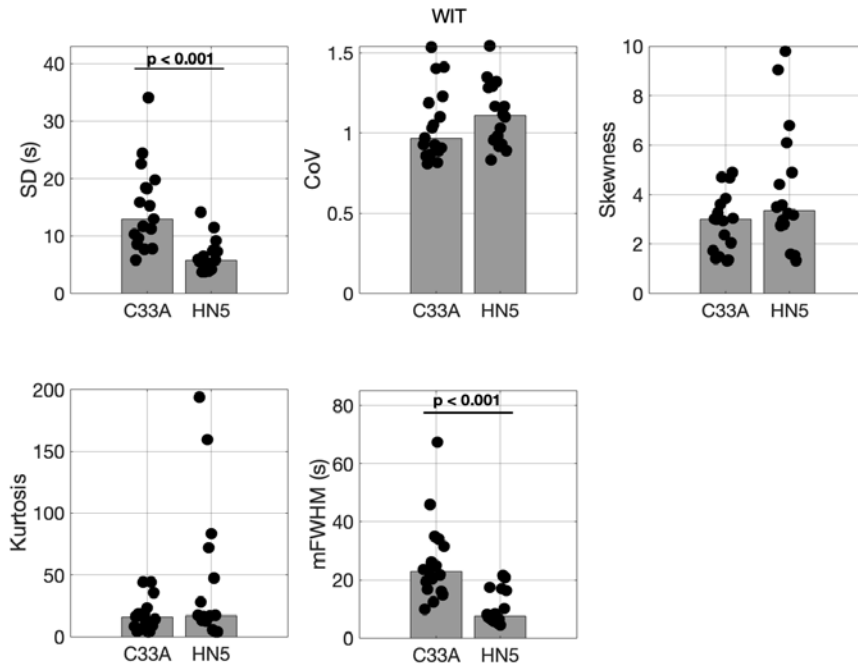


Figure A1-2: Intratumour heterogeneity of WIT for C33A and HN5 tumours. Heterogeneity is characterised using SD, CoV, skewness, kurtosis and mFWHM of pixel-wise WIT.

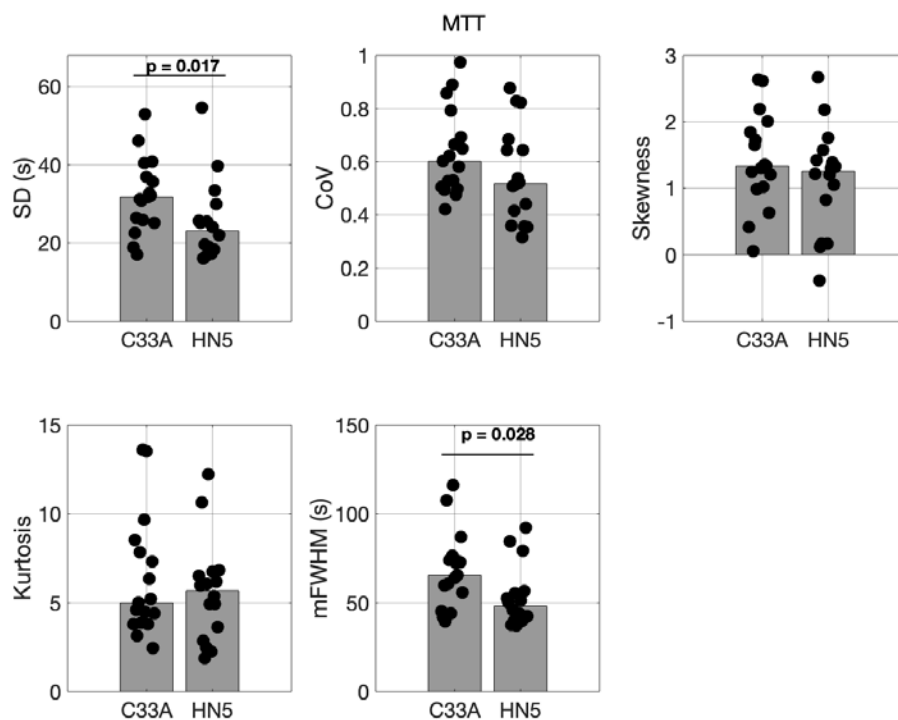


Figure A1-3: Intratumour heterogeneity of MTT for C33A and HN5 tumours. Heterogeneity is characterised using SD, CoV, skewness, kurtosis and mFWHM of pixel-wise MTT.

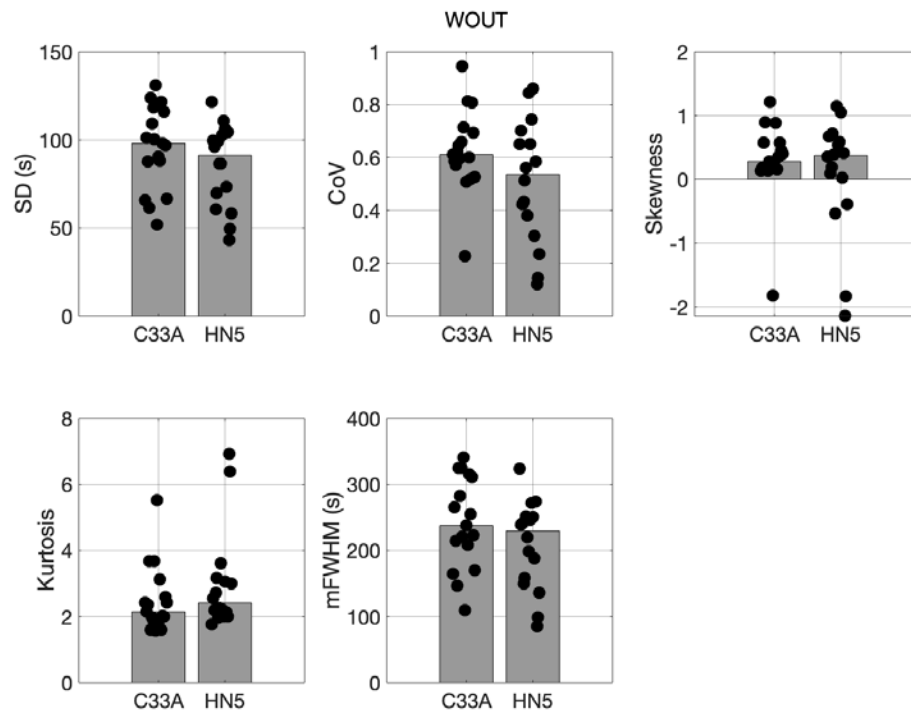


Figure A1-4: Intratumour heterogeneity of WOUT for C33A and HN5 tumours. Heterogeneity is characterised using SD, CoV, skewness, kurtosis and mFWHM of pixel-wise WOUT.

## A2. Pixel – wise TAC metric correlations

Presented here are the correlation obtained from each tumour of the HN5 and C33A models using pixel-wise TAC metrics, discussed in chapter 4.

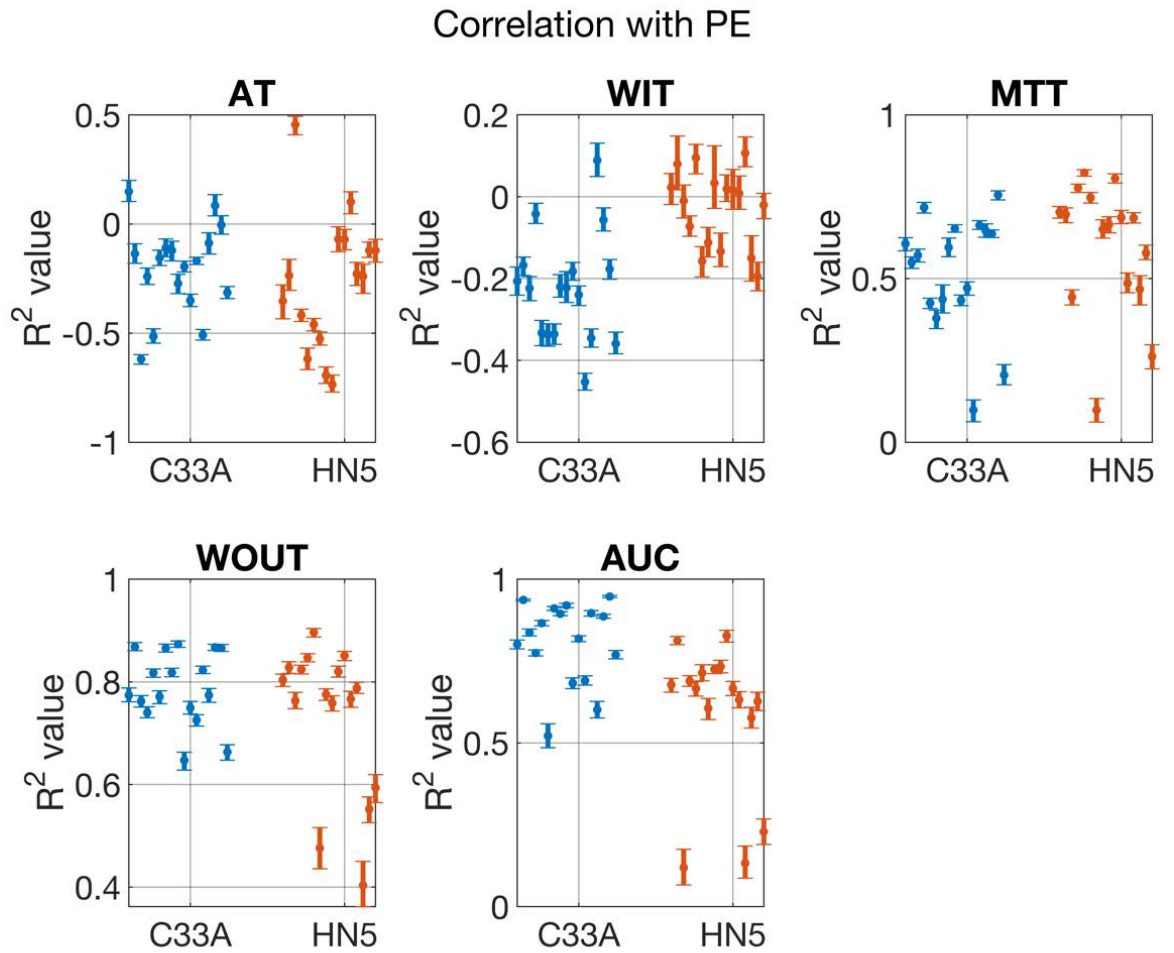


Figure A2-1: Correlation of pixel-wise PE with other DCE-US metrics obtained in all C33A (blue) and HN5 tumours (orange). The correlation coefficient of each tumour is shown with the error bars representing 95% CIs. PE was negatively correlated to AT and WIT (for C33A tumours only) and positively correlated to MTT, WOUT and AUC in both models

### Correlation with AT

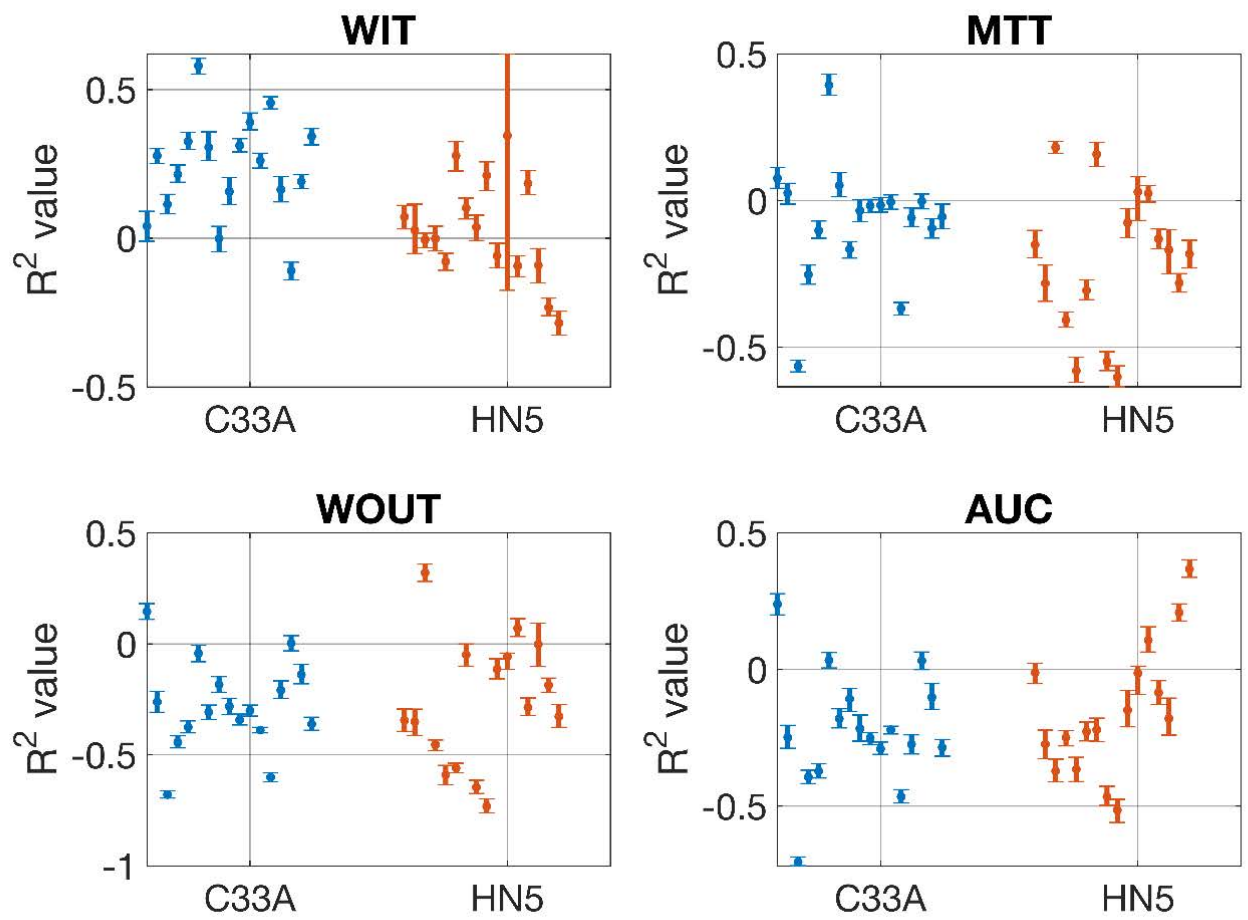


Figure A2-2: Correlation of pixel-wise AT with other DCE-US metrics obtained in all C33A (blue) and HN5 tumours (orange). The correlation coefficient of each tumour is shown with the error bars representing the 95% CIs. AT was positively correlated to WIT in the C33A model, and negatively to MTT (in HN5 tumours only), WOUT and AUC.

Correlation with WIT

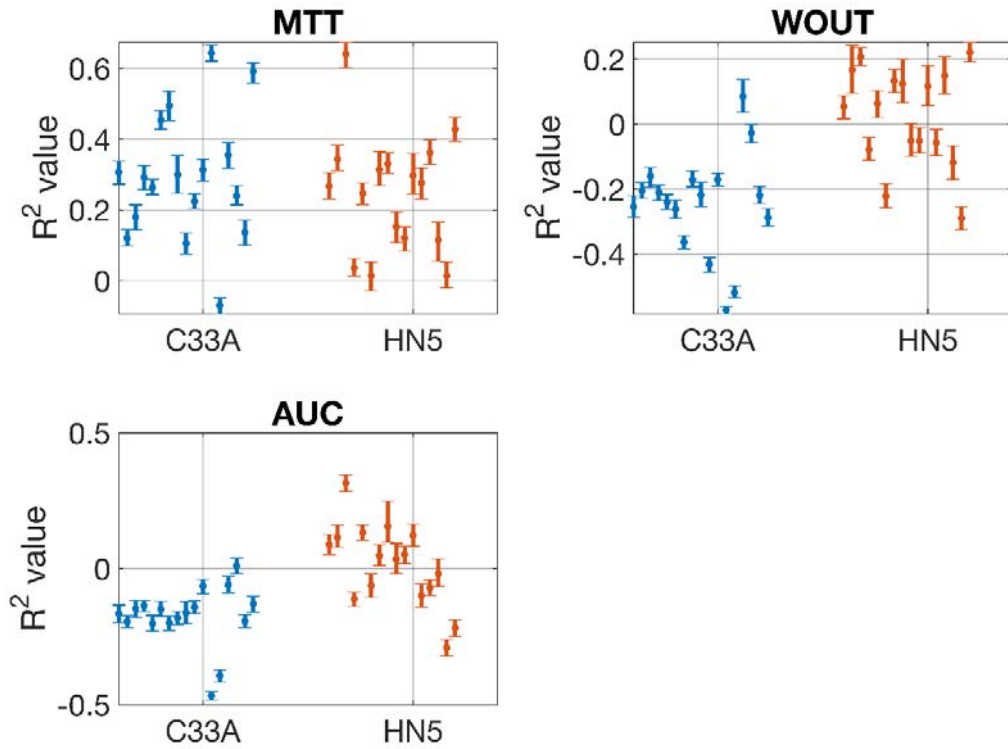


Figure A2-3: Correlation of pixel-wise WIT with other DCE-US metrics obtained in all C33A (blue) and HN5 tumours (orange). The correlation coefficient of each tumour is shown with the error bars representing the 95% CIs. WIT was positively correlated to MTT, and negatively to WOUT and AUC in C33A tumours.

Correlation with MTT

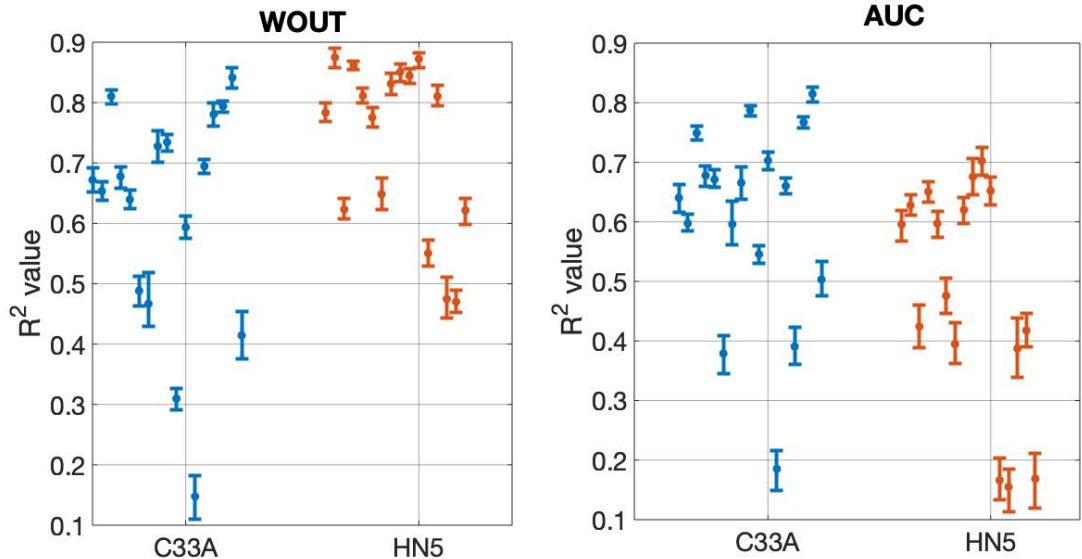


Figure A2-4: Correlation of pixel-wise MTT with other DCE-US metrics obtained in all C33A (blue) and HN5 tumours (orange). The correlation coefficient of each tumour is shown with the error bars representing the 95% CIs. MTT was positively correlated to WOUT and AUC in in both tumour models.

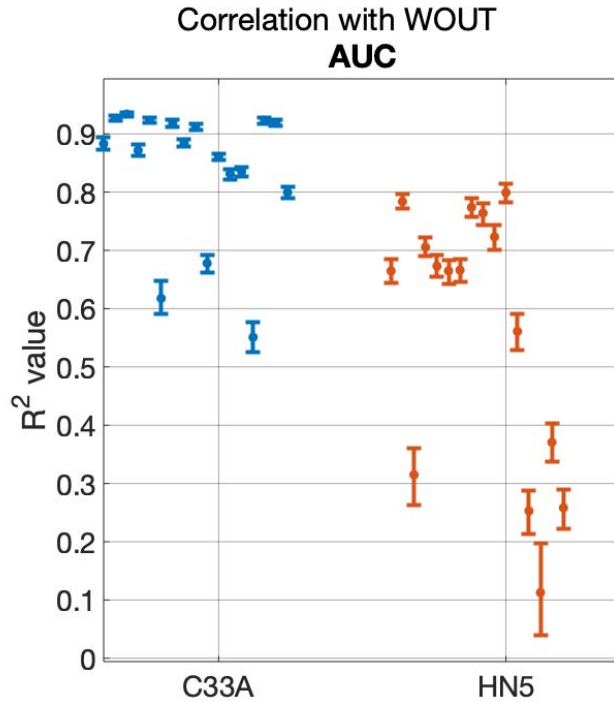


Figure A2-5: Correlation of pixel-wise WOUT and AUC obtained in all C33A (blue) and HN5 tumours (orange). The correlation coefficient of each tumour is shown with the error bars representing the 95% CIs. WOUT was positively correlated to AUC in both tumour models.

### A3. Histogram analysis of HN5 tumours

Presented here is the change in histogram parameters of PE, AUC, AT, and WOUT in the HN5 study discussed in chapter 5 (H1 study), demonstrating an increase in intratumour heterogeneity from the pretreatment imaging timepoint ( 3 -6 hours prior to radiation) to the posttreatment timepoint, 48 hours after . This was the case in all groups, complete responders, partial responders, and control tumours.

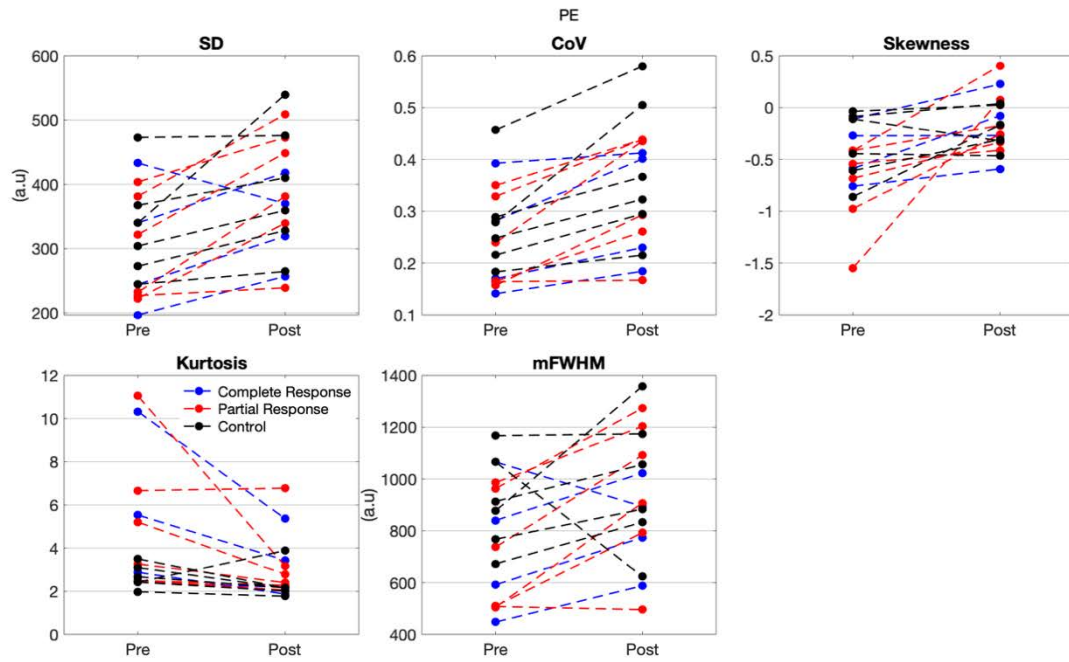


Figure A3-1: Histogram parameters for PE distribution at the two imaging timepoints in HN5 tumours. The intratumour heterogeneity of PE increased as evident by a significant increase in standard deviation (SD), coefficient of variation (CoV), skewness, and modified full width half maximum (mFWHM), and a decrease in kurtosis in all tumours, regardless of treatment or response.

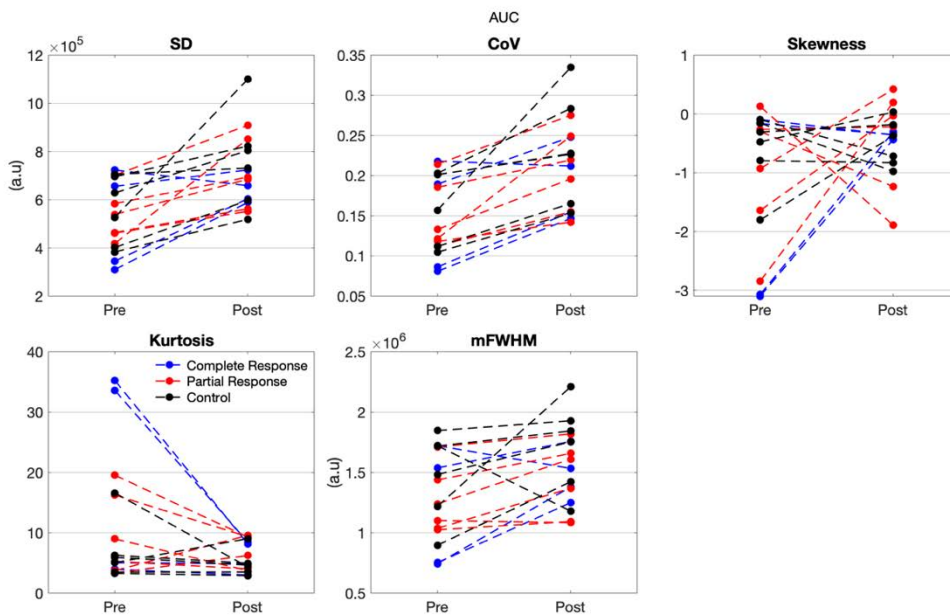


Figure A3-2: Histogram parameters for AUC distribution at the two imaging timepoints in HN5 tumours. The intratumour heterogeneity of AUC increased as evident by a significant increase in standard deviation (SD), coefficient of variation (CoV), and modified full width half maximum (mFWHM).

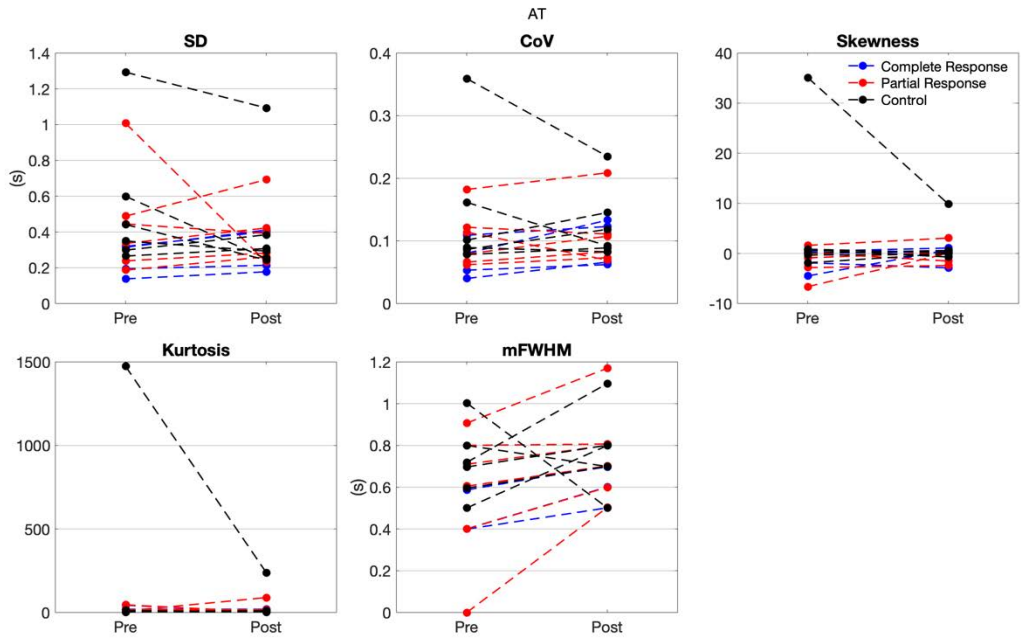


Figure A3-3: Histogram parameters for AT distribution at the two imaging timepoints in HN5 tumours. The intratumour heterogeneity of AT increased as evident by a significant increase in the mFWHM,

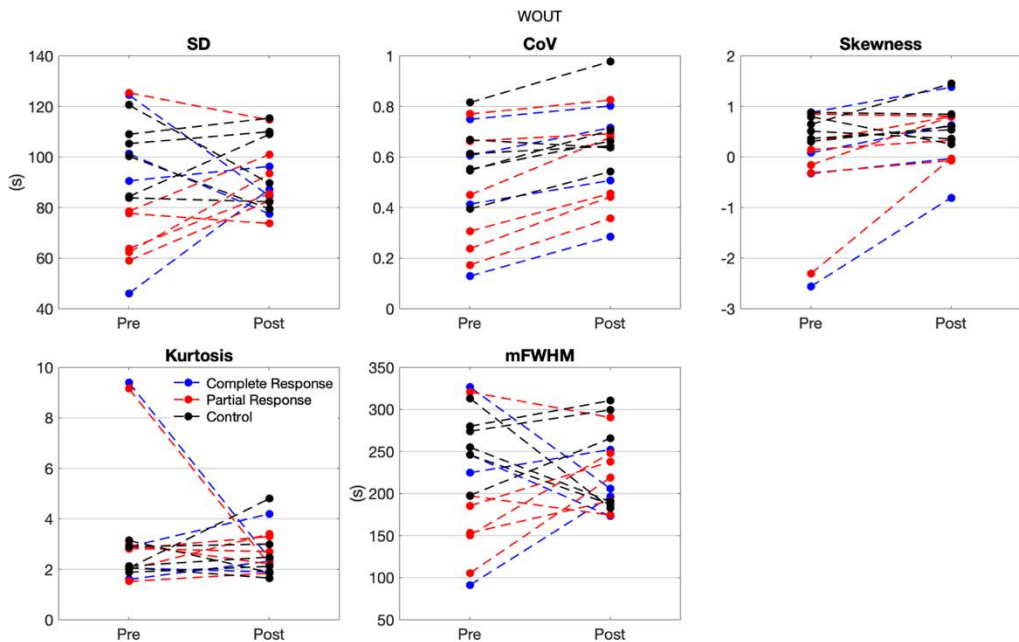


Figure A3-4: Histogram parameters for WOUT distribution at the two imaging timepoints in HN5 tumours. The intratumour heterogeneity of WOUT increased as evident by a significant increase in the coefficient of variation (CoV) and skewness.

## A4. Variation in skewness

Estimation of the skewness of pixel-wise TAC metrics obtained from repeat DCE-US imaging revealed large variation, which was excluded from the main discussion. Presented here is the signed variation in the skewness parameter for DCE-US metrics, calculated from the repeatability study discussed in chapter 5, and an example of a calculated large variation with no apparent change in the histogram.

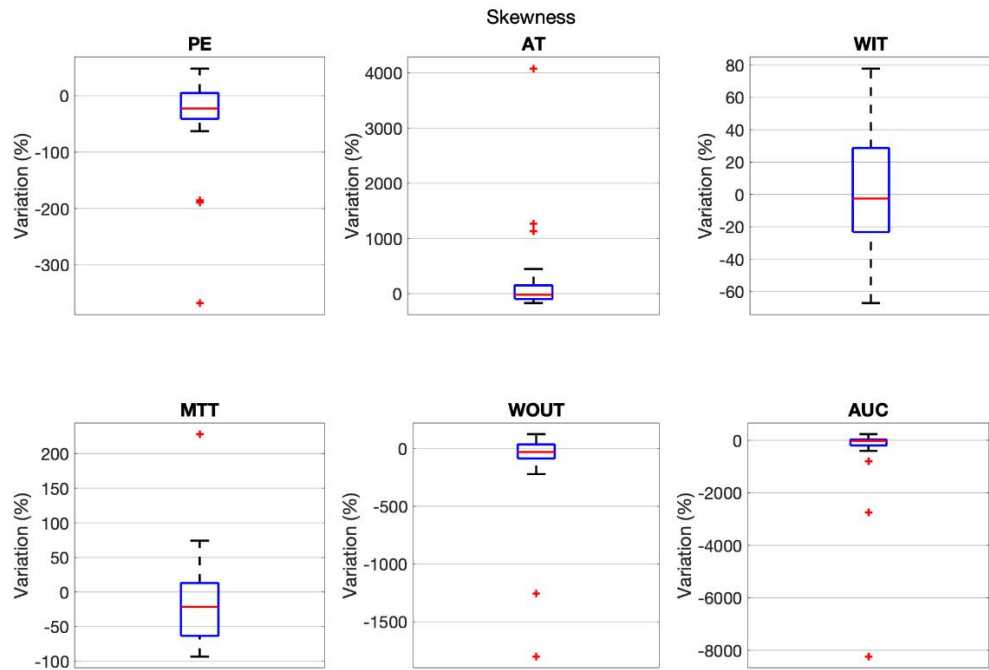


Figure A4-1: Variation in skewness of DCE-US metric histograms with high variation calculated in PE, AT, WOUT, and AUC, for some tumours (outliers).

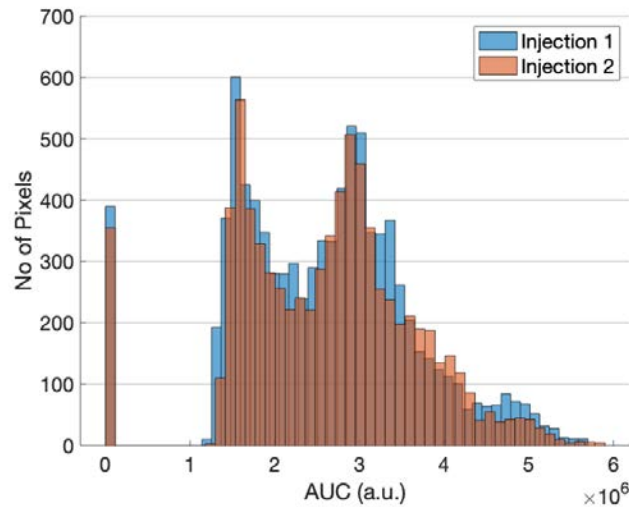


Figure A4-2: Example histogram distribution of pixel-wise AUC showing high variation in skewness ( $> 8000\%$ ) despite little overall change. Skewness for injection 1 = 0.0016 and for injection 2 = 0.1320.

## A5. Combining HN5 and C33A tumours for analysis of 3D DCE-US

In an attempt to increase the sample number, C33A tumours from studies C6 & C7, and HN5 tumours from studies H2 & H3, discussed in chapter 7, were combined for the assessment of 3D DCE-US and radioresponse. No significant results were found in comparison to the results obtained from the separate analysis of tumour models discussed in the main thesis. Presented here is the change in DCE-US metrics obtained from the whole-VOI and centre-tumour ROI of all tumours combined.

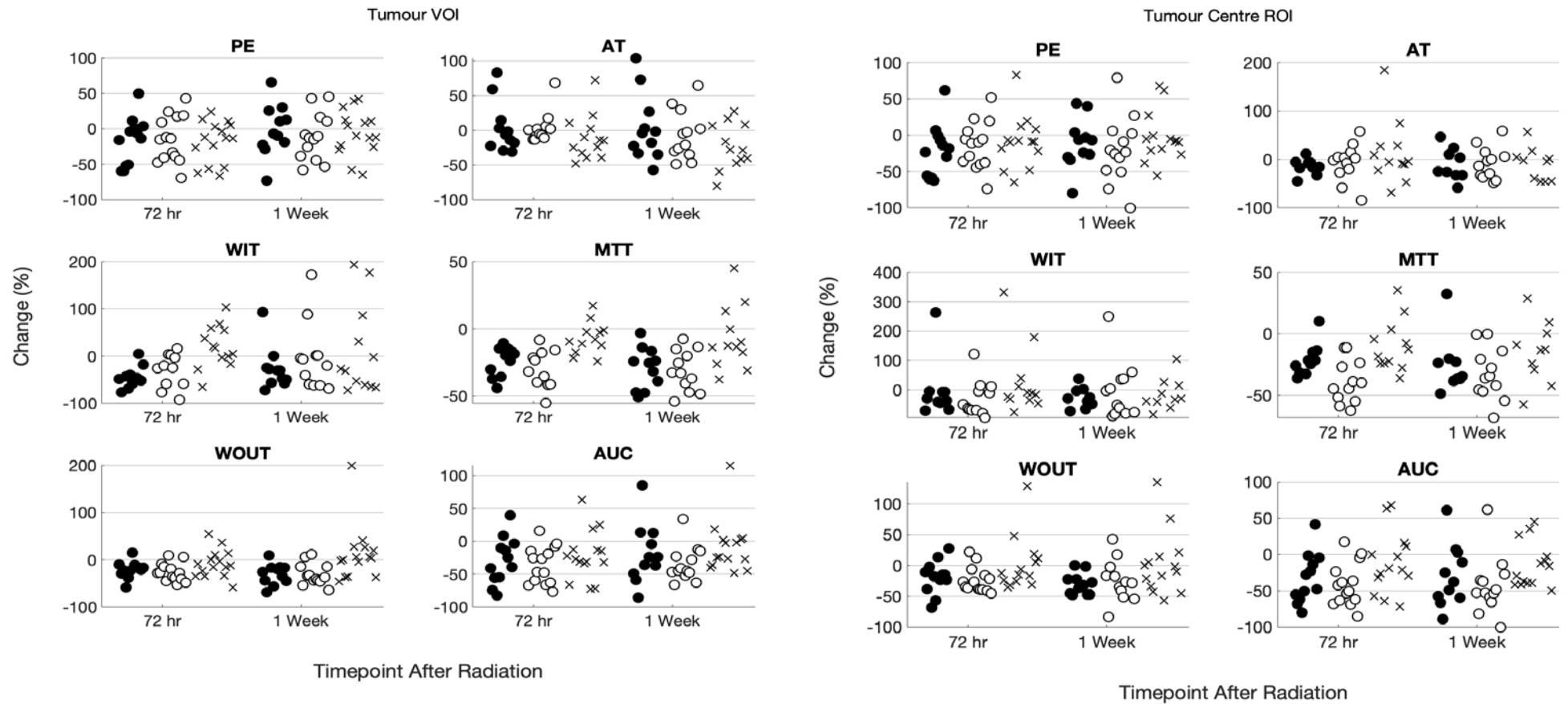


Figure A5-1: the change in DCE-US metrics obtained from the tumour volume (left) and centre-tumour ROI (right) from pretreatment to 72 hours and 1 week after radiation, for both C33A and HN5 tumours, shown according to response, with complete responders (filled circle), partial responders (white circle), and control tumours (cross).

